Development of Millifluidic Devices for Structural Characterisation of Viscoelastic Materials

Catherine T. O'Brien

The University of Sheffield

Department of Chemistry

Thesis submitted for the degree of Doctor of Philosophy

January 2021

Declaration

The work described in this thesis was carried out at the University of Sheffield under the supervision of Professor Tony J. Ryan and Dr Oleksandr Mykhaylyk between October 2016 and January 2021. It has not been submitted, either wholly or in part, for any other degree. All the work is the original work of the author except where acknowledged by references.

Signature: …………………………………

Catherine Theresa O'Brien   January 2021

Abstract

The work reported in this thesis involves the design and fabrication of millifluidic devices suitable for the investigation of viscoelastic materials by small-angle X-ray scattering (SAXS). It was found that existing designs of micro- or millifluidic devices presented in literature were unsuitable for the study of viscous materials due to the larger pressures exerted on the walls of devices by the fluid. Leakage was observed in prototypes similar to those observed in the literature, specifically at the inlet and window areas. A range of design criteria necessary for the fabrication of successful millifluidic devices for viscoelastic materials were developed. The features of such a device, created as a result of the prototypes trialled, included the use of Luer lock inlets, enclosed channels and a threaded sealed window port providing access to the sample using scattering and visualisation techniques.

Stereolithography (SLA) three-dimensional (3D) printing was utilised to provide an inexpensive, rapid and straight-forward fabrication method, using a commercially available printer. Devices could be produced with very few fabrication and assembly steps providing good print resolution and leading to a smooth internal surface non-interfering with flow. This fabrication method was found to be a viable alternative to the traditional, time-consuming and expensive, soft lithography techniques often used for microfluidic manufacture.

The design criteria formulated in this work could be employed to fabricate a range of millifluidic geometries, with straight channel and cross slot geometries demonstrated in this thesis as the most representative examples for shear and extensional flow, respectively. The devices produced could be combined with a variety of techniques, in particular optical microscopy and X-ray scattering were utilised extensively in this work. Both geometries were shown to possess a stable and reproducible laminar flow field for the materials tested at all Q values. This was confirmed by Reynolds number (Re) values estimated from finite element analysis (FEA) simulations as well as by experimental techniques such as particle tracing.

Two types of polymeric materials forming anisotropic morphologies under flow conditions were utilised as model materials within the millifluidic devices; an aqueous solution of modified cellulose and water dispersions of worm-like micelles formed by self-assembled block copolymers. The straight channel millifluidic device shows flow behaviour analogous to a slit rheometer, with polarised optical microscopy (POM) and SAXS measurements indicating alignment of the worm-like micelles under flow. Despite the fact that the cellulosic materials demonstrated optical birefringence under flow, suggesting the formation of an orientated morphologies, this morphology was not detectable by SAXS possibly because of a small volume of oriented material. The cross-slot millifluidic device has strong extensional forces along the outlet plane as seen by POM and SAXS. Extensive mapping of the cross-slot region using a synchrotron SAXS beamline in a microfocus configuration identifies regions of orientation of the worm-like micelles where extensional flow is present, as well as remarkable stability in the flow field over time.

Acknowledgements

I would like to take this opportunity to thank both of my supervisors, Professor Tony Ryan and Dr Oleksandr Mykhaylyk, for their guidance, insight and support over the past four (and a bit) years. I appreciate everything both of you have done during my time as a PhD student; from lengthy SAXS chats to fun fuelled ski trips, I will never forget my time in the group. Thank you for giving me the opportunity to research with you both. I would also like to thank everyone in the Ry-Myk group, especially those who I have spent countless hours chatting to on tea breaks, instead of doing work! Individual thanks go to Tom Franklin for always being up for a trip to Coffee Revs to 'write' and eat cake as well as everyone in the D43 office, specifically Courtney Thompson and Shannon North, who have made every day a laugh, even during COVID times.

My PhD sponsor, Diamond Light Source and the EPSRC are thanked for their funding. In particular, I would like to acknowledge Dr. Nick Terrill and the rest of the team at I22 for the support provided during the project.

I am incredibly grateful to those who have helped during my time in the Ry-Myk group, specifically Nick Penfold for the worms which turned out to be instrumental in the project(!), Nikul Khunti for all the 3D printing help and chats, as well as always being a lunch/dinner buddy at Diamond, and Matt Derry for always giving me a shoulder to cry on and an ear to complain into. To Kat Fish, thank you for mentoring me during the write up stage, the help and advice you have given me has been invaluable and you made a daunting task so much easier! Each one of you have provided essential support during my PhD in ways I will always be appreciative of.

To my family and friends who have supported me during this time, thank you for everything you have done to help keep me sane. Mum, especially, you deserve more thanks than I could ever give for always supporting me, but hopefully going to Egypt (finally) will make some headway! To Sarah Wilson, thank you for always carving time out of your day for chats and hugs, whenever I've needed them! Your friendship has kept me afloat during the past however many years and I hope I can repay the favour every time you need it.

Lastly, to Matt, thank you for being my constant during my PhD, keeping me on an even keel (especially during the first, second *and* third lockdown when I thought writing would never end). Thank you for all of your help and support with my work, and always being there to listen whenever I've needed you to and knowing what I need to make things better. I don't how you always make me laugh, but you do! You honestly bring out the best in me and I don't think I could ever find a better friend and partner. You are my family, and I wouldn't change it for the world. I am looking forward to moving onto the next chapter in our lives together, I hope it contains all you want and more.

Publication List

Primary Publications

1. **O'Brien C. T.**; Virtanen T.; Donets S.; Jennings J.; Guskova O.; Morrell A. H.; Rymaruk M. J.; Ruusuvirta L.; Salmela J.; Setala H.; Sommer J.-U.; Ryan A. J.; Mykhaylyk O.O.; Control of the aqueous solubility of cellulose by hydroxyl group substitution and its effect on processing; *Polymer*, **2021**, 223(1).

2. Rymaruk, M. J., **O'Brien, C. T.**, Gyorgy, C., Darmau, B., Jennings, J., Mykhaylyk, O. O., Armes, S. P.; Small-angle X-ray scattering studies of block copolymer worms: formation of ordered phases in concentrated solution during polymerization-induced self-assembly; *Angewandte Chemie*; **2021.**

Secondary Publications

1. Rymaruk, M. J., Hunter, S. J., **O'Brien, C. T.**, Brown, S. L., Williams, C. N., Armes, S. P.; RAFT dispersion polymerisation in silicone oil; *Macromolecules*; **2019**; 52(7).

2. Rymaruk, M. J., **O'Brien, C. T.**, Brown, S. L., Williams, C. N., Armes, S. P.; Effect of core-crosslinking on the physical properties of poly(dimethylsiloxane)-based diblock copolymer worms prepared in silicone oil; *Macromolecules*; **2019**; 52(18).

3. Sponchioni, M., **O'Brien, C. T.**, Borchers, C., Wang, E., Rivolta, M., Penfold, N. J. W., Canton, I., Armes, S. P.; Probing the mechanism for hydrogel-based stasis induction in human pluripotent stem cells: is the chemical functionality of the hydrogel important?; *Chemical Science*; **2019**; 11(1).

4. Byard, S. J., **O'Brien, C. T.**, Derry, M. J., Williams, M., Mykhaylyk, O. O., Blanazs, A., Armes, S. P.; Unique aqueous self-assembly behaviour of a thermoresponsive deblock copolymer; *Chemical Science*; **2020**, 11(2).

5. Rymaruk, M. J., **O'Brien, C. T.**, Brown, S. L., Williams, C. N., Armes, S. P.; RAFT dispersion polymerisation of benzyl methacrylate in silicone oil using a silicone-based methacrylic stabiliser provides convenient access to spheres, worms and vesicles; *Macromolecules*, **2020**, 53(5).

Symbol List

Symbol	Terminology	Units
$\dot{\gamma}$	Shear rate	s^{-1}
$\dot{\gamma}_{crit}$	Critical shear rate	s^{-1}
$\dot{\gamma}_0$	Shear rate at which the zero-shear viscosity is measured	s^{-1}
γ	Shear strain	-
δ	Deformation	m
δ_{Re}	Retardance	-
ε_H	Hencky, or true strain	-
$\dot{\varepsilon}_H$	Hencky strain rate	s^{-1}
ζ	Zeta-potential	mV
η	Viscosity	Pa s
η_a	Apparent viscosity	Pa s
η_c	Consistency	Pa s
η_E	Extensional viscosity	Pa s
η_p	Planar extensional viscosity	Pa s
η_0	Zero-shear viscosity	Pa s
θ	Angle	°
λ	Wavelength	m
ν	Excluded volume parameter	-
ξ	Scattering length density	m^{-2}
ρ	Density	kg m^{-3}
σ	Stress	Pa
σ_E	Extensional stress	Pa
ω	Frequency of light	s^{-1}
ϕ	Azimuthal angle	°
Ω	Angular frequency	s^{-1}
A	Cross-sectional area	m^2
An	Analyser	-
B	Birefringence	-
b	Kuhn length	m
b_e	Scattering length of an electron	m
C	Stress optical coefficient	Pa^{-1}
c	Speed of light	
De	Deborah number	-
D_h	Hydraulic diameter	m
DS	Degree of substitution	-
F	Force	kg m s^{-2}
$F(q)$	Form factor	nm^{-1}
$g_{particle}I$	Correlation function	-
G	Elastic modulus	Pa
G'	Storage modulus	Pa
G''	Loss modulus	Pa
H	Height	m
I	Intensity of light	A.U.
I_0	Intensity of polarised light	A.U.
$I(q)$	Intensity of scattering vector	A.U.

Symbol List

Symbol	Terminology	Units
L	Length	m
m	Mass	kg
MS	Molar substitution	-
M_n	Number-average molecular weight	kg mol^{-1}
M_w	Weight-average molecular weight	kg mol^{-1}
n	Power law index	-
n_e	Extraordinary refractive index	-
N_A	Avogrado's constant	mol^{-1}
N_w	Aggregation number	-
n_i	Refractive index	-
n_o	Ordinary refractive index	-
p	Pressure	Pa
Δp	Pressure drop along a channel	-
P	Polariser	-
P_2	Herman's orientation parameter	-
q	Scattering vector	nm^{-1}
Q	Volumetric flow rate	m^3 s^{-1}
R	Radius	m
Re	Reynolds number	-
R_g	Radius of gyration	nm
r_t	Relaxation time	s
$S(q)$	Structure factor	nm^{-1}
t	Time	s
T_g	Glass transition temperature	°C
T_m	Melting point	°C
T_r	Trouton's ratio	-
V	Volume	m^3
v	Velocity	m s^{-1}
v_0	Velocity at a channel centre	m s^{-1}
W	Width	m
Wi	Weissenberg number	-
x_{sol}	Volume fraction of solvent	-

Table of Contents

Table of Contents

Chapter 3 – Finding Suitable Worm-like Micelles to act as Model Systems

Chapter 4 – Fabricating and Designing Millifluidic Devices

Chapter 1 – Introduction

1.1 Soft Condensed Matter (SCM)

Soft condensed matter (SCM) is a term encompassing a wide range of materials, whose state of matter is not wholly liquid or crystalline solid.[1] However, one commonality between SCM materials is their non-linear response to external forces.[1,2] Materials such as colloidal dispersions, gels, liquid crystals and polymers are all examples of SCM. These materials are found in all aspects of daily life, from plastics, food, soap, cells and DNA.[1]

Due to the complex nature of these materials, it is important for full and accurate characterisation. A number of techniques are utilised for the characterisation of SCM; however, rheology is one of the most commonly employed. This characterisation technique is more fully explored in **Section 1.2**, as herein only a short review of the characterisation of SCM by rheological techniques is undertaken. One such rheological technique is measuring the non-linear response of SCM upon application of an incrementally increasing stress or strain. This methodology has been employed to examine the stiffness of many biological materials, including fibrin,[3–5] collagen[4,6] and tumour cells.[7,8] Another approach is to measure the stress and strain during oscillation to calculate the storage and loss moduli (G' and G'') of a material. This is frequently utilised to measure the strength of polymeric gels.[9–12]

Rheo-optic measurements couple rheology with optical techniques to enable the investigation of structural transitions, frequently observed with SCM, such as ordering or crystallisation. Rheo-optic measurements can be performed in either real space, with the use of microscopes and imaging techniques, or reciprocal space, using scattering techniques. Real space rheo-optic techniques have previously been utilised to observe the onset of birefringence in polymeric materials[13,14], whereas reciprocal space rheo-optic methods can be used to gain structural information about soft matter aligned with flow.[15]

A third adaption of rheological characterisation techniques is microrheology which is utilised for small samples or objects, such as cells. This technique can be either passive, utilising Brownian motion of material, or active, by the application of a force. Active microrheology is typically performed using micro- or millifluidics due to the precise control offered over small sample sizes.[16–18]

1.1.1 Polymers

Although there are many materials within SCM, polymers are of direct importance to the work undertaken in this thesis. Polymers are long-chain structures, consisting of many, linked monomer units and are often given the name macromolecules (**Figure (1.1)**). In some cases, these polymers comprise only one type of monomer unit, and as such are termed homopolymers. However, in more complex cases, there could be many different monomers which are linked to form a long chain. A copolymer, for example, is a macromolecule consisting of two or more different monomer units. The arrangement of these monomer units can vary, with the two extremes being a block copolymer and a statistical copolymer. In block copolymers, there are two distinct regions of each monomer; this can be visualised as two homopolymers linked at the terminal monomer units. Statistical copolymers, on the other hand, have a random distribution of monomer units.
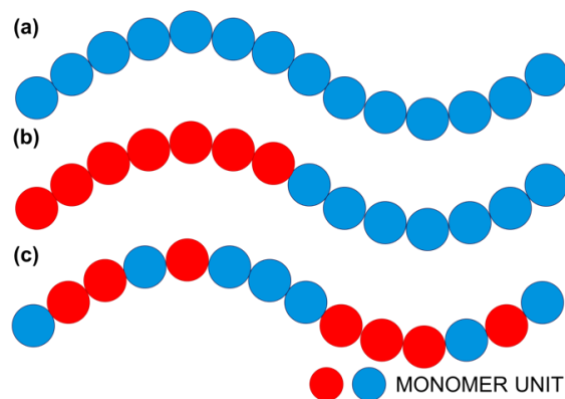
Figure (1.1). Schematic of **(a)** a simple homopolymer, with each blue circle representing a single monomer unit, **(b)** a block copolymer and **(c)** a statistical copolymer.

Polymers can be divided into two main categories: synthetic or natural. Naturally occurring polymers include materials like proteins, silk and cellulose and often have very specific biological functions, such as providing structural integrity, energy sources and protection of young. Synthetic polymers are usually derived from oil & gas and were first discovered in the 1910s; they include materials such as nylon, polyester and polypropylene. These materials have very similar backbones, comprising mainly carbon, and can be used for a wide range of applications. For example, polypropylene has been utilised in furniture, sanitary products and roofing purposes.

The application of a polymer is dependent on both the chemical and physical properties exhibited by the bulk system. The chemical properties of a polymer are, for the most part, determined by the chemical structure of the repeat units present in the polymer backbone. If many methyl functional groups are present, for example, a polymer is likely to be hydrophobic, and therefore water-insoluble; consequently, the polymer could be utilised in water-proofing applications.

Some physical properties are also established by the constituent monomer units in a polymer, such as the molecular weight, density and degree of polymerisation. However, the physical properties of a polymer are also dependent on the individual chains and the morphological structure adopted by them, including crystallinity and solubility. For example, highly ordered polymer chains, in bulk, would likely be a solid, possibly with a semi-crystalline structure. On the other hand, long polymer chains in a liquid state, or dissolved in a suitable solvent, are likely to have a high viscosity, and may even be considered gels, due to chain entanglements.

A phenomenon called self-assembly occurs in both synthetic and natural polymers. Self-assembly is when several polymer chains assimilate to form larger structures. With naturally occurring polymers, self-assembly often occurs when a polymer is amphiphilic, where both

hydrophilic and hydrophobic fragments are present. The hydrophilic parts of the molecule have favourable interactions with water, whereas the hydrophobic portions aim to minimise these interactions. By packing many amphiphilic macromolecules together, particles are formed which shields the hydrophobic parts from the solvent. Larger particles often adopt vesicle-like structures; this also occurs in many lipids which form simple bilayers; an essential element of cell walls (**Figure (1.2)(b)**). Other examples include DNA forming the iconic double helix (**Figure (1.2)(a)**), and cellulose molecules forming crystal structures which ultimately lead to microfibrils, giving the structural strength observed in flora.

Synthetic polymers can undergo self-assembly in a similar way to naturally occurring polymers, if the polymer chains are amphiphilic.[19,20] However, they can also self-assemble during synthesis when one block is solvophilic (stabiliser or corona), and the second, growing block becomes insoluble in the reaction solvent. The unfavourable solvent-polymer interactions cause the block copolymer chains to pack together, forming micelles with the solvophobic block (core) hidden, to minimise these interactions. The micelle shape adopted is dependent on the relative volume fractions of both the corona and the core; however, sphere, worm and vesicle morphologies are frequently encountered (**Figure (1.2)(c – e)**), with the less-common lamellae also seen.
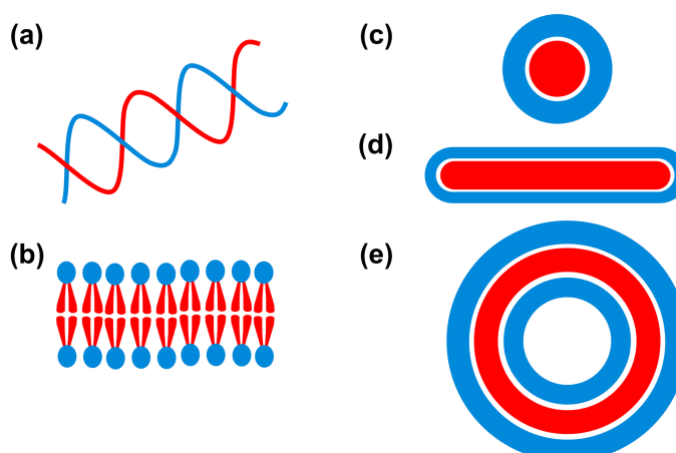
Figure (1.2). Self-assembled structures found in nature and in synthetic polymers. The self-assembled structures are as follows **(a)** DNA double helix, **(b)** phospholipid bilayer **(c)** sphere micelle **(d)** worm-like micelle and **(e)** vesicle micelle - diagrams not to scale.

The physical properties exhibited by a bulk system can be influenced by the macroscopic structures adopted by polymeric chains. A dispersion of polymeric worm-like micelles will have a much higher viscosity, for instance, than a system which has adopted a spherical morphology. Understanding both the physical and chemical properties of a polymeric system is essential for its successful application. To achieve this, the polymer needs to be fully characterised by a range of techniques. Commonly utilised techniques include rheology, microscopy and small-angle scattering.

1.2 Rheology

Rheology is the study of the flow or deformation of matter,[21] and is a technique often utilised to characterise polymeric materials. Typically, the rheological properties of a polymer are determined by applying an external force to the material and measuring the response.[22] Two terms are used to describe this situation accurately; stress (σ) and strain (γ). Stress describes the applied force per unit area, whereas strain describes how a material deforms under applied stress (**Equations (1.1)** and **Figure (1.2)**).

$$\sigma = \frac{F}{A} \tag{1.1}$$

Equation (1.1). Equation for stress (σ / Pa) where F is force applied in N and A is the sample area in m^2.[22]

$$\gamma = \frac{\delta}{H} \tag{1.2}$$

Equation (1.2). Strain (γ / dimensionless) can be calculated from the deformation of the sample (δ / m) and the sample height (H / m) is the sample.[22]

Several important features can be characterised by rheology, such as viscosity (η), the storage and loss moduli (G' and G'' / Pa), and the glass transition temperature (T_g / °C) to name a few. These features give a good overview into the physical behaviour of a polymer, such as flow resistance, and allow convenient comparison with other materials. However, for the work contained in this thesis, viscosity is the most relevant property and will be the only property discussed further.

1.2.1   Shear Rheology

A system experiencing a continuous force parallel to its cross-section is said to be undergoing shear. Studying how this force affects the system under investigation is called shear rheology; one of the most commonly used rheology techniques. The most straightforward shear flow experiments utilise two plates, with a material sandwiched between them (**Figure (1.3)**). One of the plates is fixed, and the other is free to move, leading to the application of force on the sample. Shear flow experiments can also be thought of as simple sliding flows; where the sample consists of consecutive layers sitting on top of each other and sliding past each other, but never mixing, as the plate rotates. These sorts of sliding flows occur at most boundaries of flow experiments or processing flows.
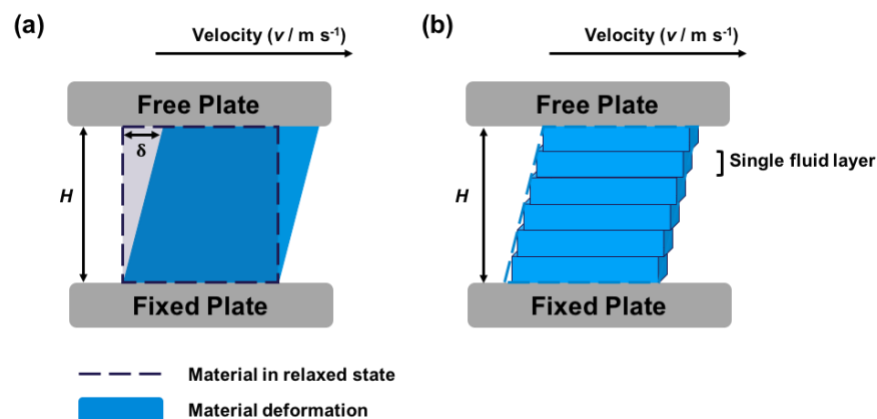
Figure (1.3). Schematic of the deformation incurred on a material as a subject of the velocity, v, or force applied to it in a plate-plate shear flow experiment **(a)** and the corresponding diagram of a sliding flow where a material exists as consecutive, unmixing, layers **(b)**. The sample gap, or thickness, is represented by H.

1.2.1.1   Shear Viscosity

Viscosity is the measure of a material's resistance to deformation.[23] Fluid samples can be split into two classes, Newtonian or non-Newtonian, depending on their viscosity, or flow behaviour under shear. A fluid is said to be Newtonian when its viscosity is independent of the experienced force, or applied shear rate (**Figure (1.4)**).[24] Examples of Newtonian fluids include water, alcohols and honey. The viscosity of a non-Newtonian fluid, on the other hand, is dependent on the applied force. Within non-Newtonian fluids, materials can be further subdivided depending on how the viscosity behaves under force.[25–28] If the material begins to flow more easily under the application of force, it is said to be shear-thinning as its apparent viscosity, η_a, decreases.[24] Materials that fall under this category include ketchup and nail varnish. A material is termed shear-thickening if the opposite is observed, where the flow of material is retarded with increasing force. In this scenario, a fluid's apparent viscosity increases. Shear-thickening behaviour can be observed with concentrated cornflour/water mixtures.
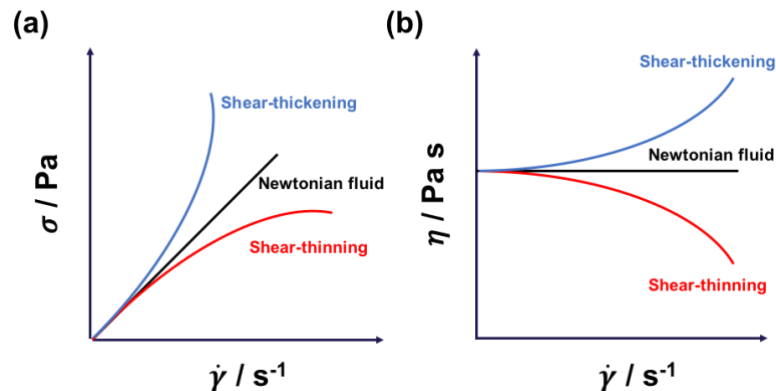
Figure (1.4). The **(a)** shear stress (σ / Pa) and **(b)** viscosity (η / Pa s) behaviour of Newtonian (black trace), shear-thinning (red trace) and shear-thickening (blue trace) fluids as a function of shear rate ($\dot{\gamma}$ / s^{-1}).

The viscosity behaviour of a sample, under an applied force, is essential to understand as it has implications for the applications of a material. For example, if a material's viscosity

increases with force, it would not be beneficial to use as an additive in toothpaste; as someone squeezes the toothpaste tube, the paste would become harder to flow out of the tube.

Non-Newtonian materials demonstrate viscoelastic behaviour where the viscosity is dependent on the shear rate it experiences, this dependence often corresponds to a power law trend. The simplest model utilised for non-Newtonian polymers is the power law model (**Equation (1.3)**).[24,25,27] Where n, the power-law index, equals one for Newtonian fluids. If a sample is shear thickening, then $n > 1$ and shear-thinning samples have a power-law index less than one. The real case scenario, however, is that the viscosity will plateau at very low shear rates, equivalent to η_0, the zero-shear viscosity. It is important to note that other models exist for non-Newtonian materials, especially polymers, such as the Cross model[29] and the Carreau model.[30]

$$\eta = k\dot{\gamma}^{n-1} \qquad\qquad\qquad \textbf{(1.3)}$$

Equation (1.3). The power-law model gives a good approximation for viscosity behaviour of a non-Newtonian fluid under shear, where η is viscosity (Pa s), k is a constant, termed the flow consistency index (Pa s), shear rate is defined by $\dot{\gamma}$ (s^{-1}). The power-law index is defined as n (dimensionless).[22]

Most polymeric samples are shear-thinning; the simplest way to test the viscoelastic behaviour of a fluid is through a simple shear flow experiment on a rheometer. In this experimental set-up, a fluid sample is sandwiched between two plates; with the free plate rotating, in a single direction, at a velocity which increases over time. The amount of torque required by the motor to rotate the plate at this velocity is dependent on overcoming the viscous forces of the sample. As such, the necessary amount of torque is a measure of the sample viscosity (**Equation (1.4)**). The velocity of the free plate is often described in terms of the shear rate ($\dot{\gamma}$ / s^{-1}) of the plate edge.

$$\eta = \frac{MK_\sigma}{\Omega K_\gamma} \qquad \textbf{(1.4)}$$

Equation (1.4). Viscosity can be determined from the moment or torque (M / N m), the angular velocity of the plate (Ω / s^{-1}), the stress constant (K_σ / m^{-3}) and the strain constant (K_γ / rad^{-1}).[22]

1.2.1.2 Relaxation time

When an applied force or stress is removed, a non-Newtonian material undergoes a relaxation period, where it returns to its original position or relaxed state.[23] The length of this period, or relaxation time (r_t), is dependent on the viscosity and the elastic modulus of the material (**Equation (1.5)**). The elastic modulus can be calculated from the stress and strain of the material, during the applied force (**Equation (1.6)**). A Newtonian material, however, relaxes instantaneously with the removal of the applied force, and as such, has no relaxation time.

$$r_t = \frac{\eta}{G} \qquad \textbf{(1.5)}$$

Equation (1.5). Relaxation time (r_t / s) of a viscoelastic, non-Newtonian material can be determined by the viscosity (η / Pa s) and the elastic modulus (G / Pa).[21]

$$G = \frac{\sigma}{\gamma} \qquad \textbf{(1.6)}$$

Equation (1.6). The elastic modulus (G / Pa) can be calculated from the stress (σ / Pa) and the strain (γ / dimensionless).[21]

1.2.1.3 Capillary Rheology

The effects of shear flow can also be measured in pressure-driven flows, such as those exhibited by capillary or slit rheometers. In a pressure-driven flow, a fluid sample is forced

through a closed channel by the application of pressure. The channel shape is either a cylinder, for capillary rheometry, or quadrilateral, for slit rheometry (**Figure (1.5)**). In a capillary, the fluid velocity (v) will be highest at the centre of the cylinder and zero at the walls. However, the shear rate ($\dot{\gamma}$) and shear stress (σ) will be highest at the walls, and non-existent in the centre of the flow (**Figure (1.6)**).[31]
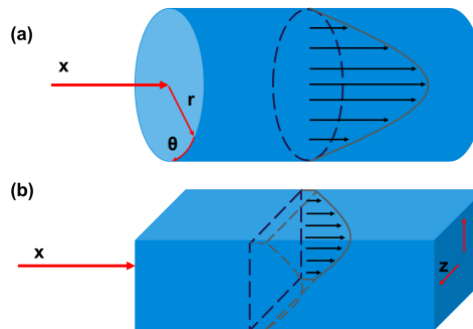
Figure (1.5). Schematic of **(a)** capillary and **(b)** slit pressure flow, assuming infinite dimensions in the z direction. The grey lines and black arrows in each diagram represent the flow profile in each geometry. The red arrows represent the co-ordinates utilised in each system; slit rheology uses standard Cartesian co-ordinates (x, y and z), whereas capillary rheology uses x to signify the direction of fluid flow, r as the radius of the capillary and θ as the circumference of the cylinder.

The shear rate exerted on a sample, at the wall, in a pressure-driven flow can be calculated from the volumetric flow rate (Q). **Equation (1.7)** describes the wall shear rate of a Newtonian fluid. For a non-Newtonian liquid, a term including the power-law index (n) is necessary to accurately calculate the corresponding shear rate (**Equation (1.8)**).[32]
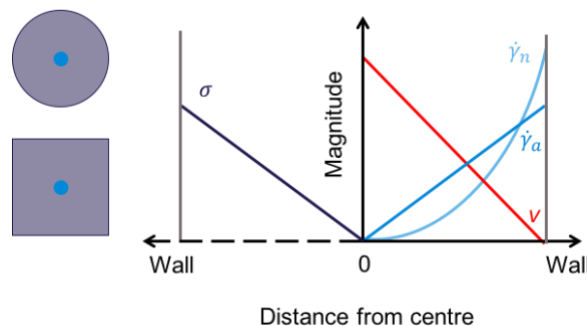
Figure (1.6). Diagram of the shear rate ($\dot{\gamma}$ / s^{-1}), shear stress (σ / Pa) and velocity (v / m s^{-1}) profiles across the cross-sectional of a capillary (circular cross-section) or slit flow (square cross-section). The apparent shear rate profile is depicted by $\dot{\gamma}_a$, and the shear rate profile of a power-law fluid is shown by $\dot{\gamma}_n$. Cross-sectional areas of a capillary and slit rheometer are shown on the left-hand side, with light blue circles indicating the centre.

$$\dot{\gamma}_w = \frac{4Q}{\pi R^3}$$

<div align="right">(1.7)</div>

Equation (1.7). Shear rate ($\dot{\gamma}_w$ / s^{-1}) at a wall for a Newtonian fluid in capillary flow can be calculated from the flow rate (Q / m^3 s^{-1}) and the radius of the cylinder (R / m) for Newtonian fluids.[22]

$$\dot{\gamma}_w = \frac{4Q}{\pi R^3}\left(3 + \frac{1}{n}\right)$$

<div align="right">(1.8)</div>

Equation (1.8). Shear rate ($\dot{\gamma}_w$ / s^{-1}) at a wall for a non-Newtonian fluid in capillary flow can be calculated from the volumetric flow rate (Q / m^3 s^{-1}), the radius of the cylinder (R / m) for Newtonian fluids and the power-law index (n / dimensionless).[22]

1.2.2 Extensional Flow

Another type of flow often employed is extensional flow. In these flow types, a material experiences compressing forces on one or two axes and stretching forces on the remaining axes. Extensional, or elongational flow is commonly encountered in many processing techniques utilised for polymers. There are three types of extensional flow commonly utilised: uniaxial, biaxial and planar extension (**Figure (1.7)**). For the sake of relevance, only planar extensional flow will be discussed further.
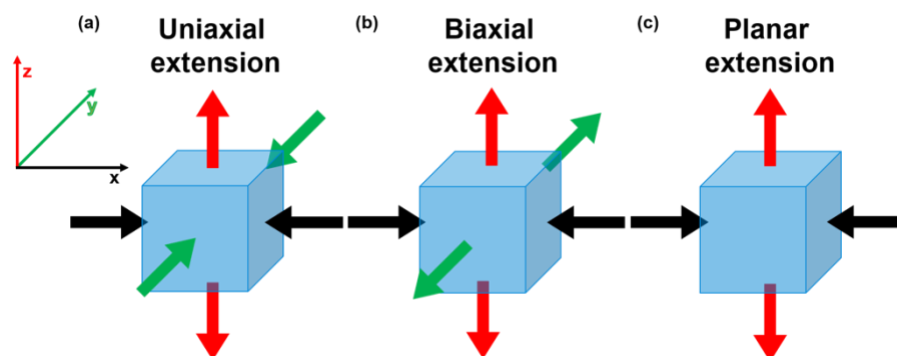
Figure (1.7). Schematic representing the forces acting on a material for three extensional flows; **(a)** uniaxial extension, **(b)** biaxial extension, **(c)** planar extension. Coloured Cartesian axes are displayed in the figure for ease of understanding.

In extensional flow, the true strain, or Hencky strain,[33] is frequently utilised to describe the flow conditions. This logarithmic strain is more appropriate for large deformations, often seen in elongational flow (**Equation (1.9)**). However, **Equation (1.9)** is only applicable for situations where the sample length varies with time, typically solid materials. If the sample length remains constant, for example in a fluid, it is much more accurate to use **Equation (1.10)** to calculate the Hencky strain, as this acknowledges the velocity of the fluid material.

$$\varepsilon_H = \ln\left(\frac{L}{L_0}\right) \qquad \qquad \textbf{(1.9)}$$

Equation (1.9). The Hencky strain (ε_H / dimensionless) is the logarithmic ratio of the sample length before (L_0 / m) and after deformation (L / m), when the length of a sample varies over time.[22]

$$\dot{\varepsilon}_H = \frac{v}{L_0} \qquad \qquad \textbf{(1.10)}$$

Equation (1.10). For a constant sample length, the Hencky strain rate ($\dot{\varepsilon}_H$ / s^{-1}) is calculated from the velocity (v / m s^{-1}) and the length of the sample (L_0 / m).[22]

1.2.2.1 Planar Extensional Rheology

In planar extensional flow, a material will be compressed along one axis (x-axis in **Figure (1.8)**) and stretched in a second axis (z-axis), with the material experiencing no force along the remaining axis (y-axis). For a solid material, the planar extensional forces will lead to a deformation in the two axes where force is experienced. This results in a lengthening in the stretching axis and a contraction in the compressing axis. The material dimension in the remaining axis should remain constant. Overall, the Hencky strain rate experienced in all axes of the material can be described by **Equations (1.11)** and **(1.12)**. The extensional stress experienced by the sample can simply be calculated from the force applied, over the material area (**Equation (1.13)**).

$$\dot{\varepsilon}_H(y) = 0 \qquad \textbf{(1.11)} \qquad\qquad \dot{\varepsilon}_H(z) = -\dot{\varepsilon}_H(x) \qquad \textbf{(1.12)}$$

Equation (1.11) and (1.12). The Hencky strain rate ($\dot{\varepsilon}_H$ / dimensionless) values along each axis for a material experiencing planar extensional flow.[21]
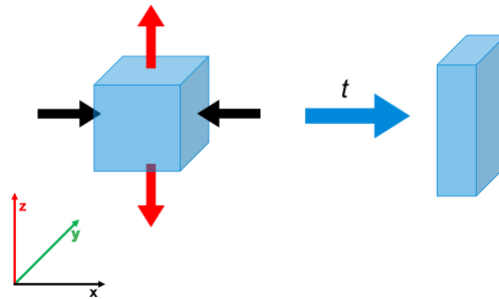
Figure (1.8). Over time, a material under a planar elongational flow will be stretched in the z-axis (extensional axis) and squashed in the x-axis (compression axis). There will be no change in the dimensions of the material in the y-axis, where no force is experienced.

$$\sigma_E(z) - \sigma_E(x) = \frac{F}{A} \qquad\qquad \textbf{(1.13)}$$

Equation (1.13). The extensional stress (σ_E / Pa) of a sample can be calculated from the force applied (F / kg m s^{-2}) and the cross-sectional area of the sample (A / m^2).[21]

A simple, macroscopic, experimental set up for planar extensional rheology is the four-roll mill (FRM).[34] FRM uses four counter-rotating cylinders, in a square layout, to apply the elongational forces to the material.[35] Invented by Taylor in 1934,[36] this geometry creates a free stagnation point at the centre of the material and an extensional force between the two sets of rollers (red arrows in **Figure (1.9) (a)**). A stagnation point occurs when the local velocity of the sample is zero, leading to infinitesimally high strain rates around this point.[35,37] Due to these velocity and strain conditions, material can be trapped in the stagnation point,[38] which allows for elongational properties of a material to be investigated without disturbance.[39] The environment

of the stagnation point can be tailored by altering the rotation speed and direction of the four rollers.[40]
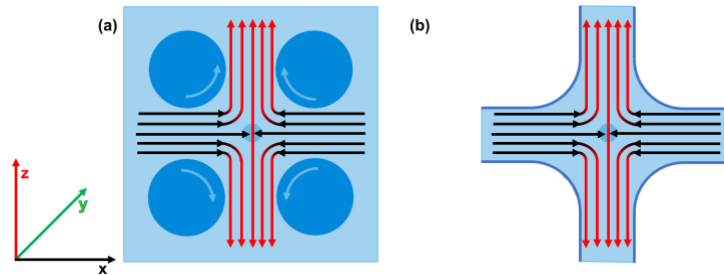
Figure (1.9). Experimental set-ups to measure planar extension **(a)** depicts the four-roll mill geometry and **(b)** shows the cross slot with two opposed fluid jets. The light blue circle demonstrates the position of the stagnation points in each set-up.

The four-roll mill experimental set-up allows for the measurement of rheological properties of materials experiencing extensional flow to be performed. For an incompressible fluid, its volume must remain constant during the elongational flow (**Equations (1.11)** and **(1.12)**). Therefore, fluid needs to be continuously supplied during an extensional measurement. This is possible in the four-roll mill experiment as the rotating cylinders allow for the continuous movement of the fluid sample; the velocity of the fluid can be calculated from the Hencky strain present in each direction (**Equations (1.14)**, **(1.15)** and **(1.16)**). Although this experimental technique was ground-breaking in the first half of the last century, FRM has fallen out of use due to the mechanical moving components, which makes it difficult to produce or miniaturise.

$$v_x = -\dot{\varepsilon}_H(x)x \qquad \textbf{(1.14)} \qquad\qquad v_y = 0 \qquad \textbf{(1.15)} \qquad v_z = \dot{\varepsilon}_H(z)z \qquad \textbf{(1.16)}$$

Equation (1.14), (1.15) and (1.16). The fluid velocity (v / m s^{-1}) along each axis can be calculated from the corresponding Hencky strain rate ($\dot{\varepsilon}_H$ / s^{-1}), and the distance travelled (x, y, z / m) by the fluid per unit time.[16]

An analogous arrangement to the four-roll mill is the cross-slot, developed in the 1970s,[41] which is applicable for both the macroscopic and microscopic analysis of fluids (**Figure**

(1.9)(b)).[42] In this experimental set-up, there are two opposing jets of fluid with two orthogonal exit streams. The extensional force is present along the outlet axis. Much like the four-roll mill apparatus, cross-slots have a free stagnation point where the two jets of fluid meet,[43] however, it is a much simpler geometry and therefore, has found much use in planar extensional techniques.[37,44,45] This geometry leads to high Hencky strain rates and large extensional stresses close to the centre of the cross.[46,47] The Hencky strain rate present in this technique can be easily calculated from the volumetric flow rate and the dimensions of the cross-slot (**Equation (1.17)**).[34,48–52] The extensional stress present can be derived from **Equation (1.18)**. In theory, particles in the fluid can get trapped in this local point for infinite time scales due to the zero-velocity position, whereas fluid around this area experience very high strain rates.

$$\dot{\varepsilon}_H = \frac{Q}{W^2 H} \tag{1.17}$$

Equation (1.17). The Hencky strain rate ($\dot{\varepsilon}_H$ / s^{-1}) present in a cross-slot geometry can be calculated from the volumetric flow rate (Q / m^3 s^{-1}), the width of the inlet channel (W / m) and the height of the channel (H / m).

$$\sigma_E = \frac{F}{A} = \frac{mv}{t}\frac{1}{A} = \frac{mQ}{A} \tag{1.18}$$

Equation (1.18). The extensional stress (σ_E) which the material is subjected to can be calculated from the mass of the fluid (m / kg), the volumetric flow rate (Q / m^3 s^{-1}) and the cross-sectional area of the inlet channel (A /m^2).[53]

1.2.2.2 Extensional Viscosity

Under elongational, or extensional flow, non-Newtonian fluids undergo viscosity thickening, regardless of their viscosity behaviour under shear. The extensional viscosity can be measured by rheometers designed to apply extensional stress (**Equation (1.19)**). However, this measurement is difficult to perform without suitable equipment.[45] The main issue surrounding

extensional viscosity measurements is creating and maintaining the purely extensional flows needed for measurements to be performed[54–56] Instead, the extensional planar viscosity can be calculated from the shear viscosity using Trouton's rule (**Equation (1.20)**).[57] For Newtonian fluids undergoing planar extensional flow, T_r equals 4, although the viscosity of non-Newtonian fluids is generally well above this ratio.[37]

$$\eta_E = \frac{\sigma}{\dot{\varepsilon}_H}$$

(1.19)

Equation (1.19). The extensional viscosity (η_E / Pa s) can be calculated from the applied stress (σ / Pa) and the Hencky strain rate ($\dot{\varepsilon}_H$ / s^{-1}).[22]

$$T_r = \frac{\eta_p(\varepsilon_H)}{\eta(2\varepsilon_H)}$$

(1.20)

Equation (1.20). The planar extensional viscosity (η_p / Pa s) can be calculated from the shear viscosity (η / Pa s) by using Trouton's rule, where the Trouton ratio (T_r / dimensionless) is 4 for Newtonian fluids.[58]

1.2.3   Downfall of Conventional Rheometers

Despite the widespread use of conventional mechanical rheometers, there are some disadvantages associated with their use. Firstly, these rheometers often require large sample volumes to perform accurate measurements of rheological properties such as viscosity.[47,59,60] Secondly, the maximum shear rate available for measurement is inversely proportional to the sample gap height, which can lead to only a narrow range of shear rates being investigated with conventional rheometers.[59] In some cases, the highest shear rates investigated are much lower than those required to measure η_∞.[61] Thirdly, conventional rheometers are often bulky and difficult to move, meaning that they are not suited to testing materials onsite or at point-of-care.[62,63]

1.2.4   Dimensionless numbers for flow characterisation

In studying the flow of material, two dimensionless numbers are essential to determine: the Reynolds number and the Weissenberg number. The Reynolds number, *Re*, is used to determine or predict flow patterns in different situations. Simply, it is the ratio of inertial and viscous forces within a flowing fluid with a velocity profile (**Equation (1.21)**).[26,64–70] This dimensionless number is often utilised to determine whether a flow is laminar or turbulent. If *Re* is less than 2100, the flow is considered laminar. Values greater than 4,000 suggest the fluid flow is turbulent.[71]

$$Re = \frac{\rho v L}{\eta} \qquad (1.21)$$

Equation (1.21). The Reynolds number (*Re* / dimensionless) is calculated from the density (ρ / kg m^{-1}) the fluid velocity (v / m s^{-1}), the length of the pathway the fluid is taking (L / m) and the viscosity (η / Pa s).

The Weissenberg number, on the other hand, deals with the ratio of elastic to viscous forces in a fluid sample (**Equation (1.22)**).[64,66,72–74] This number is a good indication for the degree of anisotropy, or orientation, in a fluid material as a function of flow.[71]

$$Wi = \frac{r_t v}{L} = \dot{\gamma}\, r_t \qquad (1.22)$$

Equation (1.22). The Weissenberg number (*Wi* / dimensionless) is calculated from the relaxation time (r_t / s^{-1}), the fluid velocity (v / m s^{-1}) and the pathway length of the fluid (L / m), or the shear rate ($\dot{\gamma}$ / s^{-1}) and the relaxation time (r_t / s).

1.3 Flow Birefringence

Most molecules, including polymers, are geometrically anisotropic in nature. Their optical properties change with direction, which is commonly described by a tensor. An anisotropic

material displays birefringence (i.e., more than one index of refraction); where the polarisation and propagation direction of light passing through the material can be altered. This property can be a useful tool for the study of orientation present in anisotropic objects, such as polymeric materials.

1.3.1   Refraction of Light

The index of refraction (n_i) indicates the speed of light through a medium.[21] The speed, or velocity, through this medium is lower than the speed of light through a vacuum, and the ratio between these two speeds defines the refractive index (**Equation (1.23)**). The reduction in speed of light is due to the interaction of light with electrons in the medium. This change in speed also results in a change of propagating direction at the interface between two media with different refractive indices (**Figure (1.10)**).[22] The angle at which the light is refracted can be calculated from Snells' law (**Equation (1.24)**).

$$n_i = \frac{c}{v}$$

(1.23)

Equation (1.23). Index of refraction (n_i / dimensionless) is calculated from the speed of light in a vacuum (c / m s^{-1}) and the phase velocity of light in a medium (v / m s^{-1}).[75]

In a medium, each axis (x, y and z) can have its own respective index of refraction. If these respective refractive indexes are the same, a material does not display birefringence; this is true for most materials. However, when the refractive indices for the three axes are not equivalent, multiple indices of refraction are present, and waves of light are travelling through a medium at different speeds; birefringence can be observed.
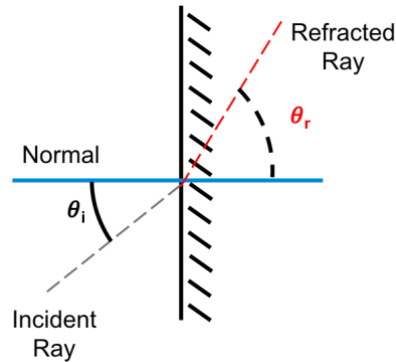
Figure (1.10). Schematic highlighting the refraction of light through a material. The line entitled 'Normal' indicates the plane 90 ° to the surface of the material. θ_i is the angle of incidence, and θ_r is the angle of refraction.

$$n_{i(1)} \sin \theta_1 = n_{i(2)} \sin \theta_2 \qquad \textbf{(1.24)}$$

Equation (1.24). Snell's law states the angle of refraction of light when it passes between two mediums can be calculated from the refractive indices of the two materials ($n_{i(1)}$ and $n_{i(2)}$ / dimensionless) and the angles of incidence (θ_1 and θ_2 / °).

1.3.2   Polarisation of Light

In the mid-1800s, Maxwell demonstrated that light is a propagating oscillation in the electromagnetic field and the direction of such oscillations are perpendicular to the direction of travel (**Figure (1.11)(a)**).[76] These oscillations of the wave can occur at any angle perpendicular to the propagation of light. The majority of light sources emit unpolarised light, where the rays will exhibit an equal mixture of all possible polarisations (**Figure (1.11)(b)**). However, light can become polarised when it is passed through a polarising material which allows only waves with a specific angle of oscillation to pass through; the light emitted from this material is now polarised (**Figure (1.11)(c)**). When polarised light passes through a second polarising material, the angle of the oscillations can be changed, unless the polarisation direction is equivalent, or orthogonal to that of the incoming polarised light (**Figure (1.11)(c)**). If the polarisation direction is equivalent, there will be no resultant change in the direction of polarisation. However, if the

second polarising filter is orthogonal to the first, all incoming polarised light will be blocked. Generally, a material that can polarise light is birefringent.
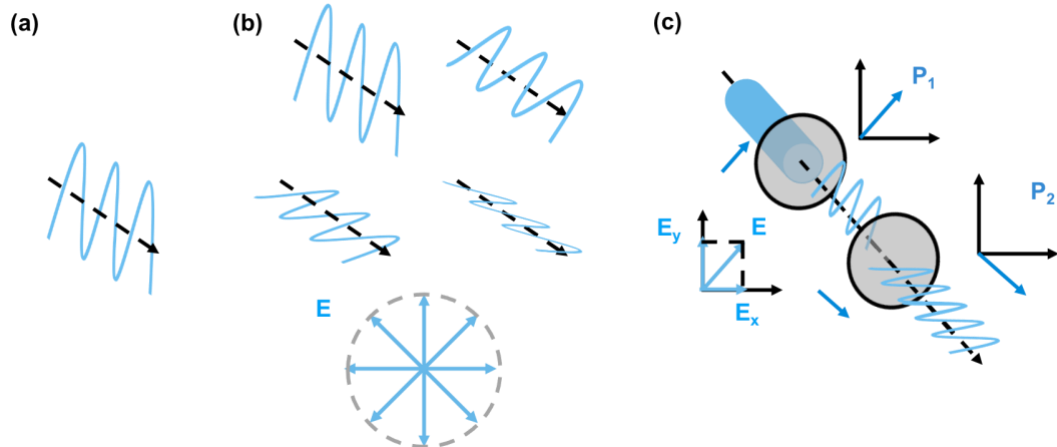
Figure (1.11). (a) The associated wave oscillation (blue line) of a ray of light (black dashed arrow – the arrow represents the direction of travel) is its polarisation. **(b)** A beam of unpolarized light will have many different polarisations, denoted by E. **(c)** A polarizing material will only allow light to pass through with a certain polarisation (blue arrow indicates the direction of polarising filter). Passing polarized light through a polarising material will lead to a change in the direction of polarisation. For clarity, only the electrical component of light is shown.

1.3.3 Birefringence

Uniaxial birefringence is the simplest form of this phenomenon. In this case, only one axis, the optical axis, has a refractive index that is dependent on the polarisation and propagation of light. When polarised light passes through this inequivalent axis, at 45°, it is refracted into two distinct rays. When the polarised light is travelling perpendicularly to the optical axis, the two refracted light components are moving at different speeds but in the same direction. Each refracted ray will have a polarisation mutually perpendicular to the other (i.e. at right angles).[77] Light polarised parallel to the incoming light will experience an extraordinary refractive index, n_e. Whereas, polarised light perpendicular to the incident light source experiences an ordinary refractive index, n_o. The birefringence observed from a material is the difference between these two indices of refraction (**Equation (1.25)**).[78] Propagating light in the direction of the optical axes will not be impacted by this refractive index, and thus will not display birefringence.

$$B = n_e - n_o \qquad\qquad \textbf{(1.25)}$$

Equation (1.25). Birefringence (B / dimensionless) of a medium is calculated from the difference between the ordinary and extraordinary refractive indices (n_o and n_e /dimensionless).

Materials which display uniaxial birefringence generally have some kind of anisotropy associated with their chemical, or molecular, structure.[22] This is classed as structural birefringence. For example, the majority of polymers exhibit structural birefringence due to the long-chain structure inherent to these macromolecules. However, under quiescent conditions, polymers do not display birefringence due to the random orientation of chains, or micelles, in solution.

1.3.4   Polarised Optical Microscopy (POM)

A birefringent material can be easily analysed by polarised optical microscopy (POM); where the material is placed between two polarising filters orientated 90 ° to each other. The first filter causes the unpolarised, light source to become linearly polarised. The second filter allows the effects of the material to be analysed by changing the polarisation of the ordinary and extraordinary ray. The placement of the two filters creates a dark field when no material is placed between them. The birefringence is brightest when the optical axis of the sample is rotated at 45 ° from the two filters. As discussed above, a birefringent material produces two waves of polarised light with different velocities (**Figure (1.12)(a)**). When these rays exit the material, they become out of phase with each other; the amount they are out of phase is called the retardance (δ) (**Equation (1.26)**). However, when they pass through the analyser, the rays are recombined with constructive and deconstructive interference (**Figure (1.12)(b)**). If the sample is placed at a 45 ° angle of rotation between the two polarisers, the retardance can be calculated, using **Equation**

(1.27).[79] Quantifying the retardance allows the birefringence to be measured (**Equation (1.26)**).[79,80]

$$\delta_{Re} = \frac{\omega HB}{c} = \frac{2\pi HB}{\lambda}$$

(1.26)

Equation (1.26). The retardance (δ_{Re} / dimensionless) of the two light components exiting a birefringent material can be calculated from the frequency (ω / s^{-1}) or the wavelength of light (λ / nm). H is the height, or thickness of the sample (m), B is the birefringence (dimensionless), and c is the speed of light (m s^{-1}).

$$I = I_0 \sin^2 \frac{\delta_{Re}}{2}$$

(1.27)

Equation (1.27). The retardance of a material can be calculated from the intensity of light measured (I / A.U.) and the intensity of polarized light (I_0 / A.U.) hitting the material.
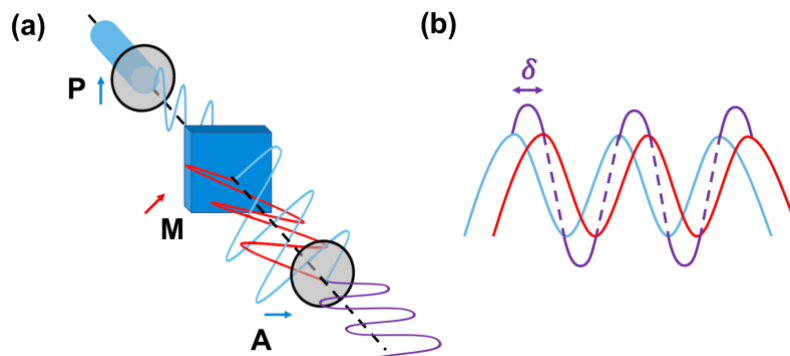
Figure (1.12). (a) Schematic of the light pathway through a polarised light microscope, with a birefringent material present (M). The unpolarised light source travels through the first polarising filter (P) to become linearly polarised (the light blue arrow indicates the direction of polarisation). The interaction of light with the birefringent material causes the propagation of two polarised light components (light blue and red waves). The light then travels through the second polarising filter, which acts as an analyser (A) to form a light wave which combines the two light components. **(b)** A schematic to show how the final polarised light contains the two components emitted from the birefringent material, where δ_{Re} is the retardance between the two waves.

1.3.5   Stress Birefringence

It was previously discussed that polymeric solutions under quiescent conditions do not exhibit birefringence, despite the anisotropic structure present. However, in cases where a net orientation of the polymer objects in solution is present, uniaxial birefringence can be observed

and measured (**Figure (1.13)**). This is classed as either stress or strain birefringence. A net orientation of particles in solution can be achieved by applying a force, causing the anisotropic micelles to align. Thus, the material becomes birefringent; this is termed flow birefringence. The resulting stress birefringence is often seen in everyday plastic objects which have encountered flow during the processing pipeline; for example, bottles, stationery (rulers, protractors, etc.) and toothbrushes.
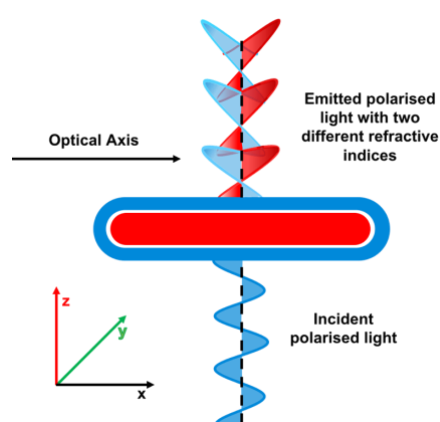
Figure (1.13). Schematic of an oriented worm-like micelle, with the optical axis depicted by the black arrow. Due to the anisotropic structure of this macromolecule, the material is birefringent and splits a ray of polarised light into light with two components.

Previously discussed in **Section 1.2**, when a material is subjected to flow, stresses occur in the sample. When a rheometer creates the flow, the stresses produced can easily be measured. In pressure-driven flows, such as capillary flow, the measurement of resultant stresses is not as easy. However, the degree of birefringence observed in flows can be used to determine the magnitude of stress experienced by the material.[81] The stress optical rule (SOR) allows for this comparison (**Equation (1.28)**).[44,82]

$$B = C\sigma + DI \tag{1.28}$$

Equation (1.28). The stress optical law relates the birefringence (B / dimensionless) to the stress (σ / Pa) by using the stress-optical coefficient (C / Pa^{-1}), a constant (D / dimensionless) and the intensity of light emitted from the sample (I / dimensionless).

The SOR can be used in this format (**Equation (1.28)**) for extensional flow. However, for shear stresses, the SOR must be adapted as there are two principal directions of stress in this geometry. The appropriate formula can be seen in **Equation (1.29)**.

$$2\sigma_{max} = |\sigma_1 - \sigma_2| = \frac{\lambda}{2\pi HC}\delta_{Re}$$

<div align="right">(1.29)</div>

Equation (1.29). The maximum shear stress (σ_{max} / Pa) can be calculated from the two principal stresses (σ_1 and σ_2 / Pa), or the wavelength of light (λ / nm), the thickness, or height of the sample (H / m), the stress optical coefficient (C / Pa^{-1}) and the retardation of the two rays (δ_{Re} / dimensionless).[13]

In **Section 1.2.2.2**, the difficulties in measuring the extensional viscosity of a material were highlighted. Generally, a specific extensional rheometer is required to map the viscosity behaviour over many extensional strain rates. Trouton's ratio[58] can give some indication of the extensional viscosity compared to the shear viscosity, however, unless T_r is known, this can give incorrect results. However, the extensional viscosity can be measured directly by utilising the stress optical rule, using **Equation (1.30)**, which provides a much more accurate quantification of the material's viscosity.[80]

$$\eta_E = \frac{\Delta\sigma}{\dot{\varepsilon}_H} = \frac{B}{C\dot{\varepsilon}_H}$$

<div align="right">(1.30)</div>

Equation (1.30). The extensional viscosity (η_E / Pa s) can be calculated from the stress ($\Delta\sigma$ / Pa) present in the sample and the applied Hencky strain rate ($\dot{\varepsilon}_H$ / s^{-1}), or the birefringence (B / dimensionless), the stress optical coefficient (C / Pa^{-1}) and the Hencky strain rate.

1.4 Shear Induced Polarised Light Imaging (SIPLI)

A convenient method to observe or measure the flow birefringence properties of a material is shear-induced polarised light imaging (SIPLI). Developed by Mykhaylyk, this technique

combines a plate-plate rheometer (discussed in **Section 1.2.1**) with full, *in-situ* sample imaging.[13,14]
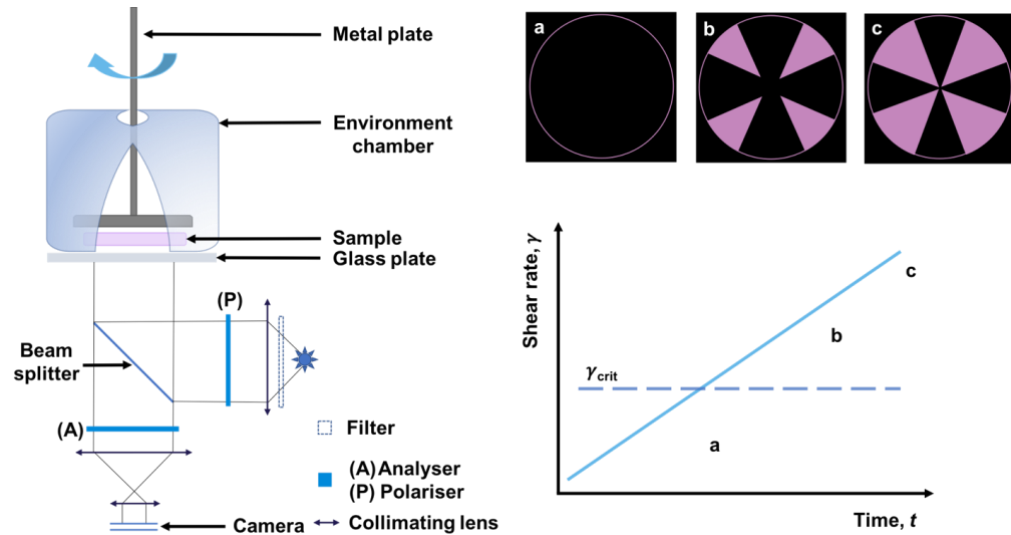
Figure (1.14). Schematic diagram of the modified plate-plate geometry utilised in SIPLI, including the arrangement of the light source, polariser, analyser, collimating lenses and CCD camera. The schematic also displays typical PLIs captured under shear; **(a)** shows a blank image, indicative of a sample being sheared below the critical shear rate, with no observable birefringence.[13,14] **(b)** A PLI of a material being sheared slightly above γ_{crit}, with a characteristic Maltese cross. **(c)** A material is sheared well above its γ_{crit}, causing the Maltese cross to extend fully to the centre of the PLI.

This is possible due to the incorporation of a highly polished steel 'rotating' plate and a transparent quartz fixed plate, which, respectively, act as a mirror and window. A light source passes through a polarising film to give the ordinary ray of light. If a material is birefringent, this ordinary ray is converted to an extraordinary ray, with a different plane of polarisation. The light is reflected off the polished, rotating plate and passes through an analyser if an extraordinary ray. A CCD camera captures these extraordinary rays, allowing polarised light images (PLIs) to be acquired while a sample is under shear.

Flow birefringence is observed when a sample is sheared above a critical rate, $\dot{\gamma}_{crit}$ (s⁻¹). At this shear rate, the anisotropic objects have aligned parallel to the direction of rotation,

resulting in net orientation within the liquid sample. PLIs will have a characteristic Maltese cross as pictured in **Figure (1.14)(a) – (c).** The shadows, which form the distinctive Maltese cross, are due to the principal stress direction coinciding with the plane of polarisation. This principal stress direction is tangential to the direction of rotation. In this case, the extraordinary ray is equivalent to the ordinary ray, and no light passes through the analyser, causing a dark section on the PLI.

1.5 Microfluidics and Millifluidics

Microfluidic devices, first developed in the 1990s by Manz *et al.*,[83] are able to utilise flow to precisely manipulate a liquid sample often while performing some type of analysis.[26,72,84–87] Typically containing channels with dimensions of less than one millimetre, these channels minimise the inertial effects of flow and allow the viscous forces to dominate.[45,88–91] Due to these small length scales,[92] the type of flow present in microfluidic devices is often described as laminar.[63,65,85,93,94] Laminar flow is attractive as it allows for the manipulation, and precise control of fluid within microfluidic channels.[86,87,91,93]

The use of microfluidics has become increasingly popular over traditional bulk techniques due to the numerous advantages they possess. Firstly, the design of microfluidics allows for better heat and mass transfer[93,95–99] throughout a sample due to the small pathway thickness, and associated high surface-to-volume ratio.[26,70,87,93] Secondly, the miniature nature of these devices results in the use of very little sample volume,[26,64,103,85–88,99–102] on the order of pico- or nanolitres, which in turn reduces both the cost and waste of precious resources.[26,93,104,105] Thirdly, microfluidic devices can be easily fabricated[90,106] using in-house equipment, allowing them to be highly integrated with other equipment,[26,35,105] and consist of complex, novel channel geometries.[91,92,107]

The use of microfluidic devices spans many research areas, from metallic nanoparticle synthesis[97,98,108,109] to protein structural dynamics,[110–113] to mimicking bodily functions.[114–116] However, the most universal use of these channels is as miniaturised rheometers; the simplest microfluidic channel geometries are analogous to capillary or slit rheometers, whilst more complex geometries exhibit reproducible extensional fluid flows. There are many advantages of using microfluidic rheometers, as opposed to conventional rheometers as they often overcome the downfalls of conventional rheometers outlined in **Section 1.2.3**.[62] One of the advantages is that the shear rheology of a sample can be measured *in situ* via the relationship between the pressure drop and volumetric flow rate in a microchannel.[23,72] This allows the sample rheology to be mapped whilst performing other measurements or analysis. Another advantage is that much higher shear rates can be achieved in a microchannel, than in conventional rheometers.[65,71,88,99,102] This allows for a broader range of shear rates to be investigated via both microfluidics and conventional rheometers. A third advantage of microfluidic devices is that a sample viscosity can be measured over a much shorter time period, and with much less sample volume required than conventional rheometers.[60,65,117]

Within microfluidics, many different channel geometries can be adopted, depending on the type of flow required and the intend use of the microfluidic device. However, there are four main geometries that are implemented: straight, hydrodynamic flow focusing, cross-slot and expansion/contraction channel geometries.

Straight channel microfluidic geometries are analogous to capillary or slit rheometers, when the channel cross-section is circular or quadrilateral.[43] These devices have very controlled shear flow conditions that have been well documented over the last 30 years.[118] Due to this, they are often employed to perform shear and viscosity measurements.[59,72] However, other uses include particle focusing,[73,94,119,120] separation[121,122] and transport,[92,123] or phase transitions of polymeric materials.[89,124,125] Examples of straight channel microfluidic devices can be seen in **Figure (1.15)**.
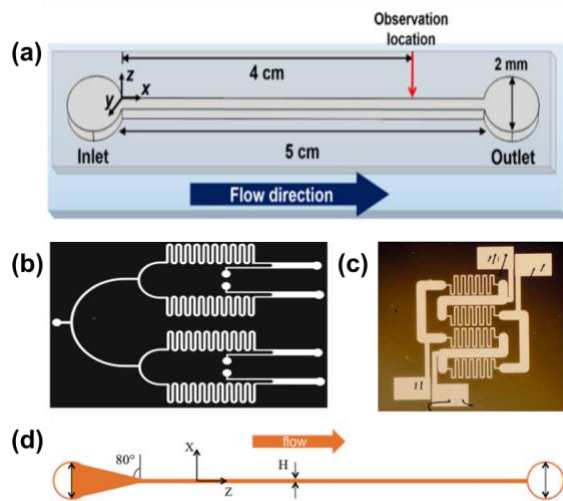
Figure (1.15). Representative figures of straight channel microfluidic devices, where the dimensions of the channel geometry are unchanging. **(a)** A straight channel geometry for particle migration.[64] **(b)** Microfluidic device for the measurement of fluid rheology.[126] **(c)** A microfluidic straight channel viscometer.[127] **(d)** A straight channel geometry to measure the relaxation time of a fluid. [128]

Hydrodynamic flow focusing (HFF) geometries have a T- or Y-junction early on in the channel pathway where a secondary fluid is introduced which sheathes the material of interest (**Figure (1.16)**). This junction allows for the study of viscous materials, as the sheath fluid minimises the pressure exerted onto the channel walls. The use of sheath flow also allows diffusive mixing to be studied, where a component in one fluid stream diffuses into another, which
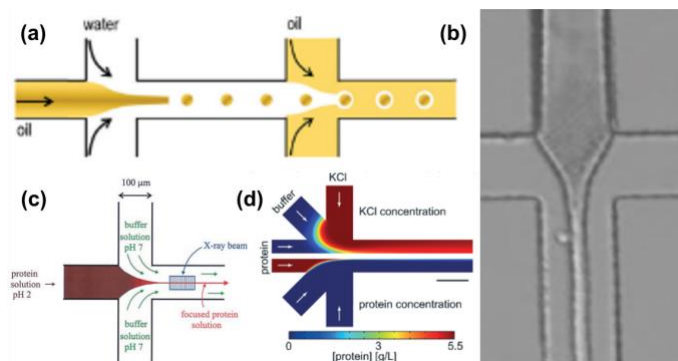
Figure (1.16). Representative microfluidic devices with a hydrodynamic flow focusing geometry (HFF). **(a)**. A HFF geometry for the production of double emulsions[129] **(b)** A microfluidic device used to investigate silk fibre formation in the presence of polyethylene oxide (PEO).[130] **(c)** HFF microfluidic device for studying protein folding.[131] **(d)** Microfluidic device with HFF geometry for investigating the process of filament assembly.[132]

causes a localised change in macromolecular structure. However, the flow profile of a fluid in this geometry is complex due to the high shear forces present within the sheathed flow and the extensional forces present on the boundary of the sheathed flow.[133] This geometry is often used for chemical reactions,[93,134] phase transitions and structure characterisation,[111,133,135,136] droplet generation[129,137] and controlling the motion of particles.[133,138]

Cross-slot, or stagnation point geometries are utilised for the planar extensional forces present in the channel. These geometries are analogous to the four-roll mill (FRM) outlined in **Section 1.2.2.1**. This geometry consists of two opposing inlet channels with two opposing outlet channels.[37] The planar extensional force is present along the outlet axis, with a stagnation point in the centre of the geometry.[37] This microfluidic geometry has been found to have a reproducible flow field (**Figure (1.17)**).[139,140] Cross-slot geometries have been mainly utilised as miniaturised extensional rheometers, focusing on measuring the extensional viscosity of a fluid sample,[44,82,141,142] localisation of chemical reactions[35] or the orientation of anisotropic particles.[46,80,140,143]
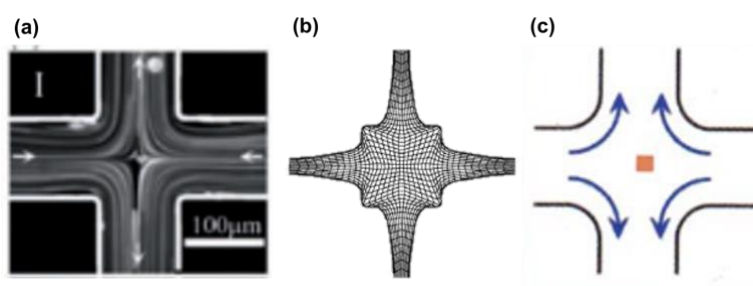
Figure (1.17). Cross-slot microfluidic devices. **(a)** The cross-slot geometry was utilised to study steady, symmetric flow of a Newtonian fluid.[28] **(b)** An optimised cross-slot geometry to minimise turbulence in fluid flow.[37] **(c)** A cross-slot geometry was adopted to investigate the orientation and stretching of DNA molecules under an extensional flow field.[140]

The final geometry is the expansion/contraction microfluidic device (**Figure (1.18)**). These microfluidic channels consist of either a contraction and subsequent expansion of the channel or the inverse (an expansion and then contraction of the channel). The channel geometry introduces

a strong uniaxial extensional flow which is fully reproducible and has been well documented.[105,106,144] This microfluidic geometry can be exploited for the orientation of particles,[145,146] rheological measurements[106,147,148] and changes in polymeric chain conformation.[144]
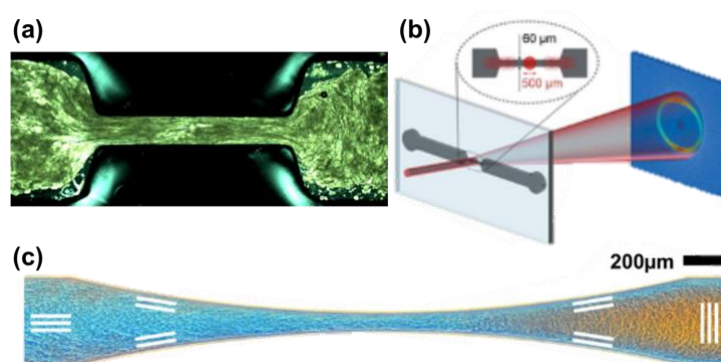
Figure (1.18). Representative expansion/contraction geometries. **(a)** A microfluidic device for the investigation into orientation of surfactant particles in solution.[145] **(b)** Microfluidic geometry used in combination with small angle neutron scattering (SANS) for a range of materials.[149] **(c)** Expansion/contraction microfluidic geometry for the investigation of anisotropic objects.[146]

Despite their extensive utilisation, microfluidics suffer from many drawbacks. The most pressing disadvantages relate to the fabrication methods adopted, which generally require vast resources including capital equipment,[150] specialist knowledge[151] and time.[152–155] Another issue frequently associated with microfluidics relate to their small channel dimensions which often lead to blockages or leakage, affecting the flow profile being investigated.[156] For these reasons, millifluidic devices have become increasingly popular as they display the same advantages of microfluidics (rapid heat and mass transfer, low reagent consumption etc.)[95,153,157–159] while overcoming many of the disadvantages exhibited by microfluidics. Millifluidics do not require channels as small as those utilised in microfluidics; this allows for more fabrication methods to be adopted,[160] which are often less expensive,[153,155,161] and easier to use.[162] The increase in channel sizes reduces the occurrences of channel blockages[163–165] as well as allowing for higher pressures and shear rates to be applied,[162] making these devices more attractive to use.

1.5.1 Finite Element Analysis (FEA)

Finite element analysis (FEA) is an important simulation tool utilised to model flow characteristics. It has become increasingly common for this technique to be used to simulate the fluid dynamics within a micro- or millifluidic channel.[27,86,129,166,167] FEA can model the flow characteristics of a fluid by subdividing a large reservoir, or channel, into smaller, finite elements. The smaller these discrete elements, the more accurate the flow simulation.

As fluids can be regarded as continuum materials, the velocity of a Newtonian fluid obeys the Navier-Stokes equation (**Equation (1.31)**), which represents $F = ma$ for unit volume.[71] However, for the majority of micro- and millifluidic systems, where the flow profile is often laminar, the Stokes equation can be employed for modelling fluid dynamics, and the non-linear term (Navier) can be ignored.[71,168] This is due to the relatively small magnitude of the inertia forces compared to the viscous forces, regardless of the Newtonian, or non-Newtonian behaviour of the fluid. Therefore, **Equation (1.31)** can be simplified to **Equation (1.32)** for an incompressible fluid.[106,169]

$$\rho \left(\frac{\partial v_i}{\partial t} + v_i \cdot \nabla v_i \right) = \nabla \cdot \vec{\sigma}_i + F_i = -\nabla p + \eta \nabla^2 v_i + F_i \tag{1.31}$$

Equation (1.31). The Navier-Stokes equation where inertia acceleration is represented on the left-hand side, and forces are represented on the right-hand side. The symbols used are for the velocity vector (v_i / m s^{-1}), density (ρ / kg m^{-3}), time (t / s), stress vector ($\vec{\sigma}_i$ / Pa), the per-unit volume force vector (F_i / Pa), pressure (p / Pa) and viscosity (η / Pa s).

$$\rho \frac{\partial v_i}{\partial t} = \nabla \sigma_i + F_i = -\nabla p + \eta \nabla^2 v_i + F_i \tag{1.32}$$

Equation (1.32). The simplified Stokes equation can be used when laminar flow is present, and is calculated from the density (ρ / kg m^{-3}), velocity vector (v_i / m s^{-1}), time (t / s), stress vector (σ / Pa), the applied force per-unit volume vector (F_i / Pa), pressure (p / Pa) and viscosity (η / Pa).

Regardless of whether the flow is laminar or turbulent, mass conservation is present (**Equation (1.33)**).[71] Mass conservation highlights that the balance of mass flow leaving or entering a fluid element is equal to the rate of change in the fluid density. Solving the Stokes equation, with the mass conservation element, for a micro- or millifluidic channel gives the velocity profile and pressure drop of a fluid, which can be compared to experimental results from other techniques, such as particle imaging velocimetry (PIV).

$$\frac{\partial \rho}{\partial t} + \nabla(pv_i) = 0 \qquad \qquad \textbf{(1.33)}$$

Equation (1.33). Conservation of mass requires that the change in fluid density ($\partial \rho$) over time (∂t) and the mass balance ($\nabla(pv_i)$) must equal zero.

1.6 SAXS

Small-angle X-ray scattering (SAXS) is also an important characterisation tool which allows for the analysis of a sample on a molecular scale. The scattering of a sample in the small-angle region contains a wealth of information on the size and shape of molecules[43] or particles, the structure factor and the orientation of particles in solution or bulk systems.[141,170] This technique is more attractive than commonly used imaging techniques such as transmission electron microscopy (TEM) due to its ability to average scattering data of millions of particles in a system.

SAXS is advantageous to the soft condensed matter community for several other reasons. First, very little sample is required as the X-ray beam is generally in the micron-range for synchrotron sources and the millimetre range for laboratory sources. Secondly, the technique is typically non-destructive to synthetic polymeric samples being measured. Thirdly, SAXS can be utilised to accurately analyse particles with a size range of 1 to around 500 nm (**Figure**

(1.19)).[171,172] Due to these advantages, SAXS has become an attractive analytical technique for researchers in soft condensed matter.
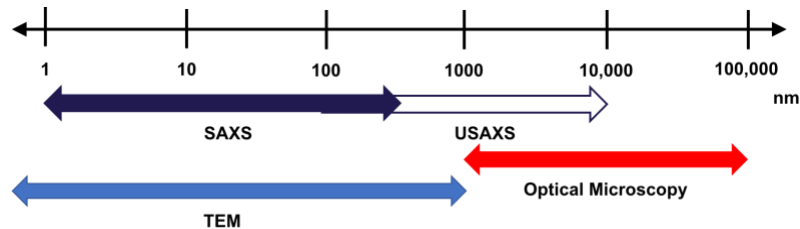
Figure (1.19). The length scales possible to image, or measure, by different techniques. Transmission electron microscopy (TEM) has the most extensive range, from 0.1 – 1000 nm, small-angle X-ray scattering (SAXS) is applicable for systems over a scale of 1 – 500 nm, this can be increased to 10,000 nm when investigating the ultra-small angle X-ray scattering (SAXS). Optical microscopy is only useful for imaging much larger objects, investigating the region of 1,000 – 100,000 nm.

X-rays are electromagnetic waves, with a wavelength much shorter than that of visible light (around 0.1 nm, compared to 500 nm) which allows for the structural analysis of particles, averaged over thousands of instances. With SAXS, the technique works in transmission mode (with the exception of GISAXS which works on the basis of grazing incidence of X-rays), where a sample is irradiated with an X-ray beam. The particles that constitute the sample then interact with the incoming beam. X-rays can interact with a sample in one of two ways, absorption or scattering. Thomson scattering occurs when the interaction between X-rays and atoms cause the electrons to oscillate at the same frequency as the X-rays. This oscillation causes the electrons to
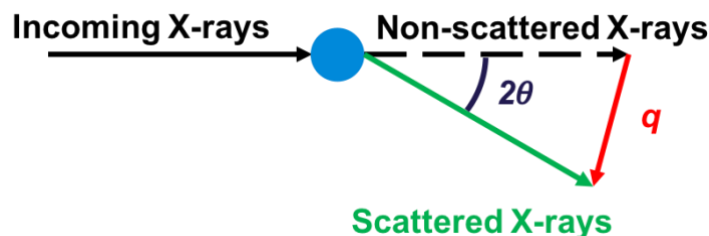
Figure (1.20). Schematic diagram of the interaction of an electron with an incoming X-ray beam. Some of the X-rays are not scattered (black, dashed line). The X-rays that are scattered by the electron are deflected in all directions. A particular direction is associated with an angle 2θ. The distance between the scattered X-rays and the transmitted beam can be represented by the scattering vector (q / nm^{-1}).

emit radiation with the same wavelength as the incoming X-ray beam. The outgoing radiation is scattered in all direction with respect to the incoming radiation direction and associated with an angle 2θ (**Figure (1.20)**). This happens across the whole sample, leading to coherent waves which in turn create interference patterns. These patterns contain information on the particle structure.

All constituent parts of the sample will scatter incoming X-rays. For a polymeric solution, this means that the solvent molecules, as well as the polymer particles, will cause X-ray scattering, and the resulting pattern will be a sum of all of these processes. The strength of X-ray scattering by a particle is dependent on the contrast of scattering length densities (SLDs) between the components that make up a system, for example, the polymeric particles and the molecules in the continuous surrounding phase. This continuous phase could be a solvent or air. If the two SLDs are similar, the scattering pattern of the particles will be very weak, or indistinguishable, from that of the background. The SLD of a component can be calculated from **Equation (1.34)**.

$$\xi = \frac{b_e \rho_m N_A}{M_W} \sum_i n_i z_i \qquad (1.34)$$

Equation (1.34). The scattering length density of a component, ξ (m^{-2}) can be calculated from the scattering length of an electron (b_e / m), the density of the molecule (ρ_m / kg m^{-3}), Avogadro's constant (N_A / mol^{-1}), the weight-average molecular weight of the molecule (M_W / kg mol^{-1}) and the sum of the number of atoms, n_i, within a molecule with the atomic number z_i.[173]

The scattered X-rays can be detected as a 2D interference pattern and are related to the positions of atoms relative to each other throughout the entire sample. These distances are inherently related to the wavelength of X-ray radiation utilised (**Equation (1.35)**).[172,174] Often, the scattering signal is represented as a function of the scattering vector, q. Bragg's law can relate q to the length of the scattering object (**Equation (1.36)**).

$$q = \frac{4\pi}{\lambda} \sin\theta \qquad (1.35)$$

Equation (1.35). The scattered X-rays can be related to the scattering vector (q / nm^{-1}) from the wavelength of incident X-rays (λ / nm) and the angle from the incident X-ray beam (θ / °).

$$L = \frac{2\pi}{q} \qquad (1.36)$$

Equation (1.36). Bragg's law ($n\lambda = 2L \sin\theta$) can be employed to enable the scattering vector (q / nm^{-1}) to be converted to the length, or distance, between scattering objects (L / nm).[175]

1.6.1   Isotropic Samples

Scattered X-rays are sensed by a detector, which records their position relative to the centre of the incoming beam, in two dimensions. The methods of X-ray detection are dependent on the type of detector being utilised. The number of X-rays absorbed in a specific location, or scattering vector, are recorded and quantified as an intensity ($I(q)$). If the sample has no net orientation, the pattern of scattered X-rays will be isotropic, *i.e.,* it will be symmetrical with

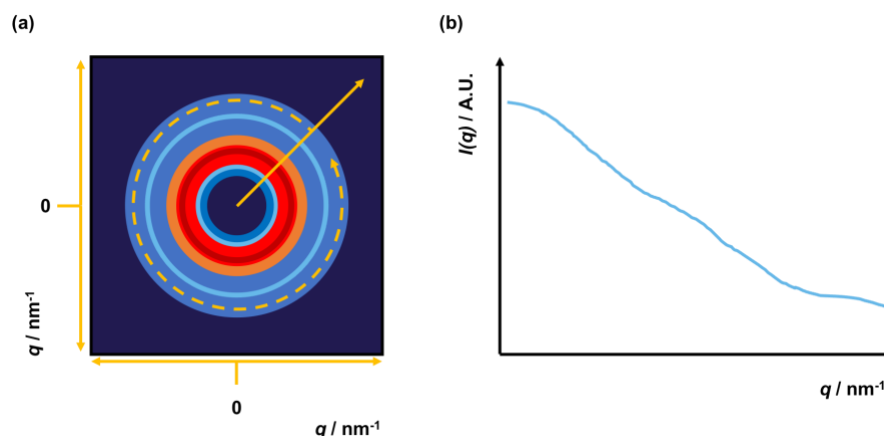**Figure (1.21). (a)** A representative schematic of isotropic scattering, which is identical in all directions from the beam. A radial integration of this pattern occurs from the centre of the beam (origin of the yellow arrow) to the edge of the detector. The intensity values are averaged at each q value (dotted yellow arrow). **(b)** Radial integration results in a representative $I(q)$ against q graph.

respect to the incoming beam centre (**Figure (1.21)(a)**). For an isotropic scattering pattern, the

easiest method for further analysis is to perform a radial integration of the 2D pattern, which

produces a 1D trace of $I(q)$ against q (**Figure (1.21)(b)**). This one-dimensional trace of the

scattering data can impart much information about the particles in a sample. The scattered

intensity, $I(q)$, includes two important terms: the form factor and the structure factor (**Equation

(1.37)**).

$$I(q) = NV_{particles}{}^2 \Delta\xi^2 F(q)S(q) \tag{1.37}$$

Equation (1.37). The intensity (I / nm^{-1}) of the scattering vector (q / nm^{-1}) at some angle is the multiplication of the number of particles (N), the volume of particles ($V_{particles}$ / m^3), the scattering length density contrast between the particles and the solvent ($\Delta\xi$ / m^{-2}), the particle form factor ($F(q)$) and the structure factor ($S(q)$).[175]

1.6.1.1   Form Factor

The form factor contains scattering information related to the size and shape of the

particles in a sample. If there are a range of sizes, or shapes, present in a sample, the scattering

pattern will contain an average of these populations. The fundamental form factor, and its

constituent terms, can be seen in **Equation (1.38)**.

$$F(q) = \frac{1}{\Delta\xi^2 V_{particle}} \int g_{particle}(r)e^{-iqr}\,dr \tag{1.38}$$

Equation (1.38). The form factor, $F(q)$, is calculated from the scattering length density contrast ($\Delta\xi$ / m^{-2}), the particle volume ($V_{particle}$ / nm^3), the correlation function of the particle ($g_{particle}$(r)/ dimensionless) and the integration over space (e^{-iqr} / dimensionless).[176]

However, instead of the form factor, the Guinier approximation can be utilised, which

contains a term describing the radius of gyration of a particle, R_g (**Equation (1.39)**).[172] This term

can be thought of as a measurement of the space occupied by a particle in solution. The SAXS

trace at very low q values will follow this Guinier approximation,[177] whereas, at high q, the Porod

approximation is more appropriate.[178]

$$I(q) \approx a_0 e^{\left(-\frac{R_g^2 q^2}{3}\right)} \hspace{2cm} \text{(1.39)}$$

Equation (1.39). The Guinier approximation uses the extrapolated intensity at zero angle (a_0 / nm^{-1}), the radius of gyration (R_g / nm) and the scattering vector (q / nm^{-1}).

The Guinier region is valid at low q, or when qR_g is much smaller than 1.3. This allows

for the simplification of the form factor of the SAXS trace as it will fit to a Gaussian curve with

the **Equation (1.39)**. In essence, the gradient of the SAXS trace at low q will indicate the particle

morphology, and dimension. Typical gradients of the one-dimensional SAXS trace at low q are

0, -1 and -2 for spheres, worms, or vesicles, respectively.
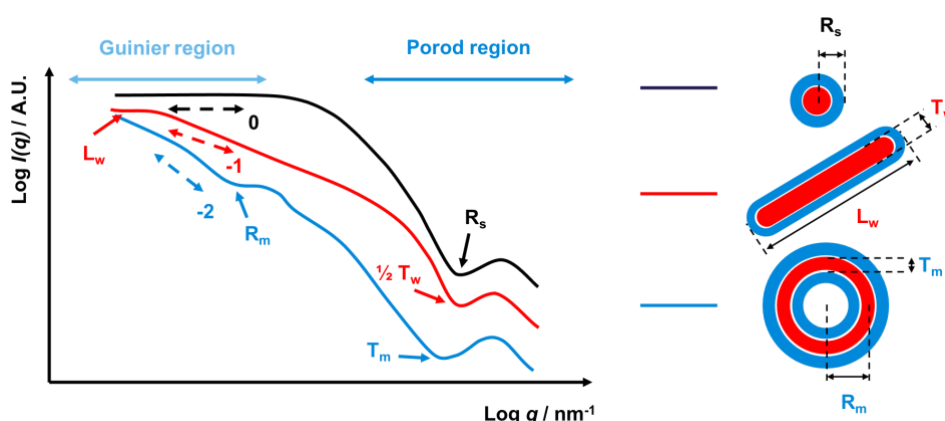
Figure (1.22). A representative schematic of scattering patterns for self-assembled synthetic polymeric materials with spheres (black trace), worms (red trace) and vesicles (blue trace). These have a slope of 0, -1 and -2 respectively in the Guinier region. Features in relevant scattering patterns represent the radius of the sphere (R_s), mean worm thickness (T_w), mean worm length (L_w), mean vesicle membrane thickness (T_m) and mean vesicle membrane radius (R_m).

1.6.1.2   Structure Factor

The second term in the intensity formula (**Equation (1.37)**) is the structure factor, which

is a term describing the relationship of particles in a system (**Equation (1.40)**). If the particles are

separated from each other by some constant distance, r, throughout the sample, then the scattering pattern will also contain this information. For a dilute sample, these distances are not as uniform and are often much larger than the wavelength of incoming X-rays. As such, for dilute concentrations, this factor can be ignored as the second term in **Equation (1.40)** tends to zero, causing the structure factor to equal one. The presence of a feature due to the structure factor leads to a much more complex one-dimensional scattering pattern, making the scattering pattern much more difficult to analyse. Therefore, care is often taken to ensure scattering patterns are gathered for dilute samples in order to exclude an effect of interparticle interactions.

$$S(q) = 1 + \frac{1}{N} \sum_{i=1}^{N} \sum_{j \neq 1}^{N} e^{iq(r_j - r_i)} \tag{1.40}$$

Equation (1.40). The structure factor, $S(q)$, contains terms for the number of particles (N) and summations of the exponential of the distance between atoms ($iq(r_j\text{-}r_i)$).[173]

1.6.2   Anisotropic Samples

Materials with no net orientation will result in an isotropic two-dimensional scattering pattern. However, if orientation of the particles is present, the 2D scattering pattern will not be the same in all directions; instead, it will be anisotropic. An anisotropic pattern will have modulations in the intensity of the scattered X-rays around the beam, which will appear as intensity peaks on the detector (**Figure (1.23)(a)**). The variation in this intensity can be analysed by performing azimuthal integrations, where the intensity values for all scattering vectors, over a specified range, are averaged for a certain angle. The resulting 1D trace can be plotted as an $I(q)$ vs ψ (**Figure (1.23 (b))**).

For polymeric chains or worm-like morphologies exhibiting net orientation, the 2D scattering pattern will display this type of anisotropic scattering. The difference in intensity

between the peaks and the troughs in the azimuthal trace indicates the degree of orientation present in the material.
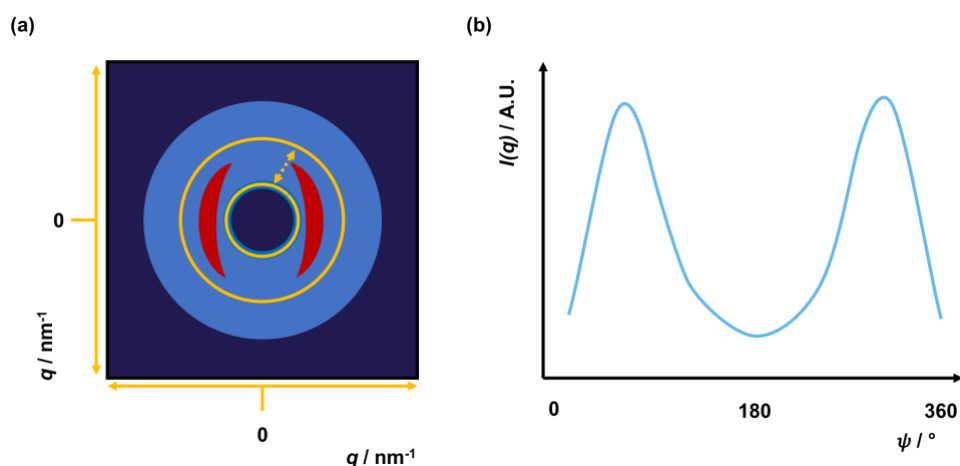
Figure (1.23). (a) A representative schematic of anisotropic scattering from an oriented sample, which has localised hotspots. An azimuthal integration of this pattern occurs between two q values (denoted by the yellow concentric circles). Intensity values are averaged at each ψ. **(b)** This produces a 1D trace which is plotted on an $I(q)$ against ψ graph.

1.6.2.1 Herman's Orientation Parameter, P_2

One frequently used method to calculate the direction, and degree of orientation present in the material is the Herman's orientation parameter, P_2 (**Equation (1.41)**).[179,180] P_2 can be any value between -1/2 and 1; where -1/2 means the orientation peaks at an angle of 90° (this is generally north/south on a SAXS detector) and for values of 1, the orientation is maximum at 0° (or east/west) with respect to the analysed structural directions. However, if the angle of orientation is unchanging, this parameter can also determine the degree of orientation. The degree of orientation is calculated from the maxima and minima intensities of the $I(q)$ against θ plot. In this case, a P_2 value of 0 indicates an isotropic scattering pattern, as seen in **Figure (1.21)(a)**.[181] As the scattering pattern becomes more anisotropic (similar to that seen in **Figure (1.23)(a)**), the P_2 value increases. This is due to an increase in the orientation of the particles in the sample. As a value of 1 is reached the material becomes increasingly more ordered.

$$P_2 = \frac{3\langle\cos{}^2\theta\rangle - 1}{2} \qquad\qquad (1.41)$$

Equation (1.41). The Hermann orientation parameter (P_2 / dimensionless) is a measure of the angle of the orientation (θ / °).

$$\langle\cos{}^2\theta\rangle = \frac{\int_0^\pi (\cos{}^2\theta)\Delta I(\theta)\sin\theta\,d\theta}{\int_0^\pi \Delta I(\theta)\sin\theta\,d\theta} \qquad\qquad (1.42)$$

Equation (1.42). The $\cos^2\theta$ function in **Equation (1.41**) is defined using the angle (θ / °), and the intensity of scattered X-rays at that angle ($I(\theta)$ / cm^{-1}).

1.7 Millifluidics and SAXS

The first reported study combining microfluidics and small-angle X-ray scattering was in 1999.[131] In this work; Pollack *et al*. developed a HFF device to investigate the effects of pH on the folding of a protein, cytochrome *c*. This straight channel geometry sheathes the material of interest in a secondary fluid, by the use of two additional inlets, one either side of the inlet delivering the protein solution. Time resolution of the protein folding was made possible by taking measurements at fixed locations along the fluid stream. This research highlighted the method of folding that occurs when a protein's environment changes rapidly.

Despite this early work bringing fluidics and X-ray scattering together, the combination of the two techniques did not gain popularity until the mid-to-late 2000s (**Table (1.2)**). The delay is likely to be due to several reasons; firstly, as already discussed in **Section 1.5**, the fabrication of microfluidic channels is a barrier to the employment of these devices by research groups without the necessary resources. However, the improvement of fabrication techniques, such as soft lithography and etching techniques, has allowed this combination to be much more accessible.

Secondly, until recently, the collection of adequate SAXS data from polymeric materials has been limited to synchrotron sources which provide the required X-ray flux for time-resolved

studies to be performed. The oversubscription of these synchrotron SAXS beamlines means that novel sample environments are not frequently employed. Although laboratory SAXS sources have been prevalent since the late 1940s,[178,182] it has only been with the last decade that the data collected from these instruments are comparable to that obtained from synchrotron sources. These laboratory-based instruments allow research groups to prototype micro- and millifluidic geometries before synchrotron access.
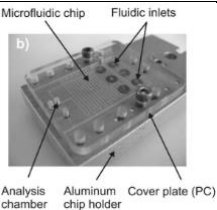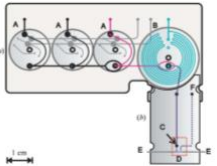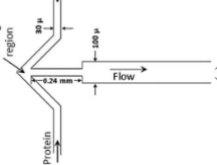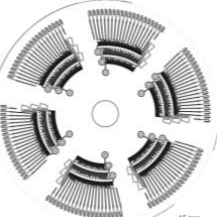
1.7.1   Development of microfluidic devices for synchrotron measurements

With the rapid uptake of milli- and microfluidic devices, some synchrotron SAXS beamlines have developed integrated fluidic environments for the soft condensed matter community[171,183–186] (**Table (1.1)**). Noteworthy research into the development of specialised microfluidic devices included the seminal work by Lafleur *et al*., who developed a microfluidic device in combination with the Swiss Light Source.[186] The device was capable of sample preparation, including mixing and fluid control, as well as data collection via SAXS and UV/vis and subsequent data analysis. It was also possible to automate these aspects of the microfluidic device, which meant that the total analysis cycle was completed in under three minutes. The work utilised protein fragments as a case study, to show that the device could map the structural space adopted by a protein by screening a wide range of conditions, in a time-efficient manner. The device was an upgrade of a previously published design by Toft and coworkers,[187] and consisted of two discrete modules; a mixing chip and a sample detection chip.

Graceffa *et al*. also developed a microfluidic device, at the Advanced Photon Source, Argonne National Laboratory.[185] The microfluidic device developed at this synchrotron was capable of investigating processes that occur on the order of microseconds (one millionth of a second). Alongside the development of a microfluidic system, the optics of the beamline were enhanced to allow for the focusing on the X-ray beam. The combination of a micron sized SAXS

beam and the turbulent microfluidic mixer allowed for the investigation of fast reactions or phase transitions, however the paper followed the folding of cytochrome *c* as a proof-of-concept study.

Table (1.1). Overview of the research published utilising microfluidics and SAXS from synchrotron beamlines.

Author	Year	Geometry	Image of Device	Material Investigated
Toft *et al.*[188]	2008	Mixing		Proteins
Lafleur *et al.*[186]	2011	Mixing		Proteins
Graceffa *et al.*[185]	2013	Mixing		Proteins
Blanchet *et al.*[183]	2014	Centrifugal		Proteins

Work undertaken at the German synchrotron, DESY, by Blanchet *et al.* produced a novel, fully automated microfluidic system capable of investigating biological material in a range of different sample environments.[183] The unfolding of ribonuclease A in different environments within this device was utilised as a case study. This 'LabDisc' was found to be useful in the rapid screening of multiple sample conditions, whilst utilising very small sample volumes. This work was further improved upon by Schwemmer *et al.*[171] and Hajizadeh *et al.*[184] in 2016 and 2018 respectively. The first enhancement to the LabDisc is the automation of both the sample chamber alignment (via bitcodes) and data acquisition. These automation steps led to a reduction in the

total measurement time for each of the 120 sample chambers, further improving the ability for rapid screening. Hajizadeh *et al*. published work on the automation of the data analysis pipeline to aid the subsequent investigation and manipulation of SAXS data.

The benefits of tailored fluidic devices are numerous. Firstly, these devices have been purposefully designed for SAXS measurements. Therefore, they are often assimilated into the beamline, allowing full and easy control over motors, syringe pumps, shutters and data acquisition from one workstation. Secondly, the fluidic devices have all been developed to be used by novice users, with very little experimental time at the synchrotron.

However, despite the advantages of the synchrotron-based devices, the environments currently available are lacking in some respects. The two main issues are as follows. Primarily, the fluidic environments available (that are discussed above) are only applicable for specific experiments involving proteins (**Table (1.1)**), and therefore are not appropriate for the broader community base interested in utilising these environments. In addition, the fluidic devices are only suitable for the investigation of low viscosity, low concentration samples, again making them inappropriate for the majority of soft condensed matter researchers. Coupled with the fact that very few synchrotron SAXS beamlines offer flow environments, these issues have often led to users fabricating their own fluidic environments for beamtime experiments. An analysis of these microfluidic devices has been undertaken.

1.7.2   User-developed fluidic devices for synchrotron applications

Due to the lack of variety of microfluidic devices offered by synchrotron beamlines, the bulk of researchers with work published utilising fluidic devices and SAXS have developed their own micro- or millifluidic systems which fulfil their research need (**Table (1.2)**). These systems are often well designed and fabricated, as well as being able to fulfil their design need. Many of

these devices have resulted in ground-breaking research. However, the devices are incorporated into synchrotron beamlines for data collection in ways that are not capable to take advantage of the possible automation available.

The majority of studies have used the combination of microfluidic devices and SAXS to investigate protein structure and crystallisation.[113,130,193–197,131,186–192] Köster *et al*. utilised a HFF microfluidic device to study the self-assembly process of collagen fibrils, as a function of pH change.[189] This work led to an increased understanding of the collagen self-assembly process. In 2007, Evans *et al.* utilised the well-defined mixing conditions present in HFF devices to follow the supramolecular assembly of liposome-DNA and their orientation with flow.[190] The relaxation of these structures was also found to show a four-fold symmetry. In 2008, Köster *et al*. furthered the understanding of the collagen assembly process through the use of microfluidics and SAXS.[191] Toft *et al.* have also developed a microfluidic system for the structural analysis of proteins, with bovine serum albumin utilised for proof of concept.[188] The device had discrete environments for the mixing, and SAXS measurement, of proteins. This work was important as the group developed software for full automation of the device, alongside the microfluidic system fabricated.

Other work involving the use of proteins include Brennich *et al*. who utilised the combination of a HFF device and SAXS to study the kinetics of intermediate filament protein assembly.[192] The use of a salt buffer as the sheath flow allowed the effects of salt on the assembly kinetics to be investigated. Skou and coworkers developed a microfluidic system capable of measuring structural changes of proteins as a result of dynamically controlled sample conditions.[197] Similarly to Toft et al. this device contained two discrete segments; a dialysis chip and a measurement chip. It was reported that this microfluidic system was suitable for concentration screening of protein solutions as well as monitoring concentration-induced structural changes and aggregation. Finally, Saldanha *et al*. developed a microfluidic device in 2017 which focused on encapsulating proteins in aqueous droplets.[113] The need for protein encapsulated within droplets was to improve the signal-to-noise ratio in, otherwise, weakly

scattering systems. Droplets also had the added advantage of preventing protein adsorption to the channel walls.

These devices were fabricated from either polydimethylsiloxane (PDMS),[113,189,191,192,197] polystyrene (PS)[188] via soft lithography, or stainless steel via micromilling.[190,198] All devices were sealed with Kapton windows, with the exception of Toft *et al.* and Skou *et al.* who both used polystyrene foils,[188,197] and Brennich *et al*. who utilised Norland Optical Adhesive 81 (NOA 81)[192] as window materials.

Two key studies have combined the use of microfluidics and SAXS to investigate cellulose.[195,196] Håkansson *et al.* investigated the formation of cellulose filaments in a HFF microfluidic device.[196] The filaments produced from this device were found to have a specific ultimate strength comparable to cellulose pulp fibres extracted from wood. Anisotropic scattering patterns show strong alignment of the fibrils at the centre of the formed cellulose filaments. The study explored the impacts of fibril alignment and gelation; by separating this process into distinct time regimes, strong and stiff cellulose filaments can be produced, as a great proportion of fibrils can align along the flow direction. The device utilised in this work was produced from stainless steel by micromilling, and Kapton windows were employed to seal the device.

Rosén *et al.* have also published work on studying cellulose fibrils under flow.[195] This publication continued the work outlined by Håkansson *et al.*, to fully characterise the orientation distribution of cellulose fibrils under flow. Full analysis of the SAXS patterns collected in the previous paper was undertaken. Using azimuthal integrations and the Herman orientation function, analysis of the anisotropic SAXS patterns allowed a snapshot of the distribution of fibril orientations to be determined. The aim of this work was to fully map and optimise the orientation of fibrils during the filament formation process.

Other frequently explored materials in these experiments are DNA[198–201] and RNA.[202] For example, Otten *et al.* utilised a HFF microfluidic device to study the intercalation of DNA into multilamellar membranes, via SAXS.[200] The alignment of these structures with the flow direction enhanced the structural characterisation of the self-assembled anisotropic objects. In 2006, Dootz *et al.* employed a HFF device to investigate the interaction between DNA molecules and dendrimers, via diffusive mixing.[198] Dendrimers can self-assemble into superstructures, and it was found that the combination of flow with SAXS would enable this self-assembly process to be followed. Pfohl *et al.* followed how flow enhanced the compaction of DNA via spatially resolved, oriented SAXS patterns. The 'hot spots' in these SAXS patterns are diffuse and broad early in the channel but become much sharper and localised as the DNA travels along the channel, showing an increase in the compaction of DNA. These three papers utilised microfluidic devices produced from stainless steel plates via micromilling and sealed with Kapton windows.[198–200]

Synthetic polymers are also explored and characterised, utilising the combination of microfluidics and SAXS.[146,203–207] Most of the work published in this area (up to the year 2020) is based on following a phase transition of polymeric chains. For example, Trebbin *et al.* reported the use of an expansion-contraction (EC) based microfluidic device in 2013 to study the orientation of anisotropic micelles consisting of poly(isoprene-b-ethylene oxide) (PI-PEO) or poly(ethylenebutylene-b-ethylene oxide) (PEB-PEO) polymer chains.[146] The orientation of cylindrical micelles along the flow direction was observed prior to the channel contraction. However, when the channel expanded, this was accompanied by the micellar orientation perpendicular to the flow. The orientation direction of these micelles was easily determined from the resultant two-dimensional scattering patterns which show anisotropy perpendicular to the orientation direction.

With *et al.* published work in 2014 which monitored the self-assembly of the amphiphilic block copolymer poly(isoprene-*b*-ethylene glycol) (PI-PEG).[203] A HFF device was utilised to

slowly incorporate water into the sheathed flow where dioxane is the solvent. As PI is insoluble in water, this initiates the self-assembly process. After the formation of the micelles, it was found that they become ordered into a face-centred cubic lattice, which could be identified easily from the six-fold symmetrical scattering pattern.
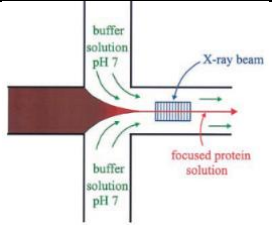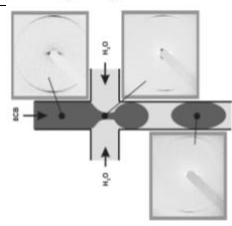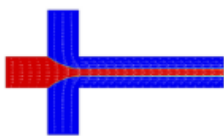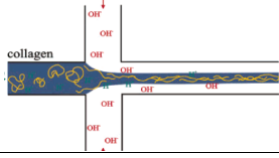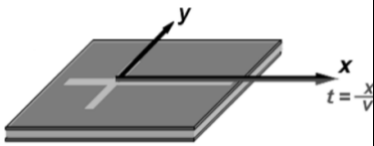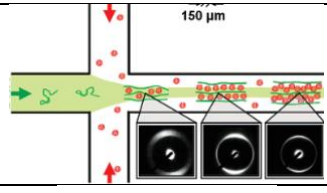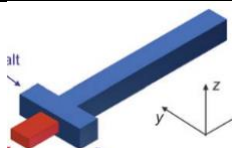
Furst *et al*. also utilised the two techniques to observe the transition of the PI-PEG block copolymer into cylindrical micelles, and their subsequent evolution into vesicles.[205] The transition into, and between micelles was probed; it was found that the use of a HFF microfluidic device causes the block copolymer chains to adopt transient cylindrical structures which are quasi-stable in water. This is in conflict to bulk studies, where vesicle micelle structures are rapidly formed in water, with no apparent adoption of the cylindrical macromolecular structure.
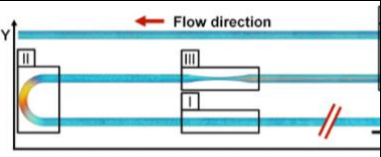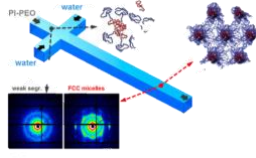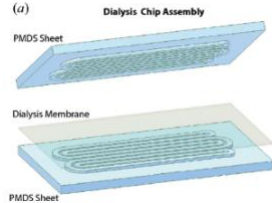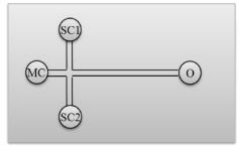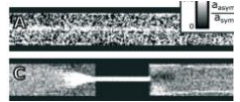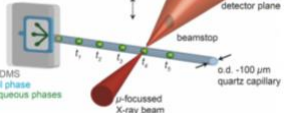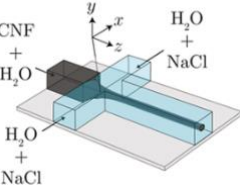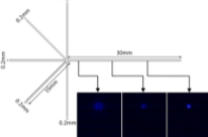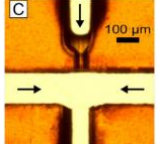
In 2016, Lutz-Bueno *et al*. published work utilising both straight channel (SC) and EC-based microfluidic device, to study the effects of flow on molecular properties.[207] Much like Trebbin *et al.*, the motivation behind this work was to study the orientation of anisotropic particles under flow. The use of a SAXS mapping measurement allowed for finer gathering of data to more accurately determine the effects of channel expansions and contractions on particle orientation. The degree of orientation of anisotropic scattering patterns was utilised to give orientation trends in channels with different concentrations and particle mixtures.

A novel block copolymer system was investigated by Kalkowski *et al.* in 2019.[204] The work focused on micellisation kinetics of poly(ethylene glycol)-b-poly(caprolactone) (PEG-*b*-PCL). The HFF microfluidic device triggered self-assembly through the introduction of water as a solvent in the THF based system. The micellisation steps of nucleation, fusion and insertion were observed directly in the formation of self-assembled structures, via time resolved SAXS measurements.

Vakili *et al.* developed a microfluidic device capable of investigating the self-assembly process of the block copolymer poly(N,N-dimethylacrylamide)-poly(2-methoxyethyl acrylate)

Table (1.2). Overview of the research published utilising microfluidic devices and SAXS. HFF denotes for hydrodynamic flow focussing, SC a straight channel geometry and EC an expansion-contraction channel. S and L denote whether the work uses a synchrotron or lab-based SAXS instrument respectively.

Author	Year	Geometry	Image of Device	Material Investigated	S or L
Pollack *et al.*[131]	1999	HFF		Proteins	S
Otten *et al.*[200]	2005	HFF		DNA	S
Dootz *et al.*[198]	2006	HFF		Proteins	S
Köster *et al.*[189]	2007	HFF		Proteins	S
Evans *et al.*[190]	2007	HFF		Proteins	S + L
Pfohl *et al.*[199]	2007	HFF		DNA	S
Köster *et al.*[191]	2008	HFF		Proteins	S
Brennich *et al.*[192]	2011	HFF		Proteins	S + L

Author	Year	Geometry	Image of Device	Material Investigated	S or L
Trebbin *et al.*[146]	2013	EC		Block Copolymer	S
Håkansson *et al.*[196]	2014	HFF		Proteins	S
With *et al.*[203]	2014	HFF		Block Copolymer	S
Skou *et al.*[197]	2014	Mixing		Proteins	S
Furst *et al.*[205]	2016	HFF		Block Copolymer	S
Lutz-Bueno *et al.*[207]	2016	SC + EC		Block Copolymer	S
Saldanha *et al.*[113]	2017	Droplet		Proteins	S
Rosén *et al.*[195]	2018	HFF		Proteins	S
Kalkowski *et al.*[204]	2019	HFF		Block Copolymer	S
Vakili *et al.*[206]	2019	HFF		Block Copolymer	S

(PDMAm-*b*-PMEA).[206] The combination of this HFF microfluidic device with time resolved SAXS allowed the stages of self-assembly to be closely followed, and analysed. An initial phase transition from chains to spherical micelles was observed before subsequent formation of a micellar face centred cubic lattice.

Three of these papers utilised a laser micromachining fabrication method to produce microfluidic devices entirely from Kapton film.[203,205,206] The latest paper, from Vakili and coworkers, described a modification to this technique which offers three-dimensional control over channel formation.[206] Both Trebbin et al. and Lutz-Bueno et al. fabricated microfluidic devices from PDMS using photolithography and soft lithography techniques.[146,207] The fourth paper, from Kalkowski *et al.* focusing on synthetic polymer self-assembly utilised a microfluidic device fabricated from quartz.[204]

Other polymeric materials, less frequently investigated with microfluidics and SAXS, include enzymes,[208,209] peptides,[210] lipids,[112,211–213] surfactants,[214–216] phospholipids,[217–219] hydrogels[220,221] and liquid crystals.[222]

The work highlighted in this review of user-based microfluidic devices can be separated based on two key topics; the research area and the channel geometry. An overview into this area of research shows that the majority of published works have been dedicated to protein studies (**Table (1.1)** and **Table (1.2)**). This can be further simplified into the investigation of protein structure, as well as exploring the kinetics of protein crystallisation or folding. As previously discussed, the use of synchrotron SAXS sources, for protein studies, gives enhanced data compared to lab SAXS sources, as the high X-ray flux and collimation allows for both time and spatially resolved studies to occur in microfluidic channels, with good signal-to-noise ratios. Other, less frequently investigated materials include DNA, block copolymers, surfactants, enzymes and lipids.

The greater part of this work has utilised dilute, or low viscosity materials, with microfluidic devices, with the exception of some work with HFF based systems. There are two main motives behind the use of low concentrations: firstly, a low concentration of material results in a one-dimensional scattering pattern with only a form factor element present. This leads to a simpler pattern to analyse as there is no structure factor component to consider. Secondly, the use of a low concentration sample generally means the material is less viscous. Microfluidic devices are often only functional for low viscosity materials, before leakage from the channel occurs or other areas of the device fails. The use of an HFF channel means the microfluidic device can withstand greater pressures from viscous, or concentrated materials, as the buffer fluid is able to 'mask' these forces.

Classifying the outlined research by channel geometry imparts information on the most frequently utilised devices. **Table (1.2)** gives an overview of the most commonly used channel geometry; in order of popularity, these are HFF, turbulent mixing (T or Y junctions), expansion-contraction and straight channel (including centrifugal and droplet-based geometries). No work combining microfluidic devices with cross-slot or other complex geometries and SAXS could be found. Despite the popularity of the HFF based microfluidic device, there are some associated problems with its use. The main issue is that the geometry is often described as shear flow-based, however, this is not strictly the case as there is a strong extensional element present along the channel. The flow present at each point along the channel is, therefore, hard to define due to unknow rheological properties of samples which has associated issues with the subsequent analysis of data. In addition, an X-ray beam crossing these geometries interacts with sample experiencing a wide range of shear rates, complicating data interpretation with respect to the flow parameters. Often, the channel geometry is not the main focus of the research and HFF-based microfluidics are only utilised to change the environment of the sample being investigated

(temperature, solvent, pH etc.). However, this is only appropriate when the effects of the channel on sample structure are fully understood.

Although the combination of microfluidic devices and SAXS has been popular over the last 20 years, it is clear that synchrotron beamlines have been slow to adopt technologies which can offer microfluidic, or millifluidic, geometries to their user base. The devices currently available are well integrated into beamlines with many aspects of fluid manipulation, data collection and data analysis being fully automated, however, these devices are often very specific in the materials they can test. Based on the volume of published work, in a wide range of areas, there is an obvious need for universal devices to be accessible for synchrotron users.

1.8   Aims

This thesis outlines work undertaken to develop a range of millifluidic devices, with variable geometries, suitable for *in situ* SAXS analysis of soft matter materials. The aim was to develop design criteria providing fast and cheap manufacturing of millifluidic devices of desired flow geometry to enable the manipulation, and study, of viscous polymeric materials. **Chapter 2** and **Chapter 3** outline the methodology utilised to find suitable materials for testing in millifluidics with the aim to find anisotropic objects which were able to orient along a flow direction. In **Chapter 4**, the design process and fabrication methods tested for the development of millifluidic devices are outlined, along with proposed design rules to successfully fabricate millifluidic devices suitable for the use with viscous materials. **Chapter 5** deals with the characterisation of a straight channel geometry, using FEA, POM and SAXS. **Chapter 6** outlines the work carried out around a cross-slot millifluidic geometry as a representative example of complex flow geometries, using particle tracing, FEA, POM and SAXS.

1.9 References

(1) Jones, R.; Weitz, D. *Phys. Today* **2003**, *56*, 63–64.

(2) Wyss, H. M. Rheology of Soft Materials. *Fluids, Colloids and Soft Materials*. May 9, 2016, pp 149–163.

(3) Ryan, E. A.; Mockros, L. F.; Weisel, J. W.; Lorand, L. *Biophys. J.* **1999**, *77*, 2813–2826.

(4) Moreno-Arotzena, O.; Meier, J. G.; Amo, C. Del; García-Aznar, J. M. *Materials (Basel).* **2015**, *8*, 1636–1651.

(5) Wu, H.; Jawerth, L.; Weitz, D. *Biophys. J.* **2011**, *100*, 388a.

(6) Arevalo, R. C.; Urbach, J. S.; Blair, D. L. *Biophys. J.* **2010**, *99*, L65–L67.

(7) Madsen, C. D.; Cox, T. R. *Bio-protocol* **2017**, *7*, e2265.

(8) Baker, E. L.; Bonnecaze, R. T.; Zaman, M. H. *Biophys. J.* **2009**, *97*, 1013–1021.

(9) Rymaruk, M. J.; Hunter, S. J.; O'Brien, C. T.; Brown, S. L.; Williams, C. N.; Armes, S. P. *Macromolecules* **2019**, *52*, 2822–2832.

(10) Chiou, B. Sen; English, R. J.; Khan, S. A. *Macromolecules* **1996**, *29*, 5368–5374.

(11) Fairclough, J. P. A.; Yu, H.; Kelly, O.; Ryan, A. J.; Sammler, R. L.; Radler, M. **2012**.

(12) Arvidson, S. A.; Lott, J. R.; Mcallister, J. W.; Zhang, J.; Bates, F. S.; Lodge, T. P.; Sammler, R. L.; Li, Y.; Brackhagen, M. **2013**.

(13) Mykhaylyk, O. O.; Warren, N. J.; Parnell, A. J.; Pfeifer, G.; Laeuger, J. *J. Polym. Sci. Part B Polym. Phys.* **2016**, *54*, 2151–2170.

(14) Mykhaylyk, O. O. *Soft Matter* **2010**, *6*, 4430–4440.

(15) Byard, S. J.; O'Brien, C. T.; Derry, M. J.; Williams, M.; Mykhaylyk, O. O.; Blanazs, A.; Armes, S. P. *Chem. Sci.* **2020**, *11*, 396–402.

(16) Hsiao, K. W.; Dinic, J.; Ren, Y.; Sharma, V.; Schroeder, C. M. *Phys. Fluids* **2017**, *29*, 1–12.

(17) Del Giudice, F.; Tassieri, M.; Oelschlaeger, C.; Shen, A. Q. *Macromolecules* **2017**, *50*, 2951–2963.

(18) Vleminckx, G.; Clasen, C. *Curr. Opin. Colloid Interface Sci.* **2014**, *19*, 503–513.

(19) Blanazs, A.; Ryan, A. J.; Armes, S. P. *Macromolecules* **2012**, *45*, 5099–5107.

(20) Blanazs, A.; Armes, S. P.; Ryan, A. J. *Macromol. Rapid Commun.* **2009**, *30*, 267–277.

(21) Morrison, F. A. *Understanding Rheology*; Oxford University Press, **2001**.

(22) Macosko, C. W. *Rheology: Principles, Measurements and Applications*; Wiley-VCH, **1994**.

(23) Del Giudice, F.; Haward, S. J.; Shen, A. Q. *J. Rheol. (N. Y. N. Y).* **2017**, *61*, 327–337.

(24) Simpson, M. M.; Janna, W. S. *ASME Int. Mech. Eng. Congr. Expo. Proc.* **2009**, *9*, 173–180.

(25) Srivastava, N.; Burns, M. A. *Anal. Chem.* **2006**, *78*, 1690–1696.

(26) Galindo-Rosales, F. J.; Campo-Deaño, L.; Pinho, F. T.; Van Bokhorst, E.; Hamersma, P. J.; Oliveira, M. S. N.; Alves, M. A. *Microfluid. Nanofluidics* **2012**, *12*, 485–498.

(27) Nejad, M. M.; Javaherdeh, K. *Case Stud. Therm. Eng.* **2014**, *3*, 68–78.

(28) Yuan, C.; Zhang, H.-N.; Li, Y.-K.; Li, X.-B.; Wu, J.; Li, F.-C. *Proc. Inst. Mech. Eng. Part C J. Mech. Eng. Sci.* **2020**, *234*, 4390–4414.

(29) Cross, M. M. *J. Colloid Sci.* **1965**, *20*, 417–437.

(30) Carreau, P. J. *Trans Soc Rheol* **1972**, *16*, 99–127.

(31) Bharati, A.; Hudson, S. D.; Weigandt, K. M. *Curr. Opin. Colloid Interface Sci.* **2019**, *42*, 137–146.

(32) Duda, J. L.; Klaus, E. E.; Lin, S. C. *Ind. Eng. Chem. Res.* **1988**, *27*, 352–361.

(33) Hencky, H. *ZAMM - Zeitschrift für Angew. Math. und Mech.* **1923**, *3*, 241–251.

(34) Sharma, V.; Haward, S. J.; Serdy, J.; Keshavarz, B.; Soderlund, A.; Threlfall-Holmes, P.; McKinley, G. H. *Soft Matter* **2015**, *11*, 3251–3270.

(35)   Brimmo, A. T.; Qasaimeh, M. A. *RSC Adv.* **2017**, *7*, 51206–51232.

(36)   Taylor, G. I. *Proc. R. Soc. London. Ser. A, Contain. Pap. a Math. Phys. Character* **1934**, *146*, 501–523.

(37)   Galindo-Rosales, F. J.; Alves, M. A.; Oliveira, M. S. N. *Microfluid. Nanofluidics* **2013**, *14*, 1–19.

(38)   Zografos, K.; Burshtein, N.; Shen, A. Q.; Haward, S. J.; Poole, R. J. *J. Nonnewton. Fluid Mech.* **2018**, *262*, 12–24.

(39)   Auhl, D. W.; Hoyle, D. M.; Hassell, D. G.; Lord, T. D.; Mackley, M. R.; Harlen, O. G.; McLeish, T. C. B. *J. Rheol. (N. Y. N. Y).* **2011**, *55*, 875–900.

(40)   Hudson, S. D.; Phelan, F. R.; Handler, M. D.; Cabral, J. T.; Migler, K. B.; Amis, E. J. *Appl. Phys. Lett.* **2004**, *85*, 335–337.

(41)   Scrivener, O.; Berner, C.; Cressely, R.; Hocquart, R.; Sellin, R.; Vlachos, N. S. *J. Nonnewton. Fluid Mech.* **1979**, *5*, 475–495.

(42)   Haward, S. J.; Oliveira, M. S. N.; Alves, M. A.; McKinley, G. H. *Phys. Rev. Lett.* **2012**, *109*, 1–5.

(43)   Bharati, A.; Hudson, S. D.; Weigandt, K. M. *Curr. Opin. Colloid Interface Sci.* **2019**, *42*, 137–146.

(44)   Haward, S. J.; Mckinley, G. H.; Shen, A. Q. *Sci. Rep.* **2016**, *6*, 1–18.

(45)   Haward, S. J. *Biomicrofluidics* **2016**, *10*, 1–27.

(46)   Galindo-Rosales, F. J.; Oliveira, M. S. N.; Alves, M. A. *RSC Adv.* **2014**, *4*, 7799–7804.

(47)   Pipe, C. J.; McKinley, G. H. *Mech. Res. Commun.* **2009**, *36*, 110–120.

(48)   Dubash, N.; Cheung, P.; Shen, A. Q. *Soft Matter* **2012**, *8*, 5847–5856.

(49)   Haward, S. J.; Odell, J. A.; Berry, M.; Hall, T. *Rheol. Acta* **2011**, *50*, 869–879.

(50)   Penfold, J.; Staples, E.; Tucker, I.; Carroll, P.; Clayton, I.; Cowan, J. S.; Lawton, G.; Amin, S.; Ferrante, A.; Ruddock, N. *J. Phys. Chem. B* **2006**, *110*, 1073–1082.

(51)   Kisilak, M.; Anderson, H.; Babcock, N. S.; Stetzer, M. R.; Idziak, S. H. J.; Sirota, E. B. *Rev. Sci. Instrum.* **2001**, *72*, 4305–4307.

(52)   Idziak, S. H. J.; Welch, S. E.; Kisilak, M.; Mugford, C.; Potvin, G.; Veldhuis, L.; Sirota, E. B. *Eur. Phys. J. E* **2001**, *6*, 139–145.

(53)   Alicia, T. G. G.; Yang, C.; Wang, Z.; Nguyen, N. T. *Lab Chip* **2016**, *16*, 368–376.

(54)   Bhattacharjee, P. K.; McDonnell, A. G.; Prabhakar, R.; Yeo, L. Y.; Friend, J. *New J. Phys.* **2011**, *13*.

(55)   EVERAGE, A. E.; BALLMAN, R. L. *Nature* **1978**, *273*, 213–215.

(56)   Aho, J.; Rolón-Garrido, V. H.; Syrjälä, S.; Wagner, M. H. *Rheol. Acta* **2010**, *49*, 359–370.

(57)   Mohos, F. Á. *Confectionery and Chocolate Engineering*; Wiley-Blackwell: Oxford, UK, **2010**.

(58)   Trouton, F. T. *Proc. R. Soc. London. Ser. A, Contain. Pap. a Math. Phys. Character* **1906**, *77*, 426–440.

(59)   Gupta, S.; Wang, W. S.; Vanapalli, S. A. *Biomicrofluidics* **2016**, *10*, 1–26.

(60)   Kim, B. J.; Lee, Y. S.; Zhbanov, A.; Yang, S. *Analyst* **2019**, *144*, 3144–3157.

(61)   Méndez-Sánchez, A. F.; Pérez-González, J.; de Vargas, L.; Castrejón-Pita, J. R.; Castrejón-Pita, A. A.; Huelsz, G. *J. Rheol. (N. Y. N. Y).* **2003**, *47*, 1455–1466.

(62)   Solomon, D. E.; Abdel-Raziq, A.; Vanapalli, S. A. *Rheol. Acta* **2016**, *55*, 727–738.

(63)   Fu, T.; Carrier, O.; Funfschilling, D.; Ma, Y.; Li, H. Z. *Chem. Eng. Technol.* **2016**, *39*, 987–992.

(64)   Cho, M.; Hong, S. O.; Lee, S. H.; Hyun, K.; Kim, J. M. *Micromachines* **2019**, *10*, 535–547.

(65)   Pan, L.; Arratia, P. E. *Microfluid. Nanofluidics* **2013**, *14*, 885–894.

(66)   Nam, J.; Lim, H.; Kim, D.; Jung, H.; Shin, S. *Lab Chip* **2012**, *12*, 1347–1354.

(67)   Omori, T.; Imai, Y.; Kikuchi, K.; Ishikawa, T.; Yamaguchi, T. *Ann. Biomed. Eng.* **2014**, *43*, 238–257.

(68) Lindner, P.; Bewersdorff, H. W.; Heen, R.; Sittart, P.; Thiel, H.; Langowski, J.; Oberthuer, R. *Prog. Colloid Polym. Sci.* **1990**, *81*, 107–112.

(69) Pipe, C. J.; Majmudar, T. S.; McKinley, G. H. *Rheol. Acta* **2008**, *47*, 621–642.

(70) Christopher, G. F.; Anna, S. L. *J. Phys. D. Appl. Phys.* **2007**, *40*, 319–336.

(71) Squires, T. M.; Quake, S. R. *Rev. Mod. Phys.* **2005**, *77*, 977–1026.

(72) Gupta, S.; Vanapalli, S. A. *Phys. Fluids* **2020**, *32*, 1–13.

(73) Xiang, N.; Zhang, X.; Dai, Q.; Cheng, J.; Chen, K.; Ni, Z. *Lab Chip* **2016**, *16*, 2626–2635.

(74) Lee, J. S.; Shaqfeh, E. S. G.; Muller, S. J. *Phys. Rev. E - Stat. Nonlinear, Soft Matter Phys.* **2007**, *75*, 15–18.

(75) Young, T. *A Course of Lectures on Natural Philosophy and the Mechanical Arts.*; Johnson: London, **1807**.

(76) Maxwell, J. C. *Philos. Trans. R. Soc. London* **1865**, *155*, 459–512.

(77) Pathak, J. A.; Hudson, S. D. *Macromolecules* **2006**, *39*, 8782–8792.

(78) Hamza, A. A.; Abd el-Kader, H. I. *Text. Res. J.* **1983**, *53*, 205–209.

(79) Rosén, T.; Wang, R.; Zhan, C.; He, H.; Chodankar, S.; Hsiao, B. S. *Phys. Rev. E* **2020**, *101*, 1–17.

(80) Haward, S. J.; Jaishankar, A.; Oliveira, M. S. N.; Alves, M. A.; McKinley, G. H. *Biomicrofluidics* **2013**, *7*, 1–15.

(81) Auhl, D.; Hoyle, D. M.; Hassell, D.; Lord, T. D.; Harlen, O. G.; Mackley, M. R.; McLeish, T. C. B. *J. Rheol. (N. Y. N. Y).* **2011**, *55*, 875–900.

(82) Hoyle, D. M.; Huang, Q.; Auhl, D.; Hassell, D.; Rasmussen, H. K.; Skov, A. L.; Harlen, O. G.; Hassager, O.; McLeish, T. C. B. *J. Rheol. (N. Y. N. Y).* **2013**, *57*, 293–313.

(83) Manz, A.; Graber, N.; Widmer, H. M. *Sensors Actuators B Chem.* **1990**, *1*, 244–248.

(84) Krishna, K. S.; Biswas, S.; Navin, C. V.; Yamane, D. G.; Miller, J. T.; Kumar, C. S. S. R. *J. Vis. Exp.* **2013**, *1*, 1–9.

(85) Guillot, P.; Panizza, P.; Salmon, J. B.; Joanicot, M.; Colin, A.; Bruneau, C. H.; Colin, T. *Langmuir* **2006**, *22*, 6438–6445.

(86) Jamshidi, R.; Rossi, D.; Saffari, N.; Gavriilidis, A.; Mazzei, L. *Cryst. Growth Des.* **2016**, *16*, 4607–4619.

(87) D'Avino, G.; Hulsen, M. A.; Greco, F.; Maffettone, P. L. *J. Nonnewton. Fluid Mech.* **2019**, *263*, 33–41.

(88) Weston, J. S.; Seeman, D. P.; Blair, D. L.; Salipante, P. F.; Hudson, S. D.; Weigandt, K. M. *Rheol. Acta* **2018**, *57*, 241–250.

(89) Nordstrom, K. N.; Verneuil, E.; Arratia, P. E.; Basu, A.; Zhang, Z.; Yodh, A. G.; Gollub, J. P.; Durian, D. J. *Phys. Rev. Lett.* **2010**, *105*, 1–4.

(90) Del Giudice, F.; Romeo, G.; D'Avino, G.; Greco, F.; Netti, P. A.; Maffettone, P. L. *Lab Chip* **2013**, *13*, 4263–4271.

(91) Mai, D. J.; Brockman, C.; Schroeder, C. M. *Soft Matter* **2012**, *8*, 10560–10572.

(92) Günther, A.; Khan, S. A.; Thalmann, M.; Trachsel, F.; Jensen, K. F. *Lab Chip* **2004**, *4*, 278–286.

(93) Hong, L.; Cheung, T.-L.; Rao, N.; Ouyang, Q.; Wang, Y.; Zeng, S.; Yang, C.; Cuong, D.; Chong, P. H. J.; Liu, L.; et al. *RSC Adv.* **2017**, *7*, 36819–36832.

(94) Paiè, P.; Bragheri, F.; Di Carlo, D.; Osellame, R. *Microsystems Nanoeng.* **2017**, *3*, 1–8.

(95) Libi, S.; Calenic, B.; Astete, C. E.; Kumar, C.; Sabliov, C. M. *Nanotechnol. Rev.* **2017**, *6*, 209–220.

(96) Testouri, A.; Arriaga, L. R.; Honorez, C.; Ranft, M.; Rodrigues, J.; van der Net, A.; Lecchi, A.; Salonen, A.; Rio, E.; Guillermic, R.-M.; et al. *Colloids Surfaces A Physicochem. Eng. Asp.* **2012**, *413*, 17–24.

(97) Shahbazali, E.; Hessel, V.; Noël, T.; Wang, Q. *Nanotechnol. Rev.* **2014**, *3*, 65–86.

(98) Roberts, E. J.; Karadaghi, L. R.; Wang, L.; Malmstadt, N.; Brutchey, R. L. *ACS Appl. Mater. Interfaces* **2019**, *11*, 27479–27502.

(99)   Kang, K.; Lee, L. J.; Koelling, K. W. *Exp. Fluids* **2005**, *38*, 222–232.

(100)   Beauchamp, M. J.; Nordin, G. P.; Woolley, A. T. *Anal. Bioanal. Chem.* **2017**, *409*, 4311–4319.

(101)   Gottesman, R.; Tangy, A.; Oussadon, I.; Zitoun, D. *New J. Chem.* **2012**, *36*, 2456–2459.

(102)   Salipante, P. F.; Meek, S. E.; Hudson, S. D. *Soft Matter* **2018**, *14*, 9020–9035.

(103)   Das, R.; Patle, S.; Seibel, E. J.; Burfeind, C. W.; Lim, S. *Microfluid. BioMEMS, Med. Microsystems XVI* **2018**, *1049118*, 2–20.

(104)   Patrick, W. G.; Nielsen, A. A. K.; Keating, S. J.; Levy, T. J.; Wang, C. W.; Rivera, J. J.; Mondragón-Palomino, O.; Carr, P. A.; Voigt, C. A.; Oxman, N.; et al. *PLoS One* **2015**, *10*, 1–18.

(105)   Oliveira, M. S. N.; Rodd, L. E.; McKinley, G. H.; Alves, M. A. *Microfluid. Nanofluidics* **2008**, *5*, 809–826.

(106)   Ober, T. J.; Haward, S. J.; Pipe, C. J.; Soulages, J.; McKinley, G. H. *Rheol. Acta* **2013**, *52*, 529–546.

(107)   Wilson, M. E.; Kota, N.; Kim, Y.; Wang, Y.; Stolz, D. B.; Leduc, P. R.; Ozdoganlar, O. B. *Lab Chip* **2011**, *11*, 1550–1555.

(108)   Krishna, K. S.; Li, Y.; Li, S.; Kumar, C. S. S. R. *Adv. Drug Deliv. Rev.* **2013**, *65*, 1470–1495.

(109)   Yaghmur, A.; Ghazal, A.; Ghazal, R.; Dimaki, M.; Svendsen, W. E. *Phys. Chem. Chem. Phys.* **2019**, *21*, 13005–13013.

(110)   Sui, S.; Perry, S. L. *Struct. Dyn.* **2017**, *4*.

(111)   Gicquel, Y.; Schubert, R.; Kapis, S.; Bourenkov, G.; Schneider, T.; Perbandt, M.; Betzel, C.; Chapman, H. N.; Heymann, M. *J. Vis. Exp.* **2018**, *134*, 1–14.

(112)   Khvostichenko, D. S.; Kondrashkina, E.; Perry, S. L.; Pawate, A. S.; Brister, K.; Kenis, P. J. A. *Analyst* **2013**, *138*, 5384–5395.

(113)   Saldanha, O.; Graceffa, R.; Hémonnot, C. Y. J.; Ranke, C.; Brehm, G.; Liebi, M.; Marmiroli, B.; Weinhausen, B.; Burghammer, M.; Köster, S. *ChemPhysChem* **2017**, *18*, 1220–1223.

(114)   Sidar, B.; Jenkins, B. R.; Huang, S.; Spence, J. R.; Walk, S. T.; Wilking, J. N. *Lab Chip* **2019**, *19*, 3552–3562.

(115)   Homan, K. A.; Gupta, N.; Kroll, K. T.; Kolesky, D. B.; Skylar-Scott, M.; Miyoshi, T.; Mau, D.; Valerius, M. T.; Ferrante, T.; Bonventre, J. V.; et al. *Nat. Methods* **2019**, *16*, 255–262.

(116)   Abdalkader, R.; Kamei, K. I. *Lab Chip* **2020**, *20*, 1410–1417.

(117)   Jang, H. K.; Hong, S. O.; Lee, S. B.; Kim, J. M.; Hwang, W. R. *J. Nonnewton. Fluid Mech.* **2019**, *274*, 1–11.

(118)   Dahl, J. B.; Lin, J.-M. G.; Muller, S. J.; Kumar, S. *Annu. Rev. Chem. Biomol. Eng.* **2015**, *6*, 293–317.

(119)   Yang, S.; Kim, J. Y.; Lee, S. J.; Lee, S. S.; Kim, J. M. *Lab Chip* **2011**, *11*, 266–273.

(120)   Leshansky, A. M.; Bransky, A.; Korin, N.; Dinnar, U. *Phys. Rev. Lett.* **2007**, *98*, 1–4.

(121)   Zeng, J.; Deng, Y.; Vedantam, P.; Tzeng, T. R.; Xuan, X. *J. Magn. Magn. Mater.* **2013**, *346*, 118–123.

(122)   Modak, N.; Datta, A.; Ganguly, R. *Microfluid. Nanofluidics* **2009**, *6*, 647–660.

(123)   Ai, Y.; Beskok, A.; Gauthier, D. T.; Joo, S. W.; Qian, S. *Biomicrofluidics* **2009**, *3*, 1–16.

(124)   Stroobants, S.; Callewaert, M.; Krzek, M.; Chinnu, S.; Gelin, P.; Ziemecka, I.; Lutsko, J. F.; De Malsche, W.; Maes, D. *Cryst. Growth Des.* **2020**, *20*, 1876–1883.

(125)   Komorowski, K.; Schaeper, J.; Sztucki, M.; Sharpnack, L.; Brehm, G.; Köster, S.; Salditt, T. *Soft Matter* **2020**, *16*, 4142–4154.

(126)   Solomon, D. E.; Vanapalli, S. A. *Microfluid. Nanofluidics* **2014**, *16*, 677–690.

(127)   Chevalier, J.; Ayela, F. *Rev. Sci. Instrum.* **2008**, *79*, 2006–2009.

(128)   Del Giudice, F.; D'Avino, G.; Greco, F.; De Santo, I.; Netti, P. A.; Maffettone, P. L. *Lab*

Chip **2015**, *15*, 783–792.

(129) Silva, B. F. B. *Phys. Chem. Chem. Phys.* **2017**, *19*, 23690–23703.

(130) Kinahan, M. E.; Filippidi, E.; Köster, S.; Hu, X.; Evans, H. M.; Pfohl, T.; Kaplan, D. L.; Wong, J. *Biomacromolecules* **2011**, *12*, 1504–1511.

(131) Pollack, L.; Tate, M. W.; Darnton, N. C.; Knight, J. B.; Gruner, S. M.; Eaton, W. a; Austin, R. H. *Proc. Natl. Acad. Sci.* **1999**, *96*, 10115–10117.

(132) Wittmeier, A.; Cassini, C.; Saldanha, O.; Perego, E.; Diaz, A.; Burghammer, M.; Köster, S. *Lab Chip* **2018**, *18*, 171–178.

(133) Brouzet, C.; Mittal, N.; Lundell, F.; Söderberg, L. D. *Macromolecules* **2019**, *52*, 2286–2295.

(134) Méndez-Ardoy, A.; Bayón-Fernández, A.; Yu, Z.; Abell, C.; Granja, J. R.; Montenegro, J. *Angew. Chemie Int. Ed.* **2020**, *59*, 6902–6908.

(135) Monteiro, D. C. F.; Von Stetten, D.; Stohrer, C.; Sans, M.; Pearson, A. R.; Santoni, G.; Van Der Linden, P.; Trebbin, M. *IUCrJ* **2020**, *7*, 207–219.

(136) Sato, K.; Yamanaka, M.; Takahashi, H.; Tokeshi, M.; Kimura, H.; Kitamori, T. *Electrophoresis* **2002**, *23*, 734–739.

(137) Li, Y.; Ward, K. R.; Burns, M. A. *Anal. Chem.* **2017**, *89*, 3996–4006.

(138) Zhang, S.; Wang, Y.; Onck, P.; den Toonder, J. *Microfluid. Nanofluidics* **2020**, *24*, 1–20.

(139) Pimenta, F.; Sousa, R. G.; Alves, M. A. *Biomicrofluidics* **2018**, *12*, 1–24.

(140) Shaqfeh, E. S. G. *J. Nonnewton. Fluid Mech.* **2005**, *130*, 1–28.

(141) Liu, Y.; Zhou, W.; Cui, K.; Tian, N.; Wang, X.; Liu, L.; Li, L.; Zhou, Y. *Rev. Sci. Instrum.* **2011**, *82*, 1–6.

(142) Coventry, K. D.; Mackley, M. R. *J. Rheol. (N. Y. N. Y).* **2008**, *52*, 401–415.

(143) Kato, M.; Shirakashi, M.; Takahashi, T. *Rheol. Acta* **2017**, *56*, 649–659.

(144) Miller, E.; Cooper-White, J. *J. Nonnewton. Fluid Mech.* **2009**, *160*, 22–30.

(145) Poulos, A. S.; Nania, M.; Lapham, P.; Miller, R. M.; Smith, A. J.; Tantawy, H.; Caragay, J.; Gummel, J.; Ces, O.; Robles, E. S. J.; et al. *Langmuir* **2016**, *32*, 5852–5861.

(146) Trebbin, M.; Steinhauser, D.; Perlich, J.; Buffet, A.; Roth, S. V.; Zimmermann, W.; Thiele, J.; Förster, S. *Proc. Natl. Acad. Sci. U. S. A.* **2013**, *110*, 6706–6711.

(147) Jagdale, P. P.; Li, D.; Shao, X.; Bostwick, J. B.; Xuan, X. *Micromachines* **2020**, *11*, 1–16.

(148) Rodd, L. E.; Scott, T. P.; Boger, D. V.; Cooper-White, J. J.; McKinley, G. H. *J. Nonnewton. Fluid Mech.* **2005**, *129*, 1–22.

(149) Lopez, C. G.; Watanabe, T.; Adamo, M.; Martel, A.; Porcar, L.; Cabral, J. T. *J. Appl. Crystallogr.* **2018**, *51*, 570–583.

(150) Cartlidge, R.; Nugegoda, D.; Wlodkowic, D. *Sensors Actuators, B Chem.* **2017**, *239*, 660–670.

(151) Hwang, Y. H.; Um, T.; Hong, J.; Ahn, G. N.; Qiao, J.; Kang, I. S.; Qi, L.; Lee, H.; Kim, D. P. *Adv. Mater. Technol.* **2019**, *4*, 1–9.

(152) Li, Y.; Sanampudi, A.; Raji Reddy, V.; Biswas, S.; Nandakumar, K.; Yemane, D.; Goettert, J.; Kumar, C. S. S. R. *ChemPhysChem* **2012**, *13*, 177–182.

(153) Li, Y.; Yamane, D. G.; Li, S.; Biswas, S.; Reddy, R. K.; Goettert, J. S.; Nandakumar, K.; Kumar, C. S. S. R. *Chem. Eng. J.* **2013**, *217*, 447–459.

(154) Engl, W.; Tachibana, M.; Colin, A.; Panizza, P. *Chem. Eng. Sci.* **2008**, *63*, 1692–1695.

(155) Lorber, N.; Sarrazin, F.; Guillot, P.; Panizza, P.; Colin, A.; Pavageau, B.; Hany, C.; Maestro, P.; Marre, S.; Delclos, T.; et al. *Lab Chip* **2011**, *11*, 779–787.

(156) Lohse, S. E.; Eller, J. R.; Sivapalan, S. T.; Plews, M. R.; Murphy, C. J. *ACS Nano* **2013**, *7*, 4135–4150.

(157) Wang, X.; Zhu, J.; Shao, T.; Luo, X.; Zhang, L. *Chem. Eng. Technol.* **2019**, No. 6, 1330–1340.

(158) Biswas, S.; Miller, J. T.; Li, Y.; Nandakumar, K.; Kumar, C. S. S. R. *Small* **2012**, *8*, 688–698.

(159) Testouri, A.; Ranft, M.; Honorez, C.; Kaabeche, N.; Ferbitz, J.; Freidank, D.; Drenckhan, W. *Adv. Eng. Mater.* **2013**, *15*, 1086–1098.

(160) Fuad, N. M.; Zhu, F.; Kaslin, J.; Wlodkowic, D. *SPIE BioPhotonics Australas.* **2016**, *10013*, 1–6.

(161) Cheung, T. L.; Hong, L.; Rao, N.; Yang, C.; Wang, L.; Lai, W. J.; Chong, P. H. J.; Law, W. C.; Yong, K. T. *Nanoscale* **2016**, *8*, 6609–6622.

(162) V Kinhal, K.; Bhatt, N.; Subramaniam, P. *Ind. Eng. Chem. Res.* **2019**, *58*, 5820–5829.

(163) Tran, T. T.; Nguyen, M. H.; Tan, Y. Z.; Chew, J. W.; Khan, S. A.; Hadinoto, K. *Eur. J. Pharm. Biopharm.* **2017**, *112*, 196–203.

(164) Kitson, P. J.; Rosnes, M. H.; Sans, V.; Dragone, V.; Cronin, L. *Lab Chip* **2012**, *12*, 3267–3271.

(165) Nguyen, L. T.; Yang, K. L. *J. Colloid Interface Sci.* **2014**, *428*, 146–151.

(166) Mitchell, M. J.; Qiao, R.; Aluru, N. R. **2000**, *9*, 435–449.

(167) Parant, H.; Muller, G.; Le Mercier, T.; Poulin, P.; Tarascon, J. M.; Colin, A. *Microfluid. Nanofluidics* **2017**, *21*, 1–11.

(168) Stone, H. A.; Stroock, A. D.; Ajdari, A. *Annu. Rev. Fluid Mech.* **2004**, *36*, 381–411.

(169) Lee, J. S.; Dylla-Spears, R.; Teclemariam, N. P.; Muller, S. J. *Appl. Phys. Lett.* **2007**, *90*, 10–13.

(170) Yaghmur, A.; Ghazal, A.; Ghazal, R.; Dimaki, M.; Svendsen, W. E. *Phys. Chem. Chem. Phys.* **2019**, *21*, 13005–13013.

(171) Schwemmer, F.; Blanchet, C. E.; Spilotros, A.; Kosse, D.; Zehnle, S.; Mertens, H. D. T.; Graewert, M. A.; Rössle, M.; Paust, N.; Svergun, D. I.; et al. *Lab Chip* **2016**, *16*, 1161–1170.

(172) Denz, M.; Brehm, G.; Hémonnot, C. Y. J.; Spears, H.; Wittmeier, A.; Cassini, C.; Saldanha, O.; Perego, E.; Diaz, A.; Burghammer, M.; et al. *Lab Chip* **2017**, *18*, 171–178.

(173) Roe, R.-J. *Methods of X-Ray and Neutron Scattering in Polymer Science*; Oxford University Press, **2000**.

(174) Wang, L.; Topham, P. D.; Mykhaylyk, O. O.; Yu, H.; Ryan, A. J.; Fairclough, J. P. A.; Bras, W. *Macromol. Rapid Commun.* **2015**, *36*, 1437–1443.

(175) Schnablegger, H.; Singh, Y. *The SAXS Guide*; Anton Paar: Austria, **2013**.

(176) Pedersen, J. S. *J. Appl. Crystallogr.* **2000**, *33*, 637–640.

(177) Guinier, A.; Fournet, G.; Walker, C. B. *SCATTERING OF X-RAYS*; Sons, J. W. &, Ed.; **1955**.

(178) Kratky, O.; Porod, G.; Kahovec, L. *Zeitschrift für Elektrochemie und Angew. Phys. Chemie* **1951**, *55*, 53–59.

(179) Afeworki, M.; Brant, P.; Lustiger, A.; Norman, A. *Solid State Nucl. Magn. Reson.* **2015**, *72*, 27–40.

(180) Vainio, U. **2016**, 1–6.

(181) Somani, R. H.; Yang, L.; Hsiao, B. S.; Sun, T.; Pogodina, N. V.; Lustiger, A. *Macromolecules* **2005**, *38*, 1244–1255.

(182) Kratky, O.; Stabinger, H. *Colloid Polym. Sci.* **1984**, *262*, 345–360.

(183) Blanchet, C. E.; Spilotros, A.; Schwemmer, F.; Graewert, M. A.; Kikhney, A.; Jeffries, C. M.; Franke, D.; Mark, D.; Zengerle, R.; Cipriani, F.; et al. *J. Appl. Crystallogr.* **2015**, *48*, 431–443.

(184) Hajizadeh, N. R.; Franke, D.; Svergun, D. I. *J. Synchrotron Radiat.* **2018**, *25*, 906–914.

(185) Graceffa, R.; Nobrega, R. P.; Barrea, R. A.; Kathuria, S. V.; Chakravarthy, S.; Bilsel, O.; Irving, T. C. *J. Synchrotron Radiat.* **2013**, *20*, 820–825.

(186) Lafleur, J. P.; Snakenborg, D.; Nielsen, S. S.; Mller, M.; Toft, K. N.; Menzel, A.; Jacobsen, J. K.; Vestergaard, B.; Arleth, L.; Kutter, J. P. *J. Appl. Crystallogr.* **2011**, *44*, 1090–1099.

(187) Toft, K. N.; Vestergaard, B.; Nielsen, S. S.; Snakenborg, D.; Jeppesen, M. G.; Jacobsen, J. K.; Arleth, L.; Kutter, J. P. *Anal. Chem.* **2008**, *80*, 3648–3654.

(188) Toft, K. N.; Vestergaard, B.; Nielsen, S. S.; Snakenborg, D.; Jeppesen, M. G.; Jacobsen, J. K.; Arleth, L.; Kutter, J. P. *Anal. Chem.* **2008**, *80*, 3648–3654.

(189) Köster, S.; Leach, J. B.; Struth, B.; Pfohl, T.; Wong, J. Y. *Langmuir* **2007**, *23*, 357–359.

(190) Evans, H. M.; Dootz, R.; Köster, S.; Struth, B.; Pfohl, T. *Bull. Polish Acad. Sci. Tech. Sci.* **2007**, *55*, 217–227.

(191) Köster, S.; Evans, H. M.; Wong, J. Y.; Pfohl, T. *Biomacromolecules* **2008**, *9*, 199–207.

(192) Brennich, M. E.; Nolting, J. F.; Dammann, C.; Nöding, B.; Bauch, S.; Herrmann, H.; Pfohl, T.; Köster, S. *Lab Chip* **2011**, *11*, 708–716.

(193) Pham, N.; Radajewski, D.; Round, A.; Brennich, M.; Pernot, P.; Biscans, B.; Bonneté, F.; Teychené, S. *Anal. Chem.* **2017**, *89*, 2282–2287.

(194) Skou, M.; Skou, S.; Jensen, T. G.; Vestergaard, B.; Gillilan, R. E. *J. Appl. Crystallogr.* **2014**, *47*, 1355–1366.

(195) Rosén, T.; Brouzet, C.; Roth, S. V.; Lundell, F.; Söderberg, L. D. *J. Phys. Chem. C* **2018**, *122*, 6889–6899.

(196) Håkansson, K. M. O.; Fall, A. B.; Lundell, F.; Yu, S.; Krywka, C.; Roth, S. V.; Santoro, G.; Kvick, M.; Prahl Wittberg, L.; Wågberg, L.; et al. *Nat. Commun.* **2014**, *5*.

(197) Skou, M.; Skou, S.; Jensen, T. G.; Vestergaard, B.; Gillilan, R. E. *J. Appl. Crystallogr.* **2014**, *47*, 1355–1366.

(198) Dootz, R.; Otten, A.; Köster, S.; Struth, B.; Pfohl, T. *J. Phys. Condens. Matter* **2006**, *18*, 639–652.

(199) Pfohl, T.; Otten, A.; Köster, S.; Dootz, R.; Struth, B.; Evans, H. M. *Biomacromolecules* **2007**, *8*, 2167–2172.

(200) Otten, A.; Köster, S.; Struth, B.; Snigirev, A.; Pfohl, T. *J. Synchrotron Radiat.* **2005**, *12*, 745–750.

(201) Balbino, T. A.; Serafin, J. M.; Malfatti-Gasperini, A. A.; De Oliveira, C. L. P.; Cavalcanti, L. P.; De Jesus, M. B.; De La Torre, L. G. *Langmuir* **2016**, *32*, 1799–1807.

(202) Plumridge, A.; Katz, A. M.; Calvey, G. D.; Elber, R.; Kirmizialtin, S.; Pollack, L. *Nucleic Acids Res.* **2018**, *46*, 7354–7365.

(203) With, S.; Trebbin, M.; Bartz, C. B. A.; Neuber, C.; Dulle, M.; Yu, S.; Roth, S. V.; Schmidt, H. W.; Förster, S. *Langmuir* **2014**, *30*, 12494–12502.

(204) Kalkowski, J.; Liu, C.; Leon-Plata, P.; Szymusiak, M.; Zhang, P.; Irving, T.; Shang, W.; Bilsel, O.; Liu, Y. *Macromolecules* **2019**, *52*, 3151–3157.

(205) Fürst, C.; Zhang, P.; Roth, S. V.; Drechsler, M.; Förster, S. *Polymer (Guildf).* **2016**, *107*, 434–444.

(206) Vakili, M.; Merkens, S.; Gao, Y.; Gwozdz, P. V; Vasireddi, R.; Sharpnack, L.; Meyer, A.; Blick, R. H.; Trebbin, M. *Langmuir* **2019**, *35*, 10435–10445.

(207) Lutz-bueno, V.; Zhao, J.; Mezzenga, R.; Pfohl, T.; Fischer, P.; Liebi, M. *Lab Chip* **2016**, *16*, 8–11.

(208) Hong, L.; Sesen, M.; Hawley, A.; Neild, A.; Spicer, P. T.; Boyd, B. J. *Soft Matter* **2019**, *15*, 9565–9578.

(209) Møller, M.; Nielsen, S. S.; Ramachandran, S.; Li, Y.; Tria, G.; Streicher, W.; Petoukhov, M. V.; Cerione, R. A.; Gillilan, R. E.; Vestergaard, B. *PLoS One* **2013**, *8*, 1–13.

(210) Streck, S.; Clulow, A. J.; Nielsen, H. M.; Rades, T.; Boyd, B. J.; McDowell, A. *J. Colloid Interface Sci.* **2019**, *555*, 438–448.

(211) Di Cola, E.; Torbensen, K.; Clemente, I.; Rossi, F.; Ristori, S.; Abou-Hassan, A. *Langmuir* **2017**, *33*, 9100–9105.

(212) Ghazal, A.; Gontsarik, M.; Kutter, J. P.; Lafleur, J. P.; Ahmadvand, D.; Labrador, A.; Salentinig, S.; Yaghmur, A. *J. Phys. Chem. Lett.* **2017**, *8*, 73–79.

(213) Eş, I.; Montebugnoli, L. J.; Filippi, M. F. P.; Malfatti-Gasperini, A. A.; Radaic, A.; de Jesus, M. B.; de la Torre, L. G. *Chem. Eng. J.* **2020**, *382*, 122821.

(214) Gospodarczyk, W.; Kozak, M. *RSC Adv.* **2017**, *7*, 10973–10984.

(215) Martin, H. P.; Brooks, N. J.; Seddon, J. M.; Luckham, P. F.; Terrill, N. J.; Kowalski, A. J.; Cabral, J. T. *Soft Matter* **2016**, *12*, 1750–1758.

(216) Poulos, A. S.; Nania, M.; Lapham, P.; Miller, R. M.; Smith, A. J.; Tantawy, H.; Caragay, J.; Gummel, J.; Ces, O.; Robles, E. S. J.; et al. *Langmuir* **2016**, *32*, 5852–5861.

(217) Clemente, I.; Torbensen, K.; Di Cola, E.; Rossi, F.; Ristori, S.; Abou-Hassan, A. *RSC Adv.* **2019**, *9*, 33429–33435.

(218) Khaliqi, K.; Ghazal, A.; Azmi, I. D. M.; Amenitsch, H.; Mortensen, K.; Salentinig, S.; Yaghmur, A. *Analyst* **2017**, *142*, 3118–3126.

(219) Balbino, T. A.; Aoki, N. T.; Gasperini, A. A. M.; Oliveira, C. L. P.; Azzoni, A. R.; Cavalcanti, L. P.; de la Torre, L. G. *Chem. Eng. J.* **2013**, *226*, 423–433.

(220) Seibt, S.; With, S.; Bernet, A.; Schmidt, H. W.; Förster, S. *Langmuir* **2018**, *34*, 5535–5544.

(221) Hermida-Merino, D.; Trebbin, M.; Foerster, S.; Rodriguez-Llansola, F.; Portale, G. *Macromol. Symp.* **2015**, *358*, 59–66.

(222) Silva, B. F. B.; Zepeda-Rosales, M.; Venkateswaran, N.; Fletcher, B. J.; Carter, L. G.; Matsui, T.; Weiss, T. M.; Han, J.; Li, Y.; Olsson, U.; et al. *Langmuir* **2015**, *31*, 4361–4371.

Chapter 2 – Finding Suitable Cellulose Materials as Model Systems

Introduction

Cellulose is an abundant, naturally-occurring polymer found in algae,[1,2] bacteria[1–5] and green plants[1,2,6,7] where it exists in a semi-crystalline state.[8–12] The monomer unit consists of two six-membered carbon rings, with each ring containing one hydroxymethyl group and two hydroxyl groups (**Figure (2.1)**).[13] The presence of such functional groups leads to many hydrogen bonding sites along the polymer chain.[14] This extensive hydrogen bonding produces a stiff chain,[15] enabling its use in plant cell walls where it acts as a scaffold.[11,16] Surprisingly, despite the high number of hydrogen bonding sites per chain, cellulose is insoluble in water and most organic solvents,[14] as the cellulose molecules preferentially hydrogen bond to each other, rather than with solvent molecules.[17]
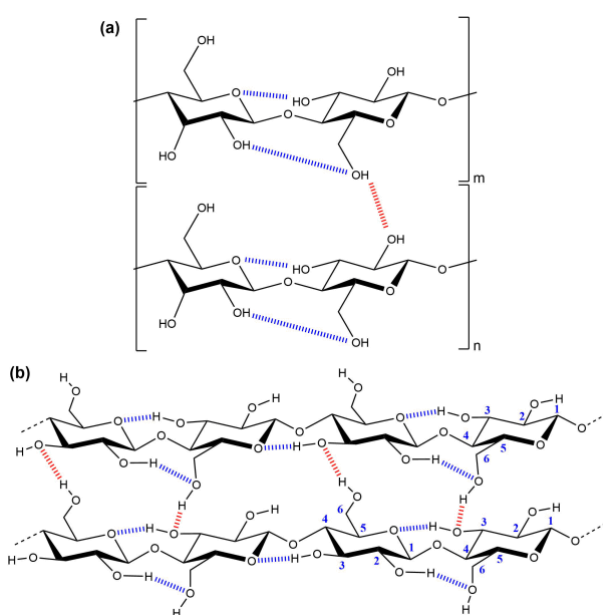
Figure (2.1). (a) Cellulose repeat unit structure, depicting the glycosidic linkages between the carbon rings, intramolecular hydrogen bonds (blue dashed lines) and intermolecular hydrogen bonds (red dashed lines);[2,18,19] n and m indicated the degree of polymerisation of the adjacent molecules. **(b)** Extended cellulose structure depicting intra- and intermolecular hydrogen bonds and the numbering system of carbons in a cellulose ring indicated by the blue numbers $(1 - 6)$.

The inherent stiffness of the molecules, as well as the extensive hydrogen bonding leads to the formation of highly oriented structural domains, causing cellulose to be birefringent.[20] Birefringence occurs when a material exhibits more than one refractive index, with each

depending on the polarisation and propagation direction of incident light. The degree of birefringence observed in cellulosic materials is directly related to the amount of lateral order within a fibre.[20] Due to this property, birefringence measurements have been utilised extensively in the research of these materials.[17,21–24] For example, birefringence has been used to demonstrate the alignment of individual nano-fibres of crystals in cellulose. Work performed independently by Mendoza-Galvan *et al.* and Hamza *et al.* investigated the degree of orientation in fibres during, or after, being stretched.[24,25] Both observed birefringence caused by the presence of long-range order of cellulose molecules within the fibre. The manifestation of birefringence in cellulose films has led to research into the application of cellulose in optical displays, such as liquid crystal displays (LCDs).[26]

Typically, the water-insolubility of cellulose prevents it from being utilised in most industrial applications. Therefore, chemical modification to alter its structure has proven necessary.[27,28] As such, the modification of cellulose has received considerable attention over the last 150 years,[13] from both industry and academia, with a recent wave of interest motivated by the move away from traditional petroleum-based polymers.[1,2,5,29] Of the different modification strategies utilised, the most common target functionalisation is the hydroxyl groups present on the cyclic backbone.[11,30–32]

By performing selective modification of these hydroxyl groups, a range of properties can be altered or introduced depending on the substitution groups being used. For example, the aqueous solubility of cellulose can be improved through modification of the polymer. According to Bochek, the higher the degree of substitution of the hydroxyl groups, the lower the solubility parameter of cellulose acetate from 55.7 $\sqrt{J}$ cm^{-3}.[33] The Hildebrand solubility parameter provides an estimation for the degree of interaction between materials; a solute and solvent with similar solubility parameters are likely to be miscible.[34] Furthermore, when the solubility parameter is equal or lower to that of water (23.5 $\sqrt{J}$ cm^{-3}), the dissolution of cellulose occurs.[33] This work highlights the ability to tailor the properties of cellulosic samples by simple modification routes

to produce desirable effects. Another property of cellulose that can be altered through modification is the gelation behaviour of cellulose solutions; Gallego *et al.* found that the gel strength, of cellulose modified with isocyanates, was dependent on the amount of non-polar groups present after modification.[35] Many important properties such as solubility and viscosity behaviour of modified celluloses are dependent on the degree of molar substitution (MS), type of substituent and cellulose itself. For example, Gosecki *et al.* prepared hydroxypropyl celluloses with various degree of substitutions and further modified them to methyl carbamate derivatives.[36] The solubility behaviour and cloud point of HPC methyl carbamates were clearly dependent on the MS and molar masses of cellulose derivatives.

A number of optical and structural techniques are used to characterise the derived cellulosic products. Despite the high volume of work published on measuring and understanding the birefringence of cellulose, (over 1000 papers in 2019 alone) most of this work is performed after some type of processing technique, e.g. thin film or fibre formation.[37–39] However, birefringence-based techniques could be efficient for studying (and monitoring) an effect of chemical modification on cellulose solubility and, consequently, processability. In this respect, shear-induced polarised light imaging (SIPLI),[40] could be suitable to study the birefringent properties of cellulose samples under shear flow, without irreversible changes occurring to the sample. This technique uses a mechanical rheometer to shear samples, whilst full *in situ* imaging occurs using polarised light, allowing the birefringent, and rheological properties of a material to be studied simultaneously without sample destruction.

Small- and wide-angle X-ray scattering (SAXS/WAXS) has proven useful in the characterisation of cellulosic material by providing structural information by averaging over many thousands of particles.[41] For example, Leppänen *et al.* utilised WAXS to find a relationship between the width of the cellulose crystals and the degree of extraction,[42] and Crawshaw *et al.* studied the modification of native cellulose with sodium hydroxide using SAXS.[43] By performing

experiments on cellulosic suspensions, the dimensions,[41,44] shape[42] and solubility[45] properties can be analysed.

SAXS as a structural technique enables data averaged over many thousand scattering objects to be collected, giving an accurate overview of their size and shape *in situ*, and in this respect, it is more advantageous over imaging techniques such as TEM. It is commonly accepted that polymer solutions or gels can be represented as two-component systems where the small-scale component represents single polymer chains and the large-scale component represents possible aggregated multiple junctions or clusters formed by those chains. Thus, an equation for intensity scattered by these systems is usually composed of two terms expressed via Lorentzian associated with Ornstein-Zernike formalism (molecules) and squared Lorentzian associated with Debye-Bouche formalism (clusters).[46–48] However, other expressions for the terms could be used such as Debye function, more analytically correct for Gaussian polymer chains,[49] and a power-law function based on variations of Porod's law,[50] respectively. This common approach has also been adopted for aqueous solutions of cellulose derivatives using the generalised scattering equation (**Equation (2.1)**).[51]

$$I(q) = (\Delta\rho)^2 \left[\frac{K_1}{\left(1 + q^2 R_{gc}^2\right)^2} + \frac{K_2 P(q)}{1 + K_3 e^{-q^2 K_4^2}} \right] \tag{2.1}$$

Equation (2.1). Equation describing the scattering pattern of a two-component polymeric system where $\Delta\rho$ is the excess scattering length density of the polymer (cellulose derivative) in the solvent (water) and K_1, R_{gc}, K_2, K_3 and K_4 are fitting parameters associated either with the volume fraction of clusters or averaged local polymer volume fraction fluctuations caused by inhomogeneity of polymer aggregates, averaged size of the clusters or correlation length of the fluctuations, the averaged single polymer chain volume and polymer concentration, the strength of repulsive interactions between the polymer chains and the correlation length of the repulsions, respectively. *P(q)* is the polymer chain form factor, which is expressed further in **Equation (2.2)**.[52]

$$P(q) = \left[\frac{1}{\nu U^{1/(2\nu)}} \Gamma\left(\frac{1}{2\nu} U\right) - \frac{1}{\nu U^{1/\nu}} \Gamma\left(\frac{1}{\nu} U\right) \right] \tag{2.2}$$

Equation (2.2). The polymer chain form factor (*P(q)*) consists of a modified variable (*U*) which is expressed in **Equation (2.3)**. The excluded volume parameter is represented by ν and Γ is the lower incomplete gamma function ($\Gamma(s,x) = \int_0^x t^{s-1} e^{-t} dt$).

$$U = (2\nu + 1)(2\nu + 2)\frac{q^2 R_{gm}^{\;2}}{6} \tag{2.3}$$

Equation (2.3). U consists of terms for the excluded volume parameter, ν, the average radius of gyration of molecules in solution, R_{gm} and the scattering vector, q.

The terms of **Equation (2.1)** are independent of each other and represent the two populations of structural objects where the larger objects (characterised by R_{gc}) and the smaller objects (characterised by R_{gm}) produce scattering signal asymptotically at high q-values. These scattering signals are described by power functions with exponent -4 and close to -2, for R_{gc} and R_{gm} respectively. In case of the polysaccharide systems, the first term of **Equation (2.1)** was assigned to assemblies of polymer chains which may attract each other and form entanglements.[51,53] The second term was assigned to the macromolecules distributed over the whole system homogeneously where possible repulsive interactions among the polymer chains and an existence of correlation distance between the chains were accounted for by the structure factor of Gaussian form. This approach enabled transformation of the systems to be followed by SAXS all the way from a state of associated molecules to a completely dissolved state through intermediate stages. In this respect, **Equation (2.1)** could also be used for analysing cellulose modified by HP and HPTMAC groups, which could lead to a partial or complete dissolution of the synthesised products.

For systems containing dissolved molecules with strong interactions of a repulsive nature the first term of **Equation (2.1)** should be neglected, reducing the scattering equation to the second term only. Alternatively, if molecules dissolved in a solution are not strongly interacting or their concentration is sufficiently low, K_3 is equivalent to zero and **Equation (2.1)** can be simplified to **Equation (2.4)**.[51,54]

$$I(q) = (\Delta\rho)^2 \left[\frac{K_1}{\left(1 + q^2 R_{gc}^{\;2}\right)^2} + K_2 P(q) \right] \tag{2.4}$$

Equation (2.4). Simplified version of **Equation (2.1)**, which is appropriate for systems with a low concentration of polymeric material, or weakly interacting molecules.

In theory, the material properties of cellulose can be tuned for a desired application by selectively controlling both the degree of modification and the chemical nature of the modifying groups. However, there has been no systematic analysis of the effect of modification extent and type on the bulk properties of modified cellulose. This study aims to provide such guidelines, by introducing different quantities of both 2-hydroxypropyl and (2-hydroxypropyl)trimethylammonium chloride functional groups to the cellulose chain, and studying their effect on solubility, structural morphologies, birefringence and rheological behaviours, with a view to produce products suitable for fibre formation. The two functional groups were chosen due to their proven capability in increasing the aqueous solubility of cellulosic material.[36,60] Two complementary techniques, TEM and SAXS, were used to assess structural morphology of the modified celluloses. While direct imaging by TEM provides detailed local information on shape and size of particles and aggregates, SAXS is a more statistically robust technique averaging information over a relatively larger sample volume and evaluating structural organisation of matter *in situ* from macromolecules, sub-nanometric clusters to submicron aggregates.

Experimental

Spruce cellulose powder [22183-1KG-F, Sigma Aldrich, Missouri, USA; weight-average and number-average molecular weights of $M_w = 92$ kDa and $M_n = 18.5$ kDa, respectively, both determined by size exclusion chromatography using 2 x PL gel MiniMixed A columns with a precolumn in DMAc/0.8% LiCl eluent (0.36 ml/min, T=80 °C) and a Waters 2414 Refractive index detector] was used for modifications. The cellulose molar mass distribution was calculated against eight pullulan standards (6.1 kDa $\leq M_n \leq$ 70.8 kDa) using Waters Empower 3 software[55]. Propylene oxide (PO) (> 99.5 w/w %), (2-hydroxypropyl)trimethylammonium chloride (HPTMAC) (> 90 w/w % and 2-4 w/w % of chlorohydrin impurities) was used as a 70 w/w % aqueous solution, *tert*-butanol (*t*-BuOH) (> 99.5 w/w %) was used as 90 w/w % aqueous solution

(water was added before usage), NaOH (50 w/w % solution in H_2O) and NaOD [40 w/w % solution in D_2O (99 atom % D)] were all purchased from Sigma Aldrich (Missouri, USA). 10 v/v % sulfuric acid and 3.7 v/v % hydrochloric acid freshly prepared from 98 v/v % sulfuric acid and 37 v/v % hydrochloric acid, respectively were used for neutralisations.

Chemical modification of cellulose powders

Four different cellulose derivatives with various degrees of molar hydroxyl substitution by hydroxypropyl (HP) per anhydroglucose unit (AGU) (MS_{HP}) were prepared and coded to be $C_{7/0}$ (MS_{HP} = 0.21, 7%), $C_{27/0}$ (MS_{HP} = 0.8, 27 %), $C_{50/0}$ (MS_{HP} = 1.5, 50 %) and $C_{80/0}$ (MS_{HP} = 2.4, 80 %), based on the corresponding percentage degree of substitution by HP (DS_{HP}) [**Table (2.1)** and **Figure (2.2)(i)**]. They were synthesised according to the following procedure: 100 g of cellulose powder (0.617 mol of AGUs) was suspended in the mixture of 150 ml of 10 M NaOH (diluted from 50 w/w % NaOH), 450 ml of water, and 300 ml of 90 w/w % aqueous *t*-BuOH. The mixture was stirred overnight at 30 °C. 216 (3.09 mol), 430 (6.14 mol) or 648 (9.26 mol) ml of PO was then added slowly to the mixture in three portions (a single addition taking about 15-20 min) with 2-3 h intervals between additions during one working day followed by stirring overnight at 30 °C. The reaction mixture was cooled down to 20 °C and neutralised with 10 v/v % sulfuric acid until a pH of 7 – 8 was reached. The reaction mixture was then dialysed using a 3500 MWCO membrane (Thermo Fisher Scientific, Massachusetts, USA) and freeze-dried.

$C_{7/0}$, $C_{27/0}$ or $C_{50/0}$ were further used as starting materials for cationisation [**Figure (2.2)(ii)**]. The molar ratio of HPTMAC/AGU was either 2.59 or 7.91 for cationisation targets with a degree of molar substitution (MS_{cat}) of 0.24 (DS_{cat} = 8 %) or 0.75 (DS_{cat} = 25 %), respectively. The degrees of hydroxypropylation and cationisation represented as the percentage of substituents on the cellulose are used for sample labelling (Table 1). For example, $C_{50/8}$ was prepared from 20 g of $C_{50/0}$ (0.081 mol, calculated from the average molecular weight of one $C_{50/0}$ AGU, which is

247.86 g/mol) suspended in 180 ml of water. 14.6 g of 50 w/w % NaOH (0.183 mol) was added to adjust the molarity to 0.88 M (in the reaction mixture after HPTMAC addition). The reaction mixture was then heated up to 45 °C and 45.2 g of 70 w/w % HPTMAC water solution (0.209 mol of HPTMAC) was then added slowly during 10-15 min to reach the HPTMAC/AGU molar ratio of 2.59. The mixture was stirred overnight at 45 °C. The reaction mixture was cooled down to 20 °C and neutralised with the hydrochloric solution to pH 7-8. The reaction mixture was dialysed using a 3500 MWCO membrane and then freeze-dried to a white powder.

Determination of modified cellulose solubility by centrifugation

5 w/w % solutions of hydroxypropylated celluloses, prepared in deionised water by an overnight procedure of gentle mixing, were used for the measurements. The degree of solid content in each sample was analysed by centrifuging each sample for 1 h at 5000 rpm. The sediment and solution parts were divided, and the sedimented part was washed once with deionised water before being centrifuged again. The sediments thus obtained were dried in an oven at 110 °C for 2 h before being weighed and the sediment dry mass content was calculated.

Elemental analysis

C, H, N, S and O contents were determined using a FLASH 2000 series analyser (Thermo Fisher Scientific, Massachusetts, USA).The resultant cellulosic sample was weighed in tin capsules before being placed inside a MAS 2004 auto-sampler (Thermo Fisher Scientific, Massachusetts, USA) at a pre-set time and then dropped into an oxidation/reduction reactor kept at 900 – 1000 °C. The amount of oxygen required for optimum combustion was delivered into the reactor at a precise time. The reaction of oxygen with the tin capsule at elevated temperatures generates an exothermic reaction which raises the temperature to 1800 °C. At this temperature, both organic and inorganic substances are converted into elemental gases which, after further reduction, are separated into a chromatographic column and detected by a highly sensitive thermal

conductivity detector (TCD). The determination of oxygen is performed via pyrolysis in the same analyser. The detection limit of the method is 0.1 w/w %. Results were calculated using certified elemental microanalysis standards using K factor and the CHNS/CHNS-O Standards Kit (Elemental Microanalysis, Devon, UK).

Zeta potential measurements

The measurements were performed using a Malvern Zetasizer Nano ZS (Malvern Panalytical, Malvern, UK) instrument. 0.1 w/w % aqueous dispersions of modified cellulose prepared from the whole sample were analysed at 25 °C in the presence of 1 mM KCl. Zeta potentials were calculated from the Henry equation using the Smoluchowski approximation.[56] All data were averaged over ten consecutive runs.

^{13}C nuclear magnetic resonance (NMR)

The resulting chemically modified cellulose powders were characterised using solid-state ^{13}C NMR spectroscopy. The solid-state cross-polarisation (CP) magic angle spinning (MAS) ^{13}C NMR measurements were performed with a CMX 400 MHz Infinity NMR spectrometer (Chemagnetics Inc, Colarado, USA) using a 5.0 mm double-resonance MAS NMR probe operating at 100.6 MHz. For all the samples, 30,000 transients were accumulated using a 1 ms contact time, 3 s recycle time and a spinning speed of 7 kHz. The chemical shifts were referenced to hexamethylbenzene (HMB) using the methyl signal (+ 17.35 ppm) as an external reference. The DS was determined by comparing the integrals originating from HP and HPTMAC and the C1 signal of cellulose with the aid of signal deconvolution. Since the CP/MAS method emphasizes ^{13}C nuclei close to protons, it is not a quantitative method, and only gives an estimate of the total degree of substitution for comparison purposes. The solid-state CP/MAS ^{13}C NMR was used as a semi-qualitative method to prove the success of syntheses.

^{1}H nuclear magnetic resonance (NMR)

^{1}H NMR spectra were recorded for a 5 w/w % sample in D_2O using a 400 mHz Avance III HD 400 spectrometer (Bruker, Massachusetts, USA) equipped with a double resonance broadband optimized probehead. The experiment was performed with 16 scans averaged per spectrum. Spectra were analysed using TopSpin (Bruker, Massachusetts).

Transmission electron microscopy (TEM)

Imaging was performed using a Technai Spirit 2 microscope (FEI, Oregon, USA) operating at 80 kV and fitted with an Orius SC1000B camera (Gatan, California, USA). Copper/palladium TEM grids (Agar Scientific, UK), coated in-house with a thin film of amorphous carbon and subsequently subjected to a glow discharge for 20 s, were used as sample holders. Individual 10 µL droplets of 0.1 w/w % aqueous dispersions of modified cellulose (without removal of insoluble material) were placed on freshly treated grids for 1 minute and then blotted with filter paper to remove excess solution. To ensure sufficient contrast, uranyl formate (10.0 µL of a 0.75 w/w % solution) was absorbed onto the sample-loaded grid for 30 s and then blotted to remove any excess of the stain compound. Each freshly loaded grid was then dried under vacuum conditions. Size of the particles observed in TEM images was analysed using ImageJ software.[57] The average particle size for each image was calculated from 25 independent measurements.

Small-angle and wide-angle X-ray scattering (SAXS/WAXS) measurements

Small-angle and wide-angle X-ray scattering patterns (SAXS/WAXS) were collected using a laboratory SAXS/WAXS beamline (Xeuss 2.0, Xenocs, Grenoble, France) equipped with a liquid gallium MetalJet X-ray source (Excillum, Kista, Sweden, X-ray wavelength $\lambda = 0.134$ nm), FOX3D single reflection multi-layered X-ray mirror and two sets of motorised scatterless slits for beam collimation, a Pilatus 1M pixel SAXS and a Pilatus 100k pixel WAXS detectors

(Dectris, Barden, Switzerland). SAXS patterns were recorded over a range of 0.03 nm^{-1} < q < 1.3 nm^{-1}, where $q = (4\pi \sin\theta)/\lambda$ is the scattering vector length and θ is one-half of the scattering angle. SAXS/WAXS patterns of modified cellulose aqueous dispersions (without removal of insoluble material) diluted to 1 w/w % concentrations were recorded using glass capillaries of 2 mm diameter (WJM-Glas, Berlin, Germany) as a sample holder. X-ray scattering data reduction (calibration and integration) was performed using the Foxtrot software package supplied with the instrument and further data analysis (background subtraction and data modelling) was carried out using Irena SAS macro[58] for Igor Pro software package.

Rotational rheology and shear-induced polarised light imaging (SIPLI)

The measurements were performed using a stress-controlled MCR301 rheometer (Anton Paar, Graz, Austria) with a SIPLI attachment.[59] The rheometer was equipped with a Peltier temperature controller composed of bottom-plate and top-hood heaters, and plate-plate geometry (comprising of polished stainless-steel disk of 25 mm diameter and a fused quartz bottom plate). The SIPLI attachment, based on reflective polariscope principles, uses components of the parallel-plate geometry where the bottom (static) transparent plate and the top (rotating) reflective disk are parts of the optical setup allowing time-resolved reflected polarised light images (PLI) of measured samples to be recorded during shear. Descending shear rate ($\dot{\gamma}$) sweeps were performed from 500 s^{-1} to 0.1 s^{-1} at a constant temperature of 20 °C, with a sample thickness (gap between the parallel plates) of 1 mm. All modified cellulose samples were measured at a concentration of 10 w/w % in water (without removal of insoluble material). During shear sweeps, imaging of the samples under crossed polarisers was performed to identify birefringent samples. The second set of experiments was performed at a constant angular speed of rotation, ω, of the shearing disk. In these experiments, the SIPLI technique was used to capture PLIs every second for 1000 s to observe the onset of orientation of the material under flow conditions. Since the shear rate experienced by each part of a sample in a parallel-plate geometry is proportional to its radial

position ($\dot{\gamma} = \omega r / d$, where r is the radius of a corresponding sample position and d is the geometry gap), and assuming that the flow is laminar, SIPLI measurements at a constant ω enables birefringent properties of the sample to be tested within a range of share rates from 0 s^{-1} (at the sample centre) to $\dot{\gamma}_{max} = \omega R / d$ (at the sample edge where R is the sample radius) simultaneously in a single experiment.

Results and Discussion

Modification of native cellulose with the functional groups (HP and HPTMAC) were performed to different extents to give a series of modified cellulosic samples (**Table (2.1)** and **Figure (2.2)**). For example, to produce the C$_{27/8}$ sample, 27 % of the pendent cellulose hydroxyls (targeting, on average, less than one of three units per AGU) were functionalised with HP and 8% with HPTMAC, to give an overall degree of modification of 35 %. Hydroxypropyl groups provide steric hindrance, which can improve the solubility of cellulose by interrupting the intra- and intermolecular hydrogen bonding throughout the sample.[61–63] The subsequent modification group, (2-hydroxypropyl)trimethylammonium chloride, similarly introduces steric hindrance to the system but also establishes a large charge hindrance element which causes repulsion between the cellulose chains. For instance, this cationic substituent significantly improved the solubility of high molecular mass glucan (M$_w$ 189 kDa) in water above MS$_{cat}$ > 0.16.[64] It is expected that both these processes cause cellulose chains to, preferentially, form hydrogen bonds with solvent molecules.[36,60]
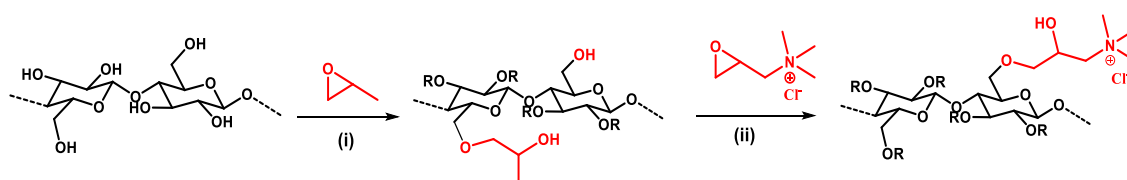

Figure (2.2). A route used for the cellulose modification: (i) hydroxypropylation with propylene oxide (PO) [R = CH$_2$CH(OH)CH$_3$, H] and (ii) following cationisation with (2,3-epoxypropyl)trimethylammonium chloride (EPTMAC) [R = CH$_2$CH(OH)CH$_3$, H or CH$_2$CH(OH)CH$_2$N(CH$_3$)$_3$Cl].

Table (2.1). Overview of modified cellulose samples with their corresponding degrees of HP and HPTMAC substitution. For example, a sample with 50 % HP and 8% HPTMAC modification is labelled as $C_{50/8}$ and is located in the third column and second row of the table.

		Degree of HP / %			
		7	**27**	**50**	**80**
Degree of HPTMAC / %	**0**	INSOLUBLE	$C_{27/0}$	$C_{50/0}$	$C_{80/0}$
	8	INSOLUBLE	$C_{27/8}$	$C_{50/8}$	NOT SYNTHESISED
	25	$C_{7/25}$	$C_{27/25}$	$C_{50/25}$	NOT POSSIBLE

NMR and Elemental Analysis

An analysis of the modified products by ^{1}H and ^{13}C NMR confirms the presence of HP, or HP and HPTMAC functional groups in the corresponding modified products and shows a close correlation of the polymer composition measured from the NMR spectra to the targeted degree of modification (**Figure (2.3)** and **Figure (2.4)**). The molar substitutions of the hydroxypropylated samples (MS_{HP}) determined with CP/MAS ^{13}C NMR were 0.2 ($C_{7/0}$), 0.8 ($C_{27/0}$), 1.5 ($C_{50/0}$) and 2.4 ($C_{80/0}$), which are in a good agreement with the expected MS_{HP} (and DS_{HP}) values.

NMR and elemental analysis of HPTMAC-modified samples has shown some variations of measured MS_{HPTMAC} from the targeted values (**Figure (2.4)** and **Table (2.2)**). In particular, this was observed for samples targeted with the same HPTMAC DS where equivalent amounts of the cationisation reagent had been used. For example, the measured ^{1}H NMR MS_{HPTMAC} of $C_{27/8}$ sample was 13 %, but for the $C_{50/8}$, the MS_{HPTMAC} value was 8.5 % yielding an average of 10.8 %. Elemental analysis results were in agreement with ^{1}H NMR, with MS_{HPTMAC} values of 13 % and 8 % for $C_{27/8}$ and $C_{50/8}$ respectively, with an average of 10.5 %. The cellulosic samples targeted
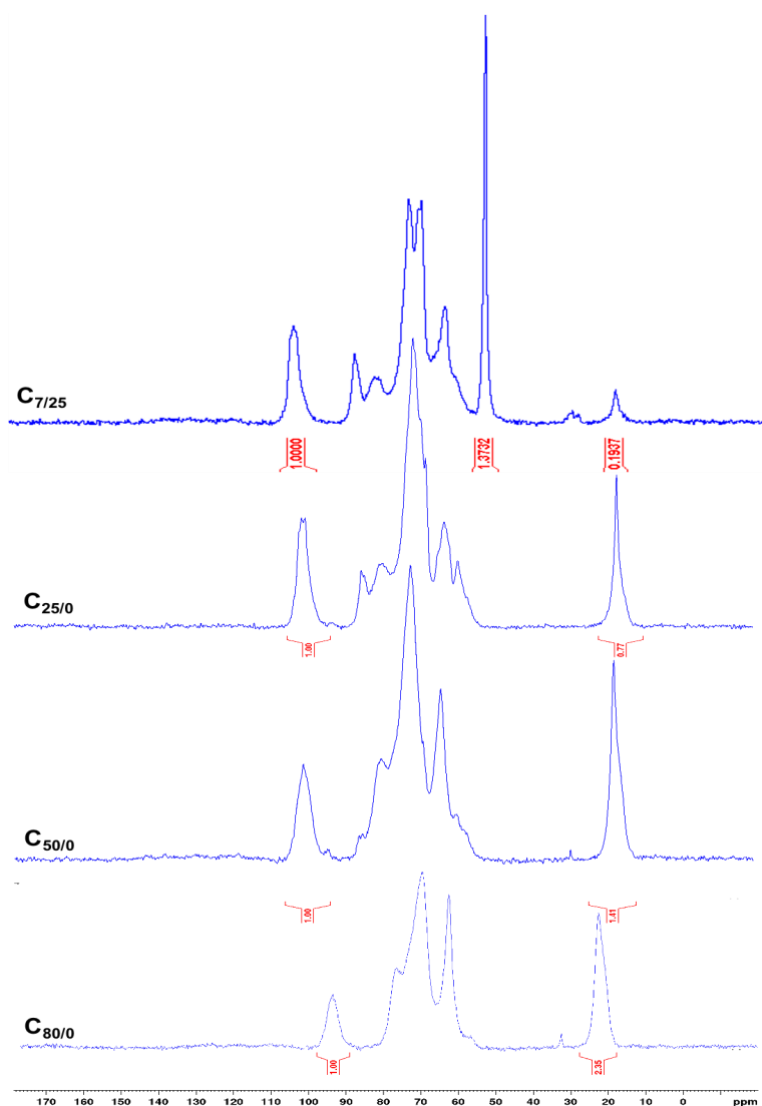
Figure (2.3). ^{13}C NMR spectra of $C_{27/0}$, $C_{50/0}$ $C_{80/0}$ and $C_{7/25}$. The C1 peak (carbon with glycosidic linkage between AHU) is at $100 – 110$ ppm and the carbon from the methyl group of hydroxypropyl substituent is at 20 ppm. The molar substitution is calculated by dividing $(2.35/3)*100 = 78$ % for $C_{80/0}$ for example. The DS_{HP} of $C_{27/0}$ was $(0.77/3)*100 = 25.7$ %. CP/MAS ^{13}C NMR spectrum of hydroxypropylated celluloses: $C_{27/0}$ with DS_{HP} 0.77 (25.7 %), $C_{50/0}$ with DS_{HP} 1.41 (47 %), and $C_{80/0}$ with DS_{HP} 2.35 (78 %).

with 25 % HPTMAC were also shown to have variations in the resulting MS_{HPTMAC} values. ^{1}H

NMR analysis shows MS_{HPTMAC} values of 16.9 %, 34.5 % and 22.9 % for the samples $C_{7/25}$, $C_{27/25}$

and $C_{50/25}$, this gives an average of 25 %. The MS_{HPTMAC} values from elemental analysis give a

similar average of 24 %. However, only the targeted DS values, expressed as percentages, are

used for the sample codes (**Table (2.4)**). The comparable results between the two methods show

the successful incorporation of HPTMAC, which can be quantified by either ^{1}H NMR or elemental analysis indicating consistent results.
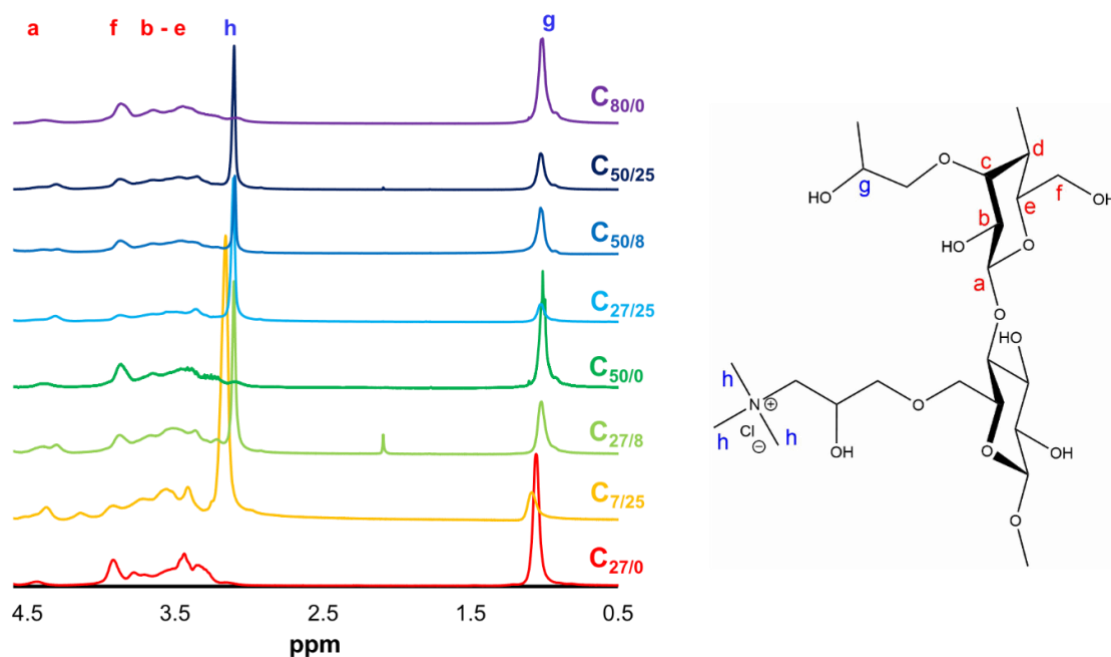
Figure (2.4). ^{1}H NMR spectra for all modified cellulose samples. The integrals of the peak corresponding to the hydrogen on C1(4.5 ppm, labelled *a*), HP peak (1.3 ppm, labelled *g*) and HPTMAC peak (3.1 ppm, labelled *h*) were compared to give DS_{HP} and DS_{HPTMAC} values.

Table (2.2). Elemental analysis and ^{1}H NMR results analysing DS_{HPTMAC} values for $C_{8/25}$, $C_{27/8}$, $C_{27/25}$, $C_{50/8}$ and $C_{50/25}$.

Sample	Targeted HPTMAC Modification / %	Resulting HPTMAC Modification / %	
		^{1}H NMR	Elemental Analysis
$C_{8/25}$	25	16.5	24.7
$C_{27/8}$	8	13	13
$C_{27/25}$	25	34.5	28.0
$C_{50/8}$	8	8.5	8
$C_{50/25}$	25	22.9	18.7

Insoluble Content

Centrifugation measurements show a general decrease in solid content as the degree of pendent hydroxyl substitution increases (**Figure (2.5)**). This is related to a higher degree of solubility of the modified cellulose. The observed solubility behaviour was not solely due to increased modification of the cellulose chains. There is a pronounced trend associated with the

degree of substitution indicating a strong effect of the hydroxypropyl units on the disruption of intra- and intermolecular hydrogen bonds within the cellulose system, resulting in the higher proportion of solvent-cellulose hydrogen bonds. The HPTMAC may also contribute to the cellulose solubility: modification of the $C_{27/0}$ with 8 % of HPTMAC ($C_{27/8}$) reduces the solid content from 53 % to 29 % (**Figure (2.5)**). However, a further increase of the HPTMAC proportion ($C_{27/25}$) does not seem to have an effect on the overall solubility of the cellulose chains (**Table (2.4)**). $C_{27/8}$ and $C_{27/25}$ show nearly the same amount of solids (29 % and 36 %, respectively), or even a slight increase, despite a three-fold increase of HPTMAC substitutes. A similar result was obtained for a cellulose sample with a higher content of HP which was further modified by HPTMAC (**Figure (2.5)**). This behaviour could be due to the bulky HPTMAC groups targeting available hydroxyl sites either on the molecules initially solubilised by the HP groups or the surface of large aggregates, which is not so effective in solubilising cellulose molecules.
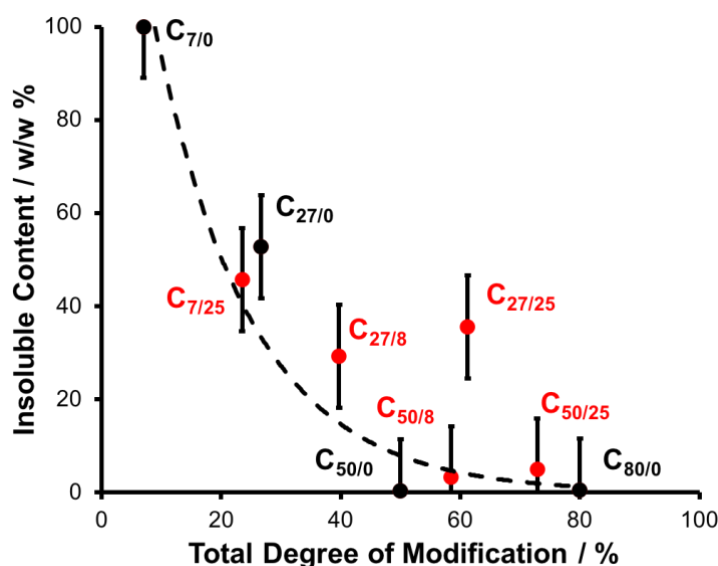
Figure (2.5). The proportion of water insoluble, solid material in 5 w/w % solutions of modified cellulosic samples, plotted against the total degree of modification (black and red symbols correspond to modified cellulose with the actual DS_{HP} and DS_{HPTMAC} values); showing a rapid decrease in the solid content with an increasing proportion of HP group present. All measured points are labelled with the corresponding sample name. The dashed curve is plotted for guidance. Error bars represent standard error.

Zeta Potential

The modification of cellulose by ionic HPTMAC was further verified by Zeta potential (ζ) measurements performed at 0.1 w/w % in the presence of 1mM KCl (**Figure (2.6)**). The results confirm the presence of the positive electrokinetic potential for all cellulose samples modified by HPTMAC cationic group. Samples modified only with the hydroxypropyl group displayed no cationic charge, regardless of the degree of substitution. A clear trend can be seen in the ζ values; as the degree of HPTMAC present increases, the ζ value increases (**Figure (2.6)** and **Table (2.4)**). Both complete series of samples with HP of 27 % and 50 % show a steady increase of the potential upon the increase of HPTMAC substituent content. Thus, in addition to the NMR results demonstrating a reasonably good correlation between the targeted cellulose modification and the sample composition, ζ-potential data further confirms the successful incorporation of the HPTMAC cationic group on to the cellulose.

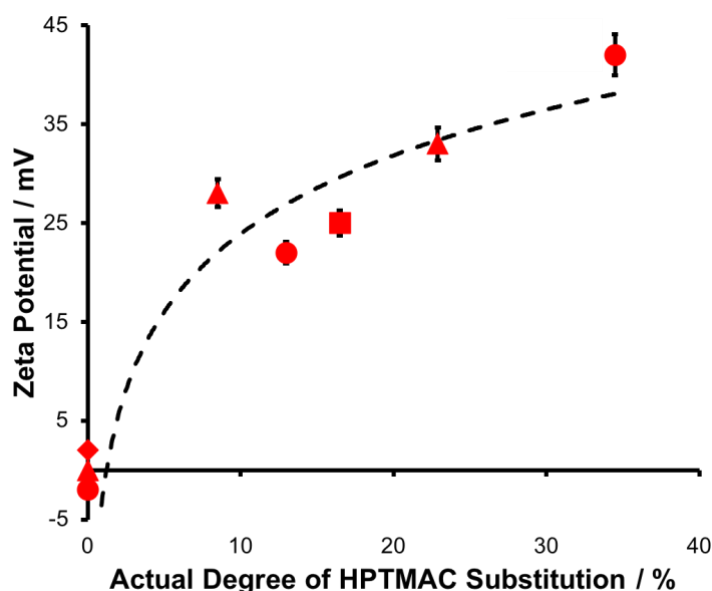**Figure (2.6).** Zeta potential of modified cellulose samples plotted versus HPTMAC degree of substitution. The data points were measured at 25 °C for 0.10 w/w % dispersions in the presence of 1 mM KCl. Error bars signify a 95% confidence interval. Data points for the samples with HP substitution of 7 % (square), 27 % (triangle), 50 % (circle) and 80 % (diamond) are shown. The dashed curve is plotted for guidance.

TEM

All TEM images showed the presence of cellulose nanoparticles (CNPs) of a needle-like shape (**Figure (2.7)**) indicating a similar morphological composition of the modified cellulose samples. The CNP mean length of around 100 nm with a relatively broad length distribution (**Table (2.4)**) is of a typical size range observed for nano-particulates derived from cellulose by various techniques such as acid[65,66] or enzymatic hydrolysis,[67] treatment with eutectic solvents[68,69] and micromilling.[70] The TEM images demonstrate a good correlation with the solid content measurements (**Figure (2.5)** and **Table (2.4)**). In particular, TEM images of cellulose samples with the degree of substitution by HP equal to or more than 50 % (**Figure (2.7)(d)** and **(f) – (h)**), characterised by a very low solid content of a few weight percent (**Figure (2.5)**), show the presence of individual needles with no signs of aggregation. In contrast, the samples with HP content of 27 % or less (**Figure (2.7)(a) – (c)** and **Figure (2.7)(e)**), with a significant amount of
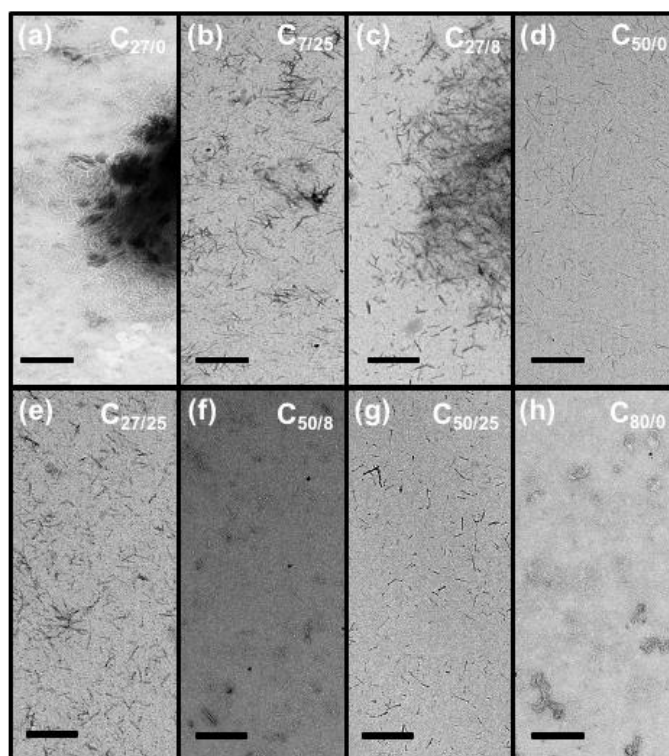

Figure (2.7). Representative TEM images of dried 0.10 w/w % aqueous dispersions of the modified celluloses: **(a)** $C_{27/0}$, **(b)** $C_{7/25}$, **(c)** $C_{27/8}$, **(d)** $C_{50/0}$, **(e)** $C_{27/25}$, **(f)** $C_{50/8}$, **(g)** $C_{50/25}$ and **(h)** $C_{80/0}$. The scale bar in each image corresponds to 500 nm.

solids (**Figure (2.5)**), show the presence of aggregates composed of needle-like objects. Thus, increasing the degree of modification, especially by HP substitution, does indicate an increased solubility of the CNPs which can be seen in the absence of large aggregates in the TEMs of samples with HP content of 50 % and above. However, an increase of HPTMAC in the modified cellulose composition also improves the material solubility which can be clearly followed using the samples with DS_{HP} of 27% (compare **Figure (2.7)(a)**, **(c)** and **(e)**). In this respect, it has to be concluded that the modification replacing the native hydroxyls impacts the formation of intermolecular hydrogen bonds and makes solvent-cellulose hydrogen bonding more favourable.

SAXS

The scattering equation based on two populations of scattering objects (**Equation (2.4)**) produced reasonably good fits to experimental SAXS patterns of the modified cellulose 1 w/w % aqueous solutions (**Figure (2.8)**). The SAXS analysis (**Table (2.3)**) shows that upon an increase of the hydroxypropyl group content in the modified cellulose the large object (aggregate) size
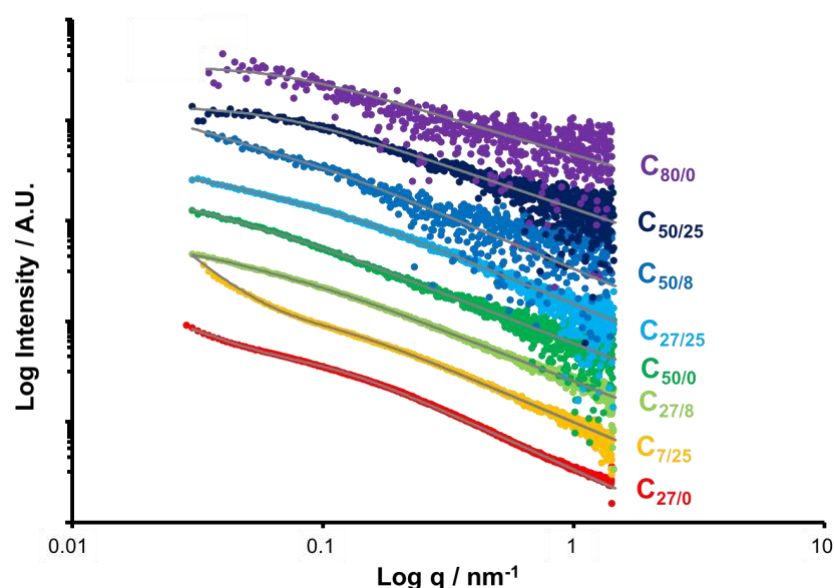

Figure (2.8). Double logarithmic plot of representative SAXS patterns of 1.0 w/w % modified cellulose aqueous dispersions (symbols). The grey lines show the fitted model, using an established two-population model for cellulose (**Equation (2.4)**). The SAXS patterns are offset for clarity.

reduces from tens of microns for $C_{7/25}$, to about 30 nm for $C_{50/0}$ and to virtually zero, a complete solubilisation of the objects undetectable by SAXS, for $C_{80/0}$. In addition, a trend towards smaller sizes can be identified for the large objects upon increase of the HPTMAC group content. For example, the SAXS results suggest that large insoluble aggregates of $C_{27/0}$ reduce to a micron size for $C_{27/25}$ and the same increase of the HPTMAC group content with greater HP content, $C_{50/0}$ to $C_{50/25}$ makes the large objects fully solubilised, undetectable by SAXS (**Table (2.3)**). TEM images indicate a presence of needle shaped CNPs (**Figure (2.7)**).

$$R_{gc}{}^2 = \frac{L^2}{12} + \frac{R_r{}^2}{2} \tag{2.5}$$

Equation (2.5). The radius of gyration of a rigid rod (R_g / m) is calculated from the length of the rod (L / m) and the cross-section radius of the rod (R_r / m).

$$R_{gm}{}^2 = \frac{L^2}{12} \tag{2.6}$$

Equation (2.6). The radius of gyration of a needle (R_g / m) is calculated from the length of the rod (L / m).

A comparison of the large object radius of gyration (**Equation (2.6)**) measured by SAXS (R_{gc}) and the CNP length obtained by TEM (L), performed using this relationship, shows a reasonably good correlation (**Table (2.3)**). This result suggests that the large objects detected by SAXS for the most of modified cellulose materials correspond to CNPs. It might be expected that the CNPs were composed of crystalline cellulose.[2] However, WAXS patterns of the modified cellulose samples, simultaneously recorded with SAXS data, are represented by a broad peak at $q \sim 16$ nm^{-1} (**Figure (2.9)**) which is commonly observed for amorphous cellulose.[71] There was no well-defined diffraction peaks which could be associated with crystalline cellulose. Thus, WAXS results indicate that the modified cellulose is mainly in an amorphous state and, possibly, the scattering measurements are not sensitive to the small fraction of crystalline material in the needle-shaped cellulose nanoparticles. A combined analysis of solid content (**Figure (2.5)**), TEM

(**Figure (2.7)**) and SAXS (**Figure (2.8)** and **Table (2.3)**) results shows that cellulose aggregates, virtually insoluble in water at small level of substitution by HP (DS_{HP} = 7 %), disintegrate into CNPs at intermediate levels of cellulose modification by HP and HPTMAC, followed by a complete solubilisation at extreme, high DS value, conditions (**Figure (2.5)** and **Table (2.3)**, $C_{80/0}$).
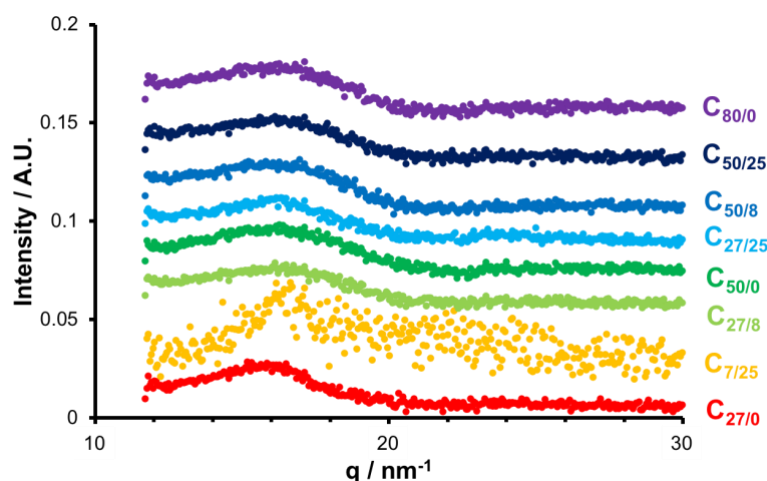
Figure (2.9). WAXS patterns for all modified cellulose samples. A broad peak can be seen in the region of 15 – 17 nm^{-1}, indicating the presence of amorphous cellulose. The patterns are offset for clarity.

A reduction of the large object population fraction, correlated with the solid content (**Figure (2.5)**), was accompanied by a relative increase of the small object population fraction associated in the scattering equation (**Equation (2.4)**) with dissolved molecules. Since molecules cannot be detected by TEM, characterisation of the modified cellulose by SAXS method is more preferable in this case. SAXS analysis shows that the second population is represented by molecules with the radius of gyration (R_{gm}) in a range of 20 nm (**Table (2.3)**). There is a gradual increase of R_{gm} with the increase of DS_{HP}. Possibly, small cellulose molecules are prone to the

$$R_{gm}^{\;2} = \frac{b^{2(1-\nu)}L_m^{\;2\nu}}{(2\nu+1)(2\nu+2)} \tag{2.7}$$

Equation (2.7). The radius of gyration of a molecule (R_{gm} / m) is calculated from the Kuhn length (b / m), the total contour length (L_{mol} / m) and the excluded volume parameter (ν / dimensionless).[52]

Table (2.3). Summary of structural parameters obtained by fitting scattering equation (**Equation (2.4)**) to SAXS patterns of the modified cellulose samples (**Figure (2.8)**), with R_{gc} and R_{gm} corresponding to the radius of gyration of large cellulose objects (aggregates) and small objects (molecules), respectively, and ν is the excluded volume parameter. L is the length of CNPs measured from TEM images (**Figure (2.7)**).

		Degree of HP present / %				Structural Parameters
		7	**27**	**50**	**80**	
Degree of HPTMAC present / %	**0**	INSOLUBLE	0.44	0.52	0.55	ν
			40.9	30.6	-	R_{gc} / nm
			14.9	23.5	25.6	R_{gm} / nm
			138 ± 33	122 ± 28	-	L / nm
	8	INSOLUBLE	0.48	0.51	NOT SYNTHESISED	ν
			21.2	31.8		R_{gc} / nm
			15.4	19.0		R_{gm} / nm
			100 ± 29	118 ± 40		L / nm
	25	0.47	0.49	0.59	NOT POSSIBLE	ν
		1029.4	21.0	-		R_{gc} / nm
		13.4	13.9	21.6		R_{gm} / nm
		109 ± 31	101 ± 35	91 ± 34		L / nm

modification first resulting in smaller R_{gm} for slightly and moderately modified cellulose. At $DS_{HP} \geq 50\%$, when most of the molecules are modified, including high molecular weight cellulose, the averaged R_{gm} appears larger. Alongside this, SAXS results indicate that for $DS_{HP} \leq 27\%$ the excluded volume parameter, ν, is less than 0.5 (**Table (2.3)**). This suggests that for celluloses with a low degree of substitution, water remains a relatively poor solvent. As such, and according to solid content results (**Figure (2.5)**) and TEM (**Figure (2.7)**), the modified cellulose still forms large aggregates. As the degree of substitution increases, ν also increases to the point where water becomes a good solvent ($\nu > 0.5$) for the modified cellulose samples leading to a larger proportion of free CNPs (**Figure (2.7)**) and molecules in solution. In particular, no aggregates or large objects are detected by SAXS for $C_{50/25}$ and $C_{80/0}$ where ν reaches 0.59 and 0.55, respectively (**Table (2.3)**).

Using **Equation (2.7)**, R_{gm} values were calculated for the modified celluloses. The molecular weight and length of the AGU is 162 Da and 0.52 nm,[71] respectively. Assuming that

the polymer molecular weight after the modification remains approximately at the same value of

78 kDa, L_{mol} = 78 kDa/162 Da x 0.52 nm ≈ 250 nm. Thus, assuming *theta*-solvent conditions (ν

= 0.5) and *b* is 15 nm, based on commonly accepted values for cellulose and its derivatives being

in a range of 10 – 20 nm,[72–75] the R_{gm} of a single molecule, calculated from **Equation (2.7)**, is

about 25 nm. The estimated R_{gm} value, considering the number of assumptions made, is in a good

agreement with the R_{gm} values measured by SAXS (**Table (2.3)**). This comparison suggests that

increasing the degree of cellulose modification enables aggregates and/or CNPs to be dissolved

into their constitutive molecules.
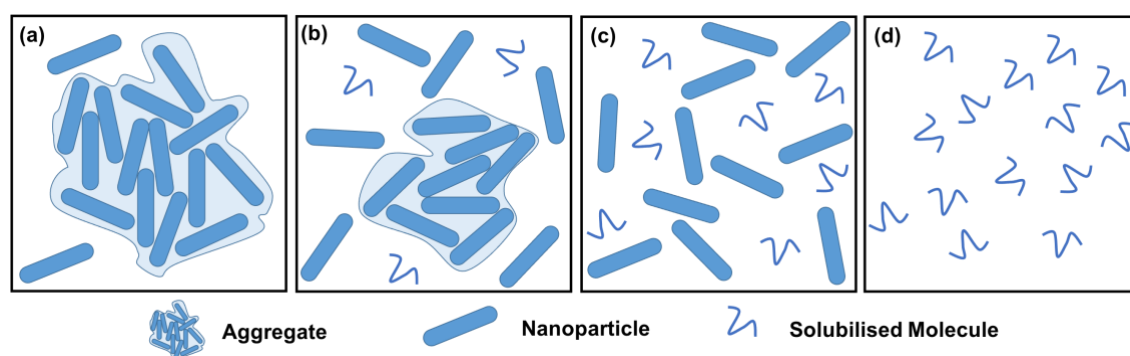
Figure (2.10). Schematic representing the fragmentation of aggregates with increasing modification: **(a)** presence of large aggregates with a few loose particles at low degrees of modification; **(b)** intermediate degrees of substitution with smaller aggregates present, a greater population of free CNPs and a small proportion of single molecules; **(c)** CNPs and molecules with no aggregates present at higher degrees of modification and **(d)** only molecules are present at the highest degrees of modification.

Based on the results of structural characterisation techniques, it can be concluded that the

increase of the degree of substitution gradually changes the cellulose solubility leading to the

formation of different morphologies upon dispersion and solubilisation in water. At low DS_{HP} (7

%) the modified cellulose appears mainly as large aggregates (**Figure (2.10)(a)**). An increase of

the HP component, also accompanied by HPTMAC substitution, to a moderate level (DS_{HP} = 27

%) leads to a partial destruction of the aggregates into CNPs and single modified cellulose

molecules (**Figure (2.10)(b)**) followed by a full disintegration of the aggregates at higher DS_{HP}

(50 %) (**Figure (2.10)(c)**) which is completed by a molecularly-dissolved material at the higher

end of the total substitution (**Figure (2.10)(d)**).

SIPLI Measurements

Rheo-optical measurements were carried out using rotational (shear) rheology combined

with *in situ* polarised light imaging (SIPLI setup) in order to investigate the rheological and

birefringent properties of the eight modified samples. Initially, experiments were performed to

determine the shear-rate dependent viscosity of the samples, and to investigate whether the

samples were birefringent. It was found that three of the modified celluloses with the highest

DS_{TOTAL} ($C_{50/8}$, $C_{50/25}$ and $C_{80/0}$) displayed low apparent viscosity (term "apparent" is used to

emphasise that parallel-plate rotational geometry was applied for the measurements; however,

this will be omitted in the following text) (**Figure (2.11)**). This is due to high proportion of

substituted hydroxyl groups leading to good solubility of these cellulose derivatives in water

(**Figure (2.10)(d)**) indicated by TEM, SAXS and solid content measurements (**Table (2.4)**). This

is also supported by the fact that the sample with the lowest DP_{TOTAL} in this group ($C_{50/8}$) is the

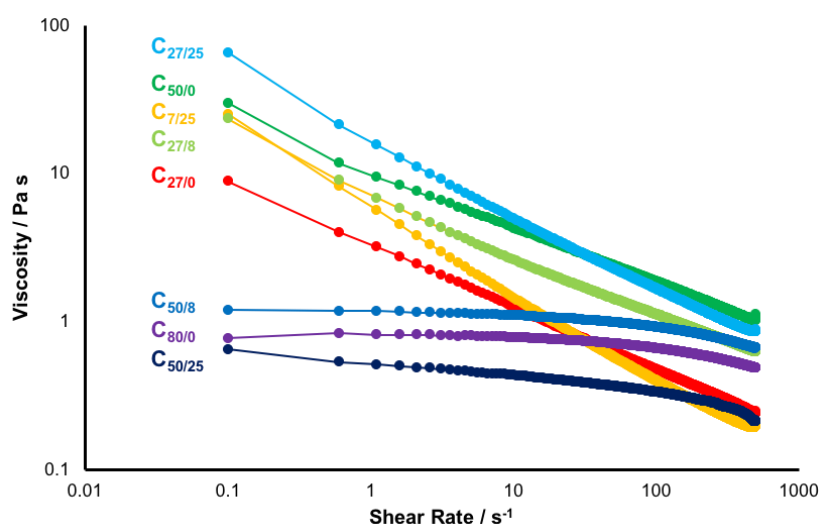**Figure (2.11).** Apparent viscosity versus shear rate profiles for all samples between 500 – 0.1 s^{-1}
at a constant temperature of 20 °C. All samples were measured at a concentration of 10 w/w %.
Since parallel-plate rotational geometry was applied for the measurements, an "apparent
viscosity" term is used. The shear rate values correspond to the disk edge.

most viscous. Shear thinning behaviour observed for these samples at high shear rates is likely to be associated with the elastic properties of the dissolved molecules. The remaining five modified cellulose samples ($C_{27/0}$, $C_{27/8}$, $C_{7/25}$, $C_{50/0}$ and $C_{27/0}$) displayed shear-thinning behaviour with a low-shear-rate viscosity up to two orders of magnitude higher than for the samples with high degree of solubilisation. This rheological result indicates strong elastic properties of cellulosic material with partially substituted hydroxyl groups. The shear thinning observed over a wide range of shear rates suggests that the material is composed of objects with short and long relaxation times which could be indicative of a polymer and particle network formation. However, considering a mixed morphology of the samples (**Figure (2.10)(a) – (c)**) and a combination of factors which could affect sample viscosity, such as anisotropic CNPs, electrostatic repulsions among the cationic side chains, and inter-cellulose and cellulose-water hydrogen bonding connectivity, it would be complicated to perform a detailed interpretation of the observed results. Nevertheless, the rheological measurements show that there is a striking change of viscoelastic properties of the modified cellulose: upon reaching high level of hydroxyl group substitution by HP or HP and HPTMAC the material turns into a low-viscosity fluid (**Figure (2.11)**) due to the complete solubilisation of the constituent cellulose chains (**Figure (2.10)(d)**). Further measurements on the $C_{50/0}$ sample found that the zero-shear viscosity was 8.99 Pa s, measured at a shear rate of 0.0104 s^{-1}. The power law index of this material was found to be 0.591.

The second part of rheo-optical results represented by PLI observations of the sheared samples has demonstrated that samples of modified cellulose corresponding to intermediate degree of substitution could be birefringent. Indeed, PLIs of $C_{50/0}$, $C_{27/25}$ and $C_{50/8}$, recorded at a constant angular speed using SIPLI, exhibit a Maltese cross pattern (**Figure (2.12)**) characteristic of a birefringent material aligned along the flow direction.[40,59] Birefringent properties are commonly described by an optical indicatrix (ellipsoid of electro-magnetic wave normal) representing the refractive index values for all directions of light (electric field vector) vibrations

propagating through a material.[76] The optical indicatrix of a viscoelastic liquid is usually represented by a sphere, all directions are equivalent in the space, and as a result the material is isotropic that is no birefringence is observed. However, an impact of a directional flow could cause deformation and/or orientation of objects comprising the liquid transforming the spherical optical indicatrix into an ellipsoidal one by introducing an uniaxial anisotropy associated with birefringence.[59,77] When the ellipsoid principal axis forms zero angle with the polariser or analyser axis, an extinction pattern similar to Maltese cross appears in PLIs.
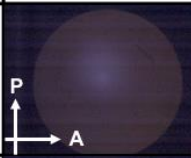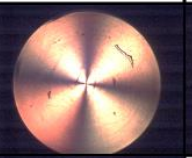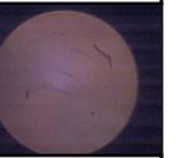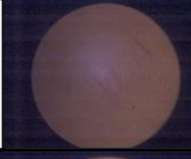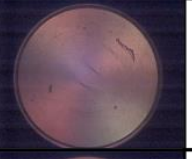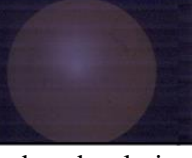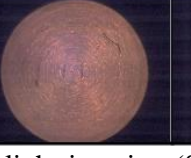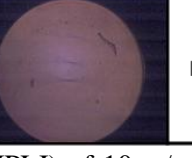

		Degree of HP present / %		
		27	50	80
Degree of HPTMAC present / %	0	INSOLUBLE		
	8	INSOLUBLE		NOT SYNTHESIZED
	25			NOT POSSIBLE

Figure (2.12). Shear-induced polarised light imaging (SIPLI) of 10 w/w % suspensions of all eight modified cellulose samples at 20 °C (parallel-plate geometry, disk diameter 25 mm, geometry gap 1 mm, angular speed 40 rad s^{-1} corresponding to a maximum shear rate of 100 s^{-1} at the sample edge. Selected PLIs represent the birefringent behaviour of the samples at different degree of substitution. The white arrows on the PLI for $C_{27/0}$ indicate the direction of the polariser (P) and analyser (A) respectively for all images. A Maltese cross pattern indicates sample birefringence (shear-induced alignment), whereas the absence of such a pattern indicates no birefringence (no alignment).

The $C_{50/0}$ sample has demonstrated a very pronounced Maltese cross through the entire sample (sheared in a parallel-plate geometry) indicating that the material becomes birefringent virtually over the whole range of shear rates used. Since the material can be aligned at a relatively low shear rates, this suggests that large objects with long relaxation times should be involved in the formation of an oriented morphology producing birefringence. It was found that the relaxation

time of $C_{50/0}$ was 3.16 s, based on the cross over point of the storage and loss moduli. This sample is mainly composed of non-aggregated CNPs and dissolved cellulosic molecules (**Figure (2.7)**, **Table (2.3)** and **Figure (2.10)(c)**). The material has not been fully solubilised at a molecular level yet, but the degree of substitution does not allow large aggregates to be formed in water solution either. At the same time the material shows a shear thinning over the entire range of share rates used for the SIPLI experiment (**Figure (2.11)**) indicating a presence of viscoelastic objects with a long relaxation time. It is likely to expect that the CNPs and cellulosic molecules, coexisting in the water solution, interact with each other via hydrogen bonds forming a polymeric/particle network which orients under a shear along the flow directions resulting in the material birefringence. These aligned structures could act as a precursor for the formation of a fibrous cellulose under a flow processing from a water solution.

In contrast, the cellulosic materials corresponding to low and high degree of substitution ($DS_{TOTAL} < 52\%$ and $DS_{TOTAL} > 58\%$, respectively) demonstrated no signs of birefringence (**Figure (2.12)**) suggesting that there is no structure with a preferable orientation formed under the shear. Considering morphologies formed by these cellulosic materials (**Figure (2.10)(a)**, **(b)** and **(d)** respectively), the cause for this non-birefringent behaviour should be different. The highly modified cellulose forms an aqueous solution of molecules (**Figure (2.10)(d)**) of a relatively low molecular weight ($M_w \sim 78$ kDa) with a fast relaxation time which cannot be aligned at the shear rates accessible in the instrument. Furthermore, they do not form inter-molecular bonds creating larger objects (molecular networks) which could be oriented under the flow processing as indicated by a low viscosity (**Figure (2.11)**). For these reasons they not only remain unaligned by the shear rate used ($\dot{\gamma} \leq 100$ s^{-1}) and but also do not form large orientable objects (molecular networks), hence no birefringence-related effects (absence of Maltese cross) are observed (**Figure (2.12)**). The celluloses with lower levels of substitution comprise of a mixture of morphologies spreading over a wide range of scales (**Figure (2.10)(a)** and **(b)**). Whereas these materials

demonstrate a high viscosity similar to a highly-birefringent $C_{50/0}$ (**Figure (2.11)**), this is mainly caused by a presence of partially solvated (swollen) large aggregates (**Figure (2.7)** and **Table (2.3)**), which also could be the cause of the slight turbidity in these samples in comparison with the transparent samples of highly-modified cellulose (**Figure (2.12)**). Perhaps, the different morphologies present at this level of DS_{TOTAL} cannot create stable interactions that would drag the aggregates of a uniform shape into the formation of a stable network aligning under the flow processing. As a result, the material appears non-birefringent in the SIPLI measurements (**Figure (2.12)**).

With the exception of $C_{50/0}$, the modified cellulosic samples were found to display very weak or no birefringence. At low total degree of substitution ($C_{7/25}$, $C_{27/0}$ and $C_{27/8}$) the samples remain heterogeneous due to the presence of large aggregates and show no structural orientation under shear conditions. However, upon the increase of HPTMAC substitution ($C_{27/25}$) the aggregates are significantly destroyed (**Figure (2.7)(e)**) and the sample becomes more homogeneous with an ability to form a polymeric network evident by an appearance of structural orientation (Maltese cross) under flow conditions (**Figure (2.12)**, $C_{27/25}$). When the modification exceeds a significant amount, the solubility of the cellulosic material is high enough due to preferential hydrogen bonding with solvent molecules over cellulose chains. These impacts lead to liquid-like behaviour under small shear rates, with little ($C_{50/8}$) to no alignment ($C_{50/25}$ and $C_{80/0}$) observed during SIPLI measurements (**Figure (2.12)**).

There is a clear relationship between birefringent properties and the total modification targeted during synthesis. A medium amount of substituted AGU hydroxyl groups (between 50 – 58%) leads to the formation of a flow-induced birefringent detectable by the presence of a Maltese cross. It is thought to be due to a 'sweet spot' in modification of hydroxypropyl functional groups, where there is good solubility present in water, but intermolecular hydrogen bonding between

Table (2.4). Overview of results for all samples including targeted modification of both hydroxypropyl (HP) and (2-hydroxypropyl)trimethylammonium chloride (HPTMAC) modification groups, the percentage solid content after modification (Solid Cont.), surface zeta potential (ζ), the length of nanocrystals (as determined by TEM), and the radius of gyration of the large aggregates (R_{gc}), molecules (R_{gm}) and the excluded volume parameter (ν), determined by SAXS.

Sample Name	DS / %			Solid Cont. / w/w %	ζ / mV	Length / nm	SAXS		
	HP	HPTMAC	Total				R_{gc} / nm	R_{gm} / nm	ν
$C_{27/0}$	27	0	27	52.8	- 2 ± 1	138 ± 33	40.9	14.9	0.44
$C_{7/25}$	7	25	32	45.7	25 ± 1	109 ± 31	1029.4	13.4	0.47
$C_{27/8}$	27	8	35	29.2	22 ± 1	100 ± 29	21.2	15.4	0.48
$C_{50/0}$	50	0	50	0.4	0 ± 1	122 ± 28	30.6	23.5	0.52
$C_{27/25}$	27	25	52	35.5	42 ± 2	101 ± 35	21.0	13.9	0.49
$C_{50/8}$	50	8	58	3.2	28 ± 1	118 ± 40	31.8	19.0	0.51
$C_{50/25}$	50	25	75	4.9	33 ± 4	91 ± 34	-	21.6	0.59
$C_{80/0}$	80	0	80	0.5	2 ± 1	-	-	19.5	0.55

cellulosic objects/molecular chains is still favourable, forming a macroscopic oriented structure under shear. This is promising behaviour for fibre formation.

Conclusions

Substituting cellulosic hydroxyls with varying amounts of two different modifications produces a range of modified celluloses with different properties. NMR and zeta potential act as characterisation tools highlighting that substitution of both hydroxypropyl and (2-hydroxypropyl)trimethylammonium chloride by the sodium hydroxide method has been achieved. TEM images show no change in the dimensions of cellulose needles with modification, however, the images show a disintegration of the large aggregates with increasing DS. This is in agreement with the amount of solid content present, which decreases with increasing hydroxypropyl content.

Small-angle X-ray scattering traces were successfully modelled with two component system representing large molecules and small particles. The SAXS traces showed a systematic increase in the solubilisation of cellulosic samples with increasing degree of modification, indicated by the excluded volume parameter, ν. This led to a reduction in the observed radius of gyration of the large aggregates, R_{gc}, with modification, which suggests greater solvent compatibility as more functional groups were introduced into the cellulose backbone. The radius of gyration of small particles, R_{gm}, was fairly uniform for all samples, which agrees well with the needles observed in TEM.

The rheology measurements of the samples found that the shear-thinning behaviour of the 10 w/w % cellulose samples disappeared when the modification target exceeded 58 %. This is of use to know, as the rheological properties can be tailored through concentration and modification of either substituent. This rheological behaviour could also be coupled with the birefringent properties of the sample where a 'sweet spot' was observed signifying the desired

structural morphology with beneficial orientation properties at moderate (~ 50 %) substitutions of hydroxypropyl. It was also observed that the incorporation of a cationic modification group destroys this strong birefringent behaviour. This is thought to be due to the repulsion present between these ionic groups on the cellulosic backbone.

This work has found that both macro- and microscopic properties can be targeted through the modification of side groups, i.e., 50 % substitution of backbone hydroxyls with HP lead to gel-like behaviour, strong birefringent properties and promising molecular behaviour for fibre formation.

Acknowledgements

References

(1) Lavoine, N.; Desloges, I.; Dufresne, A.; Bras, J. *Carbohydr. Polym.* **2012**, *90*, 735–764.
(2) Moon, R. J.; Martini, A.; Nairn, J.; Simonsen, J.; Youngblood, J. *Chem. Soc. Rev.* **2011**, *40*, 3941–3994.
(3) Nishiyama, Y.; Sugiyama, J.; Chanzy, H.; Langan, P. *J. Am. Chem. Soc.* **2003**, *125*, 14300–14306.
(4) Lu, A.; Hemraz, U.; Khalili, Z.; Boluk, Y. *Cellulose* **2014**, *21*, 1239–1250.
(5) Bondeson, D.; Oksman, K. *Compos. Interfaces* **2007**, *14*, 617–630.
(6) Tashiro, K.; Kobayashi, M. *Polymer (Guildf).* **1991**, *32*, 1516–1526.
(7) Boluk, Y.; Lahiji, R.; Zhao, L.; McDermott, M. T. *Colloids Surfaces A Physicochem. Eng. Asp.* **2011**, *377*, 297–303.
(8) Bergenståhle, M.; Wohlert, J.; Himmel, M. E.; Brady, J. W. *Carbohydr. Res.* **2010**, *345*, 2060–2066.
(9) Tulos, N.; Harbottle, D.; Hebden, A.; Goswami, P.; Blackburn, R. S. *ACS Omega* **2019**, *4*, 4936–4942.
(10) Kushwaha, S.; Singh, R.; Suhas; Chaudhary, M.; Carrott, P. J. M.; Gupta, V. K. *Bioresour. Technol.* **2016**, *216*, 1066–1076.
(11) Hokkanen, S.; Bhatnagar, A.; Sillanpää, M. *Water Res.* **2016**, *91*, 156–173.
(12) Tingaut, P.; Hauert, R.; Zimmermann, T. *J. Mater. Chem.* **2011**, *21*, 16066–16076.
(13) Klemm, D.; Heublein, B.; Fink, H. P.; Bohn, A. *Angew. Chemie - Int. Ed.* **2005**, *44*, 3358–

3393.

(14)   Lindman, B.; Karlström, G.; Stigsson, L. *J. Mol. Liq.* **2010**, *156*, 76–81.

(15)   Meesorn, W.; Shirole, A.; Vanhecke, D.; de Espinosa, L. M.; Weder, C. *Macromolecules* **2017**, *50*, 2364–2374.

(16)   Kontturi, E.; Laaksonen, P.; Linder, M. B.; Nonappa; Gröschel, A. H.; Rojas, O. J.; Ikkala, O. *Adv. Mater.* **2018**, *30*, 1–36.

(17)   Oguzlu, H.; Danumah, C.; Boluk, Y. *Can. J. Chem. Eng.* **2016**, *94*, 1841–1847.

(18)   Chundawat, S. P. S.; Bellesia, G.; Uppugundla, N.; Da Costa Sousa, L.; Gao, D.; Cheh, A. M.; Agarwal, U. P.; Bianchetti, C. M.; Phillips, G. N.; Langan, P.; et al. *J. Am. Chem. Soc.* **2011**, *133*, 11163–11174.

(19)   Huang, Y.; Zhu, C.; Yang, J.; Nie, Y.; Chen, C.; Sun, D. *Cellulose* **2014**, *21*, 1–30.

(20)   Krishna Iyer, K. R.; Neelakantan, P.; Radhakrishnan, T. *J. Polym. Sci.* **1968**, *6*, 1747–1758.

(21)   McCormick, C. L.; Callais, P. A.; Hutchinson, B. H. *Macromolecules* **1985**, *18*, 2394–2401.

(22)   Ureña-Benavides, E. E.; Ao, G.; Davis, V. A.; Kitchens, C. L. *Macromolecules* **2011**, *44*, 8990–8998.

(23)   Marchessault, R. H.; Morehead, F. F.; Walter, N. M. *Nature* **1959**, *184*, 632–633.

(24)   Hamza, A. A.; Abd el-Kader, H. I. *Text. Res. J.* **1983**, *53*, 205–209.

(25)   Mendoza-Galván, A.; Tejeda-Galán, T.; Domínguez-Gómez, A.; Mauricio-Sánchez, R.; Järrendahl, K.; Arwin, H. *Nanomaterials* **2018**, *9*, 45–57.

(26)   Uetani, K.; Koga, H.; Nogi, M. *ACS Macro Lett.* **2019**, *8*, 250–254.

(27)   Cai, J.; Zhang, L. *Biomacromolecules* **2006**, *7*, 183–189.

(28)   Budtova, T.; Navard, P. *Cellulose* **2016**, *23*, 5–55.

(29)   Lavoine, N.; Desloges, I.; Bras, J. *Carbohydr. Polym.* **2014**, *103*, 528–537.

(30)   Jedvert, K.; Heinze, T. *J. Polym. Eng.* **2017**, *37*, 845–860.

(31)   Rodionova, G.; Lenes, M.; Eriksen, Ø.; Gregersen, Ø. *Cellulose* **2011**, *18*, 127–134.

(32)   Williams, D. B. G.; Mason, J. M.; Tristram, C. J.; Hinkley, S. F. R. *Macromolecules* **2015**, *48*, 8497–8508.

(33)   Bochek, A. M. *Russ. J. Appl. Chem.* **2003**, *76*, 1711–1719.

(34)   Fink, J. K. *Reactive Polymers Fundamentals and Applications*; Elsevier, **2013**.

(35)   Gallego, R.; Arteaga, J. F.; Valencia, C.; Franco, J. M. *Chem. Eng. Sci.* **2015**, *134*, 260–268.

(36)   Gosecki, M.; Setälä, H.; Virtanen, T.; Ryan, A. J. *Carbohydr. Polym.* **2021**, *251*, 1–7.

(37)   Picken, S. J.; Sikkema, D. J.; Boerstoel, H.; Dingemans, T. J.; van der Zwaag, S. *Liq. Cryst.* **2011**, *38*, 1591–1605.

(38)   Yamaguchi, M.; Manaf, M. E. A.; Songsurang, K.; Nobukawa, S. *Cellulose* **2012**, *19*, 601–613.

(39)   Cranston, E. D.; Gray, D. G. *Colloids Surfaces A Physicochem. Eng. Asp.* **2008**, *325*, 44–51.

(40)   Mykhaylyk, O. O. *Soft Matter* **2010**, *6*, 4430–4440.

(41)   Mao, Y.; Liu, K.; Zhan, C.; Geng, L.; Chu, B.; Hsiao, B. S. *J. Phys. Chem. B* **2017**, *121*, 1340–1351.

(42)   Leppänen, K.; Pirkkalainen, K.; Penttilä, P.; Sievänen, J.; Kotelnikova, N.; Serimaa, R. *J. Phys. Conf. Ser.* **2010**, *247*, 1–11.

(43)   Cameron, R. E.; Crawshaw, J.; Mant, G. R.; Bras, W. *J. Appl. Polym. Sci.* **2002**, *83*, 1209–1218.

(44)   Khandelwal, M.; Windle, A. H. *Int. J. Biol. Macromol.* **2014**, *68*, 215–217.

(45)   Lott, J. R.; McAllister, J. W.; Wasbrough, M.; Sammler, R. L.; Bates, F. S.; Lodge, T. P. *Macromolecules* **2013**, *46*, 9760–9771.

(46)   Horkay, F.; Hecht, A. M.; Geissler, E. *Macromolecules* **1998**, *31*, 8851–8856.

(47) Benigar, E.; Dogsa, I.; Stopar, D.; Jamnik, A.; Cigić, I. K.; Tomšič, M. *Langmuir* **2014**, *30*, 4172–4182.

(48) Hammouda, B.; Ho, D.; Kline, S. *Macromolecules* **2002**, *35*, 8578–8585.

(49) Doi, M. *J. Nonnewton. Fluid Mech.* **1987**, *25*, 385–386.

(50) Hammouda, B.; Ho, D. L.; Kline, S. *Macromolecules* **2004**, *37*, 6932–6937.

(51) Dogsa, I.; Tomšič, M.; Orehek, J.; Benigar, E.; Jamnik, A.; Stopar, D. *Carbohydr. Polym.* **2014**, *111*, 492–504.

(52) Hammouda, B. *Polym. Charact.* **1993**, *106*, 87–133.

(53) Dogsa, I.; Cerar, J.; Jamnik, A.; Tomšič, M. *Carbohydr. Polym.* **2017**, *172*, 184–196.

(54) Benigar, E.; Zupančič Valant, A.; Dogsa, I.; Sretenovic, S.; Stopar, D.; Jamnik, A.; Tomšič, M. *Langmuir* **2016**, *32*, 8182–8194.

(55) Berthold, F.; Gustafsson, K.; Sjöholm, E.; Lindström, M. *11th Int. Syposium Wood Pulping Chem.* **2001**, *1*, 363–366.

(56) Kaszuba, M.; Corbett, J.; Watson, F. M. N.; Jones, A. *Philos. Trans. R. Soc. A Math. Phys. Eng. Sci.* **2010**, *368*, 4439–4451.

(57) Schneider, C. A.; Rasband, W. S.; Eliceiri, K. W. *Nat. Methods* **2012**, *9*, 671–675.

(58) Ilavsky, J.; Jemian, P. R. *J. Appl. Crystallogr.* **2009**, *42*, 347–353.

(59) Mykhaylyk, O. O.; Warren, N. J.; Parnell, A. J.; Pfeifer, G.; Laeuger, J. *J. Polym. Sci. Part B Polym. Phys.* **2016**, *54*, 2151–2170.

(60) Zhang, L. M. *Macromol. Mater. Eng.* **2001**, *286*, 267–275.

(61) Choi, P.; Kavassalis, T. A.; Rudin, A. *Ind. Eng. Chem. Res.* **1994**, *33*, 3154–3159.

(62) Brady, J.; Dürig, T.; Lee, P. I.; Li, J.-X. Polymer Properties and Characterization. In *Developing Solid Oral Dosage Forms*; Elsevier: Boston, 2017; pp 181–223.

(63) Eyley, S.; Thielemans, W. *Nanoscale* **2014**, *6*, 7764–7779.

(64) Shibakami, M.; Nemoto, T.; Sohma, M. *Cellulose* **2018**, *25*, 2217–2234.

(65) Kazharska, M.; Ding, Y.; Arif, M.; Jiang, F.; Cong, Y.; Wang, H.; Zhao, C.; Liu, X.; Chi, Z.; Liu, C. *Int. J. Biol. Macromol.* **2019**, *134*, 390–396.

(66) Shahabi-Ghahfarrokhi, I.; Khodaiyan, F.; Mousavi, M.; Yousefi, H. *Fibers Polym.* **2015**, *16*, 529–536.

(67) Pereira, B.; Arantes, V. Nanocelluloses From Sugarcane Biomass. In *Advances in Sugarcane Biorefinery*; Elsevier, 2018; pp 179–196.

(68) Le Gars, M.; Douard, L.; Belgacem, N.; Bras, J. Cellulose Nanocrystals: From Classical Hydrolysis to the Use of Deep Eutectic Solvents. In *Nanosystems*; IntechOpen, 2019; Vol. 1.

(69) Smirnov, M. A.; Sokolova, M. P.; Tolmachev, D. A.; Vorobiov, V. K.; Kasatkin, I. A.; Smirnov, N. N.; Klaving, A. V.; Bobrova, N. V.; Lukasheva, N. V.; Yakimansky, A. V. *Cellulose* **2020**, *27*, 4305–4317.

(70) Gopakumar, D. A.; Pottathara, Y. B.; Sabu, K. T.; Abdul Khalil, H. P. S.; Grohens, Y.; Thomas, S. Nanocellulose-Based Aerogels for Industrial Applications. In *Industrial Applications of Nanomaterials*; Elsevier, 2019; pp 403–421.

(71) Blackwell, J.; Kurz, D.; Su, M.-Y.; Lee, D. M. X-Ray Studies of the Structure of Cellulose Complexes. In *The Structures of Cellulose*; ACS Symposium Series; American Chemical Society, 1987; Vol. 340, pp 199–213.

(72) Saito, M. *Polym. J.* **1983**, *15*, 213–223.

(73) Moan, M.; Wolff, C. *Polymer (Guildf).* **1975**, *16*, 776–780.

(74) Davis, R. M. *Macromolecules* **1991**, *24*, 1149–1155.

(75) Gerwig, G. J.; Van Albert Kuik, J.; Leeflang, B. R.; Kamerling, J. P.; Vliegenthart, J. F. G.; Karr, C. D.; Jarroll, E. L. *Glycobiology* **2002**, *12*, 499–505.

(76) Born, M.; Wolf, E.; Bhatia, A. B.; Clemmow, P. C.; Gabor, D.; Stokes, A. R.; Taylor, A. M.; Wayman, P. A.; Wilcock, W. L. *Principles of Optics*, 7th ed.; Cambridge University Press, **1999**.

(77)   Wulf, K. *Acta Polym.* **1985**, *36*, 296–297.

Chapter 3 – Finding Suitable Worm-like Micelles to act as Model Systems

3.1 Introduction

Worm-like micelles are frequently used in combination with micro- and millifluidic devices in order to thoroughly characterise flow fields present in these channels.[1–17] Worm-like micelles are attractive due to their intrinsically large aspect ratios which enable them to be easily oriented along a flow direction. The orientation can easily be observed and measured by a variety of techniques, including polarised optical microscopy (POM) or flow birefringence,[18–20] and scattering techniques, such as X-ray,[3,21] neutron[1,22–25] or light scattering.[25,26]

The use of worm-like micelles as a model system in micro- and millifluidic devices is far reaching and has been used in combination with straight channel, expansion-contraction and cross slot geometries. Worm-like micelles have been employed in combination with straight channel microfluidics for a range of purposes. Masselon *et al*. utilised worm-like micelles in order to develop a framework to measure the length of micelles based on experimental data collected from microfluidic channels.[6] Trebbin and coworkers studied the orientation of worm-like micelles along a serpentine straight channel by small-angle X-ray scattering (SAXS), and found that the worm-like micelles orient themselves along the direction of flow, even around tight curves in the channel.[3] Salipante *et al*. investigated the phemomena of shear banding and jetting within microchannels with the use of worm-like micelles; this work indicated that both the aspect ratio and wall roughness of the channels impacts the degree to which these phenomena occur.[4] Weston *et al*. have also incorporated worm-like micelles in their work with microfluidic straight channels; using small-angle neutron scattering (SANS), they were able to quantify the micellar alignment with flow.[1] This work was also performed over a greater range of shear rates than previously tested with SANS experiments.

Worm-like micelles have been used less frequently in combination with expansion-contraction microfluidic devices. Ober *et al*. published work on the use of an extensional viscometer rheometer on a chip (EVROC), which used worm-like micelles to assess the

applicability of the device in measuring the extensional viscosity of fluids.[27] Trebbin and coworkers have also utilised worm-like micelles to study the orientation of these structures by SAXS, rather surprisingly, they found that the orientation of these micelles were perpendicular to the flow after exiting the contraction.[3]

The combination of worm-like micelles with cross-slot microfluidic devices, has also been utilised frequently in the literature. Pathak and coworkers were one of the first to use worm-like micelles in the characterisation of cross-slot microfluidics, in combination with birefringence and particle imaging velocimetry (PIV) measurements.[14] This study measured the effects of planar extension on the viscoelasticity of the fluids investigated. Haward *et al*. has used worm-like micelles to study the instability of flow frequently seen in cross-slot microfluidics. This work has led to the creation of a stability diagram based on the Weissenberg (*Wi*) and Reynolds (*Re*) numbers within the microchannel.[15,28] Finally, Dubash and coworkers have also investigated flow instability with the use of worm-like micelles, and found that the transition from stable symmetric flow to unsteady asymmetric flow occurs via stable asymmetric flow.[29] This work enabled Dubash *et al*. to determine that flow instability is influenced by *Wi*, inertial effects and the rheological behaviour of the fluid.

The aim of the work contained within this Chapter was to find a suitable worm-like micelle material as a model viscous polymeric system for the investigation of flow within the millifluidic devices whose design, construction and evaluation is the subject of **Chapter 4**, **Chapter 5** and **Chapter 6**. This model system utilises an anionic worm-like micelle system previously published by Penfold *et al*.[30] Further characterisation, including shear and oscillatory rheology, shear induced polarised optical microscopy and small-angle X-ray scattering, is performed to determine whether these worm-like micelles are a suitable material to characterise millifluidic devices.

3.2 Experimental

3.2.1 Materials

Glycidyl methacrylate (GlyMA, 97%) was purchased from Sigma Aldrich (UK) and used as received. 2-Hydroxypropyl methacrylate (HPMA; 97%) and 3-mercaptopropyltriethoxysilane (MPTES, 95%) were purchased from Alfa Aesar (UK) and used as received. 2,2-Azobis[2-(2-imidazolin-2-yl)propane dihydrochloride (VA-044) was purchased from Wako Chemicals Ltd (Japan). Deionised water was obtained from an Elgastat Option 3A water purification unit with a resistivity of 15 MΩ cm.

3.2.2 Synthesis of anionic polymeric worm-like micelles

The PEG1$_{13}$-PETTC macro-CTA and PSKPMA$_{111}$-PETTC macro-CTA were synthesised as described elsewhere.[31] A 50 ml sample vial was charged with a magnetic stirrer bar, PKSPMA$_{111}$ macro-CTA (0.2596 g, 10.1 μmol), PEO$_{113}$ macro-CTA (0.4813 g, 85.8 μmol), VA-044 (2 mg, 6.3 μmol), HPMA (2.26 g, 0.16 mol), GlyMA (0.5291 g, 3.7 mmol) and deionised water (14.01 g) to afford a target copolymer concentration of 20 w/w %. The sealed vial was immersed in an ice/water slurry bath and degassed under nitrogen for 30 minutes, before being placed in a preheated oil bath set at 50 °C for 4 h. The statistical copolymerisation was quenched by exposure to air and simultaneous cooling to 20 °C. The aqueous copolymer worm dispersion was diluted to 5 w/w % using deionised water and gently stirred at 20 °C for 24 h. Core cross-linking of these anionic worms was achieved at 20 °C by addition of 3-mercaptopropyltriethoxysilane (0.8042 g, 3.4 mmol, [GlyMA]/[MPTES] molar ratio = 1.0) with continuous stirring for 48 h.

3.2.3 Transmission electron microscopy (TEM)

Imaging was performed using a Technai Spirit 2 microscope (FEI, Oregon, USA) operating at 80 kV and fitted with an Orius SC1000B camera (Gatan, California, USA).

Copper/palladium TEM grids (Agar Scientific, UK), coated in-house with a thin film of amorphous carbon and subsequently subjected to a glow discharge for 20 s, were used as sample holders. Individual 10 µL droplets of the aqueous dispersion of worm-like micelles at a concentration of 0.1 w/w % were placed on freshly treated grids for 1 minute and then blotted with filter paper to remove excess solution. To ensure sufficient contrast, uranyl formate (10.0 µL of a 0.75 w/w % solution) was absorbed onto the sample-loaded grid for 30 s and then blotted to remove any excess of the stain compound. Each freshly loaded grid was then dried under vacuum conditions. Measurements were performed over 15 different worm-like micelles.

3.2.4   Small angle X-ray scattering (SAXS) measurements

SAXS data was collected using a laboratory SAXS/WAXS instrument (Xeuss 2.0, Xenocs, France) equipped with a liquid gallium MetalJet X-ray source (Excillium, Sweden, wavelength $\lambda = 0.134$ nm), two sets of motorised scatterless slits for beam collimation (0.6 x 0.5 mm) and a Dectris Pilatus 1M pixel SAXS detector (sample-to-detector distance 5.047 m). SAXS patterns were recorded over a q range of 0.02 nm^{-1} < q < 1.8 nm^{-1}, with $q = (4\pi \sin\theta)/\lambda$, where q is the length of the scattering vector and θ is one-half of the scattering angle. The worm-like micelle scattering pattern was recorded at 1 w/w %. Scattering patterns were acquired for 30 mins. Acquisitions were normalised, background subtracted and modelled using the Irena macro in Igor Pro 8 (Wavemetrics Inc, USA). The data was fitted to a worm model, where the form factor of worm-like micelles is expressed in **Equation (3.1)**.[32]

$$F_{w\_mic}(q) = N_w^2 C_s^2 g_{sw}(q) + N_w C_c^2 g_c(q, R_g) + N_w(N_w - 1)C_c^2 S_{cc}(q)$$
$$+ 2N_w^2 C_s C_c S_{sc}(q)$$

(3.1)

Equation (3.1). The form factor (F(q)) of a worm-like micelle consists of the number density per unit volume (N_w,) the scattering length contrast of the stabiliser block (C_s / cm^{-2}), the self-correlation term for the worm-like micelles (g_{sw}), the scattering length contrast of the core block (C_c), the radius of gyration of the stabiliser block (R_g) and the interference cross term between the worm core and the worm stabiliser (S_{cc}).

The stabiliser block and the core block X-ray scattering length contrast is given by $C_s = V_s(\xi_s - \xi_{sol})$ and $C_c = V_c(\xi_c - \xi_{sol})$, respectively. Here ξ_s, ξ_c and ξ_{sol} are the X-ray scattering length densities of the core block ($\xi_{PHPMA\text{-}PGlyMa} = 10.71 \times 10^{10}$ cm^{-2}), the corona block ($\xi_{PEG\text{-}PKSPMA} = 9.196 \times 10^{10}$ cm^{-2}) and the solvent ($\xi_{sol} = 9.40 \times 10^{10}$ cm^{-2}), respectively. V_s and V_c are volumes of the core block ($V_{PHPMA\text{-}PGlyMA}$) and the corona block ($V_{PEG\text{-}PKSPMA}$), respectively. The volumes were obtained from $V = \frac{M_{n,pol}}{N_A \rho}$, using the densities of PHPMA ($\rho_{PHPMA} = 1.15$ g cm^{-3}),[33] PGlyMa ($\rho_{PGlyMA} = 1.25$ g cm^{-3}),[34] PEG ($\rho_{PEG} = 1.12$ g cm^{-3})[33] and PKSPMA ($\rho_{PKPSMA} = 1$ g cm^{-3}),[35] where $M_{n,pol}$ corresponds to the number-average molecular weight of the block, assuming the polymerisation went to full conversion. The mean aggregation number for worm-like micelles is given by **Equation (3.2)**. The hemispherical end caps of each worm are not considered in this form factor

$$N_w = (1 - x_{sol}) \frac{\pi R_{sw}^2 L_w}{V_s} \tag{3.2}$$

Equation (3.2). The mean aggregation number (N_w) is calculated from the volume fraction of solvent within the worm core (x_{sol}), the core's radius of gyration (R_{sw}), the worm length (L_w) and the volume of the stabiliser block (V_s).

3.2.5 Oscillatory rheology

Oscillatory rheology measurements were performed using a stress-controlled MCR502 rheometer (Anton Paar, Austria) with a Couette cell attachment. The rheometer was equipped with a Pelter temperature controller composed of bottom-plate and top-hood heaters. The relaxation time of the worm-like micelles was determined for a range of concentrations (1, 2, 3, 4 and 5 w/w %) via a frequency sweep of 10 – 0.001 rad/s at a fixed strain of 1 % and a temperature of 20 °C.

3.2.6 Rotational rheology and shear-induced polarised light imaging (SIPLI)

Rotational rheology measurements were performed using a stress-controlled MCR301 rheometer (Anton Paar, Austria) with SIPLI attachment.[36] The rheometer was equipped with a

Peltier temperature controller composed of bottom-plate and top-hood heaters, and plate-plate geometry (comprising of polished stainless-steel disk of 25 mm diameter and a fused quartz bottom plate). The SIPLI attachment, based on reflective polariscope principles, uses components of the parallel-plate geometry where the bottom (static) transparent plate and the top (rotating) reflective disk are parts of the optical setup, allowing time-resolved reflected polarised light images (PLI) of measured samples to be recorded during shear. Descending shear rate ($\dot{\gamma}$) sweeps were performed from 100 s⁻¹ to 0.001 s⁻¹ at a constant temperature of 20 °C, with a sample thickness (gap between the parallel plates) of 1 mm. A concentration series of the worm-like micelles were analysed (1, 2, 3, 4 and 5 w/w %). During shear sweeps, imaging of the samples under crossed polarisers was performed to identify birefringence. The second set of experiments was performed at a constant angular speed of rotation, ω, of the shearing disk. In these experiments, the SIPLI technique was used to capture PLIs every second for 1000 s to observe the onset of orientation of the material under flow conditions. Since the shear rate experienced by each part of a sample in a parallel-plate geometry is proportional to its radial position ($\dot{\gamma} = \omega r/d$, where r is the radius of a corresponding sample position and d is the geometry gap), and assuming that the flow is laminar, SIPLI measurements at a constant ω enables birefringent properties of the sample to be tested within a range of share rates from 0 s⁻¹ (at the sample centre) to $\dot{\gamma}_{max} = \omega R/d$ (at the sample edge where R is the sample radius) simultaneously in a single experiment.

3.3 Results and Discussion

3.3.1   Synthesis of anionic worm-like micelles

The PEG₁₁₃-PETTC and PKSPMA₁₁₁-PETTC precursors were chain-extended in water, via the RAFT polymerisation of HPMA and GlyMA monomers, to form worm-like micelles comprising a statistical P(HPMA-*stat*-GlyMA) core-forming block. The target degree of polymerisation was 168 and 39 for HPMA and GlyMA respectively and the final copolymer

concentration was 20 w/w % solids. These conditions were selected based on published work by Penfold *et al*. describing the synthesis of these anionic worm-like micelles.[31] The final copolymer could not be analysed by nuclear magnetic resonance (NMR) spectroscopy or gel permeation chromatography (GPC), to measure the total degree of polymerisation, due to a lack of common solvent for the water-insoluble core-forming block, and the highly water soluble anionic PKSPMA$_{111}$ block. Nevertheless, the final dispersion was obtained as a transparent gel, as expected of concentrated worms.
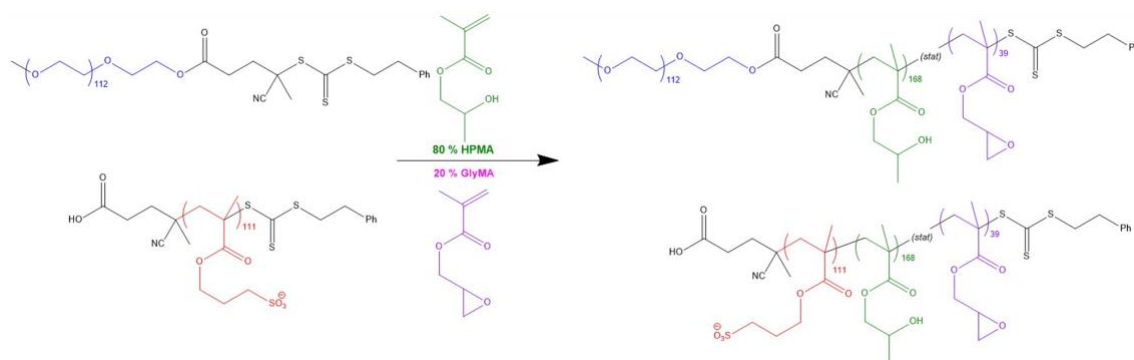

Figure (3.1). RAFT polymerisation of HPMA and GlyMA monomers using a PEG$_{113}$ macromolecular chain transfer agent and a PKSPMA$_{111}$ macromolecular chain transfer agent to produce two copolymers with a core comprising of a statistical mixture of the two monomers.

Core cross-linking of the resulting worm-like micelles was also essential, due to the thermoresponsive nature of the PHPMA in the worm cores. It is well known that PHPMA exhibits lower critical solution temperature (LCST)-like behaviour, i.e. it becomes more soluble at lower temperatures. Therefore, for worms possessing a core of PHPMA in water, decreasing the temperature leads to an increase in core solvation, which in turn, changes the relative volume fractions of the stabiliser block and the core-forming block, which may drive a worm-to-sphere transition. This is undesirable, as anisotropic morphological objects were required as model materials, and not isotropic spheres. After synthesis, therefore, the worm-like micelles were diluted to 5 w/w % before undergoing cross-linking via the method outlined by Penfold *et al*.[31]

This crosslinking covalently bonds the core-forming polymers within a worm together, thus preventing any morphological transitions from taking place due to a change in temperature.

3.3.2 Characterisation of worm-like micelles

The final copolymer morphology was confirmed to be worm-like micelles *via* post-mortem TEM (**Figure (3.2)**) and SAXS (**Figure (3.3)**) studies. TEM studies also identified a minor fraction of spheres. The width of the worm-like micelles, analysed by TEM, were found to be 27.72 ± 3.3 nm, averaged over 25 measurements. The length of the worms were qualitatively analysed to be well over 1 μm.
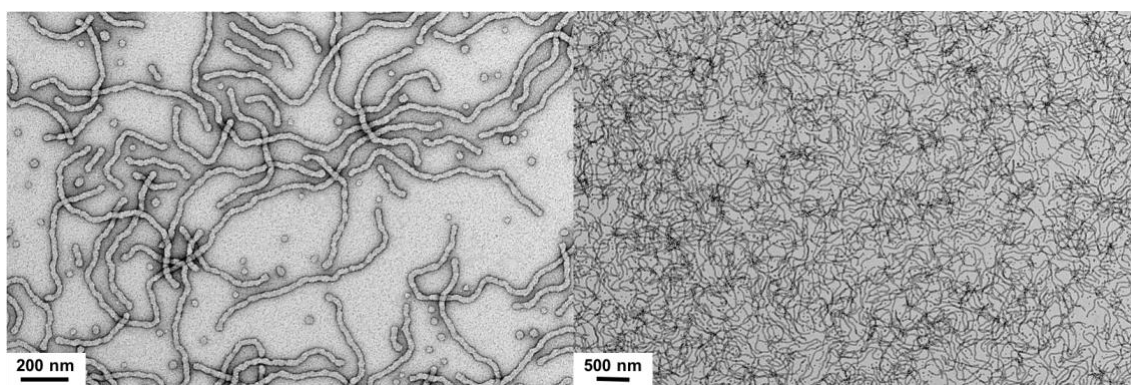
Figure (3.2). Post-mortem TEM images obtained for the anionic worm-like micelles prior to cross-linking.

A laboratory X-ray scattering instrument was utilised to characterise the cross-linked anionic worm micelles at a concentration of 1 w/w % solids, to remove the presence of a structure factor. A 2 mm borosilicate glass capillary was employed as a sample environment, and patterns were acquired over 30 minutes. Compared to TEM, which is a number-average technique, SAXS is able to provide robust structural information as X-ray scattering is averaged over many millions of nanoparticles. The presence of worms is indicated by the slope at low q with a gradient of -1.2 (**Figure (3.3)**).[37] The resulting one-dimensional scattering pattern for the worm-like micelles was modelled using a well-known worm micelle model.[32]

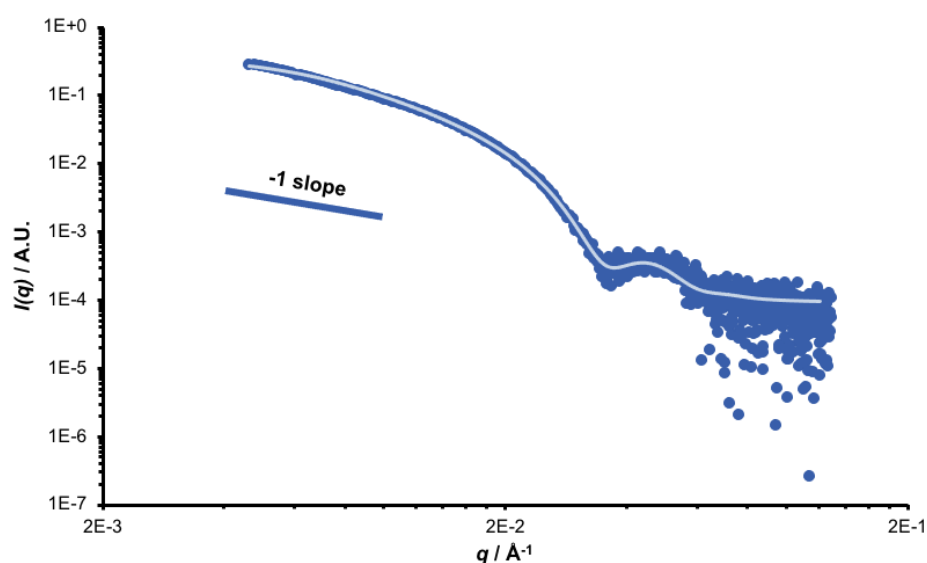**Figure (3.3).** One-dimensional SAXS pattern of the cross-linked anionic worm-like micelles (0.9 PEG$_{113}$ + 0.1 PKSPMA$_{111}$)-P(HPMA$_{168}$-*stat*-GlyMA$_{39}$) at 20 °C in water at 1 w/w %. The light blue line indicates the fitted model of the acquired data (dark blue circles).

In order to successfully model the 1D SAXS pattern, full conversion of the copolymerisation is assumed and the degree of polymerisation taken as the stoichiometric target value. This assumption is reasonable given that similar aqueous RAFT PISA syntheses of block copolymers using GlyMA and HPMA reach > 99 % monomer conversion.[31,38–41] The conversion impacts the mean degree of polymerisation, and thereby the volume of the core P(HPMA-GlyMA) block. The model indicated no solvent present (x_{sol} = 0) in the core, this is expected due to the high content of PGlyMA present, which is water insoluble, and self-assembly into large morphologies aims to reduce interactions between the core block and the solvent. The analysis of the SAXS pattern also indicated a worm width of 31.2 nm. This value is slightly larger than that acquired by TEM which does not account for the contribution of the stabiliser block due to the dry imaging state of TEM which leads to a collapse of the stabiliser block. The average worm length was found to be 3.7 μm agreeing well with TEM which showed the presence of a small population of short worms and a greater proportion of very long worms. The radius of gyration was found to be 11.1 nm for the core block and 2.23 nm for the stabiliser. The aggregation number

was calculated based on the model parameters (**Equation (3.2)**); it was found there was a mean of approximately 33,900 chains per worm-like micelle.

The anionic worm-like micelles prepared at 20 w/w % formed a soft, free-standing gel upon cooling to room temperature. In order to characterise their rheological properties, the worms were diluted to 5 w/w %, where they formed a free-flowing liquid, and were subsequently cross-linked to covalently stabilise the worm-like morphology. In order to investigate the relaxation time of the worm-like micelles, the material was analysed via oscillatory rheology. The relaxation time was calculated from the inverse of the frequency at which G'' crosses over G'; this was found to occur at 0.0225 rad s^{-1} for the 5 w/w % solution. Therefore, the relaxation time was calculated to be 44.4 s for the 5 w/w % concentration. The relaxation times of the concentration series can be seen in **Figure (3.4)** and **Table (3.1)**. As the concentration is lowered from 5 to 4 w/w %, the relaxation time decreases rapidly, from 44.4 s to 18.9 s. The lowering of the relaxation time continues with the decreasing concentration, in an exponential fashion.
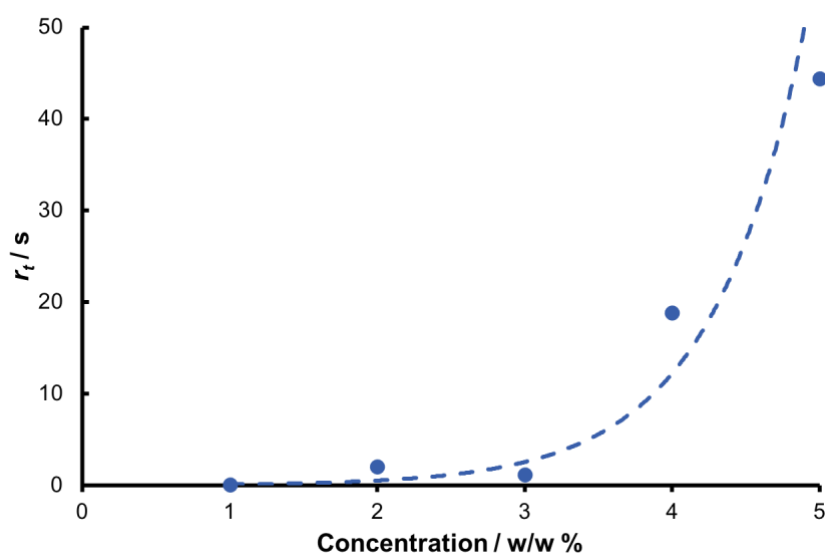

Figure (3.4). Plot of relaxation time (r_t / s) against concentration for the anionic worm-like micelles. The relaxation time was calculated from the inverse of the cross-over point of G' and G'' during a frequency sweep.

The viscosity profile as a function of shear rate was investigated using rotational rheology. The aim of this investigation was to measure the zero-shear viscosity of each concentration of worm-like micelles, and to determine the power law index of each sample. The viscosity/shear sweeps can be seen in **Figure (3.5)**. At 1 w/w %, the viscosity data measured for the worm-like micelles was very noisy due to the low concentration of polymeric material in the sample. It can be seen that the viscosity increases as the concentration of worm-like micelles increases. For all samples, the zero-shear viscosity was recorded; it was observed that the plateau of the viscosity occurred at lower shear rates as the concentration increased (**Table (3.1)**). As well as this, the power law index was found to correspond to a highly shear-thinning material at higher concentrations of the worm-like micelles, with 5 w/w % having a recorded power law index of 0.337. However, as the concentration decreased, the power law index indicated the material became more similar to a Newtonian fluid, which has a power law index of 1 (1 w/w % had a power law index of 0.822).

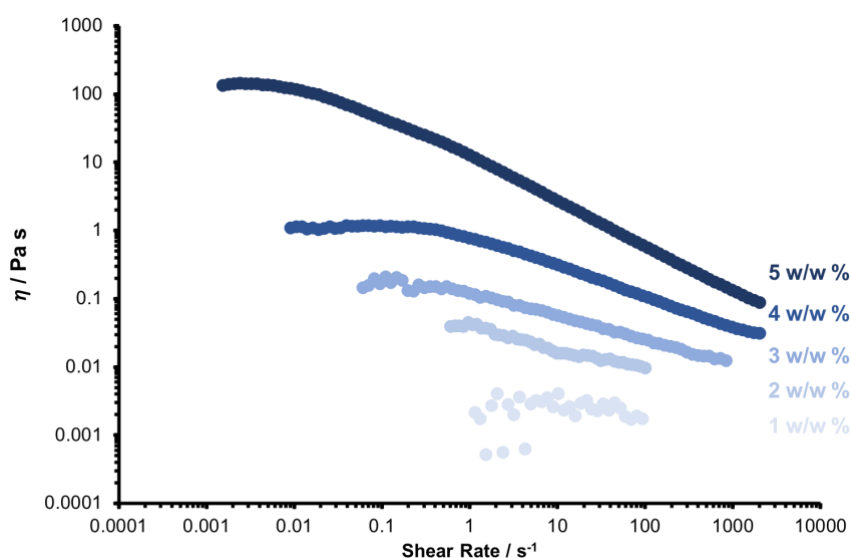
Figure (3.5). Viscosity (η / Pa s) vs. shear rate ($\dot{\gamma}$ / s^{-1}) plots obtained using rotational rheometry studies at a fixed temperature of 20 °C and gap of 1 mm, for a concentration range of the anionic worm-like micelles.

Rotational rheology was also used in combination with polarised imaging, a technique known as shear-induced polarised light imaging (SIPLI). Again, all five concentrations of the worm-like micelles were investigated. The characteristic Maltese cross was observed for all images (**Figure (3.6)**), confirming the presence of anisotropic particles in the samples, which have aligned under shear. However, it was noted that the strength of the Maltese cross increased with concentration, this was expected as the greater the concentration of worm-like micelles, the more birefringent the sample will be.

It was also observed that the shear rate corresponding to the onset of birefringence decreased as the concentration increased (**Table (3.1)**). Again, this is expected as the higher the proportion of worm-like micelles, the lower the force required to align them in the direction of flow. SIPLI was also utilised to calculate the stress optical coefficient (C) of the worm-like micelles, based on the procedure outlined by Mykhaylyk.[36] The stress optical coefficient is important for the calculation of planar extension from a birefringent image, investigated in **Chapter 6**. Using the degree of birefringence measured in the PLIs, C could be calculated using **Equations (3.3)** and **(3.4)**. The calculated values can be seen in **Table (3.1)**.

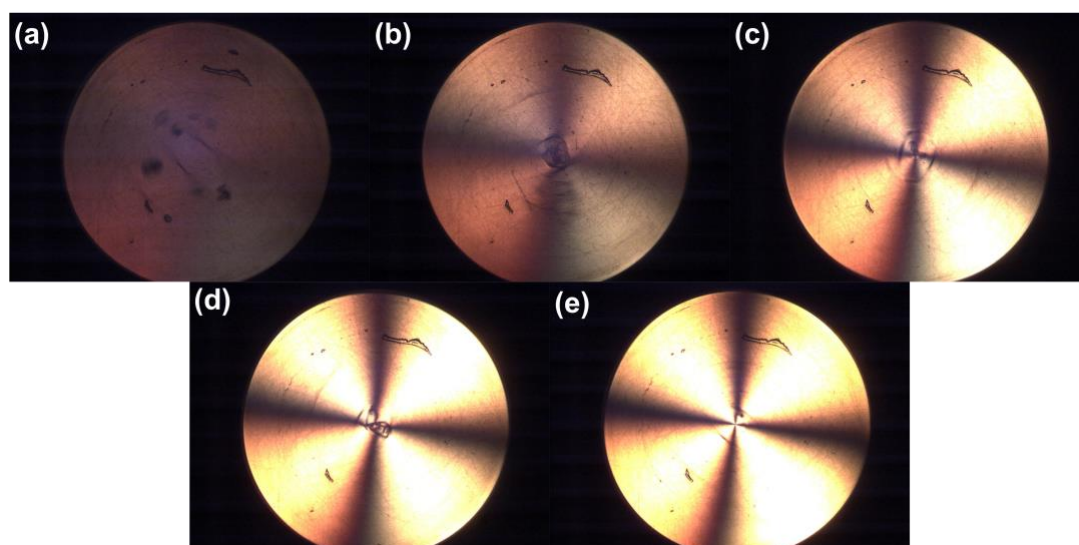**Figure (3.6).** Polarised light images obtained for the concentration series of anionic worm-like micelles; **(a)** 1 w/w %, **(b)** 2 w/w %, **(c)** 3 w/w %, **(d)** 4 w/w % and **(e)** 5 w/w %. The PLIs correspond to a shear rate of 100 s^{-1}, the strength of the Maltese cross increases with concentration, indicating the presence of aligned anisotropic objects.

$$C = \frac{B}{N_1} = \frac{B}{2\dot{\gamma}\eta \left(1 - \eta_c^2/\eta^2\right)^{0.5} \left(\eta_c^2/\eta^2\right)^{-0.7}} \qquad \textbf{(3.3)}$$

Equation (3.3). The stress optical coefficient (C / Pa^{-1}) can be calculated from the degree of birefringence (B / dimensionless) and the first normal stress difference (N$_1$ / Pa). N$_1$ can be calculated from the shear rate applied to the material ($\dot{\gamma}$ / s^{-1}), the viscosity (η / Pa s) and the material consistency (η_c / Pa s).[36]

$$\eta_c = \frac{d\sigma}{d\dot{\gamma}} \qquad \textbf{(3.4)}$$

Equation (3.4). The material consistency (η_c / Pa s) can be calculated from the change in stress (σ / Pa) and the change in shear rate ($\dot{\gamma}$ / s^{-1}).[36]

Table (3.1). Summary of rheology data for concentration series of the anionic worm-like micelles where conc. indicates concentration, η_0 is the zero-shear viscosity, $\dot{\gamma}_0$ is the shear rate at which η_0 was recorded, n is the power law index, r_t is the relaxation time, $\dot{\gamma}_{crit}$ is the critical shear rate at which the onset of birefringence was recorded and C is the stress optical coefficient.

Conc. / w/w %	η_0 / Pa s	$\dot{\gamma}_0$ / s^{-1}	n	r_t / s	$\dot{\gamma}_{crit}$ / s^{-1}	C
1	0.00260	1.14	0.822	0.0526	3.18	1.48 x 10^{-5}
2	0.096	0.756	0.684	2.04	2.15	5.82 x 10^{-6}
3	0.167	0.061	0.651	1.18	0.332	6.69 x 10^{-6}
4	1.44	0.0104	0.549	18.9	0.097	9.86 x 10^{-7}
5	137.5	0.0021	0.337	44.4	0.0062	1.32 x 10^{-7}

3.4 Conclusions

RAFT polymerisation was used to synthesis well-defined, anionic worm-like micelles with a high aspect ratio of 118.6, as observed by TEM and SAXS. TEM also showed a small population of spheres present in the sample. Similar results were reported by Penfold *et al*. who also observed long, thin worms by TEM.[31] SIPLI measurements also showed the presence of anisotropic objects, aligned with the flow direction. All concentrations of the worm-like micelles tested displayed birefringence; however, the critical shear rate was found to be inversely proportional to the concentration of worm-like micelles.

The investigation of relaxation time as a function of concentration of worm-like micelles showed that both 4 and 5 w/w % solutions had long relaxation times. However, the relaxation time decayed rapidly as the proportion of worm-like micelles was reduced. The study into the relaxation time of the anionic worm-like micelles was important for the calculation of planar viscosity in **Chapter 6**.

The shear sweeps performed on the concentration series of worm-like micelles also showed that these materials spanned a large viscosity range, with the 5 w/w % sample having a zero-shear viscosity of 137 Pa s and the 1 w/w %, a zero-shear viscosity of 0.0026 Pa s. The high viscosity of the more concentrated samples also lent themselves well as model materials, as they would be appropriate, when testing the sealing limits of the millifluidic devices. If a device could flow a viscous material, such as the concentrated worm-like micelles, with no leakage, the devices could be deemed successful.

Overall, these worm-like micelles show promise as a model material to enable characterisation of the millifluidic channels discussed in **Chapter 5** and **Chapter 6**. The higher concentrations (4 and 5 w/w %) were selected as these model materials due to the strong birefringence observed during SIPLI measurements. An added benefit of these materials is the strong scattering observed at 1 w/w %, which lends the material well to orientation SAXS studies within the millifluidic devices.

3.5 Acknowledgements

3.6 References

(1)   Weston, J. S.; Seeman, D. P.; Blair, D. L.; Salipante, P. F.; Hudson, S. D.; Weigandt, K. M. *Rheol. Acta* **2018**, *57*, 241–250.
(2)   Moss, G. R.; Rothstein, J. P. *J. Nonnewton. Fluid Mech.* **2010**, *165*, 1–13.

(3)   Trebbin, M.; Steinhauser, D.; Perlich, J.; Buffet, A.; Roth, S. V.; Zimmermann, W.; Thiele, J.; Förster, S. *Proc. Natl. Acad. Sci. U. S. A.* **2013**, *110*, 6706–6711.

(4)   Salipante, P. F.; Little, C. A. E.; Hudson, S. D. *Phys. Rev. Fluids* **2017**, *2*, 1–25.

(5)   Méndez-Sánchez, A. F.; Pérez-González, J.; de Vargas, L.; Castrejón-Pita, J. R.; Castrejón-Pita, A. A.; Huelsz, G. *J. Rheol. (N. Y. N. Y).* **2003**, *47*, 1455–1466.

(6)   Masselon, C.; Salmon, J. B.; Colin, A. *Phys. Rev. Lett.* **2008**, *100*, 1–4.

(7)   Masselon, C.; Colin, A.; Olmsted, P. D. *Phys. Rev. E* **2010**, *81*, 1–15.

(8)   Buscema, M.; Deyhle, H.; Pfohl, T.; Zumbuehl, A.; Müller, B. *Mater. Today Bio* **2019**, *1*, 100003.

(9)   Mair, R. W.; Callaghan, P. T. *J. Rheol. (N. Y. N. Y).* **1997**, *41*, 901–924.

(10)   Kato, M.; Shirakashi, M.; Takahashi, T. *Rheol. Acta* **2017**, *56*, 649–659.

(11)   Haward, S. J.; Kitajima, N.; Toda-Peters, K.; Takahashi, T.; Shen, A. Q. *Soft Matter* **2019**, *15*.

(12)   Kalb, A.; Villasmil-Urdaneta, L. A.; Cromer, M. *J. Nonnewton. Fluid Mech.* **2018**, *262*, 79–91.

(13)   Kalb, A.; Villasmil, U. L. A.; Cromer, M. *Phys. Rev. Fluids* **2017**, *2*, 1–10.

(14)   Pathak, J. A.; Hudson, S. D. *Macromolecules* **2006**, *39*, 8782–8792.

(15)   Haward, S. J.; McKinley, G. H. *Phys. Rev. E - Stat. Nonlinear, Soft Matter Phys.* **2012**, *85*, 1–14.

(16)   Zhao, Y.; Cheung, P.; Shen, A. Q. Microfluidic Flows of Wormlike Micellar Solutions. *Advances in Colloid and Interface Science*. 2014.

(17)   Bharati, A.; Hudson, S. D.; Weigandt, K. M. *Curr. Opin. Colloid Interface Sci.* **2019**, *42*, 137–146.

(18)   Rehage, H.; Wunderlich, I.; Hoffmann, H. Shear Induced Phase Transitions in Dilute Aqueous Surfactant Solutions. In *Polymers as Colloid Systems*; Springer, J., Ed.; Steinkopff: Darmstadt, 1985; pp 51–59.

(19)   Wunderlich, I.; Hoffmann, H.; Rehage, H. *Rheol. Acta* **1987**, *26*, 532–542.

(20)   Hu, Y.; Wang, S. Q.; Jamieson, A. M. *J. Rheol. (N. Y. N. Y).* **1993**, *37*, 531–546.

(21)   Castelletto, V.; Hamley, I. W. *Polym. Adv. Technol.* **2006**, *17*, 137–144.

(22)   Schmitt, V.; Schosseler, F.; Lequeux, F. *Epl* **1995**, *30*, 31–36.

(23)   Berret, J. F.; Gamez-Corrales, R.; Oberdisse, J.; Walker, L. M.; Lindner, P. *Europhys. Lett.* **1998**, *41*, 677–682.

(24)   Oda, R.; Weber, V.; Lindner, P.; Pine, D. J.; Mendes, E.; Schosseler, F. *Langmuir* **2000**, *16*, 4859–4863.

(25)   Truong, M. T.; Walker, L. M. *Langmuir* **2002**, *18*, 2024–2031.

(26)   Boltenhagen, P.; Hu, Y.; Matthys, E. F.; Pine, D. J. *Europhys. Lett.* **1997**, *38*, 389–394.

(27)   Ober, T. J.; Haward, S. J.; Pipe, C. J.; Soulages, J.; McKinley, G. H. *Rheol. Acta* **2013**, *52*, 529–546.

(28)   Haward, S. J.; Ober, T. J.; Oliveira, M. S. N.; Alves, M. A.; McKinley, G. H. *Soft Matter* **2012**, *8*, 536–555.

(29)   Dubash, N.; Cheung, P.; Shen, A. Q. *Soft Matter* **2012**, *8*, 5847–5856.

(30)   Penfold, N. J. W.; Parnell, A. J.; Molina, M.; Verstraete, P.; Smets, J.; Armes, S. P. *Langmuir* **2017**, *33*, 14425–14436.

(31)   Penfold, N. J. W.; Parnell, A. J.; Molina, M.; Verstraete, P.; Smets, J.; Armes, S. P. *Langmuir* **2017**, *33*, 14425–14436.

(32)   Pedersen, J. S. *J. Appl. Crystallogr.* **2000**, *33*, 637–640.

(33)   Warren, N. J.; Mykhaylyk, O. O.; Mahmood, D.; Ryan, A. J.; Armes, S. P. *J. Am. Chem. Soc.* **2014**, *136*, 1023–1033.

(34)   Hatton, F. L.; Derry, M. J.; Armes, S. P. *Polym. Chem.* **2020**, *11*, 6343–6355.

(35)   Chu, X.; Yang, J.; Liu, G.; Zhao, J. *Soft Matter* **2014**, *10*, 5568–5578.

(36)   Mykhaylyk, O. O.; Warren, N. J.; Parnell, A. J.; Pfeifer, G.; Laeuger, J. *J. Polym. Sci. Part B Polym. Phys.* **2016**, *54*, 2151–2170.

(37) Schnablegger, H.; Singh, Y. *The SAXS Guide*; Anton Paar: Austria, **2013**.

(38) Lovett, J. R.; Ratcliffe, L. P. D.; Warren, N. J.; Armes, S. P.; Smallridge, M. J.; Cracknell, R. B.; Saunders, B. R. *Macromolecules* **2016**, *49*, 2928–2941.

(39) Hatton, F. L.; Park, A. M.; Zhang, Y.; Fuchs, G. D.; Ober, C. K.; Armes, S. P. *Polym. Chem.* **2019**, *10*, 194–200.

(40) Penfold, N. J. W.; Ning, Y.; Verstraete, P.; Smets, J.; Armes, S. P. *Chem. Sci.* **2016**, *7*, 6894–6904.

(41) Ratcliffe, L. P. D.; Ryan, A. J.; Armes, S. P. *Macromolecules* **2013**, *46*, 769–777.

Chapter 4 – Designing and Fabricating Millifluidic Devices

4.1 Introduction

4.1.1 Fabrication Methods

The fabrication routes of micro- and millifluidic devices are wide-ranging and fall under two categories: top-down and bottom-up. Top-down fabrication methods work on the basis of removing material to form channels and other desired features, with common techniques consisting of nanofabrication, soft lithography and both wet and dry etching.[1–5] The advantages of top-down manufacturing include the possibility to mass-produce designs, a wide range of readily available, compatible materials and the ability to control the size and shape of large areas of a product.[6] However, there are many disadvantages to using top-down methods for micro- and millifluidic devices. Firstly, many of these technologies require several steps to produce a final product, which leads to long fabrication times and high costs. Secondly, the fabrication methods utilised necessitate specialist knowledge and equipment, such as cleanroom facilities, and thus the technology is only accessible to those with significant expertise and funding.

On the other hand, bottom-up fabrication is arguably more elegant since a structure is formed from 'building blocks' on the molecular or atomic scale. Techniques that fall under this category include additive manufacturing and chemical vapour deposition.[7–15] As is expected, there are also disadvantages and advantages to bottom-up techniques. For example, very few materials are currently available for bottom-up techniques – the majority of additive manufacturing methods only utilise polymeric materials.[16] However, current research in this area constantly yields new potential resources such as ceramics, metal and glass. Another disadvantage is that the mass production of devices fabricated by bottom-up approaches is currently not feasible due to the limitations in print bed sizes.[16]

Nevertheless, there are many advantages to utilising bottom-up techniques for the production of micro- and millifluidic devices. Firstly, the cost of fabrication is generally much lower than for top-down techniques.[17–20] Secondly, fabrication is easy and rapid,[18,20–22] with

novel geometries and components effortlessly incorporated into a build.[16] Thirdly, bottom-up approaches benefit from having very few fabrication steps, compared to top-down methodologies.[20,23,24] Clearly, both bottom-up and top-down fabrication methods have their benefits and drawbacks; however, for users new to the fabrication of micro- and millifluidic devices, the bottom-up approach of additive manufacturing is very attractive.

4.1.2   Additive Manufacturing

Additive manufacturing, or 3D printing, is a bottom-up technique which has received a lot of attention within the micro and millifluidic community over the last few years due to the ease and relatively low cost of producing channel-based devices. This fabrication method operates on the principle of separating the designed object into many consecutive layers, which are then built up in an additive way to form the final product. For example, a cube would be 'sliced' along one axis to form many square layers of a nominal thickness, each square would then be built sequentially to assemble the desired cube (**Figure (4.1)**). There are many techniques available for additive manufacturing, each with different methods to fabricate the desired object. The main types of 3D printing utilised for micro- and millifluidic fabrication are laser sintering, fused deposition modelling and stereolithography.
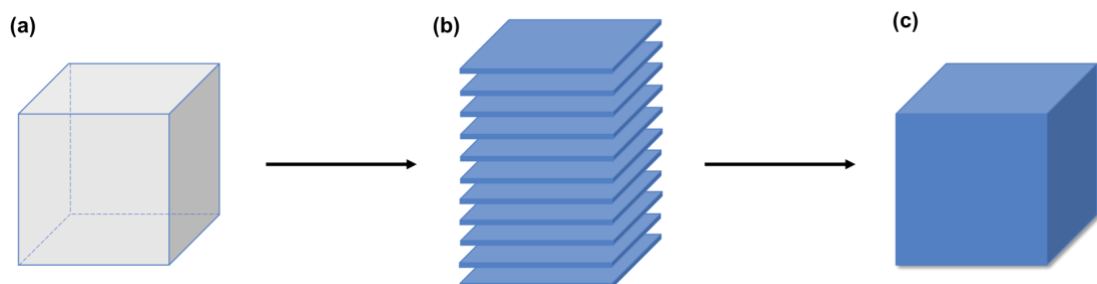

Figure (4.1). Process of additive manufacturing which takes **(a)** an object to be printed, often designed on computer software, and **(b)** simplifies this three-dimensional shape by producing individual layers before **(c)** these layers are bonded together during printing to produce a solid product.

4.1.2.1 Selective Laser Sintering

Selective laser sintering (SLS) was developed in the 1980s by Deckard and Beaman and uses a laser to melt powdered material to build a three-dimensional object (**Figure (4.2)**).[25,26] The laser sintering technique uses a material in its powdered form, which is heated to just below its melting point, while a CO_2 laser is used to 'draw' each layer (**Figure (4.2)(c)**).[27,28] When the laser comes into contact with the powdered material, a layer is formed as the particles are sintered together due to localised heating.[28,29] This process also allows bonding of the material to any previous layers that have been fabricated.[25] After the fabrication of each layer, the print bed moves down by a nominal amount, allowing space for fresh powder to be deposited and the succeeding layer to be printed. Once printing is complete, the unused powered material can easily be removed from channels and other features with compressed air or washing cycles – the presence of this unprocessed material acts as a support during fabrication, removing the need for a secondary, sacrificial material.[29] The material used in this technique is generally polymeric, such as nylon; however, research in this area has shown that metal-, ceramic- and glass-based powders are also suitable.[25,28,29] Depending on the type of printer used, SLS benefits from a layer thickness range of between 0.06 and 0.15 mm, allowing fine resolution prints to be produced.[27]
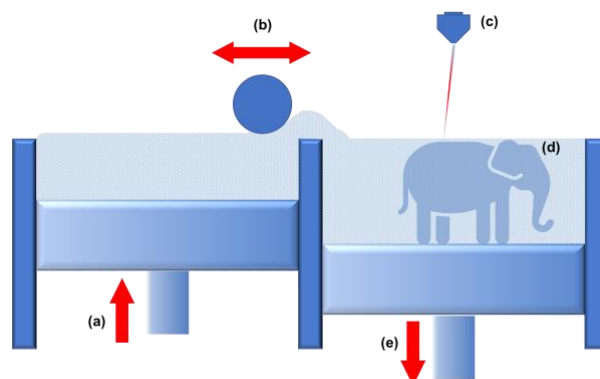
Figure (4.2). Diagram of the processes involved in selective laser sintering. **(a)** and **(b)** At the beginning of each layer, a thin coating of powder is deposited onto the print bed, **(c)** a CO_2 laser selectively targets areas where the build layer should be. **(d)** The heat from the laser causes the powder particles to melt slightly and sinter together, **(e)** once the layer is completed, the print bed moves down before the process is repeated.

Additionally, SLS is one of the fastest additive manufacturing techniques, lending itself to rapid prototyping of designs. Due to the materials that can be employed by SLS, the resulting parts often have excellent mechanical properties, including high strength and stiffness and good chemical resistance.[29] However, this additive manufacturing technique leads to printed parts with a porous surface which is often undesirable. This problem can be resolved by introducing post-processing steps such as lacquering or applying a metallic coating, although such additional processes can increase production time and overall costs.[28] Furthermore, SLS is often not used in commercially available printers due to the associated cost and potential danger associated with the high-powered laser used in this technique.

4.1.2.2 Fused Deposition Modelling

Fused deposition modelling (FDM) works by melting a thermoplastic filament while a nozzle deposits the materials in the required area (**Figure (4.3)(b)**).[30] The melted polymer then cools and solidifies; as this occurs, it bonds to the surrounding material. A nozzle, continuously moving along the print bed, leads to the application of an even thickness of
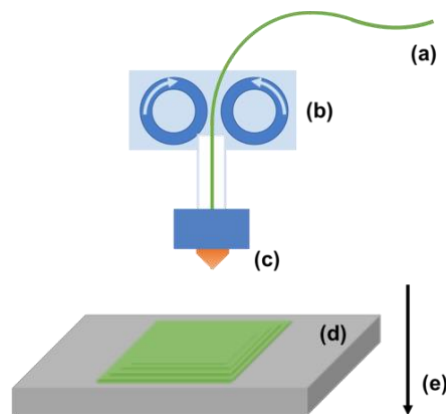
Figure (4.3). Schematic outlining the method of fused deposition modelling which occurs as follows: **(a)** a filament of thermoplastic polymer, **(b)** is fed into the printing nozzle by the use of two rollers. **(c)** The filament is then heated to its melting point as it is extruded through the nozzle, **(d)** and laid onto the print bed to form a layer of material. **(e)** Once the layer has been completed, the print bed moves down to allow for the process to be repeated for the next layer in the design.

material.[30–32] As the polymer is extruded onto the print bed, two rollers above the print head feed the filament spool into the nozzle, establishing a continuous source of printing material.[31] After a layer has been completed, the print bed lowers to allow the fabrication of the next layer.[31] Common materials utilised with FDM include polylactic acid (PLA), acrylonitrile butadiene styrene (ABS), polyethylene terephthalate (PET), polypropylene (PP) and polyurethane (PU). Research in this area is continuously uncovering other appropriate thermoplastic and composite materials.[31] Due to the broad range of materials available, properties of the final print can be easily tailored to the end-use.

Due to the technique of heat application in a localised area, and the deposition method, FDM is the cheapest of the three additive manufacturing methods frequently used for device fabrication. In addition, the set-up of FDM allows for the incorporation of a second material during printing, which can act as a sacrificial support material for finer builds. Despite this, FDM suffers from some downfalls such as the achievable layer thickness: at 0.1 – 0.33 mm for commercial printers, it is significantly thicker than either stereolithography or SLS. Another disadvantage of the technique is that the thermoplastics employed often suffer from inferior mechanical properties, leading to brittle prints.

4.1.2.3   Stereolithographic Printing

Stereolithographic (SLA) printing, was developed simultaneously by Hull,[33] Kodama,[34] and Le Mehaute, de Witte & André,[35] in the 1980s. The technique involves a reservoir of photopolymeric resin, or UV curable resin, which is cured by a laser at specific points to produce each layer of the final build (**Figure (4.4)(a)** and **(b)**).[36] The method of curing is generally via UV laser-initiated photochemical polymerisation of the liquid monomer.[37] For a build to be successful, this polymerisation reaction has to be fast and localised – this is achieved by controlling the power of the laser, scanning speed and exposure

time, as well as optimising the kinetics of the solidification process.[38] After each layer has been successfully formed, the print bed is slightly lifted to raise this layer away from the reservoir floor and allow for the succeeding layer to be produced.[39] Support materials are often included in the print to prevent deformation of the final device while printing occurs. After printing has finished, prints are washed to remove any excess, uncured, resin before the final curing step proceeds under UV light to harden the material before its intended use. Any supports that have been used in this process must then be removed, further increasing the number of post-processing steps required. SLA benefits from having the highest resolution of all commercially available additive manufacturing techniques, with layer thicknesses within a range of $0.01 - 0.15$ mm.[38] In order to achieve such fine resolution however, SLA is a much slower printing technique.
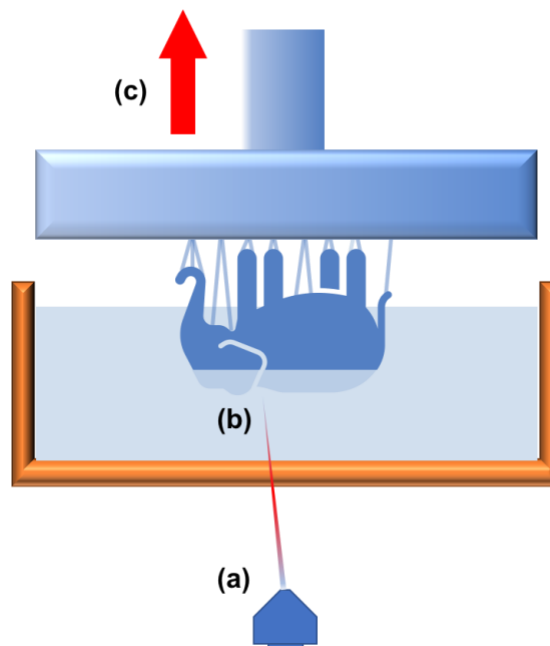
Figure (4.4). Stereolithography process where the print bed sits in a bath of photo-curable resin **(a)** and a UV laser shines through the resin, focusing on the area where hardened material is desired for the print **(b).** The light emitted initiates polymerisation of the surrounding resin, forming solid material onto the print bed **(c)**. After the laser has finished tracing a layer, the print bed raises out of the resin bath slightly, before the printing of the next layer begins. The thin blue lines in the figure, connecting the design to the print bed, represent supports included in the print.

Although there are advantages and disadvantages for each additive manufacturing technique discussed here, the final choice is dependent on the materials obtainable and their properties, the end-use of the fabricated design, the available funds and the required resolution of the final print. When choosing a fabrication method based on the end-use, it is essential to consider the materials that are compatible with that particular printing method and which mechanical and chemical properties are required. For instance, does the final device require chemical resistance against a particular solvent, or does the device need to be thermally resilient to allow temperature studies of a sample to be undertaken? When considering the resolution of the additive manufacturing techniques, it is ideal that this is lower than or equal to the smallest feature size present in the design. If the resolution is lower than the channel dimensions, the channels will be printed unsatisfactorily and will often contain blockages or poorly defined edges, thus reducing the capabilities of the device. Herein, a review of the commercially available 3D printing fabrication methods utilised within the field of millifluidic devices is undertaken.

4.1.3   3D Printing of Millifluidic Devices

Since millifluidics is a relatively new research area, relatively few papers have utilised additive manufacturing methods to fabricate these types of devices. **Table (4.1)** shows an overview of the majority of published work in this area to this date. A quick glance highlights the favourability of stereolithography within the research community, with all but two of these reports using this technique.

In 2012, Cronin *et al.*[18] published the earliest work combining additive manufacturing with millifluidics, utilising a serpentine-based straight channel to monitor organic, inorganic and metallic nanoparticle syntheses. With square channel sizes measuring 1 x 1 mm, this device is just within the millifluidic regime. Using FDM to produce an enclosed device from polypropylene, reactions were monitored using IR and UV/vis spectroscopy. However, this

device could be described as reasonably primitive since measurements could not be made *in situ*. Instead, aliquots were delivered to respective instruments via tubing secured to the device with epoxy adhesive. This shortcoming to the design was highlighted by the authors as an area of improvement.

Kong *et al.*[40] subsequently reported further use of additive manufacturing, fabricating two devices with channel dimensions of 0.05 x 0.05 mm and 1.15 x 1.15 mm, respectively, meaning that this work also straddles the boundary between micro- and millifluidic devices. An optically transparent device was fabricated using SLA to follow the DNA assembly pathway. The channels manufactured consisted of straight channels culminating in a T-junction to aid mixing. The final device consisted of three separate regimes: input, mixing and incubation. However, despite the elegance of the device, analysis was again performed *ex situ*.

In 2015, Cronin *et al.*[41] revisited millifluidics with a semi-transparent device, again fabricated with polypropylene using FDM. The designs utilised in this work take advantage of the possibilities of additive manufacturing; creating enclosed, visible channels in devices which could be joined together through simple connections. The channels consisted of two straight, rectangular channels which met at a T-junction to form liquid droplets in air. The channel dimensions were 0.8 x 1.2 mm, which, like Kong's work, straddles the boundary between micro- and millifluidics. The designs published in this paper also have an element of programmability with LEDs and sensors fitted within the print to facilitate *in situ* analysis of droplet generation. This is the latest published work using fused deposition modelling for the production of millifluidics.

Shor *et al.*[20] were the next to adopt 3D printed millifluidics in 2017, utilising a channel to study, and control, cell culturing. By using clear resin with SLA, an optically transparent device was fabricated which lent itself well to *in situ* measurements via optical and fluorescent microscopy. This research was a good proof-of-concept of how millifluidic devices can be
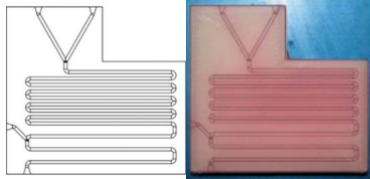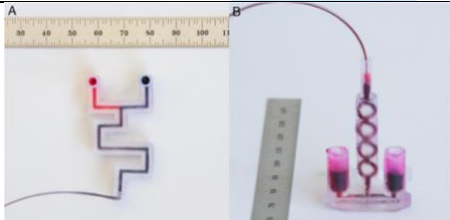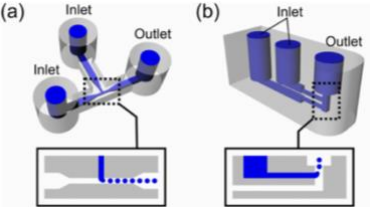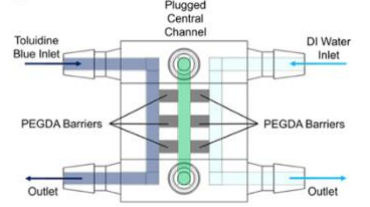
fabricated rapidly and inexpensively for a variety of research uses and measurement techniques.

In 2018, Park *et al.*[42] investigated the use of millifluidic devices to purify biological samples, successfully developing a methodology which was applicable to large sample volumes. They used SLA with clear resin to develop a millifluidic device consisting of a large chamber connected by two, offset channels. The channels serving the chamber were 2 x 2 mm while the chamber itself measured 5 x 2 mm. However, gel electrophoresis measurements investigating the purification efficiency were performed on samples after exiting the device, leaving room for improvement in this work.

2019 was an active year with six publications reporting additive manufactured millifluidic devices; all using SLA printing. The majority of these papers adopted clear resin for the devices. Firstly, Hashemi *et al.*[43] created a device with open channels which were sealed by the application of a PMMA sheet and secured in place with screws. This paper was the first to adopt Luer lock inlet and outlets. The channel design was a straight channel which culminated in a Y-junction, with dimensions of 1 x 1 mm. By incorporating electrodes either side of the channel, the work studied the separation of electrolysis products within the device, with oxidised products taking one exit pathway and reduced products taking the other. Optical microscopy and thermal conductivity were used to characterise these two distinct channels, and analysis was also performed on the products after they left the millifluidic device. This work illustrated the applicability of millifluidic devices in scientific research.
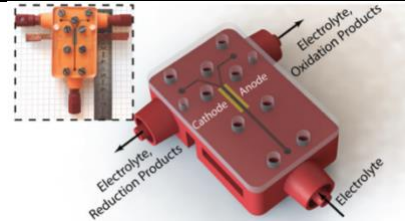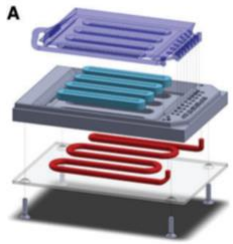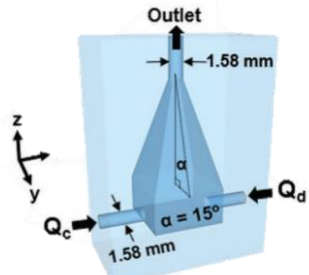
The second paper published in 2019 was from Datta *et al.*[44] who also fabricated an open channel device, which was sealed by the use of an acrylic plate. The channel consisted of a series of expansions and contractions measuring 4 mm in height, 2.4 mm at its widest and 0.8 mm at its narrowest. The reason for the bottlenecks was to study the deformation of hydrogel beads as a model system for oil recovery, filtration and microfluidic applications. Due to the optical transparency of the device, imaging was performed of the particles *in situ*,

Table (4.1). Overview of the use of additive manufacturing for millifluidic devices, including the type of 3D printing, the material used, the resulting channel dimension and the maximum volumetric flow rate (Q / ml min^{-1}) investigated. Images of the devices are also included

Ref. No.	Research Area	Year	3D Printing Method	Material	Channel Dimensions (W x H) / mm	Q / ml min^{-1}	Device
4	Chemistry	2012	FDM	Polypropylene	1 x 1	0.2	
26	Biological Engineering	2015	SLA	Clear resin	0.05 x 0.05 1.15 x 1.15	0.3	
31	Biological Engineering	2015	FDM	Polypropylene	0.8 x 1.2	2.8	
6	Chemical and Biomolecular Engineering	2017	SLA	Clear resin	2 x 2	0.1	

Ref. No.	Research Area	Year	3D Printing Method	Material	Channel Dimensions (W x H) / mm	Q / ml min^{-1}	Device
28	Mechanical Engineering	2018	SLA	Clear resin	5 x 2 2 x 2	10	
30	Chemical and Biological Engineering	2019	SLA	Clear resin	4 x 0.8 4 x 2.4	120	
32	Materials Science and Engineering	2019	SLA	Clear resin	Dia. 1.14	24	
33	Biological Engineering	2019	FDM	PDMS based	15 x 3.6	4.27	

Ref. No.	Research Area	Year	3D Printing Method	Material	Channel Dimensions (W x H) / mm	Q / ml min⁻¹	Device
29	Energy Environment Science	2019	SLA	*Not stated*	1 x 1	20	
34	Neuron regeneration	2019	SLA	Clear resin	63.5 x 10 x 5	6.3	
35	Chemical Engineering	2019	SLA	Clear resin	Funnel base: 10 x 18	4	

to study their pathway and behaviour throughout the channel.

The Cattaneo group[45] again utilised additive manufacturing to fabricate a range of connectors and reactor geometries in 2019. Unusually, circular channels with a diameter of 1.14 mm were adopted within which bimetallic nanoparticles with excellent size-control and well-defined composition were synthesised. Despite printing with a transparent resin, *in situ* measurements were not performed. UV/vis spectroscopy and optical imaging were performed after the synthesis had been performed, and the sample had left the millifluidic regimes.

Morizane *et al.* developed a 3D printer based on FDM techniques to produce a millifluidic device from a novel material incorporating polydimethylsiloxane (PDMS).[46] The custom-built printer enabled the device to be fabricated directly onto a glass slide, thereby ensuring a good seal between the print and the window. This device was utilised to study the effects of flow on cell culturing. With the channel measuring 15 mm wide and 3.6 mm high, this device is squarely in the millifluidic regime. Despite the novel printer developed during this work, the resolution of the print was very low (layer sizes of 0.4 mm), leading to a poor finish in the print, as can be seen in **Table (4.1)**. Moreover, the majority of the imaging and measurement techniques were carried out on the cells once they were removed from the millifluidic device, reducing its usefulness.

Kaslin *et al.*[47] also fabricated devices in 2019, using a clear resin on an SLA printer (ProJet 7000HD), sealed devices were achieved by securing PMMA sheets to the print. These devices were required to mount zebrafish larvae within channel bottlenecks in order to study the regeneration of spinal cord neurons. The measurements were undertaken via *in situ* optical and fluorescence imaging, as well as bioassays. The device utilised in this work was fairly complex, consisting of multiple assembled parts, but only the holder was fabricated using additive manufacturing techniques.

Finally, Kim *et al.* investigated the suitability of 3D printed devices for the production of monodisperse microdroplets.[48] This device incorporated a novel funnel shaped geometry to fabricate water droplets in hexadecane. Changing the dimensions of the funnel allowed the

resulting droplet size to be tailored. The formation of these droplets was followed by optical imaging, but the polydispersity was measured *ex situ* via optical microscopy. The use of 3D printing in this work allowed multiple geometries to be fabricated to fully understand the role of geometry on droplet generation.

In summary, the majority of the highlighted work utilised clear resin due to the desirable optical properties this material offers, allowing a transparent device to be fabricated. Fused deposition modelling has also been used, but only in the early stages of millifluidic devices and additive manufacturing.

Millifluidic devices have been used in a wide range of research areas from cellular biology to mechanical engineering, highlighting the universality of these sample environments. The majority have combined millifluidic devices with a range of microscopy and imaging techniques, as well as finite element analysis, immunoassays, UV and IR spectroscopy, which also emphasises the possible interconnectivity of 3D printed millifluidic devices. They have also adopted square or rectangular channels in the millifluidic devices opposed to circular channels. This is likely to be due to the ease of fabrication of square channels, giving a smoother finish than for circular objects. This is one of the downfalls of additive manufacturing; the smoothness of a print is limited by the step size, or resolution, of the printer and printing method adopted. If attaching windows to the print, square channels do, however, allow the continuation of the channel geometry.

4.1.4 Designing Millifluidic Devices

When micro- and millifluidic devices are fabricated through additive manufacturing techniques, they are first designed using computer-aided design (CAD) software. The most commonly used software includes Autodesk and SolidWorks, but a simple Google search for this type of programme will show that there are many to choose from, each with slightly different user interfaces and design features. CAD software also differs significantly in terms of whether it is

opensource or subscription based. With the latter, the cost of licenses varies from a couple of hundred pounds to a few thousand. However, there is a higher level of support available and a much more user-friendly layout with subscription software, which is beneficial to beginners. In this work, Autodesk Fusion 360 was utilised; a subscription-based piece of software that is freely accessible for academic users.

When using the CAD software to design and fabricate both micro- and millifluidic devices, it is necessary to first think of the intended applications of the final device as this will affect certain aspects of the design process. This will then produce a set of criteria that can be used as a device is designed to avoid unnecessary fabrications of many prototypes. The four main areas that could impact the design procedure are the final use of the micro- or millifluidic device, the volumetric flow rates utilised, whether the device will be single-use or reusable and whether the device will be micro- or millifluidic.

The final use of the fabricated device will impact a few areas of the design process. Firstly, depending on the type of analysis to be performed, particular windows or optical properties of the fabrication material might need to be utilised. For example, performing optical microscopy measurements would require either the use of a transparent fabrication material or the incorporation of suitable windows in the location where measurements are required. Secondly, depending on the flow material being studied, certain features may need to be added. These could include temperature control, flow geometry, sheathed flow, T-junctions or electrical components. Thirdly, it is also imperative to consider how the device would be incorporated into an instrument for ease of measurement. This might require features such as screw threads, for alignment or fastening within the instrument, to be assimilated into the design to reduce the number of necessary fabrication steps.

Another area that needs to be thoughtfully designed is the inlet and outlets ports exploited in the device. The chosen geometry of these parts is dependent on the volumetric flow rates and viscosities of the studied samples. For example, typical 'reservoir' inlets are suitable for low

volumetric flow rates and low viscosity solutions with minimal leakage observed. However, for faster volumetric flow rates and highly viscous samples, these types of inlets tend to fail and instead require inlets and outlets that seal the device more securely.

The lifetime of the device is a vital consideration when designing micro- and millifluidic system since this will dictate how complex the design could be and thus how many fabrication steps are required for its assembly. For instance, if the device is required to be hard-wearing and long-lasting, a more complex assembly with more fabrication steps would be acceptable. Designing a device that can readily be taken apart and cleaned, or with replacement parts would be beneficial to allow for the device to be used for days, weeks or years. However, if the device is likely to be single use, having an encapsulated design with very few fabrication steps is attractive as, in theory, a device can be manufactured and utilised within a short timeframe and with little hassle for the user.

The final aspect of the design that requires consideration is whether the device will be micro- or millifluidic, as this will impact the size of the channels. If a genuinely microfluidic device is desired, then the channel width and height need to be less than 1 millimetre. However, if a millifluidic device is preferred, then the channel dimensions can be larger than this.

The work presented in this chapter outlines how millifluidic devices can be designed, with their end-use in mind for studying viscous materials by SAXS. The devices were produced by three additive manufacturing methods: selective laser sintering; stereolithography and fused deposition. When designing the millifluidic devices, a simple straight channel geometry was utilised until a successful device was fabricated. These designs were initially printed using stereolithography before other additive manufacturing methods were investigated.

4.2 Experimental

4.2.1 Stereolithographic Printing (SLA)

All millifluidic devices were designed on CAD software (Autodesk Fusion 360, Autodesk). PreForm was used to prepare the design for 3D printing. In PreForm, the layer

thickness was set to 25 μm and supports were generated for all prints with a touchpoint size of 0.6 mm (radial diameter of support material connecting to the design). Millifluidic devices were fabricated using a Formlabs Form 2 SLA 3D printer, equipped with a standard clear photoreactive resin (a mixture of methacrylic acid esters and photo-initiators). After printing was completed, devices were washed for 20 minutes in isopropanol and dried with compressed air before being post-cured under UV light (405 nm) at 45 °C for a further 20 minutes. Supports were then removed from the devices, post-curing. Where necessary, the surface finish of the open channels was improved by lightly sanding with wet and dry paper, before undergoing a second wash and post-cure cycle.

4.2.2   Fused Deposition Modelling (FDM)

CAD designs for the millifluidic devices were prepared using Ultimaker Cura fabricated from the thermoplastic polymer; PLA, using the Ultimaker S5 printer from Ultimaker. Polyvinyl alcohol (PVA) was utilised as support material during the build. A 0.2 mm print head nozzle was used, giving a print resolution of 200 μm, due to the slight compression of the layer from the print head. After printing, the build was allowed to cool before removing it from the print bed. The device was then immersed in water to remove the support material.

4.2.3   Selective Laser Sintering (SLS)

Millifluidic devices that were fabricated using the SLS technique used the EOS Formiga P100, with a 30 W CO_2 laser. The material used was nylon-11, with a layer thickness in this print of 60 μm. Final prints needed excess powder to be removed by compressed air and were then cleaned in water or isopropanol.

4.2.4   Small-Angle X-ray Scattering (SAXS)

SAXS data was collected using a laboratory SAXS/WAXS instrument (Xeuss 2.0, Xenocs, France) equipped with a liquid gallium MetalJet X-ray source (Excillium, Sweden,

wavelength $\lambda = 0.134$ nm), two sets of motorised scatterless slits for beam collimation (0.6 x 0.5 mm) and a Dectris Pilatus 1M pixel SAXS detector (sample-to-detector distance 3.79 m). SAXS patterns were recorded over a q range of 0.003 nm^{-1} < q < 0.17 nm^{-1}, with $q = (4\pi \sin\theta)/\lambda$, where q is the length of the scattering vector and θ is one-half of the scattering angle. Scattering patterns were acquired for 300 seconds.

4.2.5 Differential Scanning Calorimetry (DSC)

DSC studies were performed using a TA Instruments Discovery DSC instrument equipped with TZero low-mass aluminium pans. Nylon discs, printed by SLS, were equilibrated at 40 °C for 5 minutes before the following thermal cycles were performed; 40 – -90 °C (with a cooling ramp rate of 30 °C min^{-1}), -90 – 250 °C (heating ramp rate of 40 °C min^{-1}) and 250 – 25 °C (cooling ramp rate of 30 °C min^{-1}).

4.2.6 Temperature Bonding Experiments

A dual-sided hot press was used to investigate window bonded to selective laser sintered prints. The hot press was equipped with a digital temperature controller. Experiments were performed with SLS prints sandwiched between two glass microscope slides at one of four set temperatures (40, 48, 173 or 180 °C), 5 tons of pressure were applied for either 1, 2 or 5 minutes before allowing the sandwich to cool.

4.3 Results and Discussion

There were four essential design criteria for the devices that had to be fulfilled. These were that the device would be (i) transparent for X-rays and therefore suitable for SAXS measurements, (ii) appropriate for the study of highly viscous polymeric materials, (iii) easy to assemble, with little specialist knowledge required and (iv) be millifluidic, rather than microfluidic. Initial

designs employed a straight channel geometry to find a successful design base, before moving on to more complex geometries. A few avenues for a millifluidic device that attempted to fulfil the four criteria, as described above, were investigated before an appropriate design evolved.

4.3.1 Prototype One

The initial design consisted of an insert-based device where a flat channel bed was fabricated and then sandwiched between Kapton® windows, with the aid of double-sided tape in a post-processing step. Inlets resembled the reservoir-based inlets often utilised in microfluidics. A representative CAD design of this device can be seen in **Figure (4.5)**.
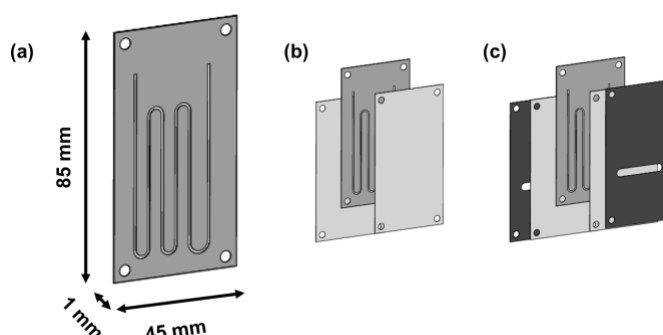

Figure (4.5). (a) The first straight channel prototype fabricated had channels which measured 1 mm wide and 1 mm high. **(b)** Kapton® windows which were 0.076 mm thick were attached over the entire device. **(c)** Improvements to the device included the incorporation of a metal frame.

Much of the first prototype was based on relevant literature surrounding micro- and millifluidic devices.[4,30,32–35] However, it was found that these devices were not appropriate for use with viscous polymeric materials due to the pressure required to generate flow. The failure of the insert-based devices was due to two main reasons. Firstly, the window material did not provide a sufficient seal to the insert, leading to sample leakage. Secondly, the inlets and outlets incorporated into the device were not appropriate for viscous materials. Accordingly, attempts to improve this device were undertaken.

Kapton®, a polyimide film, was initially chosen as window material, due to its well-known minimal X-ray scattering.[49] However, the flexibility of the thin film material lead to deformation of the windows when a viscous material was flowing. This distortion ultimately resulted in the windows becoming detached from the insert, causing the sample to leak out of the channel. Improvements to the seal between window and print were investigated and a metal supporting frame was incorporated to encase the device (**Figure (4.5)(c)**). The aim of this was to restrict the movement, or warping, of the Kapton® under high pressures from the fluid in channel. However, it was found that this provided little improvement to the device and a significant amount of leakage was observed even when the metal frame was present.

The inlet ports incorporated into the first design were simple conduit reservoirs connecting the external space to the inner channel, where the inlet was larger than the channel it was feeding into. This design was based on the inlets utilised in microfluidic technology,[4,30,32–35] However, it was found that the connection led to a large amount of leakage, especially with viscous materials. This was due to a build-up in pressure when entering the constricted channel. To alleviate this issue, a better seal between the channel and tubing was investigated. Many different improvements to the inlets were attempted. These included the use of magnets to hold the tubing in place against the reservoir inlet, using epoxy resin and needles to provide a secure connection between tubing and channel, and attaching the tubing directly into the channel geometry. However, these changes did not improve the delivery of fluid into the channel. Any improvements to this design were deemed ineffectual, therefore, the design itself was altered in an attempt to enhance the capability of the millifluidic device.

4.3.2   Prototype Two

Due to the failures of the initial prototype, the design was modified to incorporate Luer slips. The representative CAD design can be seen in **Figure (4.6)**. As the inlets in the first device

were poor at delivering a fluid sample into the channels, it was proposed that these inlets would offer an improvement. It was found that the Luer slips provided a good seal between the tubing and the channels, resulting in no sample leakage. The integration of these inlets led to a significant enhancement compared to the initial design.

Despite the benefits of the Luer slips in the device, it was found that the incorporation of these inlets made the prints extremely brittle. The prints often snapped or shattered around the inlets when a small amount of force was applied to attach the tubing. Breakages often occurred when windows were being attached or removed, or when female Luer connectors were being attached. This problem was inherent to the design and as such, no attempts to improve this aspect of the printed device were undertaken. However, this meant that most devices were single-use and thus it did not fulfil the criteria set out at the beginning of the project.
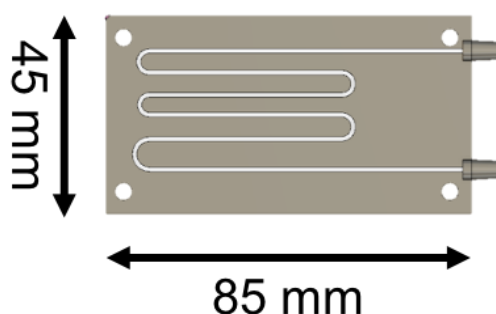

Figure (4.6). CAD design of prototype 2, with Luer slip inlets incorporated into the print.

As the main design of the device had minimal changes, issues with the sealing of the window were still encountered. It was deemed that Kapton® tape, or film, was not sufficient in creating a good seal to the print. At this point, a few solutions to this issue were tested in an attempt to improve the device. As well as different window materials, various sealing methods were investigated.

A secondary window material comprising laminating film (a base of polyethylene terephthalate with ethylene-vinyl acetate as an adhesive) was thermally bonded to the printed

insert. This material was found to have strong bonding properties to the cured resin device, with little leakage or deformation of the window layer observed during flow experiments. As such, it was a more suitable window material than Kapton® due to its superior sealing properties. However, it was found to exhibit strong X-ray scattering in the small-angle region (**Figure (4.7)**), rendering this window material impractical for the intended use of the design.
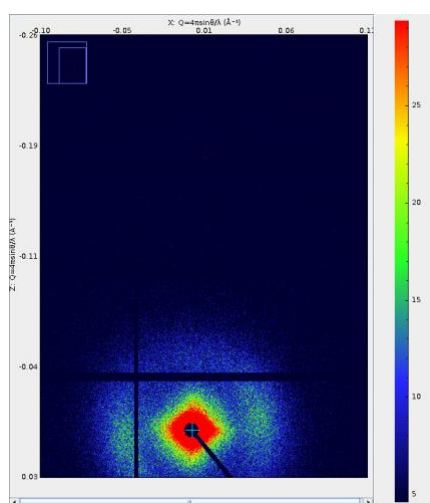

Figure (4.7). 2D SAXS pattern of a channel in the millifluidic device with the laminating film (consisting of polyethylene terephthalate and ethylene-vinyl acetate) attached, showing the strong anisotropic scattering from the windows.

4.3.3   Prototype Three

The third prototype investigated can be seen in **Figure (4.8)**. This design had been altered slightly to include Luer locks instead of Luer slips in an attempt to reduce the brittleness previously observed. The Luer locks were found to provide an enhanced connection between tubing and channel compared to the simple Luer slips, as the connectors were fastened to the inlets by the use of a threaded surface.

The number of screw ports present across the device was also changed in this design. By incorporating more screw ports, it was hoped that the window seal to the channel could be improved, as this would allow for the pressure of the screws to be spread more fully across the

whole of the window material against the print. However, it was found that these screw ports did little to improve the seal of the window and did not reduce the amount of leakage observed.
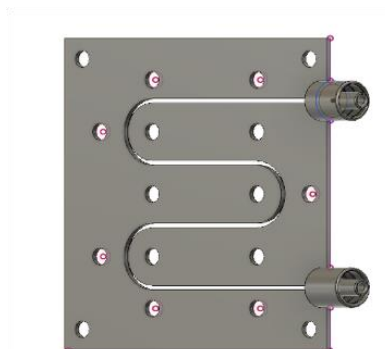

Figure (4.8). CAD image of the third prototype investigated. This prototype had Luer locks and many screw ports.

As well as the attempted improvements previously discussed, a flexible gasket was printed via SLA. The purpose of this flexible gasket was to enhance the sealing of the windows to the device. The gasket was placed between the window and the metal support to apply pressure between the windows and print. However, this attempt was found to be ineffectual in increasing the seal of the device, and fluid still leaked freely out of the channels.

4.3.3.1 Improvements to Window Bonding

Due to the multiple failures of the devices printed by stereolithographic printing, another printing method was investigated: SLS. SLS was chosen due to its ability to utilise non-commercial materials, allowing the surface chemistry of prints to be tailored for specific uses. This was advantageous as it allowed different window bonding methods to be investigated. Namely, temperature and solvent bonding were desirable as these were often utilised in the literature[1,5,17,50–52] and were recognised as imparting a reliable seal between a window and channel. Devices printed by this method were fabricated using nylon-11, a polymer with well-understood surface chemistry.
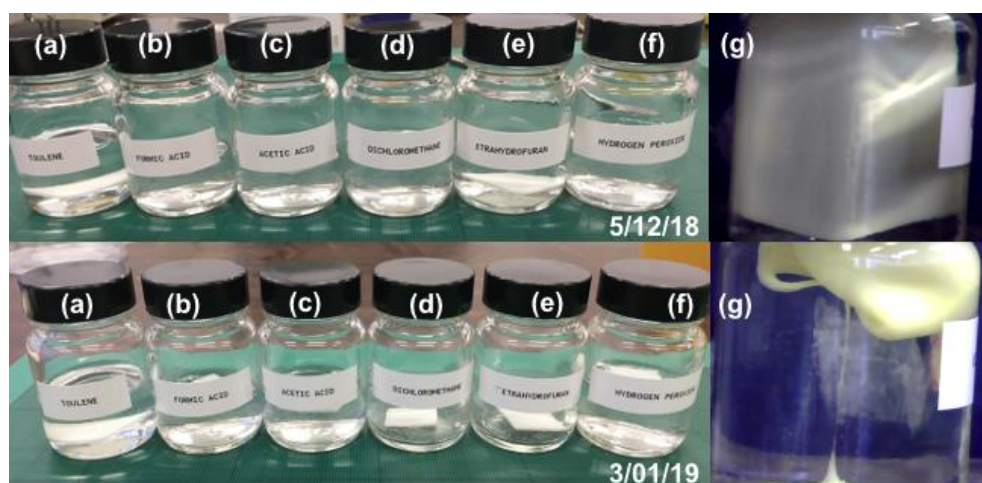
Figure (4.9). Solubility study of the SLS nylon print immersed in a range of solvents and left for 30 days. Solvents tested were **(a)** toluene, **(b)** formic acid, **(c)** acetic acid, **(d)** dichloromethane, **(e)** tetrahydrofuran, **(f)** hydrogen peroxide and **(g)** nitric acid. The nitric acid images were taken one hour after each other.

In order to bond windows to the device fabricated by SLS, a common solvent was required for both window and print materials. This solvent had to dissolve the surface of both materials, to form physicochemical bonds between them, thus ensuring a good seal in the device. To find a common solvent, sections of the SLS print were immersed in a range of solvents (**Figure (4.9)**). Of the seven solvents investigated, it was found that only concentrated nitric acid (68 %) dissolved the print. However, the immersion of the print led to a complete distortion of the dimensions. As such, nitric acid was deemed unsuitable as a common solvent. Thus, solvent bonding methods were not investigated further.

In order to temperature bond a window material to the nylon print, the thermoplastic print must be heated to a temperature close to either its glass transition temperature, T_g, or melting point, T_m. When the material has been heated to a sufficient temperature, pressure can be applied to the window material and print to ensure an adequate bond is made between the two layers. Differential scanning calorimetry (DSC) was used to determine the T_g (44 °C) and T_m (178 °C) of the print, **Figure (4.10)**. In order to test the applicability of temperature bonding, model channels were fabricated using a 5 mm hole punch in a small square of nylon. Next, the print was heated

to various temperatures around the T_g or T_m of the polymer before either 1, 2 or 5 tons of pressure was applied to a sandwich of glass slides and polymer for either 1 or 5 minutes, using a hot press.
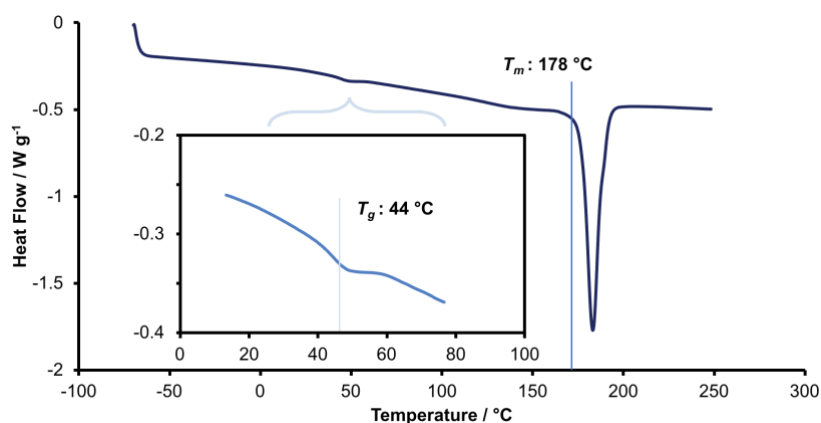

Figure (4.10). DSC data for SLS-printed nylon-11. The data show a clear melting point (T_m) peak at 178 ºC. The insert shows the expanded region of 0 – 100 ºC, with the presence of a slight peak at 44 ºC corresponding to the glass transition temperature (T_g).

A few issues were encountered during this procedure. Firstly, the instrument used had poor temperature control, and the placement of the print on the hot press plate provided variable results. Prints placed at the centre of the plates were heated to a higher temperature than those at the edge of the plate. Furthermore, the temperature of the plates was always lower than the set temperature of the hot press. This led to bonding tests which were not repeatable due to the fluctuations in temperature.

Secondly, for successful temperature bonding to occur, two thermoplastic materials are required with similar T_g values. This is not the case here since glass is not a polymeric material and thus it is difficult to create an effective bond between the glass and nylon print. When a temperature close to the T_g of nylon was used, no bond was formed between the glass and the print. However, it was found that by heating to well above T_m (200 ºC) and applying 5 tons of pressure for 5 minutes, a sufficient, strong bond was formed, which had the added benefit of lasting for a long time (over a year), see **Figure (4.11)(a)**.
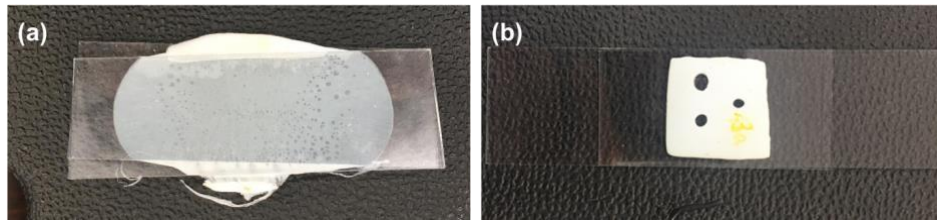
Figure (4.11). (a) Resulting bond when the glass-print-glass sandwich is pressed with 5 tons of force at 200 ℃, well above its melting point. **(b)** Experiments performed around the melting point of the nylon print lost the definition of the 'channel', this can be seen in the above image. Conditions for this experiment were 183 ℃, 2.5 tons of pressure for 5 minutes.

Thirdly, it was observed that the process of heating to the print's melting point and applying pressure led to a loss in the 'channel' definition, and in some cases the 'channel' disappeared completely (**Figure (4.11)(b)**). This was disadvantageous as, without the channel, there is no millifluidic device. However, heating to temperatures much lower than the melting point resulted in no bond formation between the glass and the print. Overall, these issues meant that the temperature bonding method was not suitable for the millifluidic devices fabricated by SLS.

4.3.4 Prototype Four

After these experiments with prototype designs, it was concluded that an insert-based device printed by stereolithography would not be appropriate for the reasons discussed above. Therefore, the design was modified to consist of an enclosed channel, with window ports secured by a 3D printed screw (**Figure (4.12)(a)** and **(b)**). The inlets incorporated the successful Luer locks from previous prototypes which provided a tight seal between the channel and the tubing (**Figure (4.12)(c)**). The benefits of this sort of design were numerous. Firstly, the enclosed channel would be leak-proof and robust. With the majority of the channel enclosed, the millifluidic device is suitable for viscous fluids as there is less opportunity for the leaking to occur. This is also reinforced by the presence of a single, small window area which reduces the likelihood of window bowing from pressure build-up at Q values up to 54 ml/min. Secondly, this small window area also increases the variety of window materials available to test due to the reduced

surface area where coverage is required. Thirdly, the threaded window port allows for a window to be securely placed by the use of a 3D-printed screw and an O-ring, this further increases the effectiveness of the device.

The new millifluidic design fulfils all the criteria initially set out; the window material can be tailored for a specific use, in this case SAXS studies. The enclosed channel allows for viscous polymeric materials to be studied and the fabrication method is simple, cheap and produces a reusable millifluidic device.
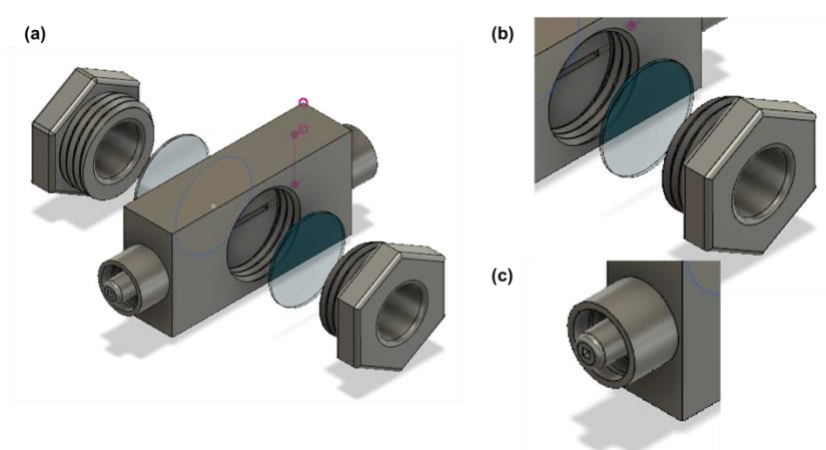
Figure (4.12). (a) CAD rendering of the fourth, and final, prototype developed. This prototype utilised enclosed channels with **(b)** a small, threaded window port and accompanying 3D-printed screw. **(c)** Luer lock inlets are used to provide a sealed conduit from tubing to channel.

As previously stated, the design of the millifluidic device allowed the window material to be tailored to the specific need of the user. In this case, for a window that was transparent to X-rays for SAXS measurements, there were a few window materials available. One material is Kapton®; this material was used extensively in the previous prototypes but was found to be unsuitable due to distortion under pressure. However, due to the smaller window size of prototype 4, and more secure mounting, it was found that Kapton® was moderately successful in sealing the device. An added benefit of this window material is that it is transparent, allowing for *in situ* optical measurements in addition to SAXS analysis.

Other appropriate window materials included borosilicate glass, mica and polyetherimide (PEI). These three materials benefit from being less flexible than the previously tested Kapton® film and so were less likely to distort under the flow pressure. Measurements using borosilicate glass (diameter of 15 mm, thickness of 0.15 mm) found that this material was too brittle to be a successful window. For a window to be successful, it needs to be pressed against the surface of the print, requiring the screw to be fastened tightly which, in turn, allows for the O-ring to press onto the window and form a seal. However, when the borosilicate glass was used, the pressure from the screw and O-ring caused the glass to fracture across the window disc. After these preliminary measurements, the borosilicate glass was proven to be an unsuitable window material.

The next potential window material tested was mica, which has very minimal X-ray scattering in the small-angle region.[53] This material was found to be more suitable than either the borosilicate glass or Kapton® and could withstand much higher volumetric flow rates and pressures from more viscous samples, with little distortion or leakage observed. These windows did not fail with water at any volumetric flow rate within the limits of the syringe pump (up to 54 ml/min). Since these mica windows were transparent and colourless, they were suitable for optical measurements, such as microscopy, as well as SAXS.

In conclusion, both mica and Kapton® discs were found to be suitable window materials due to their relatively low X-ray scattering in the small-angle region and the ability to contain fluid samples in the channel geometries. Therefore, these windows were utilised throughout the rest of the work.

Efforts taken to print millifluidic devices using fused deposition modelling were unsuccessful (**Figure (4.13)(b)**). Delamination of layers was observed in the final print, resulting in a product which was unusable. The same result was seen whether supporting material was utilised or not. This is thought to be due to the presence of overhanging material in the design, especially surrounding the inlets of the device which is where the print often failed. The weight
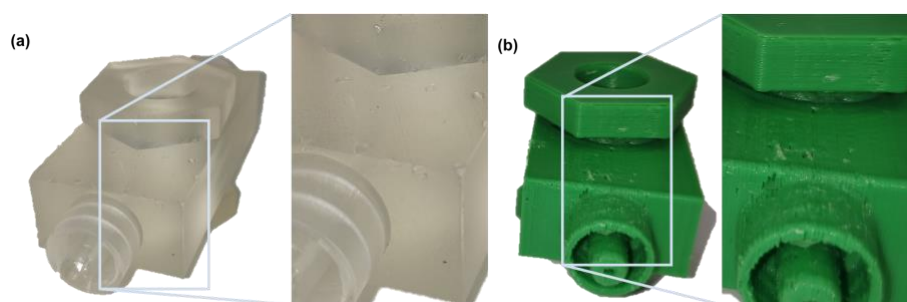
Figure (4.13). Images of the millifluidic device printed by **(a)** stereolithography and **(b)** fused deposition modelling. The print produced by SLA shows a print with a smooth surface finish whereas the FDM printed device has many defects and the layers of the print can clearly be seen (insert shows magnified image for clarity).

of the molten polymer was too much to be supported in place during printing. As well as this, the resolution of the FDM printer was less fine than for SLA, which led to a much rougher print. However, better results may be found if a finer extruder head was utilised. This would lower the height of each layer, thereby possibly producing a much smoother print. Yet, these defects were not observed in the devices fabricated by SLA (**Figure (4.13)(a)**), suggesting this is a more appropriate technique for the production of millifluidic devices.

4.4 Conclusions

A set of criteria was outlined as a benchmark for a successful device. These criteria were that the device should occupy the millifluidic range, should be suitable for SAXS measurements, be appropriate for the study of viscous polymeric fluids, and be reusable, easy to assemble and straightforward to use for novice users.

A variety of prototypes were examined before a suitable millifluidic device was designed and fabricated. The initial designs were insert-based, where a print was sandwiched between two sheets of window material to give a final device. It was found that these simple designs were not suitable for sealing viscous polymer samples as copious amounts of leaking was present. The leakage observed was due to the inefficient sealing of the windows to the print. Attempts to

improve this by changing the window material, adding supports and changing the bonding method all proved inadequate.

Another downfall of these early devices was the inlets utilised. Initial inlets were simple reservoir-type inlets often used in the literature. These have been shown to be successful for low viscosity samples, but, were found to be impractical for viscous polymer solutions. In this case, the reservoir inlets were poor conduits from the tubing to the channel and did not prevent sample leakage. Finally, these initial devices suffered from being very brittle and often shattered during assembly. This downfall meant the prints had a very short lifetime and were not suitable for novice users.

However, a successful prototype was designed and fabricated, which fulfilled the aims set out at the beginning of the work. This device comprised enclosed channels which was vital for studying viscous polymer materials and providing a reinforced device, necessary for a reusable device. The print also incorporated a small window port with a threaded screw to allow for the installation of windows suitable for SAXS measurements that could be held securely in place. Finally, the device used Luer locks as inlets which provided a sealed conduit for fluids to travel from tubing to channel. These were all essential components of the millifluidic device.

Attempts to produce the device by fused deposition modelling were unsuccessful, primarily due to the smaller layer resolution afforded by this technique. During printing, many defects were introduced, and the surface finish was very rough, compared to devices printed by SLA. Therefore, to produce a successful millifluidic device by additive manufacturing, stereolithographic printing with a small layer resolution (or a technique with comparable resolution) is required.

4.5 References

(1)   Gale, B.; Jafek, A.; Lambert, C.; Goenner, B.; Moghimifam, H.; Nze, U.; Kamarapu, S. *Inventions* **2018**, *3*, 60–85.
(2)   Bhattacharjee, N.; Urrios, A.; Kang, S.; Folch, A. *Lab Chip* **2016**, *16*, 1720–1742.

(3)   Ren, K.; Zhou, J.; Wu, H. *Acc. Chem. Res.* **2013**, *46*, 2396–2406.

(4)   Nguyen, N.-T.; Wereley, S. T.; House, A. *Fundamentals and Applications of Microfluidics - Second Edition*; **2002**.

(5)   Tsao, C.-W.; DeVoe, D. L. *Microfluid. Nanofluidics* **2009**, *6*, 1–16.

(6)   Mijatovic, D.; Eijkel, J. C. T.; van den Berg, A. *Lab Chip* **2005**, *5*, 492–500.

(7)   Peng, F.; Månsson, L. K.; Holm, S. H.; Ghosh, S.; Carlström, G.; Crassous, J. J.; Schurtenberger, P.; Tegenfeldt, J. O. *J. Phys. Chem. B* **2019**, *123*, 9260–9271.

(8)   Cui, Y. *Science (80-.).* **2001**, *291*, 851–853.

(9)   Zhou, C.; Chen, Y.; Yang, Z.; Khoshnevis, B. *Rapid Prototyp. J.* **2013**, *19*, 153–165.

(10)   Zheng, X.; Deotte, J.; Alonso, M. P.; Farquar, G. R.; Weisgraber, T. H.; Gemberling, S.; Lee, H.; Fang, N.; Spadaccini, C. M. *Rev. Sci. Instrum.* **2012**, *83*, 1–6.

(11)   Guijarro, N.; Prévot, M. S.; Yu, X.; Jeanbourquin, X. A.; Bornoz, P.; Bourée, W.; Johnson, M.; Le Formal, F.; Sivula, K. *Adv. Energy Mater.* **2016**, *6*, 1–13.

(12)   Song, X.; Chen, Y.; Lee, T. W.; Wu, S.; Cheng, L. *J. Manuf. Process.* **2015**, *20*, 456–464.

(13)   Song, X.; Chen, Z.; Lei, L.; Shung, K.; Zhou, Q.; Chen, Y. *Rapid Prototyp. J.* **2017**, *23*, 44–53.

(14)   Wu, X.; Lian, Q.; Li, D.; Jin, Z. *J. Mater. Process. Technol.* **2017**, *243*, 184–196.

(15)   Nakano, T.; Ishimoto, T. *KONA Powder Part. J.* **2015**, *32*, 75–84.

(16)   Cocovi-Solberg, D. J.; Worsfold, P. J.; Miró, M. *TrAC Trends Anal. Chem.* **2018**, *108*, 13–22.

(17)   Beauchamp, M. J.; Nordin, G. P.; Woolley, A. T. *Anal. Bioanal. Chem.* **2017**, *409*, 4311–4319.

(18)   Kitson, P. J.; Rosnes, M. H.; Sans, V.; Dragone, V.; Cronin, L. *Lab Chip* **2012**, *12*, 3267–3271.

(19)   Shallan, A. I.; Smejkal, P.; Corban, M.; Guijt, R. M.; Breadmore, M. C. *Anal. Chem.* **2014**, *86*, 3124–3130.

(20)   Kadilak, A. L.; Rehaag, J. C.; Harrington, C. A.; Shor, L. M. *Biomicrofluidics* **2017**, *11*, 1–16.

(21)   Zhang, J. M.; Ji, Q.; Liu, Y.; Huang, J.; Duan, H. *Lab Chip* **2018**, *18*, 3393–3404.

(22)   Chen, Q. L.; Liu, Z.; Shum, H. C. *Biomicrofluidics* **2014**, *8*, 1–12.

(23)   Fuad, N. M.; Carve, M.; Kaslin, J.; Wlodkowic, D. *Micromachines* **2018**, *9*, 1–11.

(24)   Fuad, N. M.; Zhu, F.; Kaslin, J.; Wlodkowic, D. *SPIE BioPhotonics Australas.* **2016**, *10013*, 1–6.

(25)   Simchi, A. *Mater. Sci. Eng. A* **2006**, *428*, 148–158.

(26)   Deckard, C. R.; Beaman, J. J.; Darrah, J. F. Method and Apparatus for Producing Parts by Selective Sintering. 4863538, **1992**.

(27)   Kruth, J. P.; Mercelis, P.; Van Vaerenbergh, J.; Froyen, L.; Rombouts, M. *Rapid Prototyp. J.* **2005**, *11*, 26–36.

(28)   Kumar, S. *J. Miner. Met. Mater. Soc.* **2003**, *55*, 43–47.

(29)   Goodridge, R. D.; Tuck, C. J.; Hague, R. J. M. *Prog. Mater. Sci.* **2012**, *57*, 229–267.

(30)   Ning, F.; Cong, W.; Qiu, J.; Wei, J.; Wang, S. *Compos. Part B Eng.* **2015**, *80*, 369–378.

(31)   Zein, I.; Hutmacher, D. W.; Tan, K. C.; Teoh, S. H. *Biomaterials* **2002**, *23*, 1169–1185.

(32)   Ferraro, G. A.; Corcione, A.; Nicoletti, G.; Rossano, F.; Perrotta, A.; D'Andrea, F. *Aesthetic Plast. Surg.* **2005**, *29*, 181–183.

(33)   Gabriel, S.; Hull, C. W. Apparatus for Production of Three-Dimensonal Objects By Stereolithography. 4575330, **1984**.

(34)   Kodama, H. *Rev. Sci. Instrum.* **1981**, *52*, 1770–1773.

(35)   Andre, J.-C.; Le Mehaute, A.; De Witte, O. Dispositif Pour Realiser Un Module de Piece Industrielle. 2567668, **1984**.

(36)   Sun, C.; Fang, N.; Wu, D. M.; Zhang, X. *Sensors Actuators, A Phys.* **2005**, *121*, 113–120.

(37)   Griffith, M. I.; Halloran, J. W. *J. Am. Ceram. Soc.* **1996**, *79*, 2601–2608.

(38)   Melchels, F.; Feijen, J.; Grijpma, D. *Biomaterials* **2010**, *31*, 6121–6130.

(39)   D'Urso, P. S.; Effeney, D. J.; Earwaker, W. J.; Barker, T. M.; Redmond, M. J.; Thompson, R. G.; Tomlinson, F. H. *Br. J. Plast. Surg.* **2000**, *53*, 200–204.

(40)   Patrick, W. G.; Nielsen, A. A. K.; Keating, S. J.; Levy, T. J.; Wang, C. W.; Rivera, J. J.; Mondragón-Palomino, O.; Carr, P. A.; Voigt, C. A.; Oxman, N.; et al. *PLoS One* **2015**, *10*, 1–18.

(41)   Tsuda, S.; Jaffery, H.; Doran, D.; Hezwani, M.; Robbins, P. J.; Yoshida, M.; Cronin, L. *PLoS One* **2015**, *10*, 1–13.

(42)   Kim, Y.; Lee, J.; Park, S. *Micromachines* **2018**, *9*, 472–484.

(43)   H. Hashemi, S. M.; Karnakov, P.; Hadikhani, P.; Chinello, E.; Litvinov, S.; Moser, C.; Koumoutsakos, P.; Psaltis, D. *Energy Environ. Sci.* **2019**, *12*, 1592–1604.

(44)   O'Connell, M. G.; Lu, N. B.; Browne, C. A.; Datta, S. S. *Soft Matter* **2019**, *15*, 3620–3626.

(45)   Cattaneo, S.; Althahban, S.; Freakley, S. J.; Sankar, M.; Davies, T.; He, Q.; Dimitratos, N.; Kiely, C. J.; Hutchings, G. J. *Nanoscale* **2019**, *11*, 8247–8259.

(46)   Homan, K. A.; Gupta, N.; Kroll, K. T.; Kolesky, D. B.; Skylar-Scott, M.; Miyoshi, T.; Mau, D.; Valerius, M. T.; Ferrante, T.; Bonventre, J. V.; et al. *Nat. Methods* **2019**, *16*, 255–262.

(47)   Friedrich, T.; Douek, A. M.; Vandestadt, C.; Wlodkowic, D.; Kaslin, J. *Zebrafish* **2019**, *16*, 37–46.

(48)   Hwang, Y. H.; Um, T.; Hong, J.; Ahn, G. N.; Qiao, J.; Kang, I. S.; Qi, L.; Lee, H.; Kim, D. P. *Adv. Mater. Technol.* **2019**, *4*, 1–9.

(49)   Barrett, R.; Faucon, M.; Lopez, J.; Cristobal, G.; Destremaut, F.; Dodge, A.; Guillot, P.; Laval, P.; Masselon, C.; Salmon, J.-B. *Lab Chip* **2006**, *6*, 494.

(50)   Lange, T.; Charton, S.; Bizien, T.; Testard, F.; Malloggi, F. *Lab Chip* **2020**, *20*, 2990–3000.

(51)   Ghazal, A.; Gontsarik, M.; Kutter, J. P.; Lafleur, J. P.; Ahmadvand, D.; Labrador, A.; Salentinig, S.; Yaghmur, A. *J. Phys. Chem. Lett.* **2017**, *8*, 73–79.

(52)   Cao, Z.; Wu, Z.; Sundén, B. *Chem. Eng. J.* **2018**, *344*, 604–615.

(53)   Bretagne, A.; Cotot, F.; Arnaud-Roux, M.; Sztucki, M.; Cabane, B.; Galey, J. B. *Soft Matter* **2017**, *13*, 3812–3821.

Chapter 5 – Straight Channel Millifluidics

5.1 Introduction

The straight channel geometry is the most commonly used channel geometry in millifluidics: a device with a straight channel geometry has either a square or circular cross-section which is of a constant dimension throughout the length of the channel. The pathway of the channel is not restricted; a millifluidic channel based on this geometry can be serpentine-like, with turns in the channel, or can have a simple straight-through path (**Figure (5.1)**). The geometry has been utilised for a range of applications including chemical synthesis,[1,2] emulsion formation[3,4] as well as the characterisation,[5–14] and manipulation of soft condensed matter systems.[9,15–20]
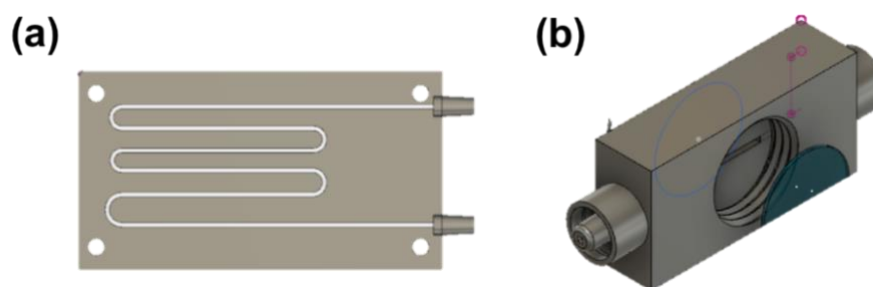

Figure (5.1).(a) A typical serpentine channel where the channel has a series of curves to connect the inlet and outlet. **(b)** A linear straight channel has an undeviating, linear path between the two inlets. In both cases, the cross section of the channel does not change along the channel length.

A straight channel millifluidic device with a square, or rectangular cross-section is analogous to the slit rheometer (**Section 1.2.1.3**, **Chapter 1**). As previously discussed, a fluid in a slit rheometer will have a velocity which increases from zero, at the channel walls, to a maximum at the centre. Conversely, both the shear rate and shear stress follow an inverse relationship to the velocity; they are maximum at the wall, and non-existent at the centre. The shear rate of a non-Newtonian fluid, at the wall of a square channel, can be calculated using **Equation (5.1)**.[22] From this, the shear rate profile across the channel cross-section can be calculated (**Equation (5.2)**).

$$\dot{\gamma}_w = \frac{8Q/H^2}{\sqrt{2H^2}}\left(3 + \frac{1}{n}\right)$$

(5.1)

Equation (5.1). The shear rate at the wall ($\dot{\gamma}_w$ / s^{-1}) can be calculated from the volumetric flow rate (Q / m^3 s^{-1}), the channel height (height = width in a square channel) (H / m) and the power law index of the sample (n / dimensionless) as measured in **Section 2.3.6**, **Chapter 2** and **Section 3.3.2**, **Chapter 3**.[21]

$$\dot{\gamma}_d = \left(\frac{h}{H}\right)^{1/n} \dot{\gamma}_w$$

(5.2)

Equation (5.2). The shear rate at some position, d, in the channel ($\dot{\gamma}_d$ / s^{-1}) can be calculated from the shear rate at the wall ($\dot{\gamma}_w$ / s^{-1}), the power law index of the sample (n / dimensionless), the height of the channel (H / m) and the height at position d (h / m).
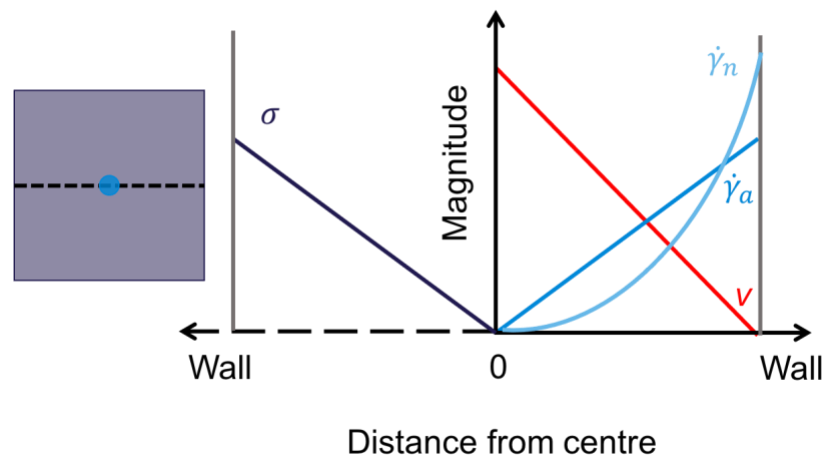

Figure (5.2). Diagram of the shear rate ($\dot{\gamma}$ / s^{-1}), shear stress (σ / Pa) and velocity profile (v / m s^{-1}) profiles across the cross-section of a square channel under pressure flow, indicated by the dashed black line on the channel cross-section. The apparent shear rate profile is depicted by $\dot{\gamma}_a$ and the shear rate profile of a power-law fluid is shown by $\dot{\gamma}_n$. The cross-sectional area of a square channel is shown on the left-hand side, with a light blue circle indicating the centre.

$$Q_{crit} = \frac{\dot{\gamma}_{crit} H^3 n}{4\sqrt{2}(3n + 1)}$$

(5.3)

Equation (5.3). The minimum volumetric flow rate for flow orientation (Q_{crit} / m^3 s^{-1}) can be calculated from the critical shear rate ($\dot{\gamma}_{crit}$ / s^{-1}), the channel height (H / m) and the power law index of the sample (n / dimensionless).[25]

It is well established that anisotropic objects orient along the flow direction in a micro-
or millifluidic channel when a critical Q is reached.[23,24] This is due to the combination of
relaxation time and shear, outlined in **Section 1.3.5**, **Chapter 1**. The minimum volumetric flow
rate (Q) required for the orientation of anisotropic objects can be calculated from the critical shear
rate ($\dot{\gamma}_{crit}$) (**Equation (5.3)**). This critical shear rate can be conveniently measured by shear-
induced polarised light imaging (SIPLI). At this Q, the shear rate at the wall is equal to $\dot{\gamma}_{crit}$, and
birefringence will be observed in the material. As $Q > Q_{crit}$, a greater volume of the material in
the channel experiences shear rates large than $\dot{\gamma}_{crit}$ and, therefore, becomes oriented.

$$v_d = v_0 \left[1 - \left(\frac{2h}{H}\right)^{(n+1)/n} \right] \tag{5.4}$$

Equation (5.4). The velocity (v / m s^{-1}) at some position, d, can be calculated from the velocity
at the centre of the channel (v_0 / m s^{-1}), the height of the channel (H / m), the power law index (n /
dimensionless) and the channel height at position h (h / m).[26]

$$v_0 = \frac{H}{2} \left(\frac{n\dot{\gamma}_0}{n+1}\right) \left(\frac{H\Delta p}{2\eta_0\dot{\gamma}_0 L}\right)^{1/n} \tag{5.5}$$

Equation (5.5). The velocity at the centre of the channel (v_0 / m s^{-1}) is calculated from the channel
height (H / m), the power law index (n / dimensionless) the pressure drop along the channel
(Δp / dimensionless), the zero-shear viscosity (η_0 / Pa s), the shear rate at which the zero-shear
viscosity is recorded ($\dot{\gamma}_0$ / s^{-1}) and the length of the channel (L / m).[26]

$$\Delta p = \left[\left(\frac{2Q}{H^3}\right)\left(\frac{2n+1}{n\dot{\gamma}_0}\right)\right]^n \left(\frac{2\eta_0\dot{\gamma}_0 L}{H}\right) \tag{5.6}$$

Equation (5.6). The pressure drop along the channel (Δp /dimensionless) is calculated from the
volumetric flow rate (Q / m^3 s^{-1}), the channel height (H / m), the power law index (n /
dimensionless), the zero-shear viscosity (η_0 / Pa s), the shear rate at which the zero-shear viscosity
is recorded ($\dot{\gamma}_0$ / s^{-1}) and the channel length (L / m).[27]

Another important parameter to characterise in a straight channel is the fluid velocity
profile across the channel cross-section (**Equation (5.4)**). In order to accurately calculate the fluid

velocity profile, the velocity at the centre of the channel (v_0) is required (**Equation (5.5)**), as is the pressure drop along the channel length (Δp) (**Equation (5.6)**).

It was assumed that the straight channel geometry would be analogous to slit geometry and provide a stable, quantifiable shear rate and velocity profile across the channel. The aim of the work outlined in this Chapter is to fully characterise the straight channel millifluidic device. Three experimental techniques were employed; finite elemental analysis (FEA), polarised optical microscopy (POM) and small-angle X-ray scattering (SAXS) with the use of two different fluids; a modified cellulose solution and a worm-like micelle solution prone to form oriented morphologies under flow. It was expected that these model anisotropic materials would align, and stretch along the flow direction, which could be quantified by the use of POM and SAXS techniques.

5.1.1 Uses of straight channel geometries

As outlined above straight channel micro- and millifluidic devices are analogous to slit or capillary rheometers (**Chapter 1, Section 1.2.1.3**), depending on whether the channel cross-section is rectangular or circular. Before the widespread use of these fluidic systems, many studies utilised conventional slit and capillary rheometers for the investigation into soft condensed matter. **Table (5.1)** shows an overview of the research discussed below. For example, in 1988 Duda *et al*. published work on the rheological effects of temperature on non-Newtonian fluids by using a capillary rheometer.[28] The work utilised stainless steel capillaries with radii of 0.1 – 0.3 mm (which would nowadays be classified as millifluidic capillary rheometry). This study helped to develop measurements, and calculation, of the viscosity of non-Newtonian fluids at high shear rates in capillary viscometers. In a related study by Lindner *et al.* in 1990, a pipe was utilised to study turbulent flow of surfactant solutions by small-angle neutron scattering (SANS) and static light scattering (SLS).[29] Alongside the investigation of laminar flow, with the use of a Couette
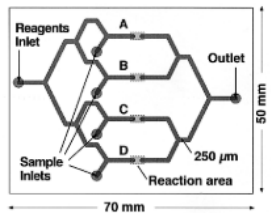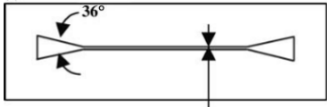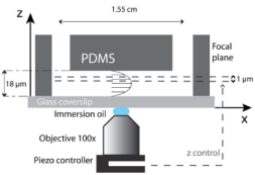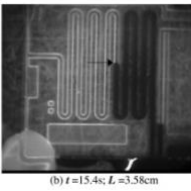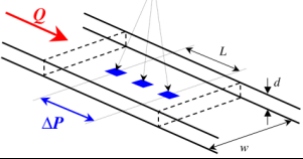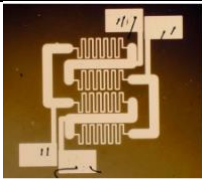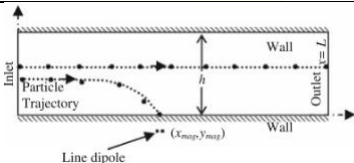
geometry, this work investigated the effects of flow on the orientation of polymeric material. It was found that good alignment of the anisotropic objects occurred when the flow was within the laminar regime, but this orientation was destroyed when the flow became turbulent. The research ultimately highlighted the necessity for accurate calculation of the Reynolds number which can be used to predict whether laminar or turbulent flow occurs.
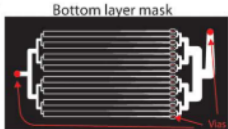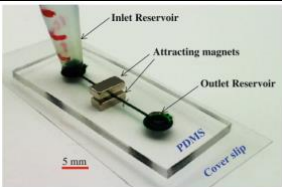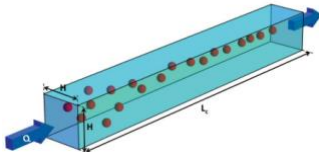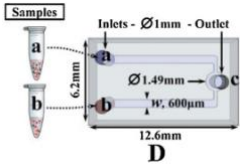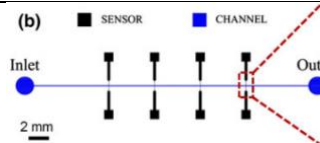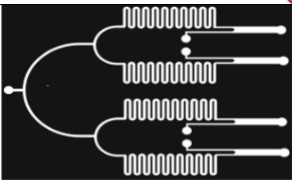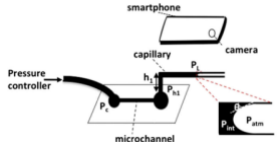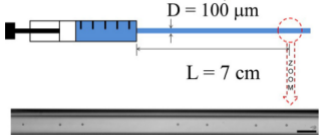
Méndez-Sanchez and coworkers also investigated turbulent flow within a capillary for surfactant systems.[30] Particle imaging velocimetry (PIV) was adopted to study the flow instabilities present in the capillary, which can be used to determine the accuracy of Re calculation. It was found that turbulent flows lead to shear banding in the sample, which is more prevalent at higher shear rates. The presence of shear banding is one of the reasons that turbulent flow is undesirable in capillary rheometry and, subsequently, micro- and millifluidics.
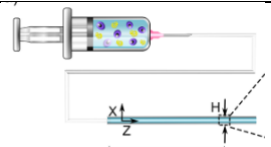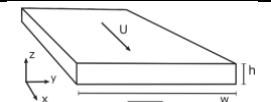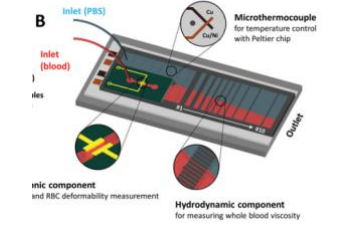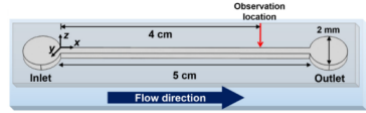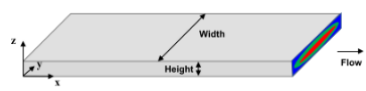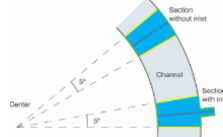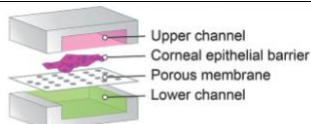
Straight channel micro and millifluidic devices have been widely adopted since the early 2000s. The uses for these devices are wide ranging, and include the synthesis and manipulation of inorganic materials,[1,31–34] point-of-care systems[35–39] and investigation into cellular processes,[40,41] to name a few. For relevance, only devices utilised for soft condensed matter materials are discussed further in this literature review, which aims to highlight the materials investigated in the channels and the techniques utilised.

One of the first reported uses of straight channel microfluidic devices was by Sato *et al.* in 2002.[42] These researchers developed a microfluidic system which allowed for simultaneous assays to be performed on multiple samples, by the use of branch points in the channel geometry. The work utilised interferon-γ, a protein with a role in immunity, as a proof-of-concept system. It was found that this assay system was completed within 50 minutes, which is slower than a standard assay technique (circa. 30 minutes). However, the employment of multiple channels meant that four assays could be performed simultaneously, leading to a higher throughput of the device. Similar work was performed by Novo *et al.* in 2013, where assays were performed to

Table (5.1). Overview of the literature on straight channel microfluidic devices, the materials utilised and the techniques employed. The materials and concentrations utilised are stated where published. Abbreviations used: polyethylene oxide (PEO), hydroxyethyl cellulose (HEC), polystyrene (PS), polyvinylpyrrolidone (PVP), polyacrylamide (PAM), hyaluronic acid (HA), centylpyridinium chloride (CPyCl), xantham gum (XG), red blood cells (RBC), thermal lens microscopy (TLM), optical microscopy (OM), particle imaging velocimetry (PIV), finite element analysis (FEA), fluorescence microscopy (FM) and digital holography microscopy (DHM).

Author	Year	Device	Materials	Techniques Used
Sato et al.[42]	2002		Interferon-γ	TLM
Kang et al.[43]	2005		PEO (4 x10^6 g/mol, 2 w/w %) HEC (720 x10^3 g/mol, 1 w/w %)	OM
Degré et al.[52]	2006		PEO (5 x 10^6 g/mol, 7.5 g/l)	PIV
Srivastava et al.[48]	2006		PEO (4 x10^6 g/mol, 2000 ppm) PAM (8 x10^6 g/mol, 2000 ppm)	OM
Pipe et al.[50]	2008		PEO (2 x10^6 g/mol, 0.1 w/w %)	Viscosity
Chevalier et al.[49]	2008		SiO$_2$ nanoparticles (8 v/w %)	Viscosity
Modak et al.[16]	2009		*Theoretical*	FEA
Ai et al.[17]	2009		Chlorophyceae	OM, FEA

Author	Year	Device	Materials	Techniques Used
Hansson et al.[35]	2012		Fluorescent microspheres (0.5 v/v %)	FM
Zeng et al.[15,18]	2013		PS (5 x 10^6 particles/ml)	OM, PIV
Del Giudice et al.[57]	2013		PVP (8 w/w %)	PIV, FEA
Novo et al.[6]	2013		White wine Beer Red Wine	OM
Pan et al.[51]	2013		XG (2 x10^6 g/mol, 5000 ppm)	PIV, FEA
Solomon et al.[44]	2014		PEO (4 x 10^6 g/mol, 5000 ppm)	OM
Del Giudice *et al.*[53]	2015		PEO (4 x 10^6 g/mol, 0.8 g/dl) PAM (6 x10^6 g/mol, 0.8 g/dl)	PIV
Solomon et al.[45]	2016		PEO (2 x 10^6 g/mol, 2 w/w %)	OM
Xiang et al.[58]	2016		PEO (2000 kDA)	OM, FM, PIV
Del Giudice *et al.*[54]	2017		PS (6.9 x 10^6 g/mol, 0.14 w/w %) HA (1.6 x 10^6 g/mol, 0.08 w/w %)	PIV

Author	Year	Device	Materials	Techniques Used
Del Giudice et al.[19]	2017		HA (1.6 x 10^6 g/mol, 0.8 w/w %)	PIV
Salipante et al.[56]	2017		CPyCl (100 mmol/L)	DHM, PIV
Li et al.[46]	2017		Glycerol	OM
Kim et al.[47]	2019		RBC (0.4 w/w %)	OM
Cho et al.[59]	2019		XG (0.05 w/w %)	PIV
Gupta et al.[60]	2020		PEO (4 x 10^6 g/mol, 1 w/w %)	DHM, PIV, FEA
Stroobants et al.[9]	2020		Egg lysozyme (72 mg ml^-1)	OM, FEA
Abdalkader et al.[12]	2020		Human corneal epithelial cells	FM

detect the presence of fungus in alcoholic drinks.[6] This work highlights one of the main advantages of microfluidics; they provide a high-throughput system with comparable results to bulk methods.[6,42]

In 2005, Kang and coworkers developed a microfluidic straight channel system for use as a high shear rheometer, to measure sample viscosity.[43] The microfluidic device manufactured was capable of producing shear rates up to 10^6 s^{-1}, shear rates larger than traditional, commercial rheometers by a factor of three. Importantly, where the shear rates investigated in the microfluidic

device overlapped with a commercial rheometer, it was found that the viscosity data was in agreement between the two techniques. Similar work has been performed by many other research groups[44–47] including Srivastava *et al.*,[48] Chevalier and coworkers,[49] Pipe *et al.*[50] as well as Pan and coworkers.[51] The widespread adoption of microfluidic channels for viscosity measurements highlights both the applicability, and need, for a straight channel microfluidic device to act as a capillary or slit rheometer.

Since the use of PIV by Méndez-Sanchez *et al.* in 2003,[30] this technique has become frequently used in combination with straight channel microfluidic devices. In 2006, Degré *et al.* developed a microfluidic system compatible with an optical microscope to image tracer particles within a flow stream.[52] The use of PIV in this work enabled the shear rate and stress to be quantitatively measured from the velocity profile of the channel cross-section. This technique has subsequently been employed by many researchers.[53–56] These succeeding papers have developed methodology which allows PIV to measure the relaxation time of polymeric materials.

There are also a number of reports regarding the use microfluidic straight channel geometries for cell and particle focusing or separation. In 2009, both Modak *et al.*[16] and Ai *et al.*[17] published reports on the use of this technique. Modak and coworkers employed a microfluidic system to computationally model the separation of particles using magnetic microspheres. This work was found to be promising in the operation and design of practical microfluidic cell separators. Ai *et al.* studied the effects of an electric field on cylindrical cells in a straight microfluidic channel. The orientation of algae cells was measured as a function of electrical field. It was found that an electrical field aided the transport of cells, as the cells aligned their longest axis parallel to the imposed electric field. Since 2009, separation and focusing of particles within a flow field has become a fruitful field of study.[15,18,19,35,57–59,61]

Many papers were published in 2020 which focused on the use of microfluidic devices for polymeric materials and built on the previous groundwork of preceding research into microfluidics. Gupta *et al*. described the use of digital holography microscopy (DHM) which provides three-dimensional visualisation of the velocity field in a microfluidic straight channel.[60] The combination of DHM with PIV for polymeric materials can be utilised as a measure of shear rheology from the velocimetry of particles in the channel. Using DHM had the added benefit of allowing the investigation of wall slip in a microchannel, which is problematic for non-Newtonian fluids.

Stroobants *et al*. utilised a microfluidic straight channel to investigate the effects of shear on protein crystallisation.[9] The design of this microdevice enabled a constant shear rate to be achieved across the entire channel by rotating the upper window, or 'lid' of the microchannel. This led to a linear velocity profile. The novel design enabled the protein crystallisation process to be studied at a constant shear rate. The device also exhibited temperature control, within 0.5 °C, via the inclusion of six Peltier elements.

Abdalkader and coworkers have also published work which focussed on developing a microfluidic device mimicking a human corneal barrier capable of eye blinking.[12] The device enabled the shear stresses associated with eye blinking to be studied, and the consequent effect of these stresses on epithelial cells. The fabrication of multiple compartments in the device allowed for comparison of different flow dynamics on the cells. This work highlights the growing area of organ-on-a-chip which aims to mimic various bodily functions with the aid of micro- and millifluidic devices.

This brief literature review (**Table (5.1)**) demonstrates that straight channel microfluidic and millifluidic devices offer many uses and can be combined with a variety of techniques. The most often utilised techniques include microscopy-based techniques, particle imaging

velocimetry and finite element analysis. These techniques all aid in attempting to understand and investigate the flow present in microfluidic channels. It has been clearly demonstrated that a straight channel microfluidic device is analogous to capillary or slit rheometry in terms of the flow profile and associated dimensionless numbers. Due to this, the straight channel microfluidic geometry has become an attractive geometry for performing measurements when only small volume of sample is available. Fully understanding the flow present in a straight channel geometry lays good groundwork for more complex geometries to be employed.

Despite the copious literature, the straight channel geometry has often been employed for the study of dilute samples, with low viscosity. However, millifluidic devices can be developed to expand capability of devices designed for small sample volumes which is especially appropriate for the investigation into more viscous polymeric materials.

5.2 Experimental

5.2.1 Materials

The modified cellulose, $C_{50/0}$ (degree of hydroxyls targeted by hydroxypropyl = 1.5, M_n = 15,543 g mol^{-1}), was donated by VTT Technical Research Centre of Finland (Finland) as a powder and was diluted to 10 w/w % in deionised water prior to use. Worm-like micelles were prepared based on the procedure outlined in **Section 3.2.2**, **Chapter 3**. The worm-like micelles were diluted to 4 and 5 w/w % prior to use.

5.2.2 Assembly of Millifluidic Device

The straight channel millifluidic device and screw ports were designed on Autodesk Fusion 360 before the CAD file was prepared for 3D printing by PreForm. In PreForm, supports with a support contact diameter (touch size) of 0.6 mm were generated and a printing resolution of 25 μm was employed. A Formlabs Form 2 SLA 3D printer was used to fabricate the millifluidic device, equipped with a standard clear photoreactive resin (a mixture of

methacrylic acid esters and photo-initiators). After printing was completed, the device was washed in isopropanol for 20 minutes in the Formlabs Form Wash and dried with compressed air. The print was then post-cured under UV light (405 nm) at 45 °C for a further 20 minutes in the Formlabs Form Cure. Supports were removed from the device with wire cutters. Where necessary the surface finish of the open channels was improved by lightly sanding with wet and dry paper, before undergoing a second wash and cure cycle.

The resulting channels in the millifluidic device measured 1 x 1 x 40 mm (width x height x length). Mica discs (15 mm diameter, 0.15 mm thickness) from Attwater (UK) were used as windows and were secured in place by the use of a nitrile rubber O-ring (11.6 mm diameter) from RS Components (UK) and the 3D printed screw. For sample delivery, a syringe pump (Harvard PHD Ultra 70-3009, Harvard Apparatus) was used in combination with 20 ml Plastipak syringes (BD Company), flangeless, flat-bottomed poly(ethylene-*co*-tetrafluoroethylene) (PETFE) ferrules (3.175 mm inner diameter), flangeless polyether ether ketone (PEEK) M6 nuts with a 3.175 mm furrow, PEEK tubing (3.175 mm outer diameter, 2.03 mm inner diameter) and PETFE Luer lock connectors (female Luer to M6 thread, flat-bottom female with a 1 mm through hole). All connectors, fittings and tubing were supplied by IDEX (Illinois, USA).

5.2.3 Finite Element Analysis (FEA)

Computational Fluid Dynamics (CFD, Autodesk, California, USA) was used to perform finite elemental analysis on the flow conditions present in the straight channel millifluidic device. Simulations were performed in the laminar flow regime, with fully developed flow conditions,

$$\rho(\boldsymbol{u}\,\boldsymbol{\nabla})\boldsymbol{u} = \boldsymbol{\nabla}\left\{-P\boldsymbol{I} + \mu[\boldsymbol{\nabla}\boldsymbol{u} + (\boldsymbol{\nabla}\boldsymbol{u})^T]\right\}$$

$$\rho\boldsymbol{\nabla}\,\boldsymbol{u} = 0$$

(5.7)

Equation (5.7). The Navier-Stokes equation is calculated using the fluid density (ρ / g cm^{-3}), the pressure (P / Pa), the identity matrix ($\boldsymbol{I}$ / dimensionless), the dynamic viscosity (μ / Pa s) and the velocity field (u / m s^{-1}).[62]

and no-slip boundary conditions are used at the channel walls. The flow field was calculated at 20 °C and 1 atm by solving the incompressible Navier-Stokes equations under continuous flow conditions (**Equation (5.7)**).

For computational modelling on the modified cellulose sample, a density of 1.020 g cm^{-3} was used and volumetric flow rates of 4.5 x 10^{-4}, 0.2 and 2 ml min^{-1} were investigated. For the worm-like micelles, computational measurements were performed for two concentrations (4 and 5 w/w %) with densities of 1.007 and 1.01 g cm^{-3} respectively. For the 4 w/w % solution, the following volumetric flow rates were measured; 2.1 x 10^{-4}, 2, and 10 ml min^{-1}. For the 5 w/w % solution, volumetric flow rates of 0.000013, 0.2 and 6 ml min^{-1} where investigated.

5.2.4 Polarised Optical Microscopy (POM)

Optical microscopy images were captured using a Zeiss Axioscope A1 microscope fitted with the AxioCam 105 colour camera, a fixed polarising filter and a second polarising filter able to rotate 90°. The rotating sample stage was removed to allow focussing on the millifluidic channel which was positioned at 45° to the two polarising filters. Images and videos were captured and processed using ZEN lite 2012 software.

Analysis of the captured POM images and videos was done using ImageJ,[63] open access software from the National Institutes of Health (Maryland, USA). Videos were converted into frame images before being reprocessed into a 16-bit image. The millifluidic channel edges were defined using the polygon tool and the 3D printed material was removed from the image using the 'Clear Outside' tool. Pixel intensity values were measured using the batch, measure command.

5.2.5 Laboratory Small Angle X-ray Scattering (SAXS) Measurements

SAXS data was collected using a laboratory SAXS/WAXS instrument (Xeuss 2.0, Xenocs, France) equipped with a liquid gallium MetalJet X-ray source (Excillium,

Sweden, wavelength $\lambda = 0.134$ nm), two sets of motorised scatterless slits for beam collimation (exit square slit of 0.5 x 0.5 mm) and a Dectris Pilatus 1M pixel SAXS detector (sample-to-detector distance 5.083 m). SAXS patterns were recorded over a q range of 0.02 nm^{-1} $< q <$ 1.8 nm^{-1}, with $q = (4\pi \sin\theta)/\lambda$, where q is the length of the scattering vector and θ is one-half of the scattering angle. Scattering patterns were acquired in 60 s interval for 15 minutes, unless otherwise stated. Acquisitions were combined and normalised using the Foxtrot software package supplied with the instrument. Data were reduced using the azimuthal integration tool in Igor Pro with a q range of 0.0074 ± 0.005 Å^{-1}.

5.2.6   Synchrotron Small Angle X-ray Scattering (SAXS) Measurements

SAXS patterns were recorded at a synchrotron (Diamond. I22, Harwell, UK) using monochromatic X-ray radiation (wavelength = 1 Å), with a q range of of 0.0024 Å^{-1} $< q <$ 0.19 Å^{-1}, and a Dectris Pilatus 2M pixel SAXS detector (sample-to-detector distance 5.776 m). Measurements were collected, forming a map of 5 (x) x 1.1 (y) mm, with a step size of 0.5 (x) and 0.05 (y) mm. X-ray scattering data were reduced and normalised using standard routines implemented in DAWN software available from Diamond Light Source.[64] Azimuthal integrations were performed over the q range of 0.007 – 0.08 Å^{-1} (0.0075 ± 0.005 Å^{-1}). Windows consisting of Kapton® film were utilised in the millifluidic device.

5.3 Results and Discussion

5.3.1   Limits of the Millifluidic Device

The straight channel device was designed on CAD software and 3D printed using stereolithography (**Figure (5.3)**). The design is based on necessary criteria for a millifluidic device suitable for the investigation of viscous polymeric materials (**Chapter 4, Section 4.4**). The channel has a square cross-section with dimensions of 1 mm (width) x 1 mm (height) x 40 mm

(length). The use of support material while printing was required to maintain the shape of the final device, these supports were removed from the device to ensure a smooth finish. The device had a threaded window port, which allowed for *in situ* measurements, by a range of techniques. Mica discs or Kapton® film, as windows, were held in place with an O-ring and a threaded open screw.
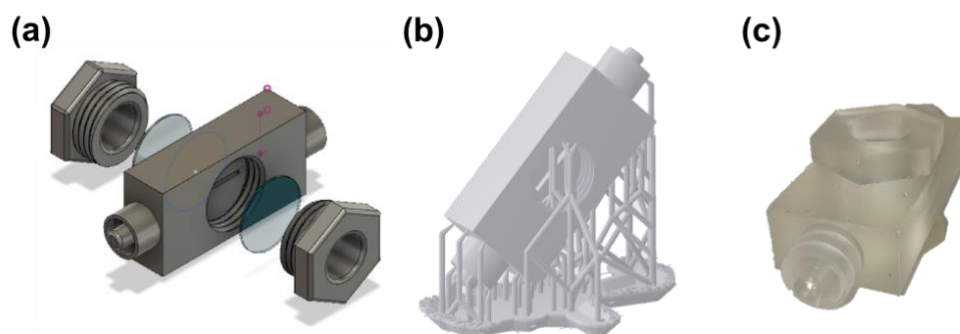
Figure (5.3). Representative images of the straight channel design during **(a)** the CAD process (drawing), **(b)** the printing process (drawing), showing the supports during 3D printing and **(c)** the final print with the supports removed (photograph).

Initial investigations with the straight channel millifluidic device were based around the capabilities of the windows. The sealing of the window material to the device was the area most likely to fail as a result of pressure build up in the channel from viscous fluids. The window material utilised for these tests were mica discs and Kapton® film, as these have very weak X-ray scattering in the small angle region. The window material was held in place against the device wall by the use of an O-ring and a threaded screw, which created a seal between the window and the device. It was found that the seal created using mica discs was leak-proof to a higher volumetric flow rate than the seal created with Kapton® film in preliminary tests, and therefore the mica discs were utilised during all experiments, unless otherwise stated.

For the investigations into the window seal, materials of increasingly higher viscosity were utilised in the millifluidic channel, these were a range of concentrations of both the modified cellulose, $C_{50/0}$ (2, 4, 6, 8 and 10 w/w %) and the worm-like micelle sample (1, 2, 3, 4 and 5 w/w

%). For each material, Q was gradually increased until window failure was observed. Window

failure was defined as the seal between the window and the device being broken, *i.e.,* the mica

disc lifting off the surface of the print. This allowed the fluid sample to leak from the channel

(**Figure (5.4)**). The straight channel millifluidic device was found to be sealed sufficiently for low

viscosity materials; flow tests with water showed that the windows did not fail up to the maximum

volumetric flow rate tested, 54 ml min^{-1}, which was the limit of the syringe pump with the 20 ml

syringes utilised (**Figure (5.5)**). Polymeric materials with a low apparent viscosity, less than 0.21

Pa s, also had no associated failure of the device windows.
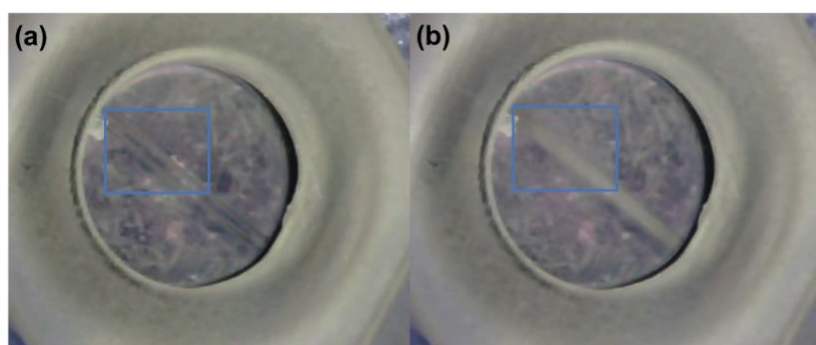
Figure (5.4). Representative images of the window failure observed in the straight channel millifluidic device. **(a)** Image showing a window completely sealed against the printed device. **(b)** Image of a window that has delaminated, with material observed under the window, not in the channel (blue box). The same area is highlighted in **(a)**. In both images, the worm-like micelle material is used at a concentration of 5 w/w %. The volumetric flow rate for each image is 0.5 ml min^{-1} **(a)** and 7 ml min^{-1} **(b)**.

$$\eta_a = \eta_0 \left(\frac{\dot{\gamma}_w}{\dot{\gamma}_0}\right)^{n-1}$$

(5.8)

Equation (5.8). The apparent viscosity of a fluid at a given Q can be calculated from the zero-shear viscosity (η_0 / Pa s), the shear rate at the wall ($\dot{\gamma}_w$ / s^{-1}), the shear rate at which the zero-shear viscosity was measured ($\dot{\gamma}_0$ / s^{-1}) and the power law index (n / dimensionless).[28]

As the zero-shear viscosity of the sample increased, the windows were more prone to

failure at lower Q. It was found that the volumetric flow rate at which window failure occurred

had some correlation with the material's apparent viscosity (**Equation (5.8)**) at the point of

failure; the higher the viscosity, the more likely the windows would fail (**Figure (5.5)**). However, all the materials investigated are shear-thinning. Therefore, the highest viscosities encountered are at the lowest volumetric flow rates as this corresponds to the lowest shear rates investigated. At these lower volumetric flow rates, where sample viscosity is highest, the windows do not fail. For example, the 5 w/w % worm-like micelle sample caused window failure at a Q of 6 ml min^{-1}, when its calculated apparent viscosity was equivalent to 0.0158 Pa s. The zero-shear viscosity of the sample is 137.5 Pa s; five orders of magnitude higher than η_a when window failure occurs, yet the windows did not fail at the higher viscosities. Therefore, the apparent viscosity of the sample cannot be the sole reason of window failure.
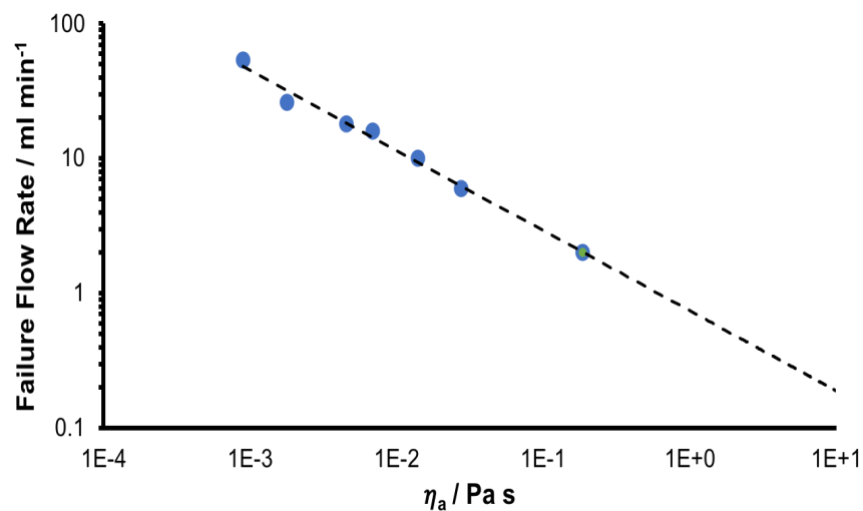
Figure (5.5). Graph of the window failure volumetric flow rate (Q / ml min^{-1}) vs the apparent viscosity of the material (η_a / Pa s), calculated using **Equation (5.8)**, for water and the worm-like micelles dilute series. A correlation is observed; as the material becomes more viscous, the device windows are more likely to unseal from the device and fail at a lower Q. The highest Q tested was 54 ml min^{-1} where water, and other low viscosity materials did not fail.

It would be beneficial to predict the possible failure of windows for a material. The window failure could be related to the pressure or normal force exerted onto the window from the fluid. This can be found experimentally by the use of pressure sensors on the window surface. However, the sealing of the device may not be as effective when this element is included. As an

alternative method, to test this hypothesis for window failure, the force exerted on the windows can be surmised by calculating the wall shear stress (**Equation (5.9)**).

$$\sigma = \frac{\Delta p}{L}\frac{H}{2} \qquad \textbf{(5.9)}$$

Equation (5.9). The shear stress (σ / Pa) can be calculated from the pressure drop along the channel (Δp /dimensionless), the length of the channel (L / m) and the channel height (H / m). The pressure drop can be calculated using **Equation (5.6)**.[21]
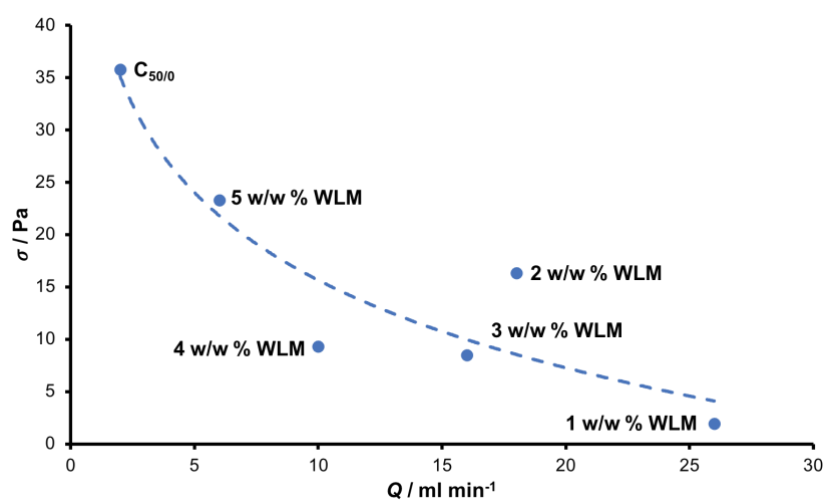
Figure (5.6). The shear stress (σ / Pa) present at the window of the straight channel millifluidic device at the corresponding failure volumetric flow rate (Q / ml min^{-1}) for a concentration series of worm-like micelle (1, 2, 3, 4 and 5 w/w %), and C$_{50/0}$ at 10 w/w %. The dashed line indicates a logarithmic trend line.

The relationship between shear stress and failure volumetric flow rate can be seen in **Figure (5.6)**. There is a good trend between the forces acting on the window and the point of failure for the device. It is possible, therefore, to utilise **Equation (5.6)** and **Equation (5.9)** to identify the behaviour, and likely failure volumetric flow rate, of a sample in the millifluidic straight channel prior to testing. Although there is a good trend between shear stress and failure volumetric flow rate, further testing is recommended.

5.3.2 Dimensionless Numbers

The Reynolds and Weissenberg numbers were calculated to investigate the flow characteristics inside the millifluidic channel, as outlined in the introduction. It is important to fully characterise the flow inside a channel to understand how the flow affects the material. These dimensionless numbers were calculated for both samples (modified cellulose and worm-like micelles) and all concentrations utilised (**Table (5.2)**).

5.3.2.1   Reynolds Number (*Re*)

The Reynolds number, which characterises the nature of flow within the channel, can be calculated from **Equation (5.10)**.[7,51,59,65] This dimensionless number is the ratio between inertia and viscous forces present in a flow and is utilised to predict whether a flow is laminar or turbulent. Although a value less that one is desirable in microfluidics to ensure no turbulent flow occurs, *Re* values below 2100 are sufficient to indicate a fully laminar flow.[66]

$$Re = \frac{\rho v H}{\eta} = \frac{\rho Q}{W \eta}$$

(5.10)

Equation (5.10). The Reynolds number (*Re* / dimensionless) can be calculated from the fluid density (ρ / kg cm^{-3}) the velocity (v / m s^{-1}), the channel height (H / m) and the fluid viscosity (η / Pa s). Alternatively, *Re* can be calculated from the density, volumetric flow rate (Q / m^3 s^{-1}), the width of the channel (W / m) and the fluid viscosity.
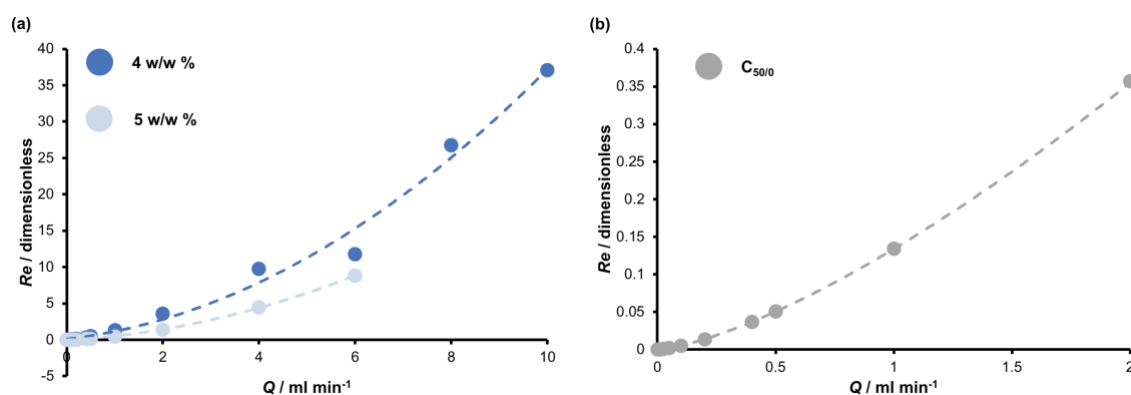
Figure (5.7). Graphs of the Reynolds number (*Re* / dimensionless) against volumetric flow rate (Q / ml min^{-1}) for 4 and 5 w/w % solutions of worm-like micelles **(a)** and the 10 w/w % modified cellulose sample **(b)**. Both samples exhibit laminar flow in the range of flow rates utilised (maximum *Re* for laminar flow is 2100).

The nature of flow through the channel for the worm-like micelles and modified cellulose samples were investigated in terms of the Reynold number associated with Q. Two concentrations of the polymeric material were studied: 4 and 5 w/w %, as well as the modified cellulose sample at 10 w/w %. It was found that for all volumetric flow rates utilised, for both materials, the flow was laminar, with Re values much lower than the 2100 limit. The highest Re values calculated were 37 (10 ml min^{-1}) and 8.8 (6 ml min^{-1}) for the 4 and 5 w/w % worm-like micelle samples respectively, and 0.36 (2 ml min^{-1}) for the 10 w/w % modified cellulose sample. The calculated Re numbers for all Q values utilised can be seen in **Figure (5.7)** for both samples. As the flow is within the laminar regime, the straight channel millifluidic device is analogous to slit rheology for both the worm-like micelle and cellulosic samples.

5.3.2.2   Weissenberg Number (*Wi*)

The Weissenberg number, *Wi*, can be utilised to quantify the degree of orientation present in a material as a result of flow deformation. Strictly speaking, this dimensionless number is a ratio of the elastic and viscous forces present in a flow. The Weissenberg number can be calculated by using **Equation (5.8)**,[7,11,58–60,65] which utilises the relaxation time calculated from the crossover point of the loss and storage moduli (G' and G'') (**Section 2.3.6**, **Chapter 2** and **Section 3.3.2**, **Chapter 3**). For Wi values close to or equivalent to 0, there is no net orientation of particles in the flow. However, as the value of *Wi* increases to the polymer chains in the system become more oriented along the flow direction, with a critical value of 1 required for orientation.[67,68]

$$Wi = r_t \dot{\gamma} = \frac{2r_t Q}{HW^2} \qquad\qquad (5.11)$$

Equation (5.11). The Weissenberg number (Wi / dimensionless) can be calculated from the relaxation time (r_t / s) and either the wall shear rate ($\dot{\gamma}_w$/ s^{-1}), or the volumetric flow rate (Q / m^3 s^{-1}), the channel height (H / m) and the channel width (W / m).

At the lowest Q for each sample, Wi is close to zero, indicating little to no orientation or alignment of the anisotropic material. However, as Q increases, Wi also increases, suggesting a greater proportion of material is oriented with the direction of flow. The greatest Weissenberg values within the millifluidic straight channel were calculated to be 6426 (10 ml min^{-1}) and 11544 (6 ml min^{-1}) for the 4 and 5 w/w % worm-like micelle samples respectively, and 21 (2 ml min^{-1}) for the 10 w/w % modified cellulose sample. At this magnitude, the polymeric material in all samples is expected to be greatly oriented in the direction of flow. The calculated Wi numbers for all volumetric flow rates utilised can be seen in **Figure (5.8)** and **Table (5.2)** for both samples.
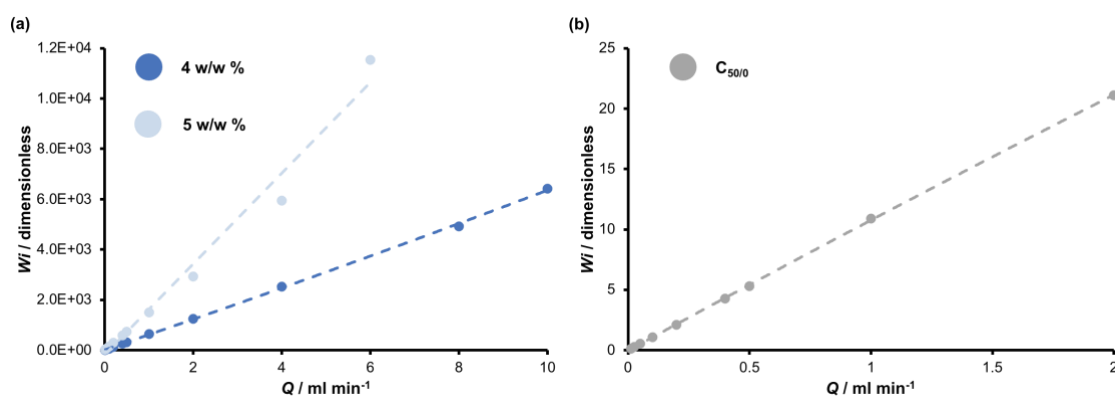
Figure (5.8). Graphs of the Weissenberg number (Wi / dimensionless) against volumetric flow rate (Q / ml min^{-1}) for **(a)** 4 and 5 w/w % worm-like micelles and **(b)** 10 w/w % modified cellulose.

Table (5.2). Calculated dimensionless numbers for a range of volumetric flow rates (Q / ml min^{-1}) for the modified cellulose sample, $C_{50/0}$ and the two concentrations of worm-like micelles (WLM), 4 and 5 w/w %. The dimensionless numbers are Re (Reynolds number) and Wi (Weissenberg number).

Sample	C / w/w %	r_t / s	$\dot{\gamma}_w$ / s^{-1}	Q / ml min^{-1}	Re	Wi
$C_{50/0}$	10	0.316	0.21	4.4 x 10^{-4}	0.0000026	0.0048
			5.53	0.0125	0.00028	0.13
			11.1	0.025	0.00075	0.27
			22.1	0.05	0.0020	0.53
			44.2	0.1	0.0053	1.1
			88.5	0.2	0.014	2.1
			177	0.4	0.037	4.3
			221	0.5	0.051	5.3
			442	1	0.13	10.9
			885	2	0.36	21.1
WLM	4	18.9	0.097	2.1 x 10^{-4}	0.0026	0.14
			5.68	0.0125	0.018	7.9
			11.4	0.025	0.025	15.8
			22.7	0.05	0.034	31.4
			45.5	0.1	0.046	64.3
			90.9	0.2	0.13	125
			182	0.4	0.35	253
			227	0.5	0.48	314
			455	1	1.3	643
			909	2	3.6	1,247
			1818	4	9.8	2,533
			2728	6	11.8	3,856
			3637	8	26.8	4,914
			4546	10	37.1	6,426
	5	44.4	0.0062	1.3 x 10^{-5}	0.000023	0.020
			7.03	0.0125	0.0025	18.5
			14.1	0.025	0.0039	37.0
			28.1	0.05	0.0061	73.7
			56.3	0.1	0.0098	151
			113	0.2	0.031	293
			225	0.4	0.098	595
			281	0.5	0.14	737
			563	1	0.45	1,510
			1125	2	1.4	2,930
			2250	4	4.5	5,950
			3376	6	8.8	11,544

5.3.3   Finite Element Analysis (FEA)

Finite element analysis is a useful simulation tool for understanding the pressure drop as well as the velocity profile present in the millifluidic channel. The Navier-Stokes equation (**Equation (5.7)**), which described the flow of incompressible fluids, was solved in two-dimensions. The equation ignores the inertia effects of a fluid, which is a common assumption in micro- and millifluidic devices, due to the observed low Re values[69]

Computer simulations were performed for a variety of volumetric flow rates for both the modified cellulose and worm-like micelle samples. For the worm-like micelles, simulations were performed for both the 4 and 5 w/w % concentrations. The results of these finite element analysis simulations are discussed below.

5.3.3.1   Modified Cellulose

The finite element analysis of the modified cellulose sample confined in the straight channel millifluidic device highlighted the laminar nature of the fluid; this was due to the uniform velocity profile across the channel cross-section. This was correct up until the maximum Q measured for this sample, 2 ml min^{-1}. The resultant velocity profiles for the representative volumetric flow rates can be seen in **Figure (5.9)**. A typical plug-like velocity profile for a shear thinning material is observed, where the maximum fluid velocity is in the centre of the channel.
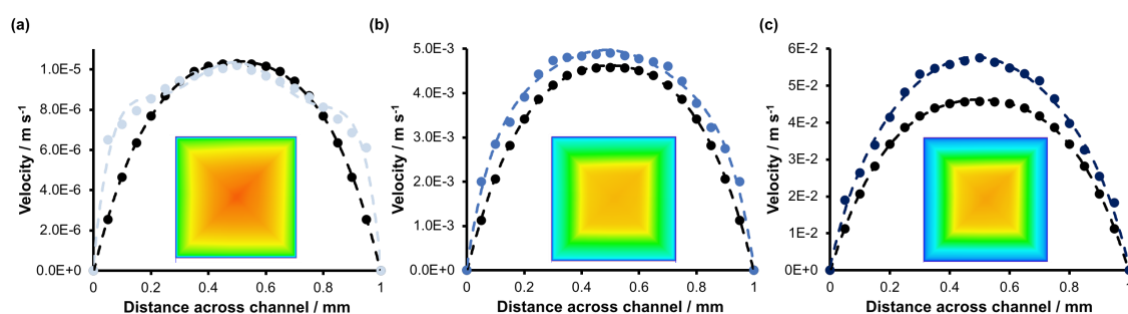
Figure (5.9). Velocity profiles for $C_{50/0}$ across the millifluidic channel as calculated using finite element analysis for the following Q values; **(a)** 0.00045 ml min^{-1}, **(b)** 0.2 ml min^{-1} and **(c)** 2 ml min^{-1}. Black data points represent the velocity profile calculated using **Equation (5.4)**, the blue data points are calculated using FEA. Inserts show FEA results across the millifluidic channel.

The fluid velocity decreases to zero at the channel walls. Overall, the FEA simulations in this case, agree well with the theoretical calculation of the Reynolds number, which also suggested laminar flow (**Figure (5.7)**).

5.3.3.2   Worm-like Micelles

The finite element analysis calculations of worm-like micelles in the straight channel millifluidic device also highlighted the laminar nature of the flow. The cross-sectional velocity profile of the channel during different volumetric flow rates can be seen in **Figure (5.10)** for both concentrations, showing the maximum fluid velocity at the centre of the channel, with a decrease in the velocity towards the channel walls. Comparing the velocity profile to the profile calculated from **Equation (5.4)**, there is good agreement between the simulation and the
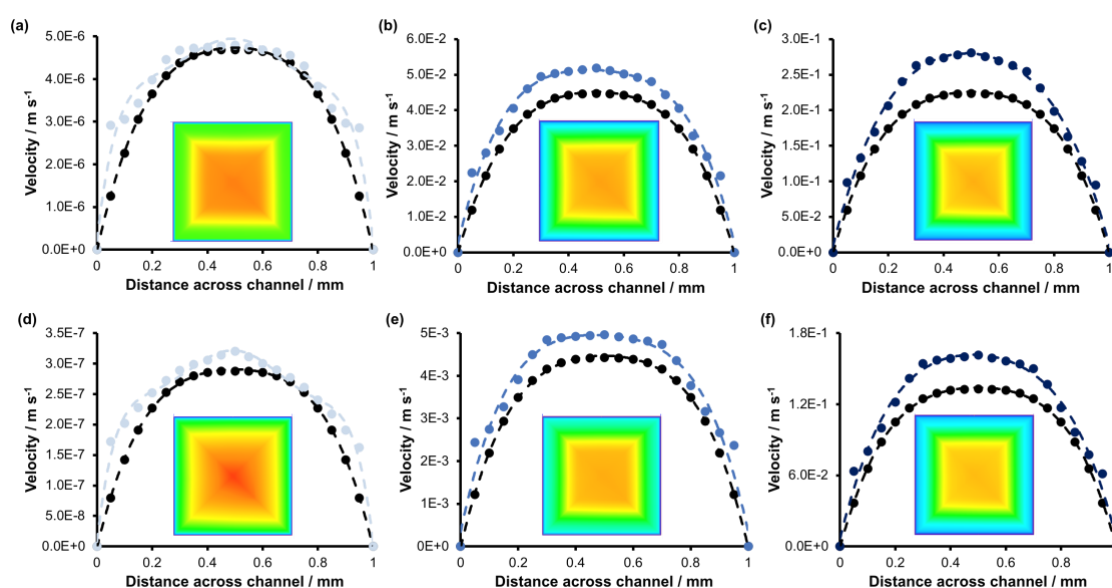
Figure (5.10). Velocity profiles for the 4 w/w % ((**a**) – (**c**)) and 5 w/w % ((**d**) – (**f**)) wormlike micelles across the millifluidic channel as calculated using finite element analysis for the following Q values; (**a**) 0.00021 ml min^{-1}, (**b**) 2 ml min^{-1} and (**c**) 10 ml min^{-1} (4 w/w %) and (**d**) 0.000013 ml min^{-1}, (**e**) 0.2 ml min^{-1} and (**f**) 6 ml min^{-1} (5 w/w %). All velocity profiles are plug-like in nature, with the highest velocity in the centre of the channel. This is due to the shear thinning nature of this material. Black data points represent the velocity profile calculated using **Equation (5.4**), the blue data points are calculated using FEA. Inserts show FEA results across the millifluidic channel.

theoretical calculation, suggesting that both FEA and Equation **(5.4)** are suitable to characterise the velocity profile within the millifluidic straight channel.

5.3.4   Polarised Optical Microscopy (POM)

Polarised optical microscopy measurements of the straight channel were performed in order to compare the flow birefringence behaviour of fluid in the millifluidic device to the results collected using SIPLI. The use of POM can also assess the appropriateness of the equations set out in **Section 5.1**. For example, if **Equation (5.2)**, which calculates the shear rate profile across the channel, is correctly applied then the location of the critical shear rate should correspond to the onset of birefringence. POM can also be used to quantify the birefringence as a function of volumetric flow rate which can also be used to compare against the Weissenberg number calculated in **Section 5.3.2.2**.

5.3.4.1   Shear Rate Profile

In a micro- or millifluidic channel, the shear rate is non-existent (i.e. zero) at the centre, and is at its maximum at the channel wall. In a pressure-driven flow, the shear rate is related to Q and can be calculated using **Equation (5.1)**. Once the wall shear rate is known, the shear rate profile across a square cross section can be calculated using **Equation (5.2)**. Polarised optical microscopy was used to determine if these equations were consistent with birefringence images collected using SIPLI at known shear rates for both modified cellulose and worm-like micelles.

5.3.4.1.1 Modified Cellulose

As previously seen in **Section 2.3.6**, **Chapter 2**, the modified cellulose sample, $C_{50/0}$, was strongly birefringent when a small amount of shear was exerted onto the sample. When the sample was used in the straight channel millifluidic device, strong birefringence was also seen using polarised optical microscopy (**Figure (5.11)**) when a volumetric flow rate of 1 ml min^{-1} was

utilised. At flow rates less than 4.75 x 10^{-4} ml min^{-1}, no birefringence was observed in the channel. A volumetric flow rate of this magnitude corresponded to a wall shear rate of 0.21 s^{-1}. This is in excellent agreement with SIPLI measurements, where $\dot{\gamma}_{crit}$ was calculated to be 0.21 s^{-1}. This result showed that the modified cellulose sample behaved in a similar way in the millifluidic straight channel and macroscopic rheological measurements. It was also noted that the onset of birefringence observed in the channel moved towards the centre as the volumetric flow rate increased, this can be seen in **Figure (5.12)**.

The shear profile present across the channel can be calculated from **Equation (5.2)**, which allows the measurement of the shear rate at which birefringence occurs. The calculated shear profiles can be seen in **Figure (5.12)**, where they have been plotted on top of birefringent images of the channel. These shear rate profiles have a distinct parabolic shape, which is widely accepted to be accurate for non-Newtonian fluids.[35] As Q increased. the maximum shear rate at the wall increased as expected. The location of the onset of birefringence, for all volumetric flow rates, was in strong agreement with the critical shear rate, $\dot{\gamma}_{crit}$, of
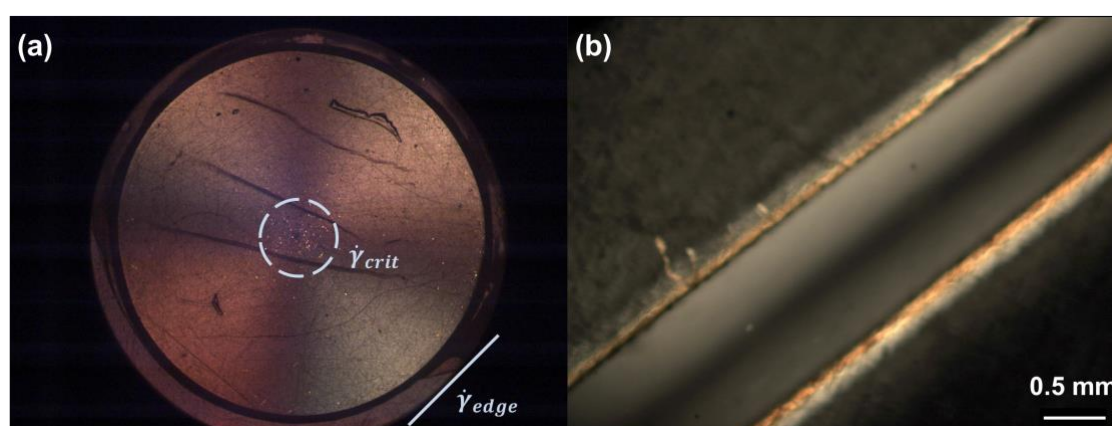
Figure (5.11). Image comparison of C$_{50/0}$ captured during **(a)** SIPLI measurements and **(b)** polarised optical microscopy measurements. **(a)** The edge shear rate, $\dot{\gamma}_{edge}$, of this PLI is 3.1 s^{-1}, signified by the solid, light blue line, with $\dot{\gamma}_{crit}$ calculated as 0.21 s^{-1} from the onset of birefringence, noted by the broken, light blue circle. **(b)** The POM image corresponds to a $\dot{\gamma}_w$ of 442 s^{-1}. Both images show strong birefringence. Different lamp intensities were used for each instrument set up.

0.21 s^{-1} which was calculated from SIPLI measurements. The shear rate of 0.21 s^{-1} is marked in **Figure (5.12)** by a vertical line, which in all cases corresponds closely with the onset of birefringence. This concurrence suggests the straight channel geometry produces a shear profile that is quantifiable, from **Equation (5.2)** when the volumetric flow rate and power law index of a material is known.
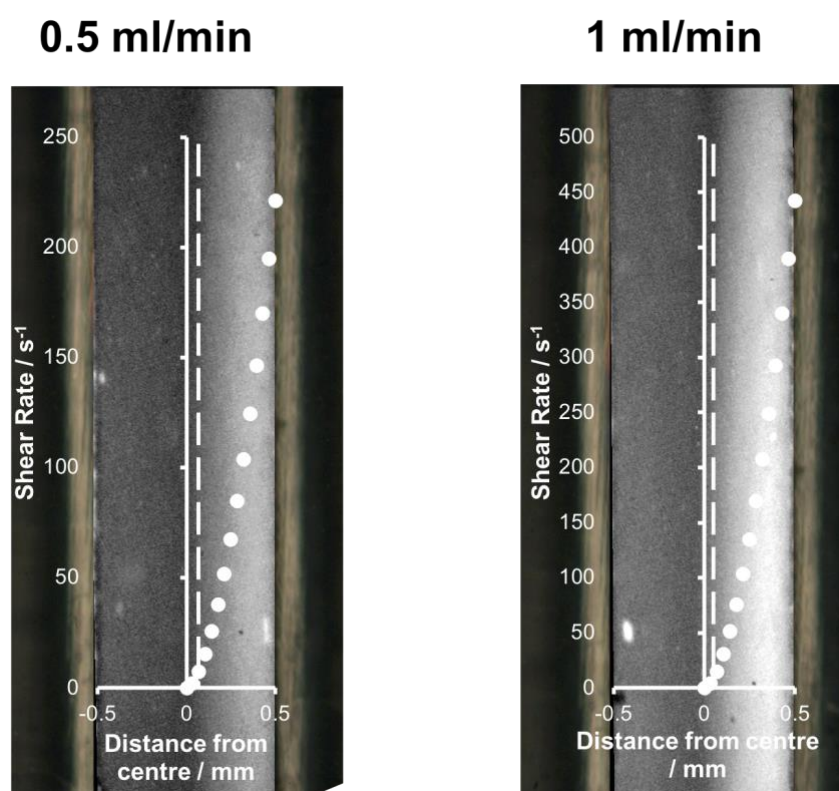
Figure (5.12). The shear rate profile overlain polarised optical microscopy images of the millifluidic channel with the modified cellulose material for two different volumetric flow rates (0.5 ml min^{-1} and 1 ml min^{-1}). The critical shear rate (0.21 s^{-1}) is shown, which corresponds to the onset of birefringence. The channel has been converted to greyscale to improve contrast for both images.

5.3.4.1.2 Worm-like Micelles

Shear induced polarised light imaging (SIPLI) measurements performed in **Section 3.3.2, Chapter 3** show the critical shear rates of the two worm-like micelle samples were 0.097 (4 w/w %) and 0.062 s^{-1} (5 w/w %). Using **Equation (5.1)**, the required Q for alignment of particles, and

thus birefringence was calculated to be 2.13 x 10^{-4} ml min^{-1} for the 4 w/w % solution and 1.1 x

10^{-5} ml min^{-1} for the 5 w/w % solution of worm-like micelles. When volumetric flow rates lower

than these were used for the two concentrations, no birefringence was seen using polarised optical

microscopy. However, at volumetric flow rates higher than the minimum stated above, both

solutions showed strong birefringence in the channel, comparable to the SIPLI measurements

(**Figure (5.13)**).
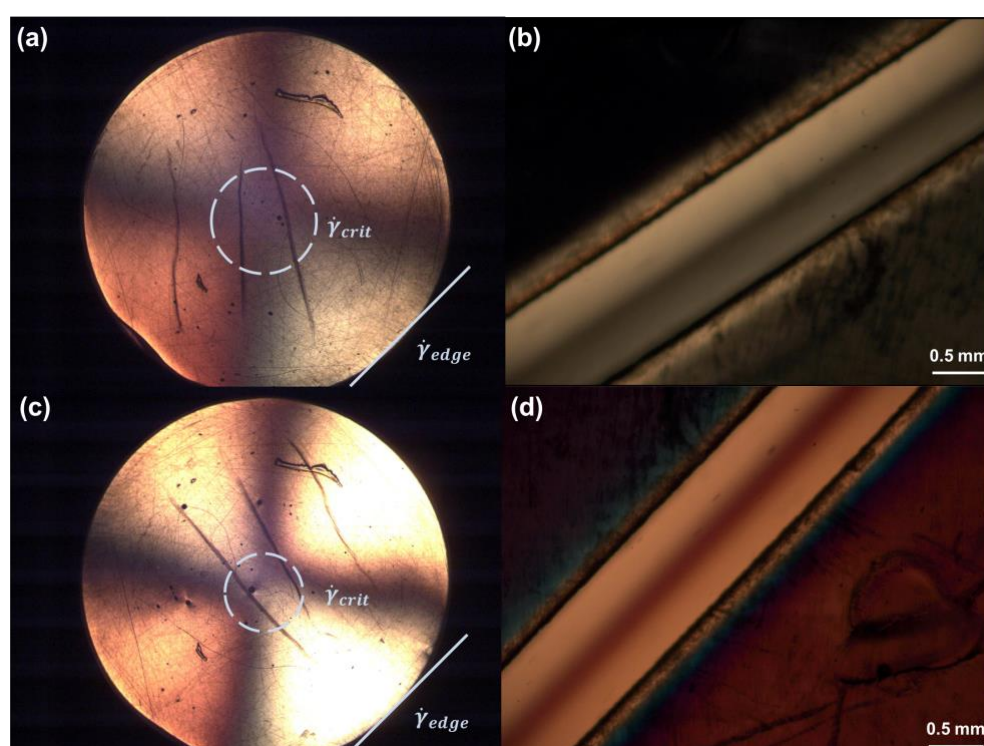
Figure (5.13). Image comparison for 4 w/w% **(a)** – **(b)** and 5 w/w % **(c)** – **(d)** worm-like micelles by SIPLI and POM. **(a)** and **(c)** show PLIs with respective $\dot{\gamma}_{edge}$ values of 1.6 s^{-1} and 4.6 s^{-1} (signified by the solid, light blue lines). $\dot{\gamma}_{crit}$ was calculated as 0.097 s^{-1} and 0.062 s^{-1} for the 4 and 5 w/w % concentration respectively, noted by the broken, light blue circle. **(b)** and **(d)** show polarised optical microscopy images with respective $\dot{\gamma}_w$ values of 454 s^{-1} and 562 s^{-1}. Both images show strong birefringence. Different lamp intensities were used for each instrument set up.

Similar to the flow experiments with the modified cellulose, the shear rate profile across

the channel was calculated (**Equations (5.2)** and **(5.4)**). From this, the shear rate at which the

onset of birefringence was found to be analogous to the critical shear rates garnered from

SIPLI measurements for both concentrations of the worm-like micelles (**Figure (5.14)** and **Figure**

(**5.15**)). This agreement furthers the ability to compare the straight channel millifluidic device to

plate-plate rheological measurements.
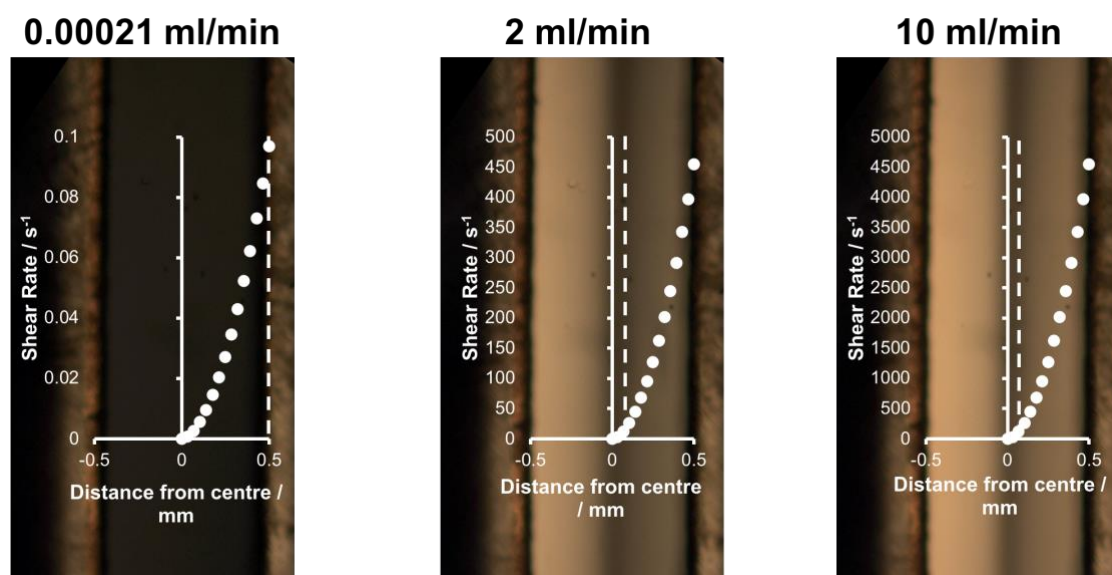
Figure (5.14). Polarised optical microscopy images with the shear rate profile overlain for the 4 w/w % worm-like micelle sample for three different volumetric flow rates (0.00021 ml min^{-1}, 2 ml min^{-1} and 10 ml min^{-1}). The critical shear rate (0.097 s^{-1}) is shown by the broken line, which aligns well with the onset of birefringence.
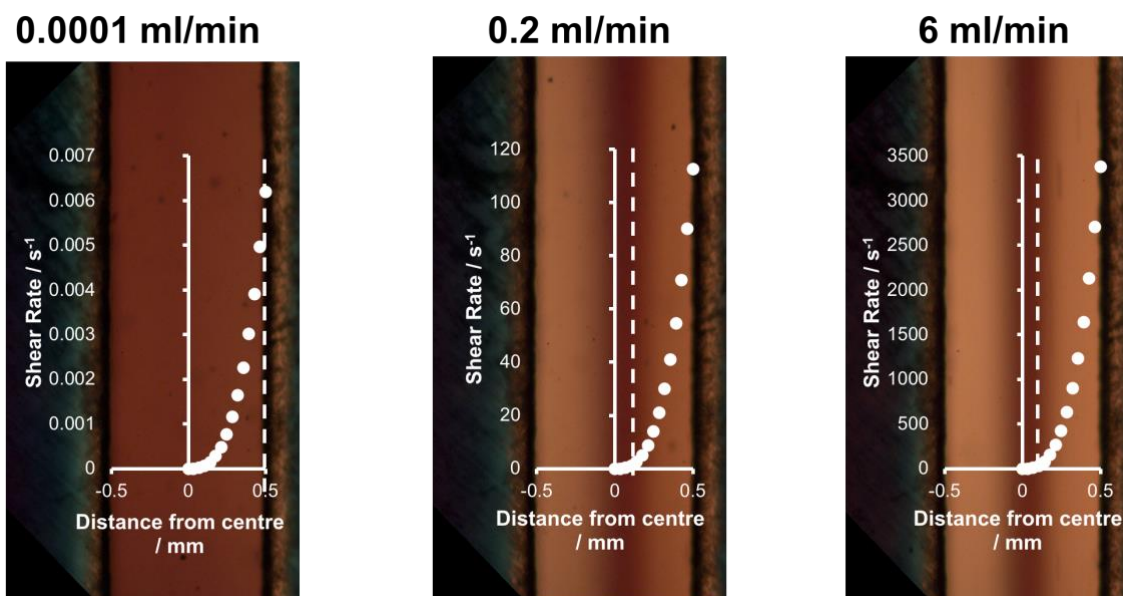
Figure (5.15). Polarised optical microscopy images with the shear rate profile overlain for the 5 w/w % worm-like micelle sample for three different volumetric flow rates (0.0001 ml min^{-1}, 0.2 ml min^{-1} and 6 ml min^{-1}). The critical shear rate (0.0062 s^{-1}) is shown by the broken line, which aligns well with the onset of birefringence.

This work has found that there is a good agreement between the birefringence behaviour observed in both SIPLI and POM for two very different polymeric materials (modified cellulose and worm-like micelles). The use of **Equation (5.2)** has also allowed for the calculation of the shear rate profile across the channel, which shows the onset of birefringence in the channel is comparable to SIPLI measurements. To calculate an accurate value for $\dot{\gamma}_w$ and the shear rate profile, only Q and n are required.

5.3.4.2 Birefringence (B) Measurements

Polarised optical microscopy was also utilised to quantify the birefringence present in the channel as a function of Q. The birefringence was qualitatively analysed earlier in the text, where the intensity of images captured using POM and SIPLI were compared for the modified cellulose and worm-like micelle samples. However, a quantitative measurement of the birefringence is appealing as it can give an indication of the degree of orientation of the anisotropic objects along the flow direction. The birefringence present in the material was calculated from **Equation (5.12)**, which use the intensity of the full beam and birefringent image, the wavelength of light and the channel height.

$$I = I_0 \sin {}^2 \frac{\delta}{2} = I_0 \sin {}^2 \frac{2\pi HB}{2\lambda}$$

(5.12)

Equation (5.12). The intensity of polarised light through a birefringent material (I / cm^{-1}) comprises the intensity of inherent polarised light (I_0 / cm^{-1}), and the retardance of light (δ / dimensionless). The retardance is calculated from the height of the channel (H / m), the birefringence (B / dimensionless) and the wavelength (700 nm) of light (λ / nm).[70]

$$B = \frac{\delta\lambda}{2\pi H} = 2\left(\sin^{-1}\left(\frac{\sqrt{I}}{\sqrt{I_0}}\right) + \pi N\right)\frac{\lambda}{2\pi H}$$

(5.13)

Equation (5.13). The equation above (**Equation (5.12)**) can be rearranged for the birefringence (B / dimensionless). B can be calculated from the intensity of light emitted from the material (I / cm^{-1}), the intensity of inherent polarised light (I_0 / cm^{-1}), some integer, N, the height of the channel (H / m) and the wavelength of light (λ / nm).

For all samples, there was a sharp increase in the birefringence as the volumetric flow rates increased between 0 and 0.5 ml min^{-1} (**Figure (5.16)**). For the modified cellulose sample, it was found that the birefringence increased logarithmically with Q, which ultimately plateaued at a volumetric flow rate around 0.4 – 0.5 ml min^{-1}. A similar trend was seen with the worm-like micelles at both concentrations, with plateaux observed at 1 ml min^{-1} (5 w/w %) and 2 ml min^{-1} (4 w/w %). The increase in birefringence with Q was expected as a greater proportion of material is oriented parallel to the flow direction as the volumetric flow rate increases. However, the plateau occurs when increasing Q has little effect; this is because a large amount of the material is already oriented along the flow, and a relatively small proportion of additional oriented material is not noticeable.
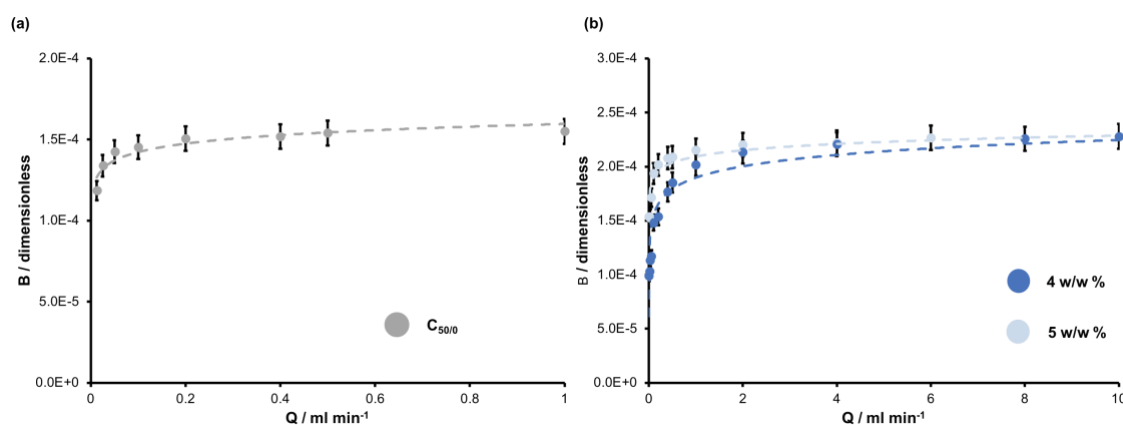
Figure (5.16). The observed birefringence (B / dimensionless) vs volumetric flow rate (Q / ml min^{-1}) for **(a)** the modified cellulose material and **(b)** the wormlike micelle samples. Error bars signify a 95 % confidence interval and dashed lines indicate the trend of birefringence with volumetric flow rate.

5.3.5   Small Angle X-ray Scattering (SAXS)

SAXS measurements, using a laboratory SAXS source were performed with all three materials at increasing Q from zero to the highest volumetric flow rates possible in the device for each sample. Due to the relatively large beam size of the laboratory SAXS instrument (0.5 x 0.5 mm), scattering patterns were only acquired in one position across the channel cross-section, with the middle of the beam in line with the centre of the millifluidic channel. Although no orientation

is expected in the centre of the channel, anisotropic scattering patterns are anticipated as the relatively large beam size leads to a large area of the channel being measured; and alignment of objects along the flow direction is expected towards the edges of the channel. These anisotropic 2D scattering patterns can be analysed using the Herman orientation function (**Equation (5.14)**) which was outlined in **Section 1.6.1.2**, **Chapter 1**. The resultant P_2 values can be compared against the degree of orientation calculations performed from POM experiments. This comparison should provide further information into the flow characteristic of the straight millifluidic channel.

$$P_2 = \frac{3\langle \cos^2 \theta \rangle - 1}{2} \tag{5.14}$$

Equation (5.14). The Hermann orientation parameter (P_2 / dimensionless) is a measure of the degree of orientation.[71]

$$\langle \cos^2 \phi \rangle = \frac{\int_0^\pi (\cos^2 \phi) \Delta I(\phi) \sin \phi \, d\phi}{\int_0^\pi \Delta I(\phi) \sin \phi \, d\phi} \tag{5.15}$$

Equation (5.15). The $\cos^2 \phi$ function in **Equation (5.14)** is defined using the azimuthal angle (ϕ / °), and the intensity of scattered X-rays at that angle ($I(\phi)$ / cm^{-1}).

5.3.5.1 Modified Cellulose

The straight channel millifluidic device was coupled with SAXS to observe the orientation of particles under flow. Initial acquisitions were gathered at a volumetric flow rate of 0.4 ml min^{-1} (well above the Q required for birefringence to be observed). However, the expected anisotropic scattering was not observed; instead, a weakly scattering isotropic pattern was collected (**Figure (5.17)(a)**). The lack of orientation was obvious when an azimuthal integration of the two-dimensional scattering pattern was performed (**Figure (5.17)(b)**). Repeated attempts, with a range of acquisition times and volumetric flow rates, were performed to collect scattering

patterns of the oriented modified cellulose. However, all scattering experiments were unsuccessful in terms of detecting any orientation; somewhat unexpected due to the strong birefringent observed during both POM and SIPLI measurements.
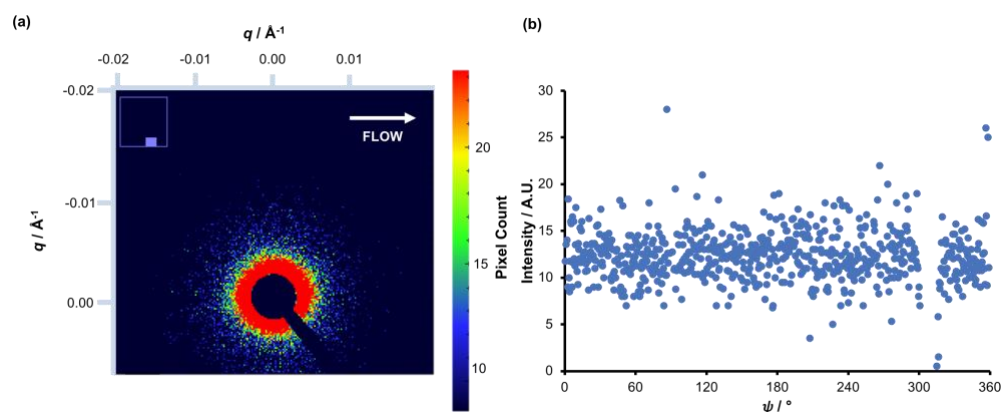
Figure (5.17). (a) Two-dimensional isotropic scattering pattern of C50/0 at 10 w/w % at a volumetric flow rate of 0.4 ml min^{-1}, with the white arrow indicating the direction of flow. **(b)** A graph of the azimuthal integration performed on the 2D image between $q = 0.005 \pm 0.001$ Å^{-1}, with no obvious orientation present.

The lack of an anisotropy in the X-ray scattering pattern is thought to be due to a relatively small quantity of oriented material and is a result of the difference in the contrast mechanism between SAXS and birefringence methods. In SAXS the scattering is from regions of different electron density, and in a polymer solution this is rather weak, regardless of the orientation of molecules. Birefringence results from the orientation of polarisable bonds and can lead to large effects in optical methods with birefringence being observed from only a small proportion of oriented material. However, a low volume of oriented polymer, surrounded by a solution which has no net orientation means that the anisotropic scattering from electron density differences is not detectable above the scattering from the large portion of unoriented material. This smearing results in an isotropic scattering pattern due to the overall random orientation of particles in the fluid channel.

It was concluded, despite the strong birefringence observed in the material, that the modified cellulose utilised was not appropriate for investigation in the millifluidic device in

combination with X-ray scattering studies. This is due to the blend of materials present, with only a small proportion able to orient with the flow, which leads to strong optical results, but little orientation observed in the small angle scattering region.

5.3.5.2 Worm-like Micelles

SAXS measurements of the worm-like micelle samples within the millifluidic straight channel geometry were performed on both a laboratory source instrument and a synchrotron beamline. Lower flow rates were utilised than for birefringence, due to the longer acquisition times required.
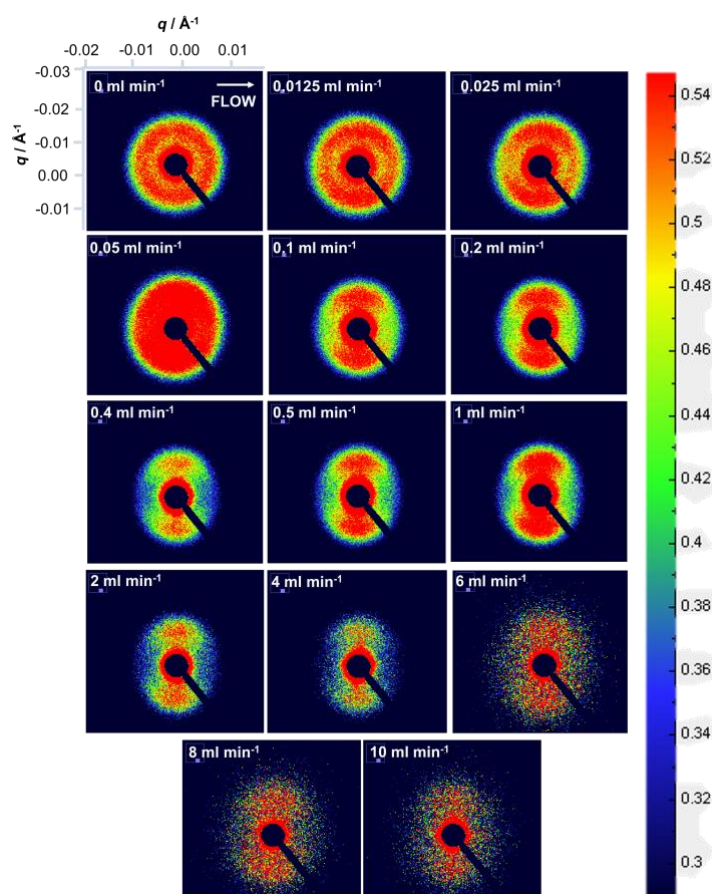
Figure (5.18). Two-dimensional anisotropic scattering pattern of the 4 w/w % worm-like micelle sample for a range of volumetric flow rates (Q / ml min^{-1}), with the white arrow indicating the direction of flow. Scattering patterns for Q values $0 – 1$ ml min^{-1} were acquired for 15 x 60 s and summed together. The data for higher Q values were acquired over shorter time periods; scattering patterns for 2 ml min^{-1} were acquired over 10 x 60 s, 4 ml min^{-1} for 6 x 60 s, and $6 – 10$ ml min^{-1} for 1 x 60 s due to limiting sample volumes.

Both instruments identified strong anisotropic scattering of the material, this is because there is strong scattering in the small-angle region from isolated worms due to the electron density contrast with the solvent. For measurements performed on the laboratory source, anisotropic scattering was not observed for either solution when the material was stationary. It was found that at low Q, (~ 0.0125 ml min^{-1}) very weak anisotropic scattering was observed, for both 4 and 5 w/w % solutions. This anisotropy became more apparent as Q increased, as can be seen in **Figure (5.18)** and **Figure (5.19)**.
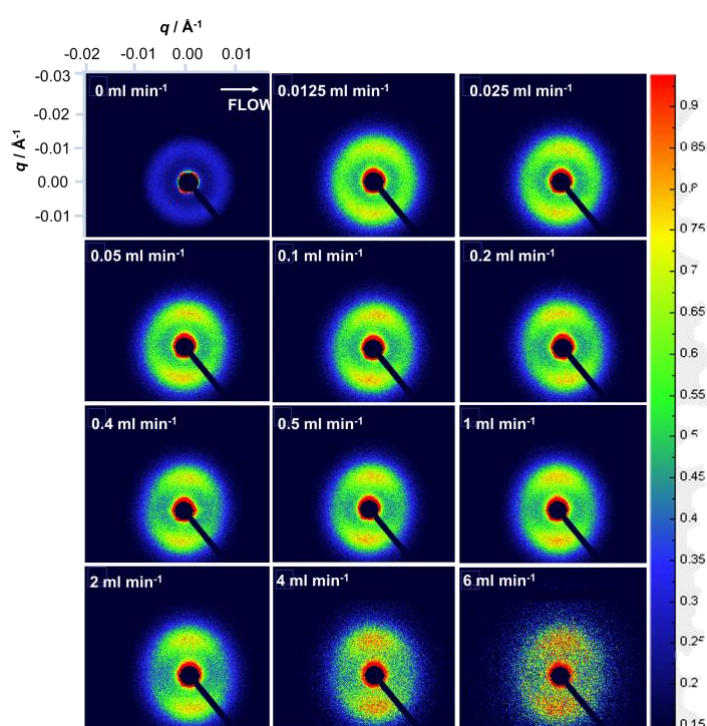
Figure (5.19). Two-dimensional anisotropic scattering pattern of the 5 w/w % worm-like micelle sample for a range of volumetric flow rates (Q / ml min^{-1}), with the white arrow indicating the direction of flow. Scattering patterns for Q values 0 – 2 ml min^{-1} were acquired for 15 x 60 s and summed together. The data for higher Q values were acquired over shorter time periods; scattering patterns for 4 ml min^{-1} were acquired over 3 x 60 s, and 6 ml min^{-1} for 1 x 60 s due to limiting sample volumes.

For both the 4 w/w % and 5 w/w % solutions of worm-like micelles, the anisotropic scattering was analysed using the Hermann orientation function. The lowest volumetric flow rate investigated, 0.0125 ml min^{-1}, gave a degree of orientation of 0.12 and 0.027 respectively. As Q increased, this degree of orientation also increased, due to the greater anisotropy seen in the

scattering pattern (**Figure (5.18)** and **Figure (5.19)**). The degree of orientation values for both

concentrations were plotted as a function of Q (**Figure (5.20)**). It was observed, for both

concentrations of worm-like micelles, the degree of orientation increased rapidly with volumetric

flow rates between 0.0125 and 1 ml min^{-1}, and then begins to plateaus around 2 ml min^{-1}. A similar

result was observed for the 5 w/w % solution of worm-like micelles; a rapid increase in the

anisotropy of the scattering pattern at low Q, which tailed off around 2 ml min^{-1}. Again, the degree

of orientation does not plateau with the volumetric flow rates investigated under SAXS.
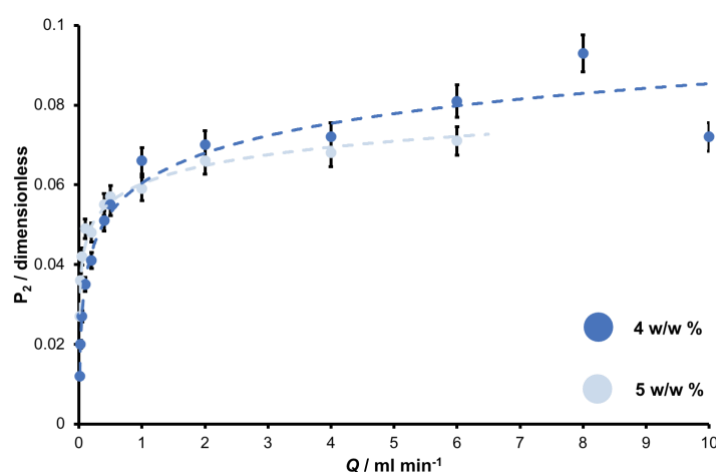
Figure (5.20). The Hermann degree of orientation function (P_2 / dimensionless) of anisotropic scattering patterns, for both 4 and 5 w/w % WLM concentrations, as a function of volumetric flow rate (Q / ml min^{-1}). The azimuthal integration was performed on the 2D image between $q = 0.0074 \pm 0.005$ Å^{-1}.

SAXS measurements performed at a synchrotron utilised the high flux and small beam

sizes available to map the millifluidic device both along, and across the straight channel. Mapping

across the millifluidic device channel allowed the investigation of anisotropic scattering as a

function of position. Both the 4 and 5 w/w % concentrations of the worm-like micelles were

investigated. It can be seen in **Figure (5.21)**, corresponding to the 4 w/w % sample, that the

mapped SAXS data shows a typical intensity profile of oriented material within a straight channel.

The images show greater brightness of the maps towards the edges of the channel, corresponding

to a greater degree of orientation of the material, and a dark section in the middle where $\dot{\gamma}$ is lower

than $\dot{\gamma}_{crit}$ and the material is unoriented.
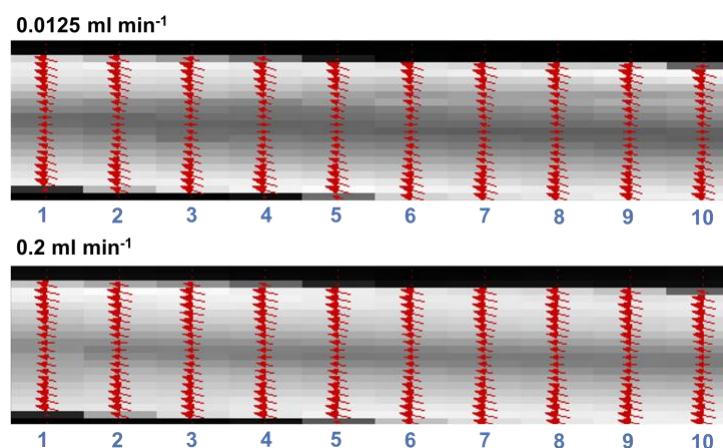
Figure (5.21). Mapped SAXS measurements for the 4 w/w % worm-like micelles at two different volumetric flow rates (0.0125, 0.2 ml min^{-1}). The scan represents a map size of 5 (width) x 1.1 (height) mm, with a step size of 0.5 (width) and 0.05 (height). The heat maps relate to the magnitude of orientation present in the SAXS pattern at a specific location in the channel, with the magnitude and direction of orientation shown with the red vectors, these are only normalised within each scan. A tilt to the vectors is observed as the channel was not perfectly horizontal.

Figure (5.22). Two-dimensional SAXS patterns of the 4 w/w % worm-like micelles showing the change in anisotropy from the edge of the straight channel to the centre for three volumetric flow rates. The numbers These images are taken from the fifth column in the maps shown in **Figure (5.21)**. Patterns in the position 1 – 3 have been omitted as they show scattering from the device wall only.

The 2D anisotropic scattering patterns, and their change as a function of both Q and channel position can be observed in **Figure (5.22)**. At the closest position to the edge of the sample, position 4 in **Figure (5.22)**, the anisotropy is the most distinct. The degree of anisotropy in the scattering pattern reduces steadily as the patterns move to the centre of the channel (position 12). The anisotropy has completely disappeared between position 10 and 11 for the 0.0125 ml min^{-1} volumetric flow rate. However, this loss of anisotropy occurs at position 12 for both the 0.2 and 0.5 ml min^{-1} volumetric flow rates.
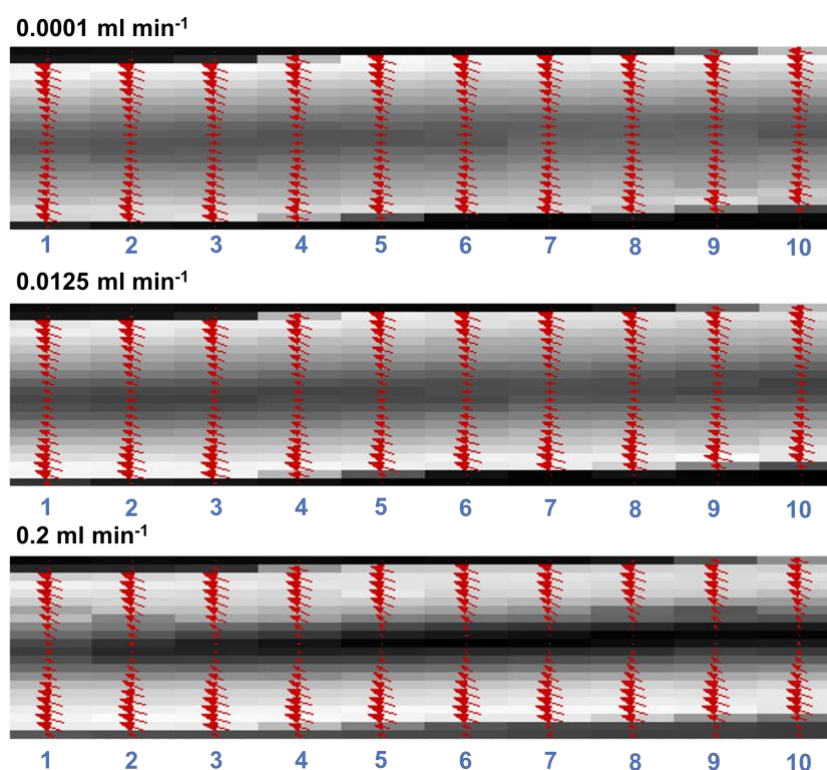
Figure (5.23). Mapped SAXS measurements for the 5 w/w % worm-like micelles at three different volumetric flow rates (0.0001, 0.0125 and 0.2 ml min^{-1}). The heat maps relate to the magnitude of orientation present in the SAXS pattern at a specific location in the channel, with the magnitude and direction of orientation shown with the red vectors. A tilt to the vectors is observed as the channel was not perfectly horizontal.

Maps of the 5 w/w % worm-like micelles showed similar results to the 4 w/w % material (**Figure (5.23))**. The 2D anisotropic scattering patterns, and their change as a function of both Q and channel position can be observed in **Figure (5.24)**. At the closest position to the edge of the

sample, position 4 in **Figure (5.24)**, the anisotropy is the most distinct. The anisotropy has

completely disappeared by position 9 for the 0.0001 ml min^{-1} volumetric flow rate. However, this

loss of anisotropy occurs at position 11 for both the 0.0125 and 0.2 ml min^{-1} volumetric flow rates.

It was expected that a loss of anisotropic would occur at position closer to the centre at

increasingly higher Q. However, this was not observed, likely because of the resolution of the

map size performed, with a step size of 0.05 mm across the channel utilised. It is likely that this

step size is too large to precisely resolve the orientation close to the centre of the channel.

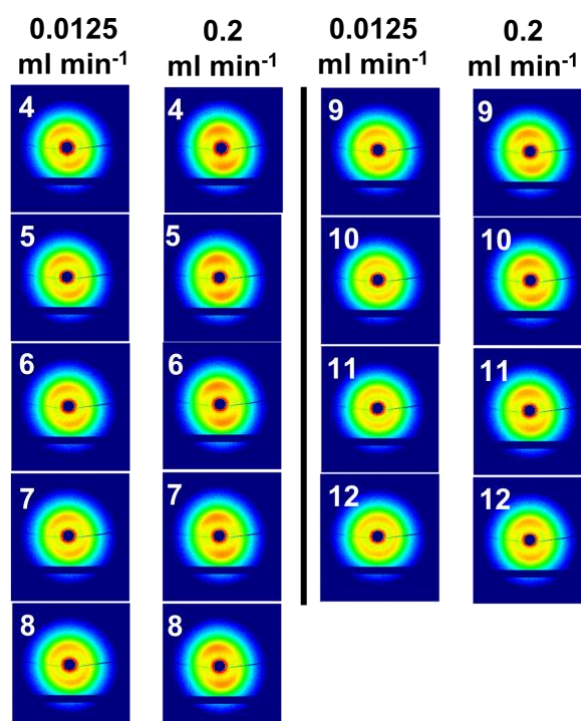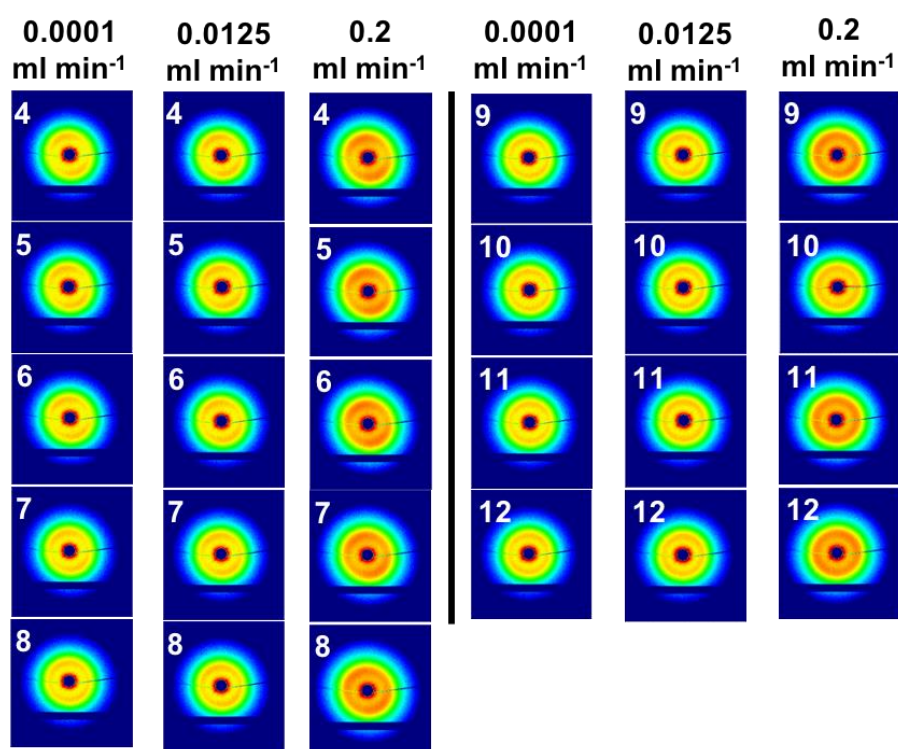**Figure (5.24).** Two-dimensional SAXS patterns of the 5 w/w % worm-like micelles showing the change in anisotropy from the edge of the straight channel to the centre for three volumetric flow rates. The numbers These images are taken from the fifth column in the maps shown in **Figure (5.23)**. Patterns in the position 1 – 3 have been omitted as they show scattering from the device wall only.

The use of SAXS to investigate the effects of flow enable a link between the molecular

and bulk length scales. Comparison between the degree of orientation of scattering patterns and

birefringence in the channel from POM show very similar trends; a sharp increase at low Q which

begins to level off at Q around 1 ml min^{-1} for both concentrations (**Figure (5.25)**). SAXS maps

also show similar intensity behaviour to POM. This indicates that the birefringence present in the

sample arises due to the orientation of particles along the direction of flow, as expected.
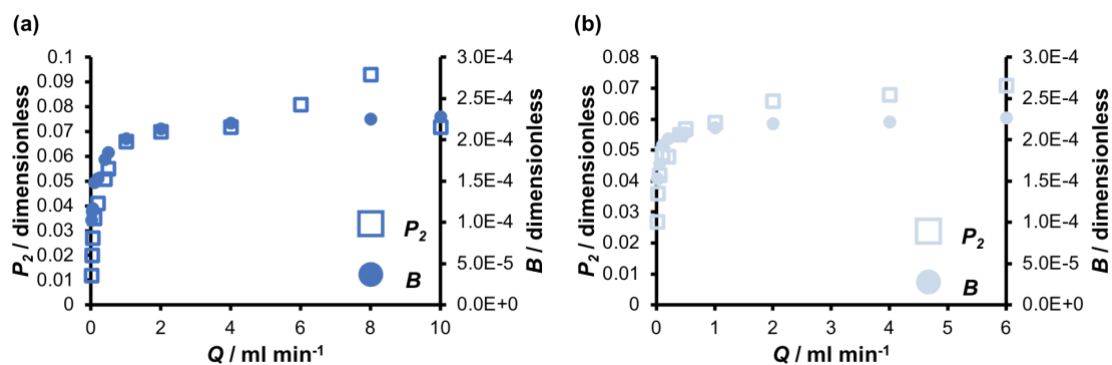
Figure (5.25). Degree of orientation (P_2 / dimensionless) and birefringence (B / dimensionless) data as a function of volumetric flow rate (Q / ml min^{-1}) for **(a)** the 4 w/w % worm-like micelles and **(b)** the 5 w/w % worm-like micelles. Degree of orientation data are signified by open squares and birefringence data are signified by filled circles.

Table (5.3). Overview of analysis data for the characterisation of the straight channel millifluidic device using the modified cellulose sample ($C_{50/0}$) and the two worm-like micelle samples. Concentration is denoted by C and volumetric flow rate, Q. The data includes wall shear rate ($\dot\gamma_w$), apparent viscosity (η_a), maximum velocity in the centre of the channel calculated using **Equation (5.4)** and FEA (v), the birefringence at the edge of the channel (B) and the degree of orientation (P_2) from lab-SAXS measurements.

| Sample	C / w/w %	$\dot\gamma_{crit}$ / s⁻¹	Q / ml min⁻¹	$\dot\gamma_{wall}$ / s⁻¹	η_a / Pa s	v / m s⁻¹ Hand	v / m s⁻¹ FEA	B	P_2
$C_{50/0}$	10	2.1×10^{-1}	4.4×10^{-4}	0.21	2.63	1.03×10^{-5}	1.02×10^{-5}	-	-
			0.0125	5.53	0.69	2.86×10^{-4}	-	1.18×10^{-4}	-
			0.025	11.1	0.52	5.71×10^{-4}	-	1.34×10^{-4}	-
			0.05	22.1	0.39	1.13×10^{-3}	-	1.43×10^{-4}	-
			0.1	44.2	0.30	2.29×10^{-3}	-	1.45×10^{-4}	-
			0.2	88.5	0.22	4.57×10^{-3}	4.91×10^{-3}	1.51×10^{-4}	-
			0.4	177	0.17	9.14×10^{-3}	-	1.52×10^{-4}	-
			0.5	221	0.15	1.14×10^{-2}	-	1.54×10^{-4}	-
			1	442	0.12	2.29×10^{-2}	-	1.55×10^{-4}	-
			2	885	0.087	5.76×10^{-2}	5.76×10^{-2}	-	-
WLM	4	9.7×10^{-2}	2.1×10^{-4}	0.097	0.59	4.74×10^{-6}	4.79×10^{-6}	9.89×10^{-5}	-
			0.0125	5.68	0.084	2.82×10^{-4}	-	1.03×10^{-4}	0.012
			0.025	11.4	0.061	5.64×10^{-4}	-	1.13×10^{-4}	0.02
			0.05	22.7	0.045	1.13×10^{-3}	-	1.17×10^{-4}	0.027
			0.1	45.5	0.033	2.26×10^{-3}	-	1.48×10^{-4}	0.035
			0.2	90.9	0.024	4.51×10^{-3}	-	1.54×10^{-4}	0.041
			0.4	182	0.018	9.03×10^{-3}	-	1.77×10^{-4}	0.051
			0.5	227	0.016	1.13×10^{-2}	-	1.85×10^{-4}	0.055
			1	455	0.012	2.26×10^{-2}	-	2.02×10^{-4}	0.066
			2	909	0.0085	4.51×10^{-2}	5.18×10^{-2}	2.13×10^{-4}	0.070
			4	1818	0.0062	9.03×10^{-2}	-	2.21×10^{-4}	0.072
			6	2728	0.0052	-	-	-	0.081
			8	3637	0.0046	1.81×10^{-1}	-	2.26×10^{-4}	0.093
			10	4546	0.0041	2.26×10^{-1}	2.81×10^{-1}	2.28×10^{-4}	0.072
	5	6.2×10^{-3}	1.3×10^{-5}	0.0062	66.2	2.88×10^{-7}	3.20×10^{-7}	-	-
			0.0125	7.03	0.63	2.76×10^{-4}	-	1.54×10^{-4}	
			0.025	14.1	0.39	5.53×10^{-4}	-	1.53×10^{-4}	0.036
			0.05	28.1	0.25	1.11×10^{-3}	-	1.71×10^{-4}	0.042
			0.1	56.3	0.16	2.21×10^{-3}	-	1.94×10^{-4}	0.049
			0.2	113	0.0099	4.42×10^{-3}	4.96×10^{-3}	2.02×10^{-4}	0.048
			0.4	225	0.0063	8.85×10^{-3}	-	2.08×10^{-4}	0.055
			0.5	281	0.0054	1.11×10^{-2}	-	2.09×10^{-4}	0.057
			1	563	0.0034	2.21×10^{-2}	-	2.15×10^{-4}	0.059
			2	1125	0.0022	4.42×10^{-2}	-	2.20×10^{-4}	0.066
			4	2250	0.0014	8.85×10^{-2}	-	2.22×10^{-4}	0.068
			6	3376	0.0010	1.33×10^{-1}	1.61×10^{-1}	2.27×10^{-4}	0.071

5.4 Conclusions

A straight channel millifluidic device has been successfully designed and fabricated by stereolithography 3D printing. The use of mica discs as windows were satisfactory in creating a seal. Calculations of the Reynold number indicated fully laminar flow behaviour for all materials, and volumetric flow rates, tested. This was further confirmed by FEA simulations, and polarised optical microscopy measurements. Polarised optical microscopy measurements also agreed well with SIPLI measurements performed in **Chapter 2** and **Chapter 3**. The $\dot{\gamma}_{crit}$ calculated from SIPLI measurements corresponds to the onset of birefringence within the millifluidic channel. Generally, the work highlights how the millifluidic device is analogous to a slit rheometer.

This work also highlights the suitability of laboratory SAXS sources to investigate the orientation of materials within a straight channel millifluidic device. Good scattering data was collected, with only fifteen minutes of data acquisition, which could be analysed to give the Hermann orientation function. Data acquisition at I22, Diamond Light source, a synchrotron SAXS beamline, allowed for the spatial resolution of orientation data across the millifluidic straight channel, due the advantage of microfocus beam and high flux capabilities.

Overall, the work discussed in this Chapter outlines how a relatively simple design and fabrication process, outlined in **Chapter 4**, can be utilised to develop millifluidic devices with a range of channel geometries, with a straight channel geometry used for a 'proof of principle' study.

5.5 References

(1)   Hong, L.; Cheung, T.-L.; Rao, N.; Ouyang, Q.; Wang, Y.; Zeng, S.; Yang, C.; Cuong, D.; Chong, P. H. J.; Liu, L.; et al. *RSC Adv.* **2017**, *7*, 36819–36832.

(2)   Méndez-Ardoy, A.; Bayón-Fernández, A.; Yu, Z.; Abell, C.; Granja, J. R.; Montenegro, J. *Angew. Chemie Int. Ed.* **2020**, *59*, 6902–6908.

(3)   Yung-Chieh Tan; Collins, J.; Lee, A. P. Controlled Fission of Droplet Emulsion in Bifurcating Microfluidic Channels. In *TRANSDUCERS '03.*; IEEE, 2003; Vol. 1, pp 28–31.

(4)   Christopher, G. F.; Anna, S. L. *J. Phys. D. Appl. Phys.* **2007**, *40*, 319–336.

(5)   Kim, M. S.; Bae, C. Y.; Wee, G.; Han, Y. M.; Park, J. K. *Electrophoresis* **2009**, *30*, 3276–3282.

(6)   Novo, P.; Moulas, G.; Prazeres, D. M. F.; Chu, V.; Conde, J. P. *Sensors Actuators, B Chem.* **2013**, *176*, 232–240.

(7)   Burshtein, N.; Chan, S. T.; Toda-Peters, K.; Shen, A. Q.; Haward, S. J. *Curr. Opin. Colloid Interface Sci.* **2019**, *43*, 1–14.

(8)   Monteiro, D. C. F.; Von Stetten, D.; Stohrer, C.; Sans, M.; Pearson, A. R.; Santoni, G.; Van Der Linden, P.; Trebbin, M. *IUCrJ* **2020**, *7*, 207–219.

(9)   Stroobants, S.; Callewaert, M.; Krzek, M.; Chinnu, S.; Gelin, P.; Ziemecka, I.; Lutsko, J. F.; De Malsche, W.; Maes, D. *Cryst. Growth Des.* **2020**, *20*, 1876–1883.

(10)   Komorowski, K.; Schaeper, J.; Sztucki, M.; Sharpnack, L.; Brehm, G.; Köster, S.; Salditt, T. *Soft Matter* **2020**, *16*, 4142–4154.

(11)   Lee, J. S.; Shaqfeh, E. S. G.; Muller, S. J. *Phys. Rev. E - Stat. Nonlinear, Soft Matter Phys.* **2007**, *75*, 15–18.

(12)   Abdalkader, R.; Kamei, K. I. *Lab Chip* **2020**, *20*, 1410–1417.

(13)   Gicquel, Y.; Schubert, R.; Kapis, S.; Bourenkov, G.; Schneider, T.; Perbandt, M.; Betzel, C.; Chapman, H. N.; Heymann, M. *J. Vis. Exp.* **2018**, *134*, 1–14.

(14)   Somani, R. H.; Yang, L.; Hsiao, B. S.; Sun, T.; Pogodina, N. V.; Lustiger, A. *Macromolecules* **2005**, *38*, 1244–1255.

(15)   Zeng, J.; Deng, Y.; Vedantam, P.; Tzeng, T. R.; Xuan, X. *J. Magn. Magn. Mater.* **2013**, *346*, 118–123.

(16)   Modak, N.; Datta, A.; Ganguly, R. *Microfluid. Nanofluidics* **2009**, *6*, 647–660.

(17)   Ai, Y.; Beskok, A.; Gauthier, D. T.; Joo, S. W.; Qian, S. *Biomicrofluidics* **2009**, *3*, 1–16.

(18)   Zeng, J.; Chen, C.; Vedantam, P.; Tzeng, T. R.; Xuan, X. *Microfluid. Nanofluidics* **2013**, *15*, 49–55.

(19)   Del Giudice, F.; Sathish, S.; D'Avino, G.; Shen, A. Q. *Anal. Chem.* **2017**, *89*, 13146–13159.

(20)   Paiè, P.; Bragheri, F.; Di Carlo, D.; Osellame, R. *Microsystems Nanoeng.* **2017**, *3*, 1–8.

(21)   Erickson, D.; Lu, F.; Li, D.; White, T.; Gao, J. *Exp. Therm. Fluid Sci.* **2002**, *25*, 623–630.

(22)   Jang, H. K.; Hong, S. O.; Lee, S. B.; Kim, J. M.; Hwang, W. R. *J. Nonnewton. Fluid Mech.* **2019**, *274*, 1–11.

(23)   Trebbin, M.; Steinhauser, D.; Perlich, J.; Buffet, A.; Roth, S. V.; Zimmermann, W.; Thiele, J.; Förster, S. *Proc. Natl. Acad. Sci. U. S. A.* **2013**, *110*, 6706–6711.

(24)   Masselon, C.; Colin, A.; Olmsted, P. D. *Phys. Rev. E* **2010**, *81*, 1–15.

(25)   Morrison, F. A. *Understanding Rheology*; Oxford University Press, **2001**.

(26)   Simpson, M. M.; Janna, W. S. *ASME Int. Mech. Eng. Congr. Expo. Proc.* **2009**, *9*, 173–180.

(27)   Barnes, H. A. *A Handbook of Elementary Rheology*; **2000**; Vol. 6.

(28)   Duda, J. L.; Klaus, E. E.; Lin, S. C. *Ind. Eng. Chem. Res.* **1988**, *27*, 352–361.

(29)   Lindner, P.; Bewersdorff, H. W.; Heen, R.; Sittart, P.; Thiel, H.; Langowski, J.; Oberthuer, R. *Prog. Colloid Polym. Sci.* **1990**, *81*, 107–112.

(30)   Méndez-Sánchez, A. F.; Pérez-González, J.; de Vargas, L.; Castrejón-Pita, J. R.; Castrejón-Pita, A. A.; Huelsz, G. *J. Rheol. (N. Y. N. Y).* **2003**, *47*, 1455–1466.

(31)   V Kinhal, K.; Bhatt, N.; Subramaniam, P. *Ind. Eng. Chem. Res.* **2019**, *58*, 5820–5829.

(32)   Xin, G.; Zhu, W.; Deng, Y.; Cheng, J.; Zhang, L. T.; Chung, A. J.; De, S.; Lian, J. *Nat. Nanotechnol.* **2019**, *14*, 168–175.

(33)   Jamshidi, R.; Rossi, D.; Saffari, N.; Gavriilidis, A.; Mazzei, L. *Cryst. Growth Des.* **2016**, *16*, 4607–4619.

(34)   Günther, A.; Khan, S. A.; Thalmann, M.; Trachsel, F.; Jensen, K. F. *Lab Chip* **2004**, *4*, 278–286.

(35)   Hansson, J.; Karlsson, J. M.; Haraldsson, T.; Brismar, H.; Van Der Wijngaart, W.; Russom, A. *Lab Chip* **2012**, *12*, 4644–4650.

(36) Martinez, A. W.; Phillips, S. T.; Whitesides, G. M.; Carrilho, E. *Anal. Chem.* **2010**, *82*, 3–10.

(37) Chin, C. D.; Linder, V.; Sia, S. K. *Lab Chip* **2012**, *12*, 2118–2134.

(38) Yetisen, A. K.; Akram, M. S.; Lowe, C. R. *Lab Chip* **2013**, *13*, 2210–2251.

(39) Srinivasan, V.; Pamula, V. K.; Fair, R. B. *Lab Chip* **2004**, *4*, 310–315.

(40) Stokes, J. R.; Boehm, M. W.; Baier, S. K. *Curr. Opin. Colloid Interface Sci.* **2013**, *18*, 349–359.

(41) Bartolo, D.; Aarts, D. G. A. L. *Soft Matter* **2012**, *8*, 10530–10535.

(42) Sato, K.; Yamanaka, M.; Takahashi, H.; Tokeshi, M.; Kimura, H.; Kitamori, T. *Electrophoresis* **2002**, *23*, 734–739.

(43) Kang, K.; Lee, L. J.; Koelling, K. W. *Exp. Fluids* **2005**, *38*, 222–232.

(44) Solomon, D. E.; Vanapalli, S. A. *Microfluid. Nanofluidics* **2014**, *16*, 677–690.

(45) Solomon, D. E.; Abdel-Raziq, A.; Vanapalli, S. A. *Rheol. Acta* **2016**, *55*, 727–738.

(46) Li, Y.; Ward, K. R.; Burns, M. A. *Anal. Chem.* **2017**, *89*, 3996–4006.

(47) Kim, B. J.; Lee, Y. S.; Zhbanov, A.; Yang, S. *Analyst* **2019**, *144*, 3144–3157.

(48) Srivastava, N.; Burns, M. A. *Anal. Chem.* **2006**, *78*, 1690–1696.

(49) Chevalier, J.; Ayela, F. *Rev. Sci. Instrum.* **2008**, *79*, 2006–2009.

(50) Pipe, C. J.; Majmudar, T. S.; McKinley, G. H. *Rheol. Acta* **2008**, *47*, 621–642.

(51) Pan, L.; Arratia, P. E. *Microfluid. Nanofluidics* **2013**, *14*, 885–894.

(52) Degré, G.; Joseph, P.; Tabeling, P.; Lerouge, S.; Cloitre, M.; Ajdari, A. *Appl. Phys. Lett.* **2006**, *89*, 1–4.

(53) Del Giudice, F.; D'Avino, G.; Greco, F.; De Santo, I.; Netti, P. A.; Maffettone, P. L. *Lab Chip* **2015**, *15*, 783–792.

(54) Del Giudice, F.; Haward, S. J.; Shen, A. Q. *J. Rheol. (N. Y. N. Y).* **2017**, *61*, 327–337.

(55) Salipante, P. F.; Meek, S. E.; Hudson, S. D. *Soft Matter* **2018**, *14*, 9020–9035.

(56) Salipante, P. F.; Little, C. A. E.; Hudson, S. D. *Phys. Rev. Fluids* **2017**, *2*, 1–25.

(57) Del Giudice, F.; Romeo, G.; D'Avino, G.; Greco, F.; Netti, P. A.; Maffettone, P. L. *Lab Chip* **2013**, *13*, 4263–4271.

(58) Xiang, N.; Zhang, X.; Dai, Q.; Cheng, J.; Chen, K.; Ni, Z. *Lab Chip* **2016**, *16*, 2626–2635.

(59) Cho, M.; Hong, S. O.; Lee, S. H.; Hyun, K.; Kim, J. M. *Micromachines* **2019**, *10*, 535–547.

(60) Gupta, S.; Vanapalli, S. A. *Phys. Fluids* **2020**, *32*, 1–13.

(61) Omori, T.; Imai, Y.; Kikuchi, K.; Ishikawa, T.; Yamaguchi, T. *Ann. Biomed. Eng.* **2014**, *43*, 238–257.

(62) Hudson, S. D.; Phelan, F. R.; Handler, M. D.; Cabral, J. T.; Migler, K. B.; Amis, E. J. *Appl. Phys. Lett.* **2004**, *85*, 335–337.

(63) Schneider, C. A.; Rasband, W. S.; Eliceiri, K. W. *Nat. Methods* **2012**, *9*, 671–675.

(64) Filik, J.; Ashton, A. W.; Chang, P. C. Y.; Chater, P. A.; Day, S. J.; Drakopoulos, M.; Gerring, M. W.; Hart, M. L.; Magdysyuk, O. V.; Michalik, S.; et al. *J. Appl. Crystallogr.* **2017**, *50*, 959–966.

(65) Gupta, S.; Wang, W. S.; Vanapalli, S. A. *Biomicrofluidics* **2016**, *10*, 1–26.

(66) Chhabra, R. P.; Richardson, J. F. *Non-Newtonian Flow and Applied Rheology*, 2nd ed.; Butterworth-Heinemann, **2008**.

(67) Weston, J. S.; Seeman, D. P.; Blair, D. L.; Salipante, P. F.; Hudson, S. D.; Weigandt, K. M. *Rheol. Acta* **2018**, *57*, 241–250.

(68) Hoyle, D. M.; Huang, Q.; Auhl, D.; Hassell, D.; Rasmussen, H. K.; Skov, A. L.; Harlen, O. G.; Hassager, O.; McLeish, T. C. B. *J. Rheol. (N. Y. N. Y).* **2013**, *57*, 293–313.

(69) Villone, M. M.; D'Avino, G.; Hulsen, M. A.; Greco, F.; Maffettone, P. L. *J. Nonnewton. Fluid Mech.* **2011**, *166*, 1396–1405.

(70) Pathak, J. A.; Hudson, S. D. *Macromolecules* **2006**, *39*, 8782–8792.

(71) Hermans, J.; Hermans, P.; Vermaas, D.; Weidinger, A. *Recl. des Trav. Chim. des Pays-Bas* **2010**, *65*, 427–447.

Chapter 6 – Cross Slot Millifluidics

6.1 Introduction

A cross-slot millifluidic device has a channel geometry analogous to the four-roll mill (FRM) (**Figure (6.1)**) outlined in **Section 1.2.2.1** (**Chapter 1**). The geometry has two opposing inlets which meet at a wide, open conduit. Two outlets are present, at right angles to the incoming fluid stream.[1] All inlets and outlets have the same channel dimensions. Where the two opposed jets meet, a stagnation point is created where material has zero velocity, but experiences infinitely high extensional strain rates.[2–4] This configuration of flow geometry is usually used for investigating the effects of extensional flow.
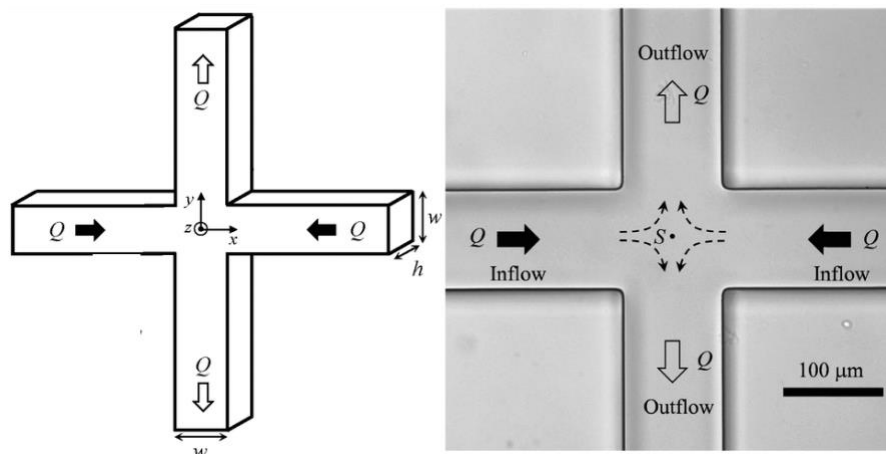
Figure (6.1). A representative cross-slot microfluidic geometry produced from Sousa *et al*.[5] The inlets are represented by the filled black arrow, and the outlets by the open arrows. A stagnation point is shown by S⋅.

A key aspect to the cross-slot device is the accurate determination of the flow conditions within the channel, which is more complicated than the straight channel geometry discussed in **Chapter 5**. The extensional, or Hencky strain rate, $\dot{\varepsilon}_H$,[6] imposed on a fluid in this device is related to the volumetric flow rate and channel dimensions (**Equation (6.1)**). Likewise, the extensional stress, σ_E, can be calculated from **Equation (6.2)**, which again utilises the volumetric flow rate and channel proportions. These parameters can give some indication into the flow characteristics of the cross-slot millifluidic device.

$$\dot{\varepsilon}_H = \frac{Q}{W^2 H}$$

(6.1)

Equation (6.1). The Hencky strain rate ($\dot{\varepsilon}_H$ / s^{-1}) present in a cross-slot geometry can be calculated from the volumetric flow rate (Q / m^3 s^{-1}), the width of the inlet channel (W / m) and the height of the channel (H / m).

$$\sigma_E = \frac{F}{A} = \frac{mv/t}{A} = \frac{m\,QA/t}{A}$$

(6.2)

Equation (6.2). The extensional stress (σ_E / Pa) which the material is subjected to can be calculated from the mass of the fluid within the channel (m / kg), the volumetric flow rate (Q / m^3 s^{-1}) the cross-sectional area of the inlet channel (A /m^2) and time of measurement (t / s).

However, one characteristic which is problematic to measure during planar extensional experiments is the fluid viscosity at specific points in the channel geometry. As previously stated in **Section 1.2.2.2**, **Chapter 1**, the planar viscosity of a fluid is much larger than their corresponding shear viscosity. A Newtonian fluid has a planar extensional viscosity which is four times greater than it's shear viscosity, characterised by a Trouton's ratio of 4. The planar viscosity of a non-Newtonian fluid can be much greater than this but can be calculated from the stress and Hencky strain rate (**Equation (6.3)**). An alternative method to calculate the viscosity is via **Equation (6.4)** which utilises the birefringence of a fluid sample. However, the stress optical coefficient holds only for relatively low stresses.[7] It is important to characterise the fluid viscosity as most samples undergo extensional thickening; the viscosity can be four times greater than the equivalent shear viscosity when a fluid experiences a planar extensional force.[8]

$$\eta_E = \frac{\sigma_E}{\dot{\varepsilon}_H}$$

(6.3)

Equation (6.3). The extensional viscosity (η_E / Pa s) can be calculated from the applied stress (σ / Pa) and the Hencky strain rate ($\dot{\varepsilon}_H$ / s^{-1}).

$$\eta_E = \frac{B}{C\dot{\varepsilon}_H} \qquad\qquad (6.4)$$

Equation (6.4). The extensional viscosity (η_E / Pa s) can be calculated from the birefringence (B / dimensionless), the stress optical coefficient (C / Pa^{-1}) and the Hencky strain rate ($\dot{\varepsilon}_H$ / s^{-1}).

The aim of the research outlined in this Chapter is to characterise the cross-slot millifluidic device. Three experimental techniques were employed for this: finite elemental analysis (FEA), polarised optical microscopy (POM) and small-angle X-ray scattering (SAXS) using two concentrations of worm-like polymeric micelles in each case. It was anticipated that these model anisotropic materials would align, and stretch along the extensional flow direction, i.e., along the outlet channels. The work contained in this Chapter shows the suitability of a 3D printing technique to produce a fully functioning cross-slot millifluidic device.

6.1.1 Cross-Slot Microfluidics in Literature

The cross-slot geometry design originates from the four-roll mill introduced by Taylor in the 1930s.[9] The FRM design utilised four, equally-spaced, free-rotating cylinders suspended in a reservoir of fluid. Due to fabrication difficulties of this instrument, the FRM was simplified by Scrivener *et al.* in the late 1970s, to the cross-slot, or opposed-jets geometry.[10] The combination of this geometry with POM allowed for the investigation into orientation, configuration and change in shape for a range of polymeric materials under flow.[11–19]

The first reported use of a microfluidic device with a cross-slot channel geometry was in 1997 by Perkins *et al.*[20] In this work, the stretching of polymers under extensional flow was investigated through the use of DNA molecules. By fluorescently labelling the DNA strands, the stretching process could be investigated, as a function of Hencky strain rate ($\dot{\varepsilon}_H$). It was observed that the time taken for stretching to occur, and the degree of stretching was highly dependent on the molecular configuration of the DNA prior to any applied extensional force. The combination

of fluorescence microscopy and cross-slot birefringence has since been utilised by Stone and coworkers,[21] Johnson-Chavarria *et al.*[12] and Valverde *et al.*[22]

Cross slot microfluidic devices have repeatedly been coupled with POM in order to study the birefringence of a fluid. One of the earliest combinations was published by Schroeder *et al.* in 2003.[23] This study is focused on the effects of planar extensional forces through the estimation of the Deborah number of DNA molecules. Akin to the study by Perkins *et al.*, this work plotted the observed extension of DNA molecules against the applied strain. Since then the combination of cross-slot microfluidic devices and POM has been widely adopted.[2,11,13,16,17,19,24–29] Most notably, some of these studies have focused on determining the onset of turbulence for non-Newtonian fluids.[13,15,26] From the observed birefringence, it has become common to determine the extensional viscosity of a fluid via **Equation (6.4)**[11,13,15–17,24–28] More recently, birefringence has also been employed to determine the relaxation time of a polymeric material.[15,19,29]

The use of finite element analysis (FEA) in combination with cross-slot microfluidic devices has also proved popular due to their utility. One of the earliest studies was published by Xi *et al.* in 2009 where modelling was employed to understand the onset of flow instability within this microfluidic geometry.[30] It was previously found that non-Newtonian fluids display instabilities in flow at extremely low Reynolds number (*Re*), whereas Newtonian fluids demonstrate flow stability up to very high *Re* values.[30] The paper by Xi *et al.* focussed on attempting to understand these flow instabilities using computational modelling. It was found the flow instabilities are related to the Weissenberg number, *Wi* (**Section 1.2.4**, **Chapter 1**); when *Wi* reaches a critical value, the flow deviates from laminar to turbulent flow. Since this research, the use of FEA in combination with cross-slot microfluidic geometries has been widespread,[31–37] with the majority of work focusing on the onset of flow instabilities.[31,33,35,37]
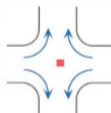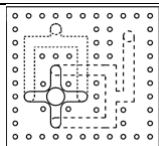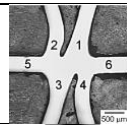
Another possible technique combination is small angle scattering (SAS) (including X-ray (SAXS) and neutron scattering (SANS)) and cross-slot microfluidics. However, these have been rarely employed, despite the wealth of orientation data these techniques can provide. In particular, the combination of SAXS and cross-slot microfluidic geometries, though rarely used, can provide invaluable information in relatively short timescales. The earliest reported use of SAXS with a cross-slot geometry was from Kisilak *et al*. in 2001.[38] SAXS studies allowed the confirmation that extensional flow occurred at the stagnation point in solutions of surfactants. This study also followed flow-induced structural changes and lamellar alignment as a function of the volumetric flow rate. The analysis of resultant anisotropic scattering patterns can be utilised to identify the alignment direction of lamellar structures, as well as the degree of orientation. Since this early work, only one other study using SAXS with cross-slot microfluidic devices by Idziak *et al*.[40] could be found. This work built on the study from Kisilak *et al*. and focussed on lamella orientation with space-resolution within the microfluidic geometry. They found strong lamellar orientation present along the extensional streamline. The degree of orientation was found to decay rapidly with increasing distance from the outlet streams.

As can be seen in **Table (6.1)**, cross-slot microfluidic devices have been utilised extensively within the soft condensed matter community, in combination with a variety of techniques. One key aspect is that FEA has been used more broadly than with straight channel microfluidic devices. This is likely to be due to the more complex nature of flow in cross-slot geometries, with both shear and extensional components present, as opposed to the simpler straight channel which consists only of shear flow. Along with the greater likelihood of flow instabilities with non-Newtonian fluids, it is of greater importance to fully understand the flow profile within cross-slot microfluidic devices.

As well as this, POM is often employed as a flow characterisation technique. Identifying the presence, and onset of birefringence within the cross-slot geometry has been proven to impart

useful information regarding the fluid extensional viscosity, *Wi* and the extensional stress present at specific volumetric flow rates. When POM is coupled with PIV, which provides information on the velocity profile within the microfluidic channel, the flow field can be extensively characterised, proving the effectiveness of combining these two techniques.

Table (6.1). Overview of the literature on cross-slot microfluidic devices, the materials utilised, and the techniques employed. The materials studied are stated where published. Abbreviations used: fluorescence microscopy (FM), small-angle X-ray scattering (SAXS), polarised optical microscopy (POM), particle imaging velocimetry (PIV), finite element analysis (FEA), deoxyribonucleic acid (DNA), sodium dodecyl sulphate (SDS), poly(dimethylsiloxane-b(ethyleneglycol-co-propyleneglycol)) (PDMS-*b*-(PEG-*co*-PG)).

Authors	Year	Geometry	Materials Used	Techniques Used
Perkins *et al.*[20]	1997		DNA	FM
Kisilak *et al.*[38]	2001		SDS	SAXS
Schroeder *et al.*[23]	2003	*Not published*	DNA	POM
Hudson *et al.*[39]	2004		PDMS-b-(PEG-co-PG)	PIV, FEA
Xi *et al.*[30]	2009		*Simulation only*	FEA

The cross-slot geometry can also be coupled with SAXS. While the X-ray scattering technique provides detailed structural information, it is less commonly used than optical techniques as data are usually collected from a particular area of sample with a relatively low special resolution defined by the X-ray beam cross-section. This problem can be resolved by using a micro-focused beam available at some synchrotron facilities but access to these sources is difficult due to oversubscription. Although lab SAXS sources are improving rapidly, brightness of modern X-ray laboratory sources still does not allow measurements to be performed with required temporal resolution (seconds or fraction of seconds). Another complication for the SAXS

measurements is caused by the fact that data across the device can be collected only in a scanning mode step-by-step and not simultaneously from different areas of the channel. In this respect scattering techniques are less favourable with respect to optical techniques, unless detailed structural information needs to be obtained on the size scale of molecules or micelles.

Another key point to note is that most research on soft matter materials traditionally involves either macrofluidic (large) rheological shear instruments or microfluidic devices. The choice is generally dictated by the volume of material available for the studies. Thus, the presented overview of techniques for the cross-slot geometry is mainly based on microfluidic devices.

There is a growing interest in millifluidic devices as they provide an opportunity to explore complex flow geometries which are not easy to implement in large instruments and are readily fabricated using current manufacturing technologies. Therefore, it is clear that extensive characterisation of millifluidic devices with complex flow is desirable. In this work, a millifluidic device with cross-slot geometry has been chosen as a representative example. There are key questions that need to be answered regarding this geometry; will the flow be laminar? Will the extensional streamline be present? Will a stagnation point develop? The work in this chapter aims to develop and characterise a millifluidic cross-slot geometry, and in doing so answer some of the above questions.

6.2 Experimental

6.2.1 Materials

Worm-like micelles were synthesised using RAFT-PISA, based on the procedure outlined in **Section 3.2.2**, **Chapter 3**. The worm-like micelles were diluted to 4 and 5 w/w/ % prior to use.

6.2.2 Assembly of Millifluidic Device

The cross-slot millifluidic device and screw ports were designed based on prototypes developed in **Chapter 4**, using Autodesk Fusion 360 before the CAD file was prepared for 3D

printing by PreForm. In Preform, supports with a touch size of 0.6 mm were generated and a printing resolution of 25 μm was employed. A Formlabs Form 2 SLA 3D printer was used to fabricate the millifluidic device, equipped with a standard clear photoreactive resin (a mixture of methacrylic acid esters and photo-initiators). After printing was completed, the device was washed in isopropanol for 20 minutes in the Formlabs Form Wash and dried with compressed air. The print was then cured under UV light (405 nm) at 45 °C for a further 20 minutes in the Formlabs Form Cure. Supports were removed from the device with wire cutters. Where necessary the surface finish of the open channels was improved by lightly sanding with wet and dry paper, before undergoing a second wash and cure cycle.

The resulting inlet and outlet channels in the millifluidic device measured 1.5 x 1.5 x 40 mm (width x height x length), the expansion section measured 4 x 4 x 1.5 mm (width x width x height) at its widest point. Mica discs (15 mm diameter, 0.15 mm thickness) from Attwater (UK) were used as windows and were secured in place by the use of a nitrile rubber O-ring (11.6 mm diameter) from RS Components (UK) and the 3D printed screw. For sample delivery, a syringe pump (Harvard PHD Ultra 70-3009, Harvard Apparatus) was used in combination with 20 ml Plastipak syringes (BD Company), flangeless, flat-bottomed ethylene tetrafluoroethylene (ETFE) ferrules (3.175 mm inner diameter), flangeless polyether ether ketone (PEEK) M6 nuts with a 3.175 mm furrow, PEEK tubing (3.175 mm outer diameter, 2.03 mm inner diameter) and ETFE Luer lock connectors (female Luer to M6 thread, flat-bottom female with a 1 mm through hole). All connectors, fittings and tubing were supplied by IDEX (Illinois, USA).

6.2.3   Finite Elemental Analysis

Computational Fluid Dynamics (CFD, Autodesk, California, USA) was used to perform finite elemental analysis on the flow conditions present in the straight channel millifluidic device. Simulations were performed in the laminar flow regime, with fully developed flow conditions, and no-slip boundary conditions are used at the channel walls. The flow field was calculated at

20 °C and 1 atm by solving the incompressible Navier-Stokes equations under continuous flow conditions (**Equation (6.5)**).

FEA simulations on the worm-like micelles were performed for two concentrations (4 and 5 w/w %) with densities of 1.0073 and 1.01 g cm^{-3} respectively. The following Q values were measured; 0.00001 ml min^{-1} (5 w/w % only), 0.00021 ml min^{-1} (4 w/w % only), 0.2 ml min^{-1} and 16 ml min^{-1}.

$$\rho(\boldsymbol{u}\,\boldsymbol{\nabla})\boldsymbol{u} = \boldsymbol{\nabla}\left\{-p\boldsymbol{I} + \mu[\boldsymbol{\nabla}\boldsymbol{u} + (\boldsymbol{\nabla}\boldsymbol{u})^T]\right\}$$

$$\rho\boldsymbol{\nabla}\,\boldsymbol{u} = 0$$

(6.5)

Equation (6.5). The Navier-Stokes equation is calculated using the fluid density (ρ / g cm^{-3}), the pressure (p / Pa), the identity matrix ($\boldsymbol{I}$ / dimensionless), the dynamic viscosity (μ / Pa s) and the velocity field (u / m s^{-1}).

6.2.4   Particle Tracking

Flow tracking by particles was performed using polystyrene latex microspheres (Alfa Aesar, USA) with a diameter of 90 μm. Fluid samples were loaded with roughly 2 g of microspheres and shaken thoroughly before being used. A Zeiss AxiosAxiocope A1 microscope fitted with the AxioCam 105 colour camera was employed to track the polystyrene particles. Videos were captured at different Q, with a frame taken every 0.2 s. Videos were converted to .avi format using the ZEN lite 2012 software. Analysis of the videos was performed using ImageJ, open access software from the National Institutes of Health (Maryland, USA). Videos were converted to an image sequence before particle tracking was performed. Particle positions were recorded using the Overlay Brush tool.

6.2.5   Polarised Optical Microscopy

Optical microscopy images were captured using a Zeiss AxioscopeScope A1 microscope fitted with the AxioCam 105 colour camera, a fixed polarising filter and a second polarising filter

able to rotate by 90°. The rotating sample stage was removed to allow focussing on the millifluidic channel which was positioned at 45° to the two polarising filters. Images and videos were captured and processed using ZEN lite 2012 software.

Analysis of the captured POM images and videos was done using ImageJ. Videos were converted into frame images before being reprocessed into a 16-bit image. The millifluidic channel edges were defined using the polygon tool and the 3D printed material was removed from the image using the 'Clear Outside' tool. Pixel intensity values were measured using the batch, measure command.

6.2.6   Laboratory Small Angle X-ray Scattering Measurements

Small-angle X-ray scattering (SAXS) data were collected using a laboratory SAXS/WAXS instrument (Xeuss 2.0, Xenocs, France) equipped with a liquid gallium MetalJet X-ray source (Excillium, Sweden, wavelength $\lambda = 0.134$ nm), two sets of motorised scatterless slits for beam collimation (0.6 x 0.5 mm) and a Dectris Pilatus 1M pixel SAXS detector (sample-to-detector distance 5.083 m). SAXS patterns were recorded over a q range of 0.002 $\text{Å}^{-1} < q <$ 0.18 Å^{-1}, with $q = (4\pi \sin\theta)/\lambda$, where q is the length of the scattering vector and θ is one-half of the scattering angle. Scattering patterns were acquired in 60 s intervals for 5 minutes, unless otherwise stated. Acquisitions were combined (2D operation; add) using the Foxtrot software package supplied with the instrument. Data were reduced to 1D patterns using the azimuthal integration tool in Igor Pro 8 (Wavemetrics Inc, USA) with a q range of 0.007 – 0.08 Å^{-1} (0.0075 ± 0.005 Å^{-1}).

6.2.7   Synchrotron Small Angle X-ray Scattering Measurements

SAXS patterns were recorded at a synchrotron (Diamond. I22, Harwell, UK) using monochromatic X-ray radiation (wavelength = 1 Å), with a q range of 0.0024 $\text{Å}^{-1} < q < 0.19$ Å^{-1}, and a Dectris Pilatus 2M pixel SAXS detector (sample-to-detector distance 5.776 m). Windows

consisting of Kapton film were utilised. Measurements were collected with fly-scanning, forming a map of 5 (x) x 5 (y) mm, with a step size of 0.1 mm (x and y). A map was completed in around 40 minutes. X-ray scattering data were reduced and normalised using standard routines implemented in DAWN software available from Diamond Light Source.[41] Azimuthal integrations were performed over the q range of 0.007 – 0.08 Å^{-1} (0.0075 ± 0.005 Å^{-1}).

6.3 Results and Discussion

6.3.1 Limits of Cross-Slot Millifluidic Device

A millifluidic device with a cross-slot geometry was designed based on the guidelines outlined in **Chapter 4**. The system, which can be seen in **Figure (6.2)**, was designed on computer aided design (CAD) software before being 3D printed using the stereolithography process. The millifluidic inlet and outlet channels had dimensions of 1.5 mm (width) x 1.5 mm (height) x 45 mm (length), the cross-slot section had a width of 3.4 mm at its widest part. Support material was required during printing to maintain the shape of the design. The supports were removed in a post-processing step to ensure a smooth finish to the channels. The device was sealed by the use of mica discs as window materials which were held in place with an O-ring and a threaded open screw.
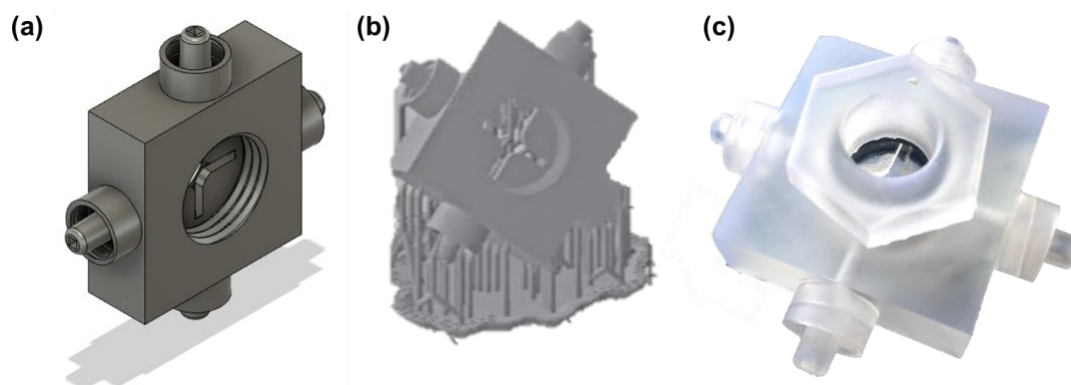

Figure (6.2). Representative images of the straight channel design during **(a)** the CAD process, **(b)** a computer rendering of the printing process, showing the supports during 3D printing and **(c)** a photograph of the final print device with the supports removed and the widows installed.

Initial investigations on the capabilities of this cross-slot millifluidic device surrounded the limits of the window material. As previously discussed in **Section 5.3.1**, **Chapter 5**, it was found that the straight channel geometry was not fully sealed for all Q values and sample viscosities, and the windows would fail when high pressures were exerted onto the window from the sample fluid. Similar experiments were performed with the cross-slot geometry with both Kapton® film and mica discs as window materials; where Q was incrementally raised with viscous materials to identify possible window failure. The two highest concentrations of the worm-like micelles were utilised (4 and 5 w/w %).

Despite the failures observed in the straight channel geometry with similar experiments, no window failure was observed in the cross-slot millifluidic device, up to the highest volumetric flow rate tested: 54 ml min^{-1}. This is true for both concentrations tested, with a maximum zero-shear viscosity of 137 Pa s (5 w/w % worm-like polymeric micelle sample). The lack of window failure, although advantageous, was surprising as the planar extensional viscosity can be much greater than the corresponding shear viscosity (**Section 1.2.2.2** in **Chapter 1**). It is thought that the pressure drop, which occurs during the rapid expansion of the channel upon entering the cross slot, is the reason for the superior sealing of the device. Therefore, it was concluded that the device was capable of withstanding much greater associated viscosities before failure occurs, compared to the straight channel millifluidic device.

The lack of window failure is likely to be because of a pressure drop occurring at the expansion of the channels (the cross-slot section of the device). This pressure drop means less pressure against the windows, explaining why no failure has been seen for the materials tested. To fully test this hypothesis, it would be beneficial to employ a pressure sensor across the expansion of the channels into the cross-slot geometry. However, the addition of this sensor is likely to impact the sealing of the device and could impair the capabilities of the device. Another

possible test would be to perform additional flow experiments with yet more viscous materials; however, this would require further modifications to the experimental set up as the syringe pump was not capable of transporting materials with very high viscosities.

6.3.2   Dimensionless Numbers

An important characteristic determining the performance of this cross-slot millifluidic device are the dimensionless numbers for flow characteristics, *Re* and *Wi*. The dimensionless numbers were calculated for the cross-slot millifluidic device for the 4 and 5 w/w % worm-like micelle samples.

6.3.2.1   Reynolds number (*Re*)

The Reynolds number (*Re*), a ratio between the inertia and viscous forces present in a flow, can be calculated from **Equation (6.6)**.[42–45] This dimensionless number outlines the nature of flow within micro- and millifluidic channels. As outlined previously in **Section 1.2.4**, **Chapter 1**, a *Re* value much lower than 2100 indicates that laminar flow is present for a Newtonian fluid,[46] which is desirable for millifluidic devices. Anything higher than this *Re* value would indicate that turbulent flow is present in the millifluidic cross-slot geometry.

$$Re = \frac{\rho v L}{\eta} \tag{6.6}$$

Equation (6.6). The Reynolds number (*Re* / dimensionless) is calculated from the density (ρ / kg m^{-1}) the fluid velocity (v / m s^{-1}), the length of the pathway the fluid is taking (L / m) and the viscosity (η / Pa s).

The *Re* value for all *Q* values was calculated at the inlet for both the 4 and 5 w/w % sample of worm-like micelles. For both concentrations of worm-like micelles, the highest *Re* values for the flow conditions used were 171 and 136 for 4 and 5 w/w %, respectively (**Q was**

expected, as for each volumetric flow rate there is a smaller quantity of unoriented material to be affected (**Figure (6.4)**).
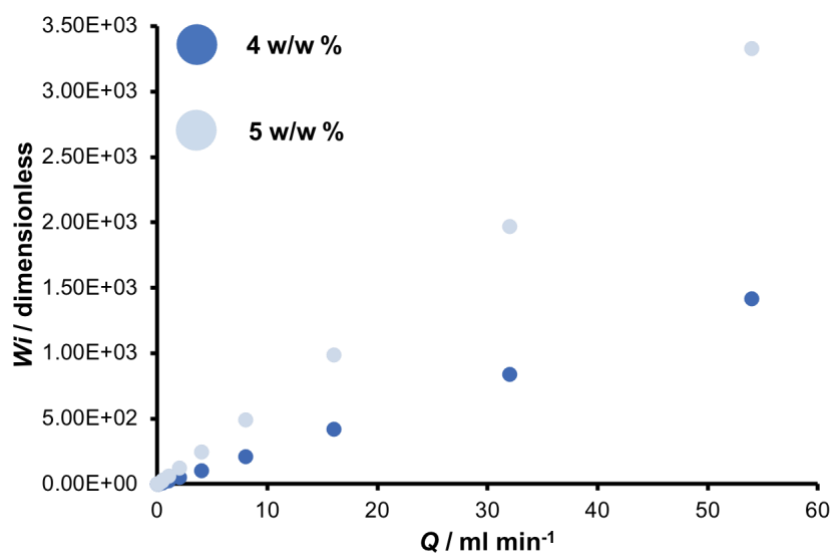

Figure (6.4). Graphs of the Weissenberg number (Wi / dimensionless) against volumetric flow rate (Q / ml min^{-1}) for 4 and 5 w/w % worm-like micelles.

Table (6.2))). These values are much lower than the 2100 limit for laminar flow. The calculated *Re* values for all *Q* values utilised can be seen in **Figure (6.3).** Graph of the Reynolds number (*Re* / dimensionless) against volumetric flow rate (*Q* / ml min^{-1}) for 4 and 5 w/w % solutions of worm-like micelles. Both samples exhibit laminar flow in the range of volumetric flow rates utilised (maximum *Re* for laminar flow is 2100).**Figure (6.3)** for both samples. Calculations using **Equation (6.6)** suggest that the nature of the flow through the cross-slot channel is expected to be laminar for all *Q* values. Therefore, the cross-slot millifluidic device is analogous to the four-roll mill (FRM) and is a suitable geometry for the investigation of the effects of planar extensional flow.
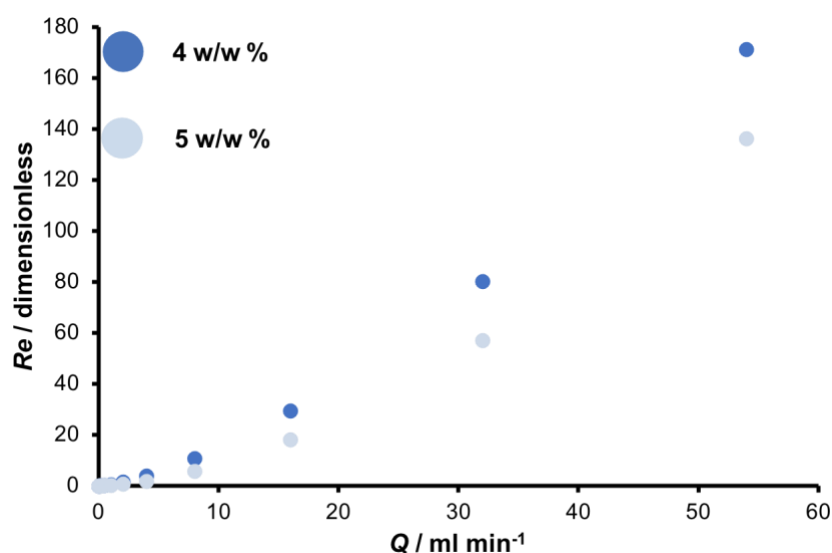
Figure (6.3). Graph of the Reynolds number (*Re* / dimensionless) against volumetric flow rate (*Q* / ml min^{-1}) for 4 and 5 w/w % solutions of worm-like micelles. Both samples exhibit laminar flow in the range of volumetric flow rates utilised (maximum *Re* for laminar flow is 2100).

6.3.2.2   Weissenberg number

The Weissenberg number, *Wi*, quantifies the degree of orientation of the particles present in a flow. This dimensionless number can be calculated using **Equation (6.7)**.[21,42–45] For this dimensionless number, a minimum value of zero indicates no net orientation of particles, whilst as *Wi* increases, it corresponds to a higher proportion of material oriented along the flow direction.[15,36,47] A Wi value of 1 is critical for the onset of birefringence.[16,29,48]

$$Wi = \frac{r_t v}{L} = \dot{\gamma}\, r_t = \frac{2 r_t Q}{W^2 H} \qquad\qquad \textbf{(6.7)}$$

Equation (6.7). The Weissenberg number (Wi / dimensionless) is calculated from the relaxation time (r_t / s^{-1}), the fluid velocity (v / m s^{-1}) and the pathway length of the fluid (L / m), or the shear rate ($\dot{\gamma}$ / s^{-1}) and the relaxation time (r_t / s). Wi can also be calculated from the relaxation time, volumetric flow rate (Q / m^3 s^{-1}) and the width and height of the channel (W and H / m).

At the lowest Q calculated for the worm-like micelle concentrations, the Wi values were

5.51 x 10^{-2} (0.0021 ml min^{-1}) and 6.17 x 10^{-3} (0.00001 ml min^{-1}) for the 4 and 5 w/w %

concentrations, respectively (**Q was** expected, as for each volumetric flow rate there is a smaller

quantity of unoriented material to be affected (**Figure (6.4)**)).

Figure (6.4). Graphs of the Weissenberg number (Wi / dimensionless) against volumetric flow rate (Q / ml min^{-1}) for 4 and 5 w/w % worm-like micelles.

Table (6.2)). These values indicated a very small proportion of material is oriented along the planar extensional stream. However, as Q increased for both concentrations, the calculated Wi values increased to a respective maximum of 1418 and 3330 for 4 and 5 w/w % at 54 ml min^{-1}. The logarithmic trend of the Wi values as a function of Q was expected, as for each volumetric flow rate there is a smaller quantity of unoriented material to be affected (**Figure (6.4)**).
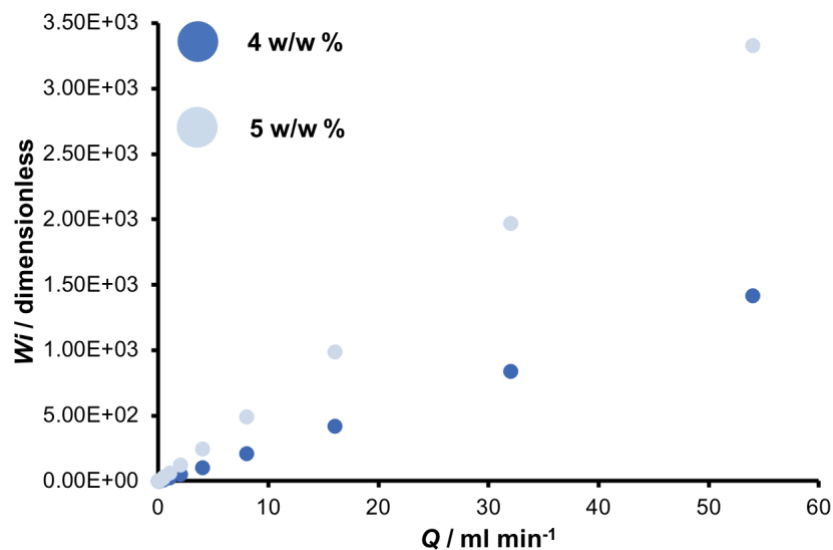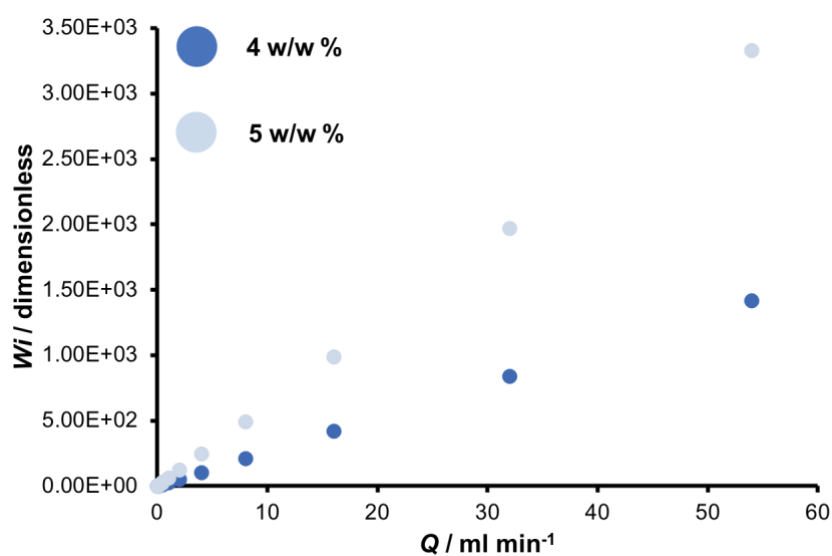

Figure (6.4). Graphs of the Weissenberg number (Wi / dimensionless) against volumetric flow rate (Q / ml min^{-1}) for 4 and 5 w/w % worm-like micelles.

Table (6.2). Calculated dimensionless numbers for a range of volumetric flow rates (Q / ml min^{-1}) for the two concentrations of worm-like micelles (WLM), 4 and 5 w/w %. The Hencky strain ($\dot{\varepsilon}_H$ / s^{-1}) values for each volumetric flow rate are included. The dimensionless numbers are *Re* (Reynolds number) and *Wi* (Weissenberg number).

C / w/w %	Q / ml min^{-1}	$\dot{\varepsilon}_H$ / s^{-1}	*Re*	*Wi*
4	2.1 x 10^{-4}	1.04 x 10^{-3}	2.44 x 10^{-5}	5.51 x 10^{-2}
	0.0125	6.17 x 10^{-2}	9.09 x 10^{-4}	3.28 x 10^{-1}
	0.025	1.23 x 10^{-1}	2.49 x 10^{-3}	6.56 x 10^{-1}
	0.05	2.47 x 10^{-1}	6.80 x 10^{-3}	1.31
	0.1	4.94 x 10^{-1}	1.86 x 10^{-2}	2.63
	0.2	9.88 x 10^{-1}	5.08 x 10^{-2}	5.25
	0.4	1.98	1.39 x 10^{-1}	10.5
	0.5	2.47	1.92 x 10^{-1}	13.1
	1	4.94	5.25 x 10^{-1}	26.3
	2	9.88	1.44	52.5
	4	19.8	3.93	105
	8	39.5	10.7	210
	16	79.0	29.3	420
	32	158	80.2	840
	54	267	171	1,418
5	1.3 x 10^{-5}	4.94 x 10^{-4}	9.25 x 10^{-10}	6.17 x 10^{-3}
	0.0125	6.17 x 10^{-2}	1.22 x 10^{-4}	7.71 x 10^{-1}
	0.025	1.23 x 10^{-1}	3.88 x 10^{-4}	1.54
	0.05	2.47 x 10^{-1}	1.23 x 10^{-3}	3.08
	0.1	4.94 x 10^{-1}	3.89 x 10^{-3}	6.17
	0.2	9.88 x 10^{-1}	1.23 x 10^{-2}	12.3
	0.4	1.98	3.90 x 10^{-2}	24.7
	0.5	2.47	5.65 x 10^{-2}	30.8
	1	4.94	1.79 x 10^{-1}	61.7
	2	9.88	5.67 x 10^{-1}	123
	4	19.8	1.80	247
	8	39.5	5.69	493
	16	79.0	18.0	987
	32	158	57.0	1,973
	54	267	136	3,330

6.3.3   Finite Element Analysis

Finite element analysis was utilised as a simulation tool which can provide information on the pressure drop along a micro- or millifluidic channel, and the velocity profile across a channel cross section. The Navier-Stokes equations, outlined in **Section 1.5.2** in **Chapter 1**,

describe the flow of incompressible fluids and were solved in two-dimensions. The equations assume the inertia effects of a fluid can be ignored, which is appropriate considering the low Reynolds values present in micro- and millifluidic devices.[4,15,49,50]

Computer simulations were performed for a variety of Q values for both concentrations of the worm-like micelle sample (4 and 5 w/w %). The finite element analysis calculations for the worm-like micelles in the cross-slot millifluidic system highlights the laminar nature of the flow. The velocity profile of the cross-section of an inlet channel is reminiscent of the straight channel millifluidic device (**Section 5.3.3**, **Chapter 5**) where the velocity is maximum in the centre of the channel, and non-existent at the walls (**Figure (6.5)** and **Figure (6.6)**). However, this changes rapidly within the expansion corresponding to the cross-slot section of the geometry. At this point, the velocity reduces drastically to zero within the stagnation point region.
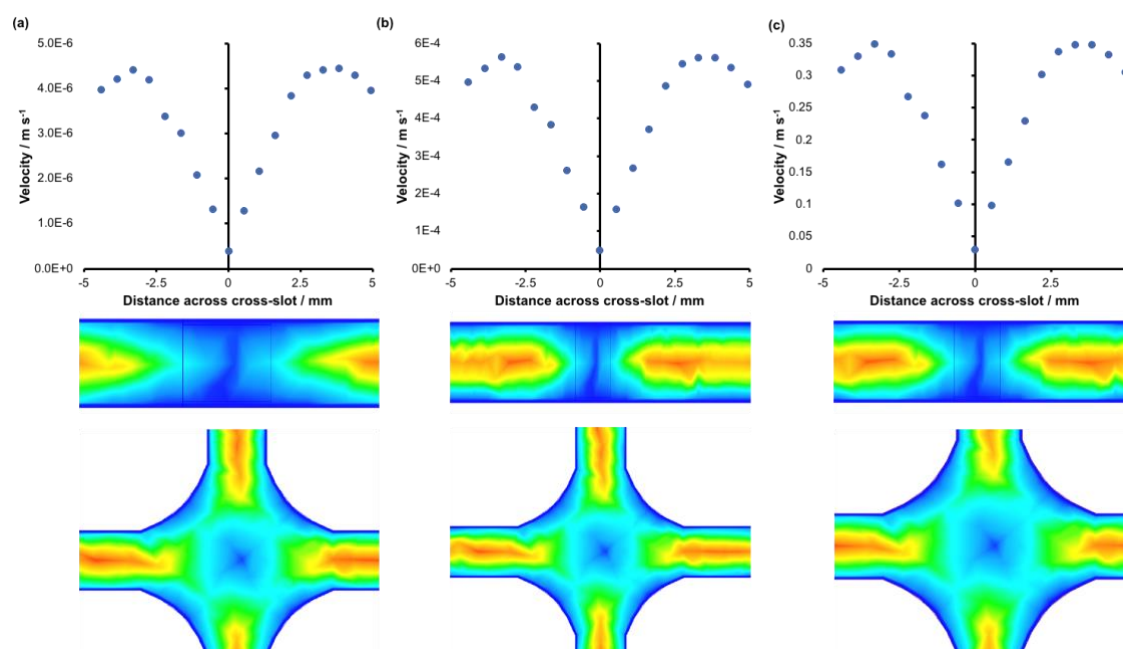

Figure (6.5). Velocity profiles across the stagnation point, and into the inlet channels for the 4 w/w % worm-like micelle sample as calculated using finite element analysis (FEA) for the following volumetric flow rates; (a) 0.00021 ml min^{-1}, (b) 0.025 ml min^{-1} and (c) 16 ml min^{-1}. The position of 0 mm indicates the centre of the cross-slot, where the stagnation point is located. Images below the graphs show the FEA along the plane of the inlet channels and across the cross-slot geometry with the stagnation point at the centre of both images.

The cross-sectional velocity profile across the cross-slot geometry during different Q values can be seen in **Figure (6.5)** for the 4 w/w % worm-like micelles and **Figure (6.6)** for the 5 w/w % worm-like micelles. These velocity profiles show a zero-velocity profile at the centre of the cross-slot geometry, where the stagnation point is located. Up until this point, the velocity is stable along the inlet channels. As Q increases, the magnitude of the velocity in the inlet channels increases as well, however, the location of the stagnation point remains stable throughout all simulations. This can be seen in the figures from FEA simulations (**Figure (6.5)** and **Figure (6.6)**), with the heat map showing the change in velocity across the cross-slot expansion.
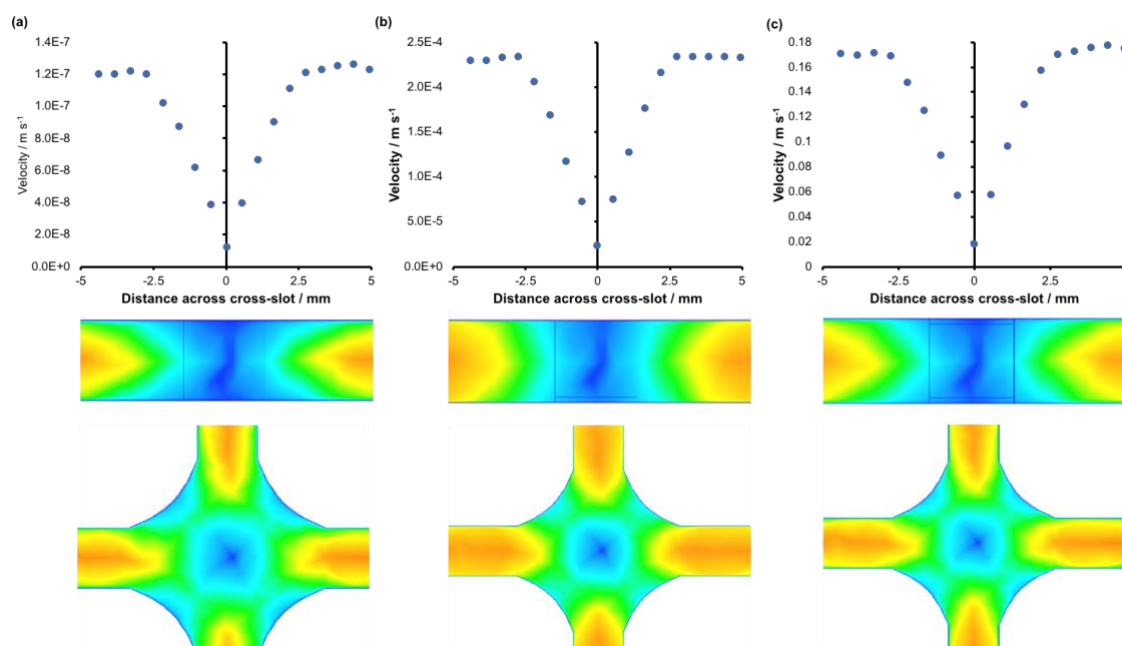

Figure (6.6). Velocity profiles across the stagnation point, and into the inlet channels for the 5 w/w % worm-like micelle sample as calculated using finite element analysis (FEA) for the following volumetric flow rates; **(a)** 0.00001 ml min^{-1}, **(b)** 0.025 ml min^{-1} and **(c)** 16 ml min^{-1}. The position of 0 mm indicates the centre of the cross-slot, where the stagnation point is located. Images below the graphs show the FEA along the plane of the inlet channels and across the cross-slot geometry with the stagnation point at the centre of both images.

The FEA simulations of the cross-slot geometry suggest this millifluidic device is suitable to investigate the effects of planar elongation on macromolecular samples, due to its low velocity at the stagnation point, which increases rapidly along the inlet and outlet channels.

6.3.4   Particle Tracking

Particle tracking was performed for the cross-slot geometry in order to compare the velocity profile qualitatively with FEA. The use of polystyrene tracer particles allowed the flow field to be qualitatively analysed for the 4 w/w % concentration. The pathway taken by the tracer particles can be seen in **Figure (6.7)** at two different Q values (0.1 and 0.5 ml min^{-1}). The movement of tracer particles over time indicates the flow is laminar. It was observed that particles at the edge of the channel had a very slow velocity and would be overtaken by particles located further away from the edge of the channel. In addition to this, particles in the centre of the inlet channels were observed slowing down as they entered the expansion of the channel before becoming trapped in the stagnation point. This work indicates the stable laminar flow within the device, with the presence of a stagnation point at the intersection of the four channels and agrees well with the FEA simulations.
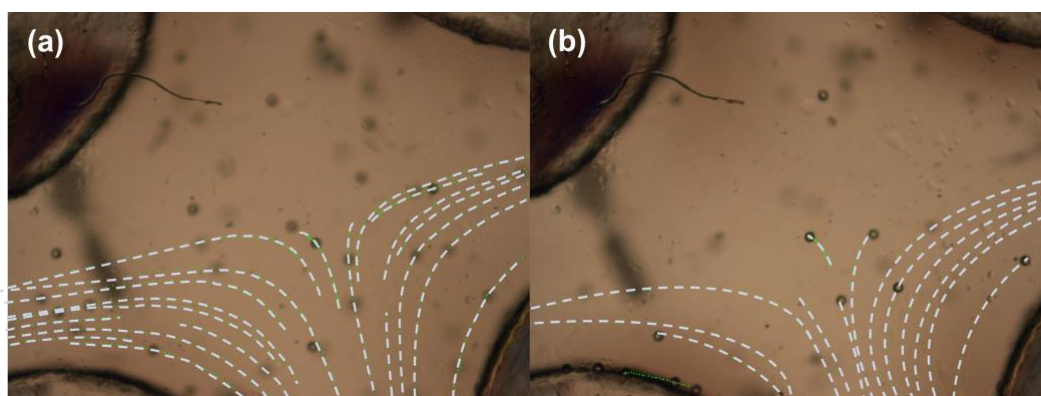

Figure (6.7). Particle tracking of the 4 w/w % concentration of worm-like micelles at two different volumetric flow rates. Green dots show the position of particles over a range of images, and the light blue broken lines show the pathway of the tracer particles through the cross-slot millifluidic device. **(a)** Q of 0.1 ml min^{-1}, particle movement traced over 50 images. **(b)** Q of 0.5 ml min^{-1}, particle movement traced over 25 images. The traces are shown only for lower part of the images.

6.3.5   Polarised Optical Microscopy

Polarised optical microscopy (POM) measurements were performed to analyse the birefringence of the material under flow in the cross-slot millifluidic geometry. The introduction of this chapter outlines how the birefringence of a material can be utilised to determine the planar

extensional viscosity (**Equation (6.4)**). As seen in **Section 5.3.4.2**, **Chapter 5**, this technique can be used to measure the degree of birefringence as a function of Q or as a function of location in the geometry.

For a cross-slot geometry, the strongest extensional flow regions are along the pathway between the two outlet channels; where planar extensional forces are present.[33,51,52] Therefore, the birefringence is expected to be brightest along this pathway as the worm-like micelles will have the greatest orientation in this region. This was observed for both concentrations of the wormlike micelle sample (**Figure (6.8)**). For the lower concentration sample, 4 w/w %, birefringence is not observed at 0.00021 ml min^{-1} but is present at 1 ml min^{-1} and strongest at 16 ml min^{-1} (**Figure (6.8)**). Images for the 5 w/w % concentration showed very weak birefringence at 0.0001 ml min^{-1} which was the lowest Q investigated for this concentration. The observed birefringence was strong at both 1 ml min^{-1} and 16 ml min^{-1} (**Figure (6.8)**).
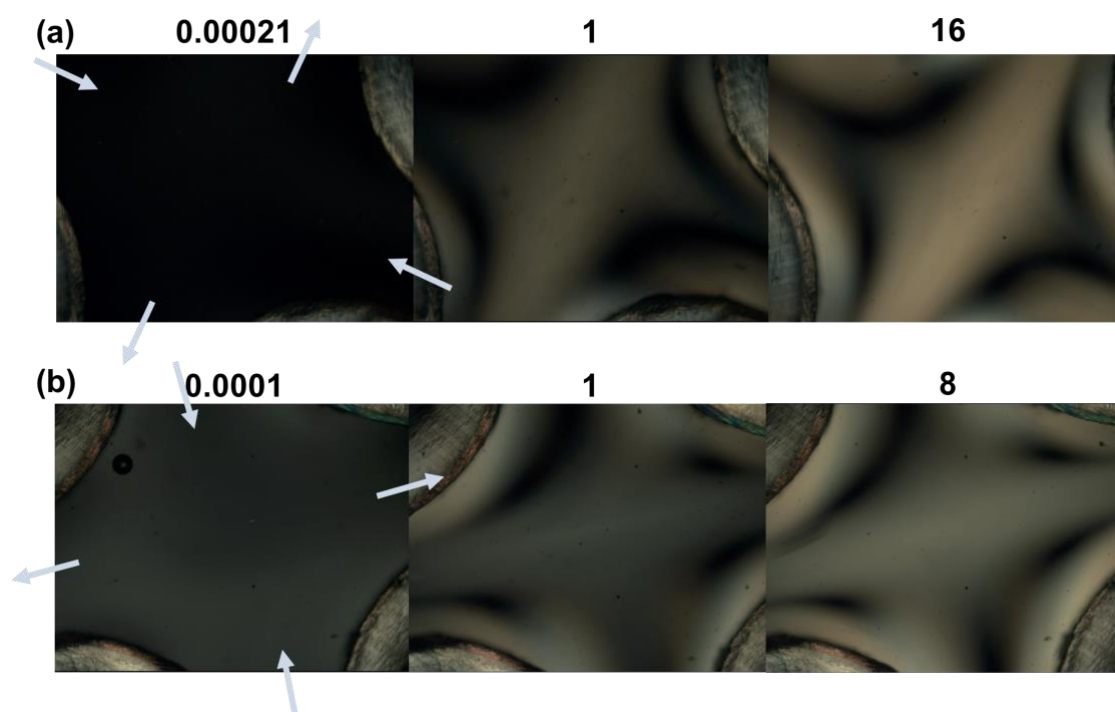

Figure (6.8). Polarised optical microscopy images with the volumetric flow rates stated above the image for **(a)** the 4 w/w % worm-like micelles and **(b)** the 5 w/w % concentration. Light blue arrows indicate the direction of flow. A slight tilt of the observed birefringence is due to the device resting at an angle in the microscope.

6.3.5.1   Degree of Birefringence (B) vs. Q

Polarised optical microscopy was also utilised to quantify the degree of birefringence present in the cross-slot geometry as a function of Q. A quantitative analysis of the degree of birefringence will indicate the degree of orientation of the anisotropic object present in the flow. The degree of orientation present in the material was calculated from **Equation (6.8)**, which uses the intensities of both the full light beam and the birefringent image, the wavelength of light and the channel height.

$$B = \frac{\delta\lambda}{2\pi H} = 2\left(\sin^{-1}\left(\frac{\sqrt{I}}{\sqrt{I_0}}\right) + \pi n\right)\frac{\lambda}{2\pi H}$$

(6.8)

Equation (6.8). The degree of birefringence (B / dimensionless) from an image can be calculated from the retardance of the extraordinary ray (δ / dimensionless), the wavelength (700 nm) of light (λ / nm) and the height of the channel (H / m). The retardance can be calculated from the intensity of light emitted from the material (I / cm^{-1}), the intensity of inherent polarised light (I_0 / cm^{-1}), and some integer, n.

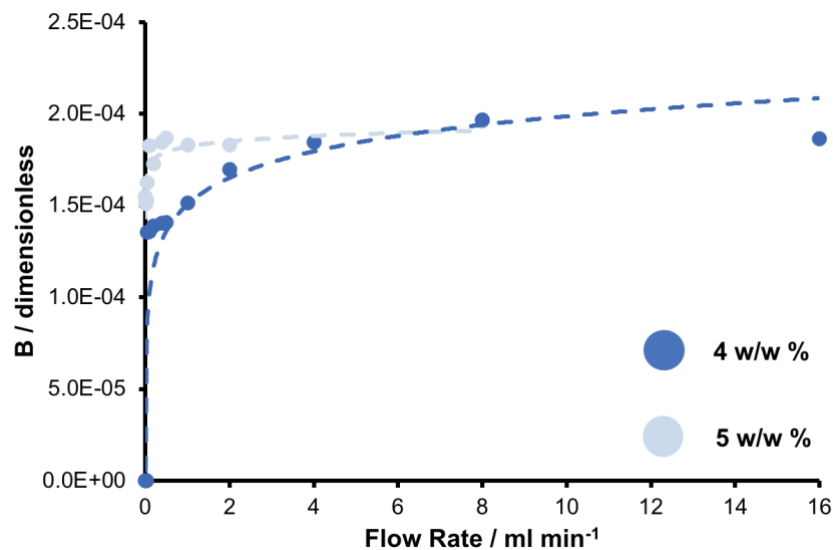**Figure (6.9).** The observed degree of birefringence (B / dimensionless) vs. volumetric flow rate (Q / ml min^{-1}) for the 4 and 5 w/w % concentrations of worm-like micelles. Dashed lines indicate data trends for the two concentrations.

The relationship between the degree of birefringence and Q within the cross-slot can be seen in **Figure (6.9)** for both the 4 and 5 w/w % sample of the worm-like micelles. As can be

seen, there was a sharp increase in the birefringence observed in the cross-slot as Q increased, up to 1 ml min^{-1}. After this Q, the change in degree of birefringence with Q slowed and began to plateau after 2 ml min^{-1}. The increase in birefringence with Q was expected as a greater proportion of material is oriented perpendicular to the inlet flow as Q increases. However, the plateau occurs when increasing Q has little effect; this is because a large amount of the material is already oriented along the flow, and a relatively small proportion of extra oriented material is not noticeable.

6.3.5.2   Calculating Planar Extensional Viscosity

It is well understood that the planar extensional viscosity is much greater than the equivalent shear viscosity.[53,54] However, accurate measurements of the planar extensional viscosity is often difficult to perform without suitable equipment.[2] As outlined in the introduction, the birefringence can also be quantitatively analysed to give an accurate calculation of the planar extensional viscosity, η_p via **Equation (6.4)**. The stress optical coefficient calculated in **Section 3.3.2**, **Chapter 3** (9.86 x 10^{-7} Pa^{-1} for 4 w/w % and 1.32 x 10^{-7} Pa^{-1} for the 5 w/w % worm-like micelles at 20 °C) was used in the calculation of the extensional viscosity.

The corresponding planar extensional viscosity was calculated for both the 4 and 5 w/w % samples of the wormlike micelles as a function of Q. The resulting viscosity values can be seen in **Figure (6.10)**. As can be observed, the planar viscosity at the lowest flow rates measured (3.7 x 10^2 Pa s at 0.05 ml min^{-1} for the 4 w/w % concentration, and 1.6 x 10^6 Pa s at 0.0001 ml min^{-1} for 5 w/w %) has been calculated to be much higher than the zero-shear viscosity (1.44 and 137 Pa s for 4 and 5 w/w % concentrations respectively, as measured in **Section 3.3.2**, **Chapter 3**). This data suggests a Trouton ratio of 257 and 11,580 for the 4 and 5 w/w % samples respectively.
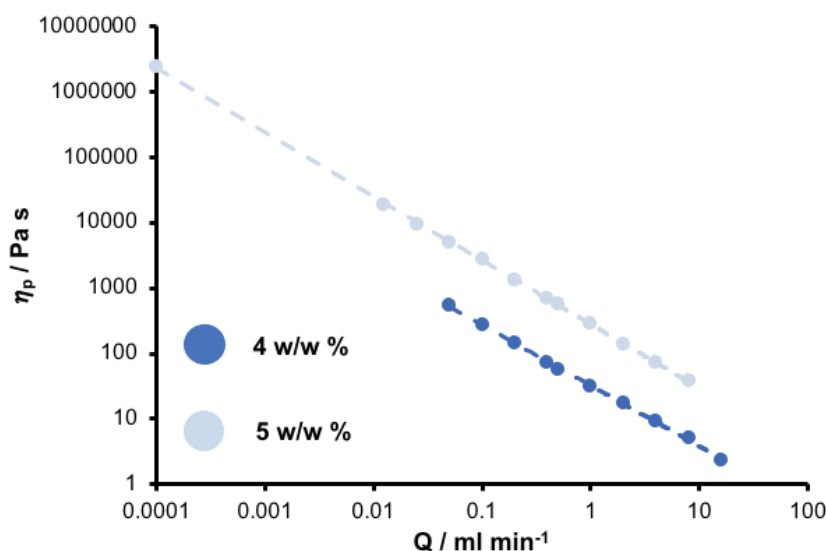
Figure (6.10). The calculated planar extensional viscosity (η_p / Pa s) as a function of volumetric flow rate (Q / ml min^{-1}) for both 4 and 5 w/w % concentrations of the worm-like micelles.

As expected, the Trouton ratio showed a strong dependency on concentration, which agrees well with literature on non-Newtonian materials.[55–57] Although these values appear large, Haward *et al*. recorded Trouton ratios of ~ 350 for a 0.05 w/w % solution of 1MDa poly(ethylene oxide) in 66 v/v % glycol.[29]

6.3.6 Small Angle X-ray Scattering (SAXS)

Laboratory SAXS measurements were performed on the 4 w/w % worm-like micelle material at various *Q*. Measurements were performed at 9 different locations in the device, along each inlet, and meeting in the middle to form a cross shape. Both anisotropic and isotropic scattering patterns were expected, depending on the location in the channel of the measurement being performed. All patterns were analysed using the Herman orientation function (**Equation (6.9)**), which was outlined in **Section 1.6.2.1**, **Chapter 1**. The resultant P$_2$ values can be compared against the birefringence from POM experiments. This comparison should provide further information into the flow characteristic of the cross-slot millifluidic channel.

$$P_2 = \frac{3\langle \cos^2 \phi \rangle - 1}{2} \tag{6.9}$$

Equation (6.9). The Hermann orientation parameter (P_2 / dimensionless) is a measure of the degree of orientation.

$$\langle \cos^2 \phi \rangle = \frac{\int_0^\pi (\cos^2 \phi) \Delta I(\phi) \sin \phi \, d\phi}{\int_0^\pi \Delta I(\phi) \sin \phi \, d\phi} \tag{6.10}$$

Equation (6.10). The $\cos^2 \phi$ function in **Equation (6.9)** is defined using the azimuthal angle (ϕ / °), and the intensity of scattered X-rays at that angle ($I(\phi)$ / cm^{-1}).
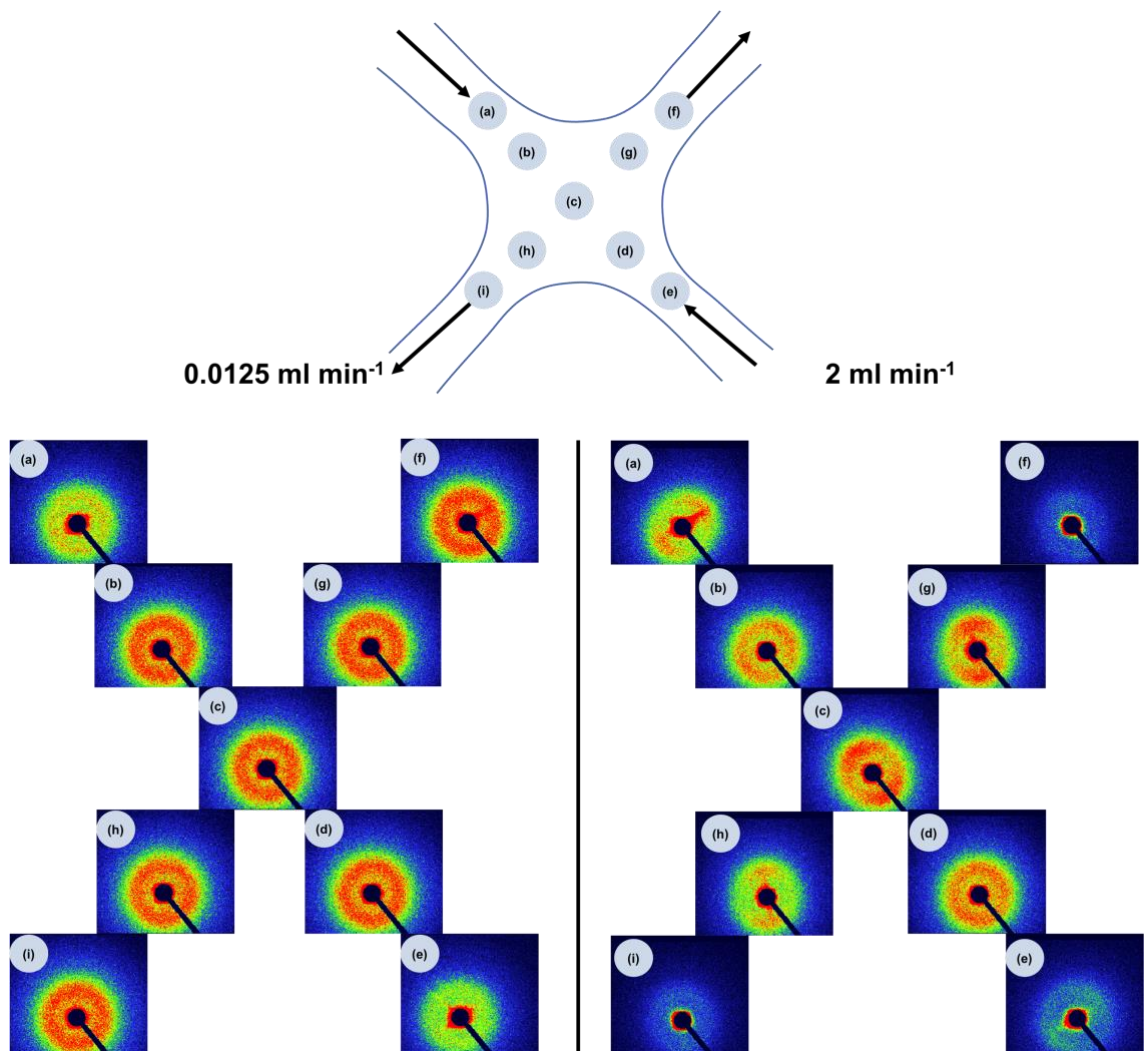

Figure (6.11). Representative SAXS patterns across the cross-slot millifluidic device for the 4 w/w % worm-like micelle sample at two different volumetric flow rates (0.0125 ml min^{-1} and 2 ml min^{-1}). The position of each SAXS pattern is recorded in the light blue circle on each 2D image as well as the schematic of the cross-slot at the top of the figure.

The lowest Q measured was 0.0125 ml min^{-1}, and the highest was 3 ml min^{-1}. Higher volumetric flow rates were not investigated due to the length of time required to complete acquisitions at each location (5 minutes), which limited the maximum Q able to be tested based on the volume of material available in fully loaded syringe (3 ml min^{-1} x 5 min requires 15 ml of sample per inlet, total volume required is 30 ml).

At the lowest volumetric flow rate investigated (0.0125 ml min^{-1}), isotropic scattering patterns were collected along the cross-slot geometry. Anisotropic scattering of the worm-like micelle sample became more obvious as Q increased but was also found to be dependent on position within the cross-slot millifluidic device, as expected. Examples of this behaviour can be seen in **Figure (6.11)** for measurements at both 0.0125 ml min^{-1} and 2 ml min^{-1}.
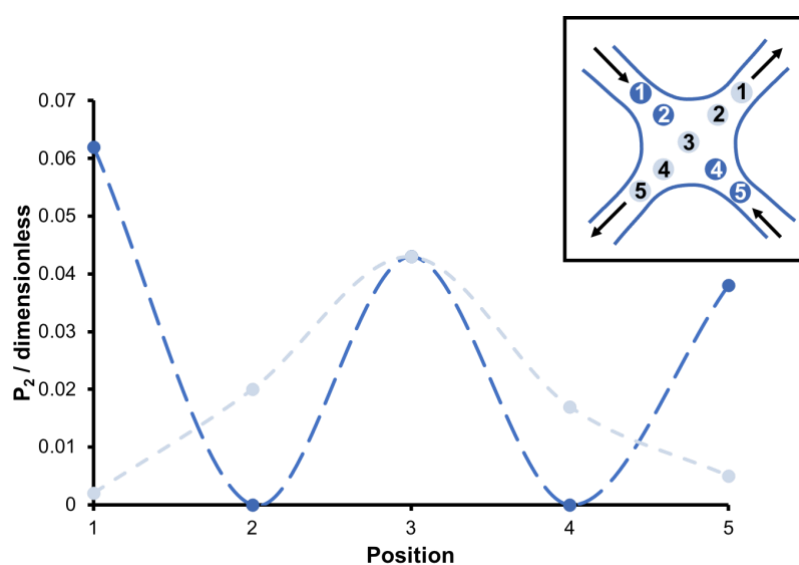
Figure (6.12). Graph of degree of orientation (P$_2$ / dimensionless) against the position in the cross-slot millifluidic device for the 4 w/w % worm-like micelle sample at a volumetric flow rate of 2 ml min^{-1}. The dark blue data points correspond to the SAXS patterns collected along the inlet plane (top let to bottom right on the inset diagram) and the light blue data points are from SAXS patterns collected along the outlet plane (top right to bottom left on the inset diagram). Position labels are identified in the inset diagram for clarity.

The trend in anisotropic scattering across the cross-slot channel can be observed when plotting the degree of orientation against position along both the inlet and outlet planes (**Figure (6.12)**). In this graph, strong orientation is observed at the mouth of the inlet channels where pipe

flow is present. If SAXS measurements were collected in the centre of the inlet channel, no orientation would be expected due to the zero shear conditions present in this location, as explored in **Section 5.2.5.2**, **Chapter 5**. However, SAXS measurements performed on the laboratory SAXS instrument measure a relatively large area of the channel due to the large size of the beam (0.6 *x* 0.5 mm for the measurements performed), compared to synchrotron SAXS measurements. Due to these large beam sizes, it is difficult to only collect scattering data for the small region of unoriented material in the centre of the inlet channel. However, as the material enters the expansion of the millifluidic geometry, the orientation disappears. When the two inlet fluid streams meet, the material is once again oriented, due to the extensional forces acting on the sample. The degree of orientation reduces as the material moves progressively closer to the outlet channels as these extensional forces are not as strong as they are at the stagnation point.
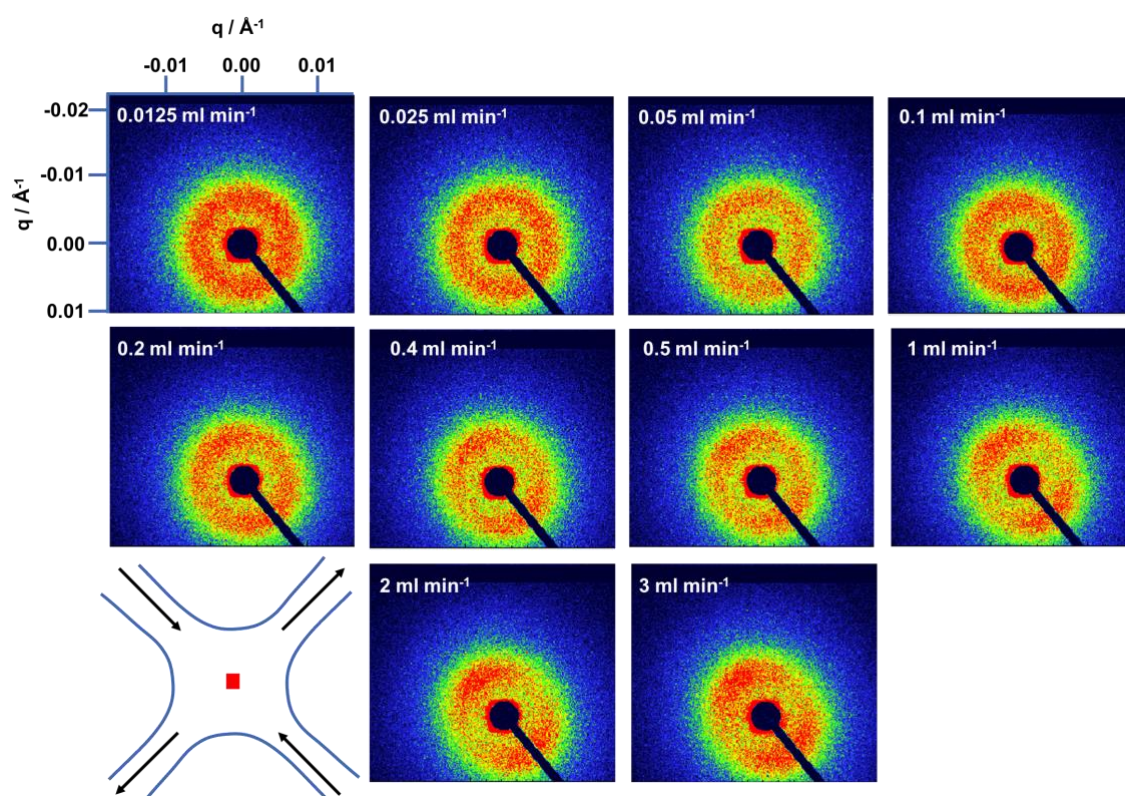
Figure (6.13). Representative 2D SAXS patterns at the centre of the millifluidic device for a variety of volumetric flow rates. The volumetric flow rates are indicated in the top left hand of each image. A schematic of the millifluidic device is shown in the bottom left with the arrows indicating the direction of flow and the red square indicating the location where the SAXS pattern was acquired. The schematic and beam stop are to scale.

As Q increased, the anisotropic scattering at the stagnation point increased (**Figure (6.13)**). It can be seen that the scattering patterns are isotropic at low volumetric flow rates (less that 0.05 ml min^{-1}). However, these scattering patterns become increasingly more anisotropic as Q increases. The relationship between the degree of orientation and Q can be seen in **Figure (6.14)**; where the trend shows a sharp increase in the degree of birefringence up until a Q of 0.5 ml min^{-1}. After this Q, the change in degree of orientation is less drastic, but is still increasing at the highest Q measured, 3 ml min^{-1}.
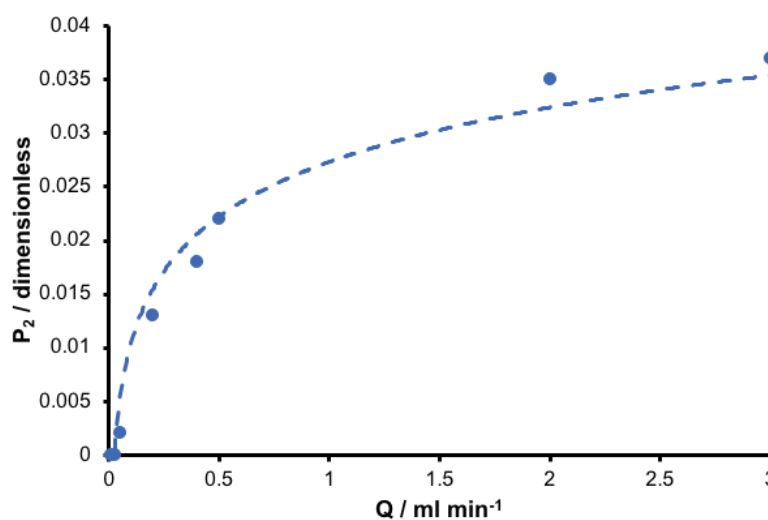
Figure (6.14). Graph of the degree of orientation (P_2 /dimensionless) against volumetric flow rate (Q / ml min^{-1})for the scattering patterns collected at the centre of the millifluidic cross-slot.

SAXS measurements performed at the I22 beamline at Diamond Light Source, UK utilised the ability to fully map the cross-slot millifluidic channel. The high X-ray flux associated with synchrotron SAXS instruments allows the collection of good quality scattering data over very short time scales: on the order of seconds. The microfocus beam capabilities also enable SAXS measurements of precise locations within the cross-slot millifluidic device. These advantages highlight the benefits of synchrotron SAXS over laboratory SAXS measurements. Mapping the cross-slot area allowed the investigation of anisotropic scattering as a function of position. Both the 4 and 5 w/w % concentrations of the worm-like micelles were
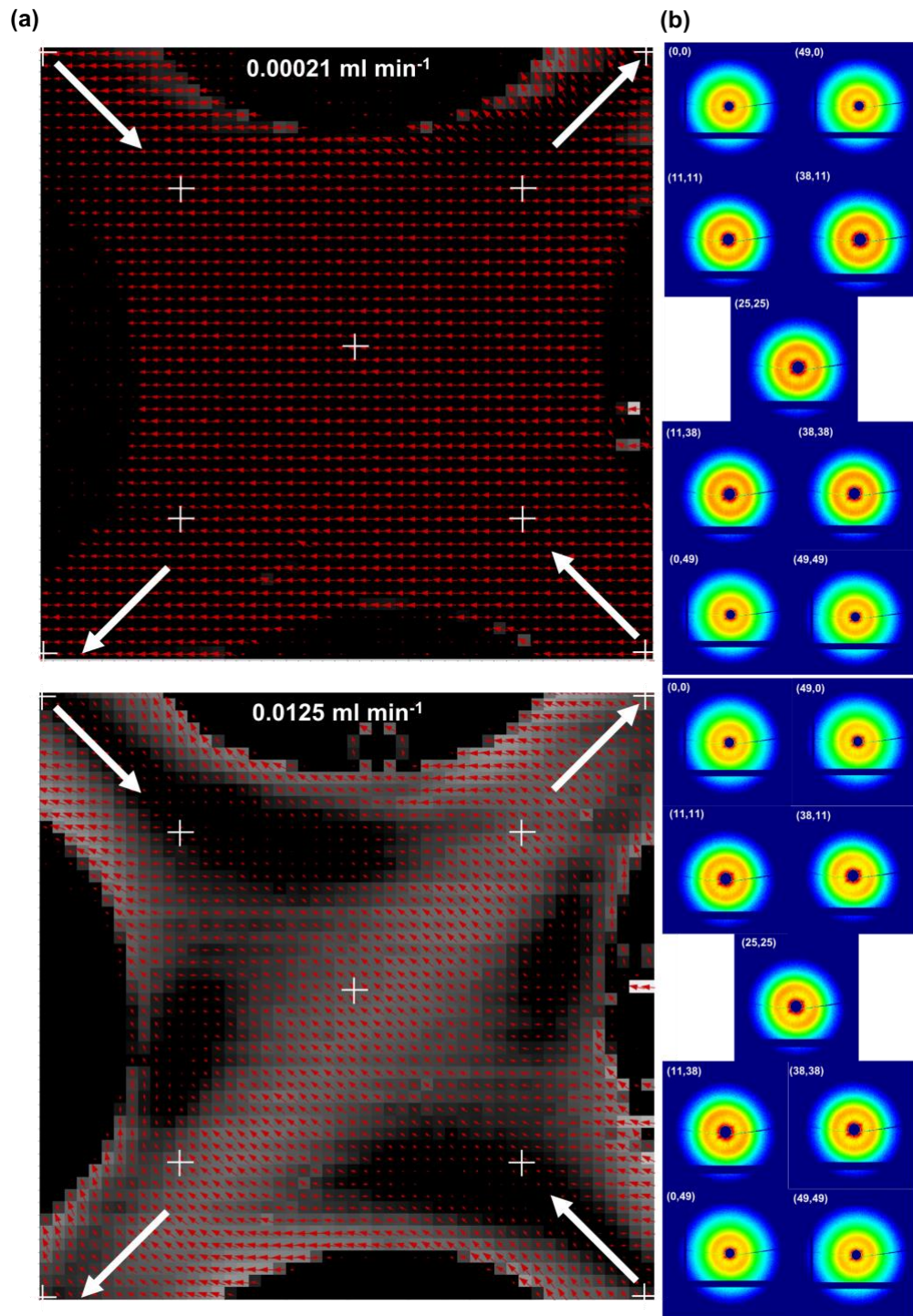
Figure (6.15). Mapped SAXS measurements of the 4 w/w % worm-like micelle at two volumetric flow rates (0.00021 and 0.0125 ml min^{-1}). **(a)** Heat map relating to the magnitude of orientation present in the two-dimensional SAXS pattern at a specific location in the cross-slot, with the magnitude and direction of orientation of the scattering pattern shown with the red vectors. The white arrows indicate the direction of flow along the inlet and outlet channels. The intersection of the white lines shows the location of the SAXS images shown in **(b)**. **(b)** Two-dimensional SAXS pattern showing the change in anisotropy across the cross-slot, from the middle of each outlet channel to the centre of the cross-slot where the stagnation point is. The numbers in the top left relate to the map co-ordinates in **(a)**.

investigated, at three different volumetric flow rates for each sample; 0.00021, 0.125 and 0.1 ml

min^{-1} for the 4 w/w % sample, and 0.0125, 0.1 and 0.2 ml min^{-1} for the 5 w/w % sample.

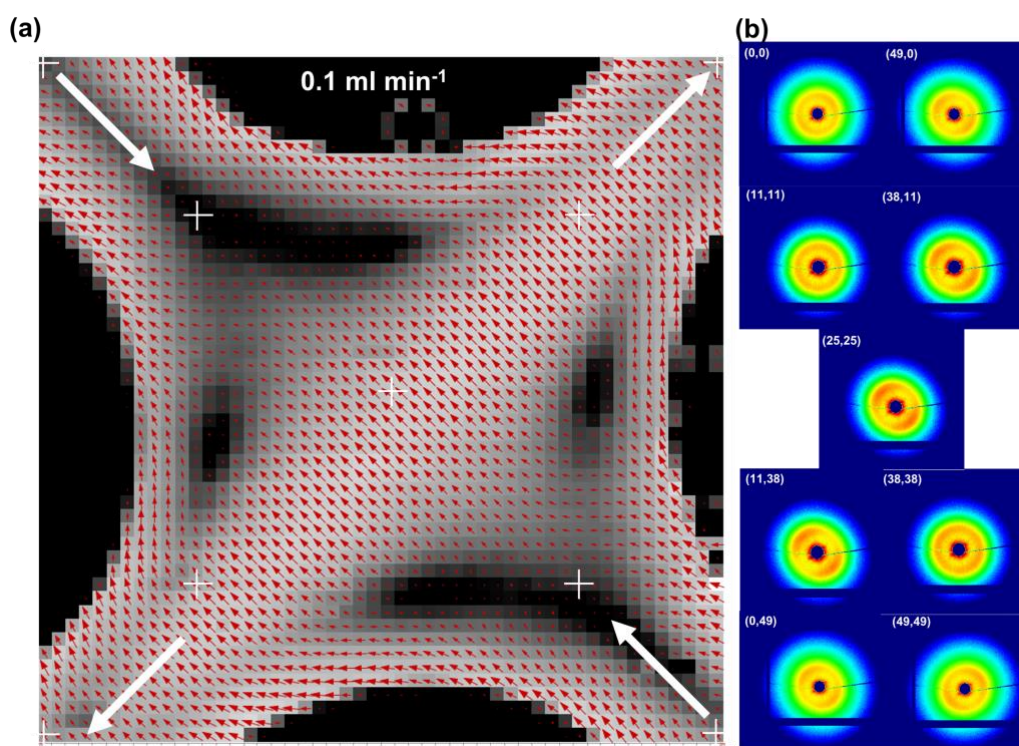**Figure (6.16).** Mapped SAXS measurements of the 4 w/w % worm-like micelle at 0.1 ml min^{-1}. **(a)** Heat map relating to the magnitude of orientation present in the two-dimensional SAXS pattern at a specific location in the cross-slot, with the magnitude and direction of the orientation of the scattering pattern shown with the red vectors. The white arrows indicate the direction of flow along the inlet and outlet channels. The intersection of the white lines shows the location of the SAXS images shown in **(b)**. **(b)** Two-dimensional SAXS pattern showing the change in anisotropy across the cross-slot, from the middle of each outlet channel to the centre of the cross-slot where the stagnation point is. The numbers in the top left relate to the map co-ordinates in **(a)**.

It can be seen in **Figure (6.15)** and **Figure (6.16)**, corresponding to the 4 w/w % sample,

how the mapped data changes as a function of Q. The images show a heat map corresponding to

the degree of orientation, with white indicating the highest values and black indicating the lowest.

A vector map placed over these heat maps shows the orientation direction of the scattering

patterns. Example 2D scattering patterns can be observed at 9 positions along the millifluidic

cross-slot geometry. It can be seen in **Figure (6.15)(a)**, which corresponds to a Q of 0.00021 ml

min^{-1}, there is little orientation present in the cross slot device. This was expected as Q is below the critical volumetric flow rate required for orientation in the straight channel millifluidic device, as explored in **Section 5.3.5.2**, **Chapter 5**. However, as Q increases (**Figure (6.15)(b)** and **Figure (6.16)(b)**) strong orientation perpendicular to the flow direction is observed in the maps collected: strong evidence that the worm-like micelles are oriented along the direction of flow.
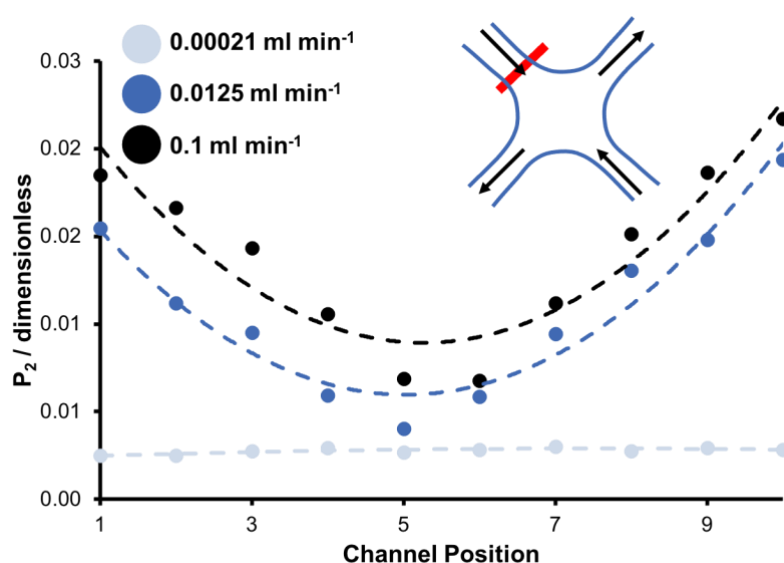
Figure (6.17). Degree of orientation (P_2 / dimensionless) against channel position in the inlet channel for the cross-slot millifluidic device, for three flow rates of the 4 w/w % worm-like micelles (0.00021, 0.0125 and 0.1 ml min^{-1}). The red box on the inset schematic shows the area where data was taken.

Another key comparison to note is that the inlet flow is analogous to the flow geometry considered in **Chapter 5**: flow through a square channel. Along the centre line the shear rate is zero, no birefringence is observed because the worm-like micelles are unoriented and the scattering patterns are isotropic, as exemplified by the patterns labelled 0,0 and 49,49 in **Figure (6.15)(b).** In contrast the scattering patterns gathered close to the wall are strongly oriented and the degree of orientation depends on the shear rate. As the flow rate increases so does the shear rate at the wall and this affect can be seen in the calculated P_2 values and the orientation in the scattering patterns **Figure (6.17)**. It is important to note that the resolution of the map is not fine enough to distinguish the lack of orientation in the middle of the inlet channel.

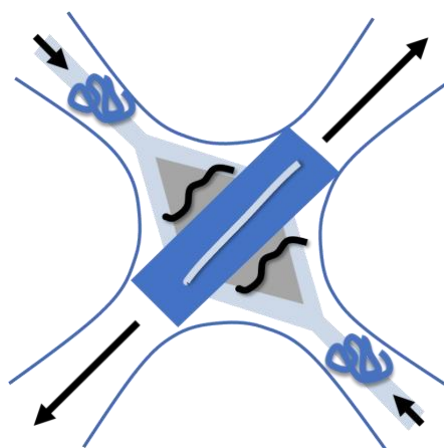**Figure (6.18).** A basic schematic of orientation of the worm-like micelles across the cross-slot millifluidic device. Three areas with different orientation were identified; The first region (light blue) was at the centre of the inlet channels and within two branches from this region, into the cross-slot expansion where no orientation was observed by SAXS. This region indicates the presence of randomly coiled worm-like micelles. Secondly, a triangular shaped region (grey) where collected SAXS patterns correlated to worm-like micelles with a small degree of orientation in the direction of the outlet channels. The third orientation region was within the centre of the cross-slot expansion region, along the outlet plane where SAXS patterns indicated strong orientation of the worm-like micelles, aligned along the path of the outlet channels.

These maps show orientation along the plane of the outlet channels, and at the edges of the inlets, creating a 'Y' shaped region of unoriented material at the exit of both inlet channels. Strong anisotropic scattering can be seen in the 2D scattering pattern along the centreline of the outlet plane, in **Figure (6.15)** and **Figure (6.16)**. The anisotropic scattering is strongest at the centre of the cross-slot geometry, where the stagnation point is located (Inset numbered (24,24) in **Figure (6.15)(b)** and **Figure (6.16)(b)**). The orientation adopted by the worm-like micelles at different regions within the cross-slot millifluidic device is represented schematically in **Figure (6.18)**. The degree of orientation, as a function of channel position can be seen in **Figure (6.18)**, with regions of unoriented material, indicating randomly coiled worm-like micelles, along the inlet channels (light blue). Regions parallel to the outlet stems, but not in line with these outlets, showed some orientation of the worm-like micelles along this direction (grey) and regions of strong orientation of the worm-like micelles (colour coded blue) along the outlet streams, where the extension force is strongest.
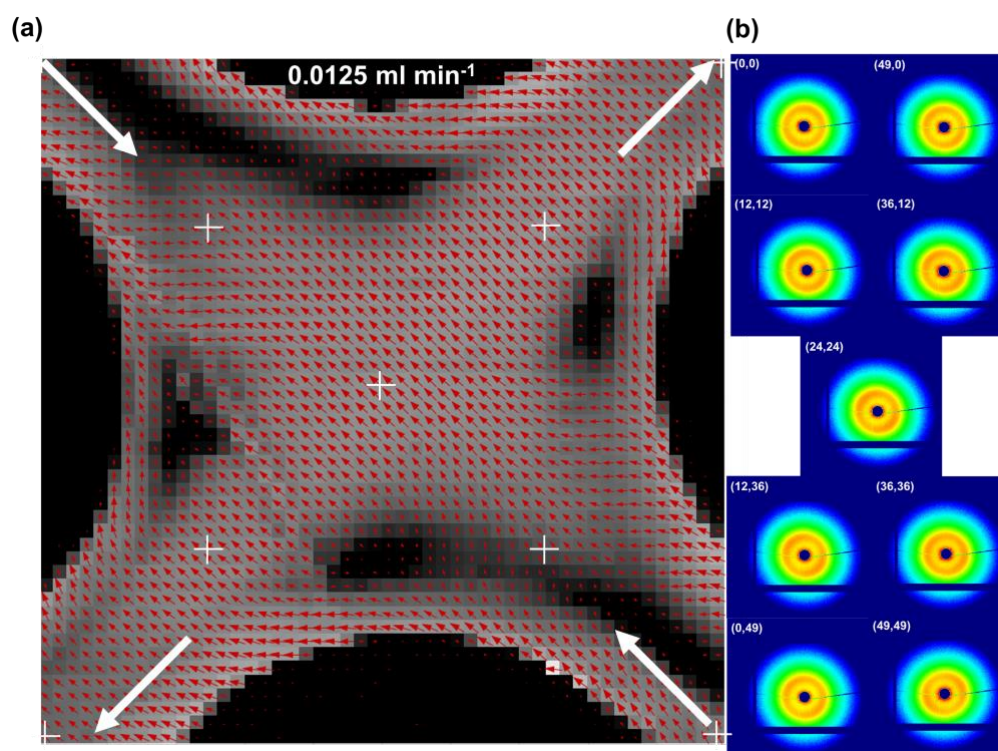
Figure (6.19). Mapped SAXS measurements of the 5 w/w % worm-like micelle at a single volumetric flow rate of 0.0125 ml min^{-1}. **(a)** Heat map relating to the magnitude of orientation present in the two-dimensional SAXS pattern at a specific location in the cross-slot, with the magnitude and direction of orientation shown with the red vectors. The white arrows indicate the direction of flow along the inlet and outlet channels. The intersection of the white lines shows the location of the SAXS images shown in **(b)**. **(b)** Two-dimensional SAXS pattern showing the change in anisotropy across the cross-slot, from the middle of each outlet channel to the centre of the cross-slot where the stagnation point is. The numbers in the top left relate to the map co-ordinates in **(a)**.

The mapped SAXS data corresponding to the 5 w/w % concentration can be seen in **Figure (6.19)** and **Figure (6.20)**. All three of the volumetric flow rates measured showed strong orientation in the cross- slot millifluidic device. However, as Q increases, the orientation observed along the outlet plane increases in intensity (see 2D scattering pattern inserts in **Figure (6.19)** and **Figure (6.20)**). As with the 4 w/w % sample, the anisotropic scattering is strongest at the centre of the cross-slot geometry, where the stagnation point is located (insert numbered (24,24) in **Figure (6.19)** and **Figure (6.20)**).
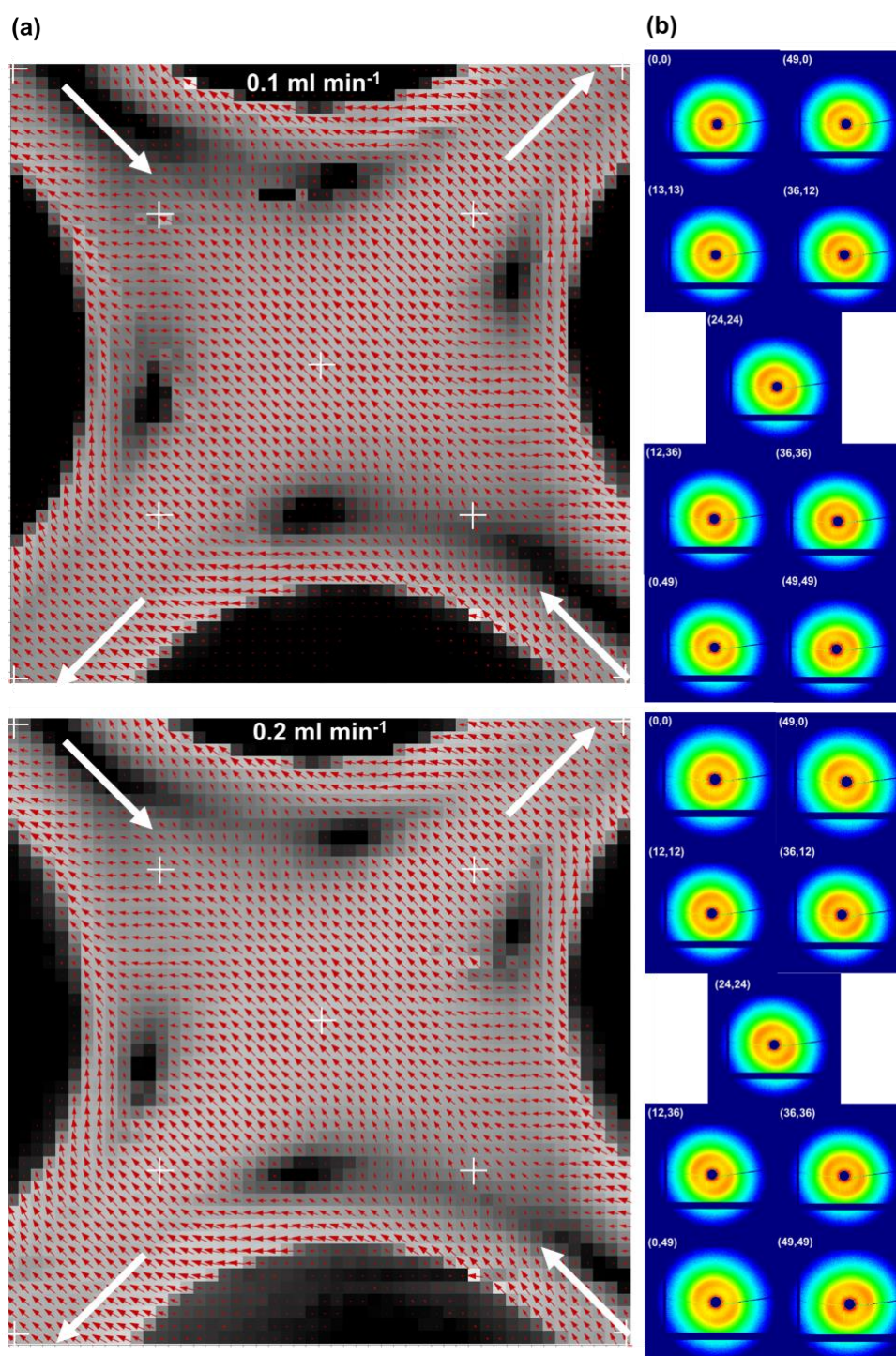
Figure (6.20). Mapped SAXS measurements of the 5 w/w % worm-like micelle at two volumetric flow rates (0.1 and 0.2 ml min^{-1}). **(a)** Heat map relating to the magnitude of orientation present in the two-dimensional SAXS pattern at a specific location in the cross-slot, with the magnitude and direction of orientation shown with the red vectors. The white arrows indicate the direction of flow along the inlet and outlet channels. The intersection of the white lines shows the location of the SAXS images shown in **(b)**. **(b)** Two-dimensional SAXS pattern showing the change in anisotropy across the cross-slot, from the middle of each outlet channel to the centre of the cross-slot where the stagnation point is. The numbers in the top left relate to the map co-ordinates in **(a)**.

In the case of the cross-slot millifluidic device, both laboratory SAXS and synchrotron SAXS impart important information about the orientation of material within the channel geometry. However, it is clear that due to microfocus capabilities offered by synchrotron SAXS beamlines, coupled with much higher flux, these instruments provide an extensive picture of the orientation as a function of position within the millifluidic channel as well as containing detailed information about structural morphology of the material (for example, cross-sectional radius of the worms, their flexibility, contour length and solubility of the core).[58,59] This has proven invaluable in both the characterisation of the device, but also in looking forward to the use of these millifluidic device in combination with novel materials.
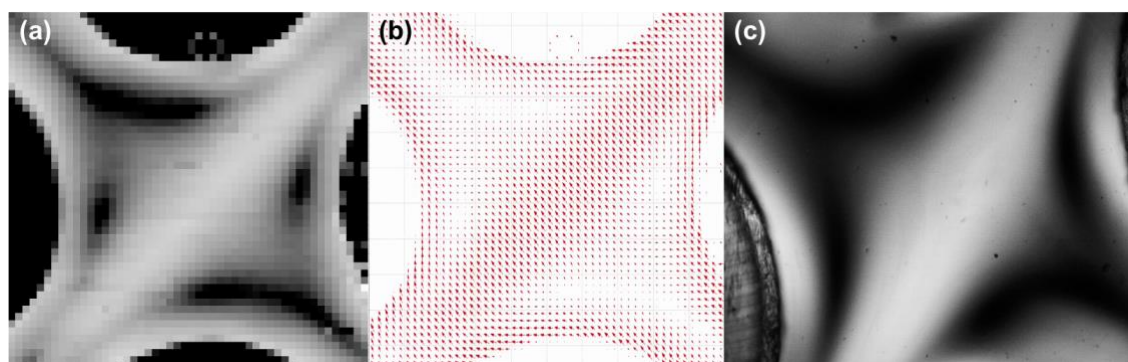
Figure (6.21). Comparison of **(a)** heat map, **(b)** vector map (both relating to the orientation of SAXS data at 0.1 ml min^{-1}) and **(c)** birefringence at 16 ml min^{-1} for the 4 w/w % worm-like micelles, converted to greyscale for ease of comparison.

Comparing the mapped data with POM images shows a similar trend of orientation across the device, with POM images also showing the 'Y' shaped area of non-oriented material (**Figure (6.21)**). The degree of orientation maps also shows a distinct pattern across the device, with a symmetry indicating the expected four-fold symmetry around the stagnation point. The maps of scattering data collected from I22 at Diamond Light Source show the excellent stability of flow in the cross-slot millifluidic device. The trend in orientation across the device indicates the stable laminar nature of flow. The claim of flow stability in the device is further evidenced by the fact that each map comprised of 2500 SAXS patterns and took over 40 minutes to acquire.

Table (6.3). Overview of analysis data for the characterisation of the cross-slot millifluidic device using the two worm-like micelle samples. Concentration is denoted by C, volumetric flow rate, Q and Hencky strain, $\dot{\varepsilon}_H$. The data includes planar extensional viscosity (η_p), the degree of birefringence (B) and the degree of orientation (P_2) from lab-SAXS measurements.

C / w/w %	Q / ml min^{-1}	$\dot{\varepsilon}_H$ / s^{-1}	η_p / Pa s	B / dimensionless	P_2 / dimensionless
4	2.1 x 10^{-4}	1.04 x 10^{-3}	-	-	-
	0.0125	6.17 x 10^{-2}	-	-	0
	0.025	1.23 x 10^{-1}	-	-	0
	0.05	2.47 x 10^{-1}	-	-	0.002
	0.1	4.94 x 10^{-1}	556	1.35 x 10^{-4}	-
	0.2	9.88 x 10^{-1}	279	1.36 x 10^{-4}	0.013
	0.4	1.98	143	1.39 x 10^{-4}	0.018
	0.5	2.47	72.2	1.41 x 10^{-4}	0.022
	1	4.94	57.8	1.41 x 10^{-4}	-
	2	9.88	31.1	1.51 x 10^{-4}	0.035
	4	19.8	17.4	1.70 x 10^{-4}	-
	6	39.5	9.47	1.84 x 10^{-4}	-
	8	79.0	5.05	1.97 x 10^{-4}	-
	16	158	2.40	1.87 x 10^{-4}	-
5	1.3 x 10^{-5}	4.94 x 10^{-3}	2379786	1.55 x 10^{-4}	-
	0.0125	6.17 x 10^{-2}	18593	1.51 x 10^{-4}	-
	0.025	1.23 x 10^{-1}	9409	1.53 x 10^{-4}	-
	0.05	2.47 x 10^{-1}	5000	1.63 x 10^{-4}	-
	0.1	4.94 x 10^{-1}	2805	1.82 x 10^{-4}	-
	0.2	9.88 x 10^{-1}	1327	1.73 x 10^{-4}	-
	0.4	1.98	709	1.84 x 10^{-4}	-
	0.5	2.47	574	1.87 x 10^{-4}	-
	1	4.94	282	1.83 x 10^{-4}	-
	2	9.88	141	1.83 x 10^{-4}	-
	4	19.8	71.2	1.85 x 10^{-4}	-
	8	39.5	37.7	1.96 x 10^{-4}	-

6.4 Conclusions

A cross-slot millifluidic device, analogous to a four-roll mill, has been successfully designed and fabricated by stereolithographic 3D printing. The use of mica discs as windows were satisfactory in creating a good seal, with no leakage observed up to the maximum volumetric flow rate tested. Calculations of *Re* numbers indicated fully laminar flow behaviour for both

concentrations of the worm-like micelles tested at all volumetric flow rates. This was further confirmed by FEA simulations, particle tracing and polarised optical measurements.

Laboratory SAXS measurements gave good preliminary data into the flow behaviour across the cross-slot, with strong orientation seen at centre of the millifluidic device, where the stagnation point was located. This confirmed the presence of strong planar extensional forces in this region. However, data acquisition at a synchrotron SAXS beamline allowed for greater spatial resolution to be achieved, due to the advantage of a small beam size and high flux. This allowed for extensive mapping of the cross-slot millifluidic device, with good comparisons between POM images and SAXS maps.

Overall, the work discussed in this Chapter outlines how a relatively simple design and fabrication process, using desktop 3D printing, enables complex flow geometries to be explored. Investigation of the capabilities of the cross-slot millifluidic device, show it can be successfully utilised to employ extensional flow onto viscous materials in combination with a range of measurement techniques.

6.5 References

(1)   Brimmo, A. T.; Qasaimeh, M. A. *RSC Adv.* **2017**, *7*, 51206–51232.
(2)   Haward, S. J. *Biomicrofluidics* **2016**, *10*, 1–27.
(3)   Galindo-Rosales, F. J.; Alves, M. A.; Oliveira, M. S. N. *Microfluid. Nanofluidics* **2013**, *14*, 1–19.
(4)   Pipe, C. J.; McKinley, G. H. *Mech. Res. Commun.* **2009**, *36*, 110–120.
(5)   Sousa, P. C.; Pinho, F. T.; Alves, M. A. *Soft Matter* **2018**, *14*, 1344–1354.
(6)   Hencky, H. *ZAMM - Zeitschrift für Angew. Math. und Mech.* **1923**, *3*, 241–251.
(7)   Wulf, K. *Acta Polym.* **1985**, *36*, 296–297.
(8)   Trouton, F. T. *Proc. R. Soc. London. Ser. A, Contain. Pap. a Math. Phys. Character* **1906**, *77*, 426–440.
(9)   Taylor, G. I. *Proc. R. Soc. London. Ser. A, Contain. Pap. a Math. Phys. Character* **1934**, *146*, 501–523.
(10)   Scrivener, O.; Berner, C.; Cressely, R.; Hocquart, R.; Sellin, R.; Vlachos, N. S. *J. Nonnewton. Fluid Mech.* **1979**, *5*, 475–495.
(11)   Haward, S. J.; Jaishankar, A.; Oliveira, M. S. N.; Alves, M. A.; McKinley, G. H. *Biomicrofluidics* **2013**, *7*, 1–15.
(12)   Johnson-Chavarria, E. M.; Tanyeri, M.; Schroeder, C. M. *J. Vis. Exp.* **2011**, *47*, 1–5.
(13)   Coventry, K. D.; Mackley, M. R. *J. Rheol. (N. Y. N. Y).* **2008**, *52*, 401–415.
(14)   Lord, T. D.; Scelsi, L.; Hassell, D. G.; Mackley, M. R.; Embery, J.; Auhl, D.; Harlen, O.

G.; Tenchev, R.; Jimack, P. K.; Walkley, M. A. *J. Rheol. (N. Y. N. Y).* **2010**, *54*, 355–373.

(15) Haward, S. J.; Mckinley, G. H.; Shen, A. Q. *Sci. Rep.* **2016**, *6*, 1–18.

(16) Sharma, V.; Haward, S. J.; Serdy, J.; Keshavarz, B.; Soderlund, A.; Threlfall-Holmes, P.; McKinley, G. H. *Soft Matter* **2015**, *11*, 3251–3270.

(17) Kato, M.; Shirakashi, M.; Takahashi, T. *Rheol. Acta* **2017**, *56*, 649–659.

(18) Dubash, N.; Cheung, P.; Shen, A. Q. *Soft Matter* **2012**, *8*, 5847–5856.

(19) Del Giudice, F.; Haward, S. J.; Shen, A. Q. *J. Rheol. (N. Y. N. Y).* **2017**, *61*, 327–337.

(20) Perkins, T. T.; Smith, D. E.; Chu, S. *Science (80-.).* **1997**, *276*, 2016–2021.

(21) Stone, P. A.; Hudson, S. D.; Dalhaimer, P.; Bischer, D. E.; Amis, E. J.; Migler, K. B. *Macromolecules* **2006**, *39*, 7144–7148.

(22) Valverde, L. R.; Li, B.; Schroeder, C. M.; Wilson, W. L. *Langmuir* **2019**, *35*, 10947–10957.

(23) Schroeder, C. M.; Babcock, H. P.; Shaqfeh, E. S. G.; Chu, S. *Science (80-.).* **2003**, *301*, 1515–1519.

(24) Haward, S. J. *Biopolymers* **2014**, *101*, 287–305.

(25) Hoyle, D. M.; Huang, Q.; Auhl, D.; Hassell, D.; Rasmussen, H. K.; Skov, A. L.; Harlen, O. G.; Hassager, O.; McLeish, T. C. B. *J. Rheol. (N. Y. N. Y).* **2013**, *57*, 293–313.

(26) Pathak, J. A.; Hudson, S. D. *Macromolecules* **2006**, *39*, 8782–8792.

(27) Haward, S. J.; Odell, J. A.; Berry, M.; Hall, T. *Rheol. Acta* **2011**, *50*, 869–879.

(28) Auhl, D.; Hoyle, D. M.; Hassell, D.; Lord, T. D.; Harlen, O. G.; Mackley, M. R.; McLeish, T. C. B. *J. Rheol. (N. Y. N. Y).* **2011**, *55*, 875–900.

(29) Haward, S. J.; Oliveira, M. S. N.; Alves, M. A.; McKinley, G. H. *Phys. Rev. Lett.* **2012**, *109*, 1–5.

(30) Xi, L.; Graham, M. D. *J. Fluid Mech.* **2009**, *622*, 145–165.

(31) Cruz, F. A.; Poole, R. J.; Afonso, A. M.; Pinho, F. T.; Oliveira, P. J.; Alves, M. A. *J. Nonnewton. Fluid Mech.* **2014**, *214*, 57–68.

(32) Galindo-Rosales, F. J.; Oliveira, M. S. N.; Alves, M. A. *RSC Adv.* **2014**, *4*, 7799–7804.

(33) Kalb, A.; Villasmil, U. L. A.; Cromer, M. *Phys. Rev. Fluids* **2017**, *2*, 1–10.

(34) Abed, W. M.; Domingues, A. F.; Poole, R. J.; Dennis, D. J. C. *Int. J. Therm. Sci.* **2017**, *121*, 249–265.

(35) Kalb, A.; Villasmil-Urdaneta, L. A.; Cromer, M. *J. Nonnewton. Fluid Mech.* **2018**, *262*, 79–91.

(36) Pimenta, F.; Sousa, R. G.; Alves, M. A. *Biomicrofluidics* **2018**, *12*, 1–24.

(37) Zografos, K.; Burshtein, N.; Shen, A. Q.; Haward, S. J.; Poole, R. J. *J. Nonnewton. Fluid Mech.* **2018**, *262*, 12–24.

(38) Kisilak, M.; Anderson, H.; Babcock, N. S.; Stetzer, M. R.; Idziak, S. H. J.; Sirota, E. B. *Rev. Sci. Instrum.* **2001**, *72*, 4305–4307.

(39) Hudson, S. D.; Phelan, F. R.; Handler, M. D.; Cabral, J. T.; Migler, K. B.; Amis, E. J. *Appl. Phys. Lett.* **2004**, *85*, 335–337.

(40) Idziak, S. H. J.; Welch, S. E.; Kisilak, M.; Mugford, C.; Potvin, G.; Veldhuis, L.; Sirota, E. B. *Eur. Phys. J. E* **2001**, *6*, 139–145.

(41) Filik, J.; Ashton, A. W.; Chang, P. C. Y.; Chater, P. A.; Day, S. J.; Drakopoulos, M.; Gerring, M. W.; Hart, M. L.; Magdysyuk, O. V.; Michalik, S.; et al. *J. Appl. Crystallogr.* **2017**, *50*, 959–966.

(42) Rodd, L. E.; Scott, T. P.; Boger, D. V.; Cooper-White, J. J.; McKinley, G. H. *J. Nonnewton. Fluid Mech.* **2005**, *129*, 1–22.

(43) Jagdale, P. P.; Li, D.; Shao, X.; Bostwick, J. B.; Xuan, X. *Micromachines* **2020**, *11*, 1–16.

(44) Gulati, S.; Muller, S. J.; Liepmann, D. *J. Nonnewton. Fluid Mech.* **2008**, *155*, 51–66.

(45) Zhao, Y.; Shen, A. Q.; Haward, S. J. *Soft Matter* **2016**, *12*, 8666–8681.

(46) Chhabra, R. P.; Richardson, J. F. *Non-Newtonian Flow and Applied Rheology*, 2nd ed.; Butterworth-Heinemann, **2008**.

(47) Malkin, A. Y.; Semakov, A. V.; Skvortsov, I. Y.; Zatonskikh, P.; Kulichikhin, V. G.;

Subbotin, A. V.; Semenov, A. N. *Macromolecules* **2017**, *50*, 8231–8244.

(48)   Haward, S. J.; McKinley, G. H. *Phys. Fluids* **2013**, *25*.

(49)   Villone, M. M.; D'Avino, G.; Hulsen, M. A.; Greco, F.; Maffettone, P. L. *J. Nonnewton. Fluid Mech.* **2011**, *166*, 1396–1405.

(50)   Squires, T. M.; Quake, S. R. *Rev. Mod. Phys.* **2005**, *77*, 977–1026.

(51)   Akbaridoust, F.; Philip, J.; Marusic, I. *Meas. Sci. Technol.* **2018**, *29*, 1–18.

(52)   Haward, S. J.; Ober, T. J.; Oliveira, M. S. N.; Alves, M. A.; McKinley, G. H. *Soft Matter* **2012**, *8*, 536–555.

(53)   Morrison, F. A. *Understanding Rheology*; Oxford University Press, **2001**.

(54)   Macosko, C. W. *Rheology: Principles, Measurements and Applications*; Wiley-VCH, **1994**.

(55)   Chan, P. S. K.; Chen, J.; Ettelaie, R.; Law, Z.; Alevisopoulos, S.; Day, E.; Smith, S. *Food Hydrocoll.* **2007**, *21*, 716–725.

(56)   Ochowiak, M.; Broniarz-Press, L.; Rozanska, S.; Rozanski, J.; Woziwodzki, S. *Procedia Eng.* **2012**, *42*, 1849–1854.

(57)   Kennedy, J. C.; Meadows, J.; Williams, P. A. **1995**, *91*, 911–916.

(58)   Pedersen, J. S.; Schurtenberger, P. *Macromolecules* **1996**, *29*, 7602–7612.

(59)   Pedersen, J. S. *J. Appl. Crystallogr.* **2000**, *33*, 637–640.

Chapter 7 – Conclusions and Further Work

7.1 Conclusions

The work reported in this thesis is primarily concerned with the development and characterisation of millifluidic devices, with the potential to be used for a broad range of channel geometries, to investigate viscoelastic materials by small-angle X-ray scattering (SAXS). This new development expands applications of laboratory small-volume flow devices for studying soft matter materials with viscosity up to, at least, 140 Pa s. Prior to this work, the majority of materials tested in combination with micro- or millifluidics have been dilute materials, however the viscosities of such fluids are rarely published, making it difficult to compare the performance of the devices reported herein with previous literature.

A review was undertaken of the existing literature published over the last 20 years has demonstrated the suitability of micro- and millifluidic devices to investigate the effects on flow on a range of materials. The majority of research has utilised devices which are fabricated as an insert-based channel system, sealed by the application of windows over the entire chip. However, this is unsuitable for viscous materials due to the larger associated pressures exerted on the windows by the fluid. Investigations into the design of millifluidic devices, performed in this thesis, led to the development of key design rules, necessary to produce devices suitable for viscous materials. Firstly, the devices should be interchangeable and compatible with existing systems generating flow which requires connectors to enable a tight seal between tubing and channel, eliminating leakage in this area. It was found that the use of Luer locks meets the necessary requirements for the connections although according to the published literature they are rarely exploited in micro- and millifluidic devices. Secondly, an enclosed channel was found to be far superior to an insert-based design; based on the observation that enclosed channels allowed for the transport of viscous fluids along the millifluidic channel with no opportunity for leakage. Thirdly, the enclosed channels produced as a single body incorporating a relatively small window port allowed for the analysis of fluid within the channel by a range of techniques. It was found

that circular window ports, with a diameter of 15 mm and an open channel area of around 15 mm^2 were better suited to providing a seal against the channel, compared to the entire channel area being 'open'. The windows could be secured easily by use of an O-ring and threaded port and could be interchangeable and made of different materials as required for a particular experimental technique.

The majority of micro- and millifluidic devices are fabricated by top-down fabrication methods, such as soft lithography and etching techniques. However, these methods are limited by long fabrication periods, high costs and the need for expert users. Additive manufacturing methods for millifluidic devices have become increasingly popular over the last decade due to their simple, inexpensive and rapid fabrication. Nonetheless, there are very few studies that have developed robust manufacturing protocols which produce millifluidic devices solely with 3D printing. This work explored different commercially available desktop 3D printers; it was found that stereolithographic (SLA) printing provides an inexpensive, single step fabrication of millifluidic devices with sufficient resolution. An added benefit of using SLA and clear resin was the production of transparent devices. Therefore, the incorporation of window ports can be avoided for visible-light-based techniques.

The established design rules and SLA printing were employed to test two millifluidic channel geometries: a straight channel producing shear flow and a more complex cross slot producing planar extensional flow. The window material in either device could be tailored for the requirements of the measurement technique. In this work, window materials of Kapton$^®$, mica and borosilicate glass were investigated as they are most suitable for SAXS measurements. Both millifluidic devices were connected to a standard push/pull syringe pump using commercially available Luer connectors and tubing. Both geometries tested were shown to possess a laminar flow regime. This was confirmed by the calculation of Reynolds number (*Re*) and velocity profiles

from finite element analysis (FEA) simulations. A laminar flow field was also demonstrated using particle tracing.

The straight channel millifluidic device had a fluid capacity of 40 mm^3 and was found to have good sealing capabilities at low Q values, and for low viscosity fluids (with η_0 up to 0.21 Pa s). However, for materials with η_0 values higher than 0.21 Pa s, failure of the window seal was observed. Sealing of the windows failed at lower Q values as η_0 increased, in a logarithmic fashion. It was found that there was a relationship between the shear stresses exerted on the window, and the volumetric flow rate on failure.

The cross slot millifluidic device, with a fluid capacity of 83 mm^3, was found to have superior sealing capabilities to the straight channel millifluidic device; the windows remained sealed for the highest volumetric flow rate measured, 54 ml min^{-1} for both concentrations of the worm-like micelles investigated. This is thought to be due to the large expansion of the channel within the cross slot region, which leads to a substantial pressure drop.

The design of the millifluidic geometry led to highly versatile devices which can be utilised for a variety of techniques. The device can be easily incorporated within optical microscopes, allowing for birefringence and fluorescence measurements to be performed, alongside standard imaging and particle tracking techniques, often used in combination with other micro- and millifluidic devices. More importantly, small dimensions of the designed millifluidic devices allows them to be combined with X-ray, neutron and light scattering techniques including both small- and wide-angle region.

As the devices can be used in combination with a range of techniques, the millifluidic geometries can be adapted to investigate many flow-induced phenomena. For example, the straight channel millifluidic device would be suitable to measure crystallisation, orientation, morphological transitions, phase transformations, nanoparticle synthesis and droplet generation

occurring under shear flow. Whereas the cross slot millifluidic device would be suitable for studying similar phenomena triggered by extensional flow.

Two materials producing anisotropic morphologies under flow were tested within the millifluidic devices: a modified cellulose aqueous solution and polymeric worm-like micelle dispersions in water. The cellulose nanocrystals had a rod-like particle morphology with a small aspect ratio and a potential to form fibrous structures. This material demonstrated promising behaviour in birefringence studies, suggesting structural orientation under shear flow. Good correlation was observed between the POM results obtained with the straight channel millifluidic device and shear induced polarised light imaging (SIPLI) recorded for this material. Despite the strong birefringent behaviour of the modified cellulose, no anisotropic scattering was observed for this material when the millifluidic device was coupled with SAXS. This was thought to be due to a relatively low proportion of oriented material within the sample. As such, this material was not investigated with the cross-slot millifluidic device.

The worm-like micelles had a large aspect ratio, making them excellent model materials. Again, this material seemed suitable for X-ray scattering measurements due to its strong birefringent properties observed by SIPLI. In this respect, the worm-like micelles were shown to be a far superior test fluid to the modified cellulose previously discussed; with strong orientation observed by POM and SAXS with the straight channel millifluidic device. Birefringence measurements were utilised to calculate the extensional viscosity of the worm-like micelles in the cross-slot millifluidic device; the calculations indicated extensional thickening compared to the measured shear viscosity, with Trouton ratios of 257 and 17,371 for the 4 and 5 w/w % concentrations of the worm-like micelles, respectively. Synchrotron SAXS measurements enabled extensive mapping of the cross slot geometry, by taking advantage of the microfocus beam capabilities and high flux. These SAXS measurements highlighted the strong orientation of

worm-like micelles along the outlet plane, with high stability of flow over the length of acquisition.

7.2 Further work

Further improvements to the design of millifluidic devices include the incorporation of additional window ports could, which would be especially useful if temporal and lateral resolution is required. As well as this, changing the Luer locks from external, male inlets, to internal, female inlets, would lead to a design improvement as it would overcome any brittleness in the connection area. A future exploration route for millifluidic device fabrication using 3D printing methods based on metal materials would also be interesting, as it would allow production of devices for experiments involving high-temperature treatments. It would be advantageous to determine the cause of window failure by the use of pressure sensors for the straight channel millifluidic device. This would allow for greater understanding in how to optimise window sealing and viscosity limits of the device.

The devices could also be employed to study different morphologies, i.e. lamellae, or phase transitions, including crystallisation or morphology changes. Future work in this area would further highlight the applicability of the design of millifluidic devices. A third channel geometry with an expansion and contraction of the geometry would also be an area useful to explore.

A key area of future work is to fully integrate the millifluidic devices into the beamline control system at I22, Diamond Light Source to be able to offer these sample environments to soft condensed matter users.